modern aspects of electrochemistry no. 31

Edited by J. O'M. BOCKRIS, RALPH E. WHITE, and B. E. CONWAY

MODERN ASPECTS OF ELECTROCHEMISTRY

No. 31

LIST OF CONTRIBUTORS

JENS E. T. ANDERSEN
Department of Chemistry
The Technical University of Denmark
DK-2800 Lyngby, Denmark

AKIKO ARAMATA
Catalysis Research Center
Hokkaido University
Sapporo 060, Japan

GREGERS BECH-NIELSEN
Department of Chemistry
The Technical University of Denmark
DK-2800 Lyngby, Denmark

ILAN BENJAMIN
Department of Chemistry
University of California
Santa Cruz, California 95064

ANNE DORTHE BISGÅRD
Department of Manufacturing Engineering
The Technical University of Denmark
DK-2800 Lyngby, Denmark

MARIA JURKIEWICZ-HERBICH
Department of Chemistry
University of Warsaw
02-089 Warsaw, Poland

SHAHED U. M. KHAN
Department of Chemistry and Biochemistry
Duquesne University
Pittsburgh, Pennsylvania 15282-1503

JOHN C. REEVE
Department of Chemistry
The Technical University of Denmark
DK-2800 Lyngby, Denmark

JERZY SOBKOWSKI
Department of Chemistry
University of Warsaw
02-089 Warsaw, Poland

MODERN ASPECTS OF ELECTROCHEMISTRY

No. 31

Edited by

J. O'M. BOCKRIS
Texas A&M University
College Station, Texas

RALPH E. WHITE
University of South Carolina
Columbia, South Carolina

and

B. E. CONWAY
University of Ottawa
Ottawa, Ontario, Canada

KLUWER ACADEMIC PUBLISHERS
NEW YORK, BOSTON, DORDRECHT, LONDON, MOSCOW

eBook ISBN: 0-306-46910-3
Print ISBN: 0-306-45650-8

Created in the United States of America

Visit Kluwer Online at: http://kluweronline.com
and Kluwer's eBookstore at: http://ebooks.kluweronline.com

Preface

Prof. Jerzy Sobkowski starts off this 31st volume of *Modern Aspects of Electrochemistry* with a far-ranging discussion of experimental results from the past 10 years of interfacial studies. It forms a good background for the two succeeding chapters.

The second chapter is by S. U. M. Khan on quantum mechanical treatment of electrode processes. Dr. Khan's experience in this area is a good basis for this chapter, the contents of which will surprise some, but which as been well refereed.

Molecular dynamic simulation is now a much-used technique in physical electrochemistry and in the third chapter Ilan Benjamin has written an account that brings together information from many recent publications, sometimes confirming earlier modeling approaches and sometimes breaking new territory.

In Chapter 4, Akiko Aramata's experience in researching single crystals is put to good advantage in her authoritative article on underpotential deposition.

Finally, in Chapter 5, the applied side of electrochemistry is served by Bech-Neilsen *et al.* in the review of recent techniques for automated measurement of corrosion.

J. O'M. Bockris, Texas A&M University
B. E. Conway, University of Ottawa
R. E. White, University of South Carolina

This Page Intentionally Left Blank

Contents

Chapter 3

MOLECULAR DYNAMIC SIMULATIONS IN INTERFACIAL ELECTROCHEMISTRY

Ilan Benjamin

Chapter 4

UNDERPOTENTIAL DEPOSITION ON SINGLE-CRYSTAL METALS

Akiko Aramata

Chapter 5

AUTOMATED METHODS OF CORROSION MEASUREMENT

Gregers Bech-Nielsen, Jens E.T. Andersen, John C. Reeve,
Anne D. Bisgård and Lars Vendelbo Nielsen

This Page Intentionally Left Blank

MODERN ASPECTS OF ELECTROCHEMISTRY

No. 31

This Page Intentionally Left Blank

1

Metal/Solution Interface: An Experimental Approach

Jerzy Sobkowski and Maria Jurkiewicz-Herbich

Department of Chemistry, Warsaw University, Warsaw, Poland

I. INTRODUCTION

The electrical double layer has been dealt with in countless papers and in a number of reviews, including those published in previous volumes of the Modern Aspects of Electrochemistry series.[1–9] The experimental double layer data have been reported and commented on in several important works in which various theories of the structure of the double layer have been postulated. Nevertheless, many double layer-related problems have not been solved yet, mainly because certain important parameters describing the interface cannot be measured. This applies to the electric permittivity, dipole moments, surface density, and other physical quantities that are influenced by the electric field at the interface. It is also often difficult to separate the electrostatic and specific interactions of the solvent and the adsorbate with the electrode. To acquire necessary knowledge about the metal/solution interface, different metals, solvents, and adsorbates have been studied.

In the earlier concepts of the interface structure, the metal was treated as a reservoir of electrons, uniformly distributed in the bulk of the phase. Spatial distribution of charges was considered mainly on the solution side. No such considerations were made for the solid electrodes, except for the

Modern Aspects of Electrochemistry, Number 31, edited by John O'M. Bockris *et al.*
Plenum Press, New York, 1997

case of semiconductors. The charge distribution in the metal, near the interface, was taken into account when the jellium model of the metal was proposed. This model was used to formulate a novel view of the double-layer structure (e.g., Refs. 9 and 10).

Significant progress in understanding the structure of the metal/solution interface was achieved by studying electrochemical processes on well-defined planes of single crystals.[6] Early studies on single-crystal electrodes were not satisfactorily reproducible because of difficulties in growing the crystals, inaccurate cutting, and insufficient control of the desired plane orientation. Later, the techniques of crystal preparation were much improved and the number of papers dealing with adsorption and electrochemical reactions on single-crystal electrodes increased substantially.

It appears that restructuring of the metal, reorientation of solvent molecules, adsorption of the electrolyte species and coadsorption of organics, and preoxidation and oxidation of the surface can be better studied on monocrystals than on more complex polycrystalline electrodes.[11] Moreover, an uncertainty inherent in determining surface roughness often makes quantitative comparisons of the polycrystalline data difficult. This is because the quantities under scrutiny (e.g., current density and differential capacity) usually have to be referred to the real surface area of the electrode. The problem of roughness also exists in the case of monocrystalline planes. However, careful polishing of the surface usually limits the problem and results in the real surface of the electrode approaching the geometrical area. Still, the lack of an unambiguous method for measuring roughness often seriously limits determination of surface concentration.

Even refined electrochemical methods cannot alone provide full information about the molecular structure of the metal/ solution interface. Hence, many nonelectrochemical techniques have been developed in the past few decades to study the double layer. They include spectroscopic, microscopic, radiochemical, microgravimetric, and other methods. A combination of electrochemical (chronovoltammetry, chronocoulometry, impedance spectroscopy, etc.) and nonelectrochemical methods is often used in studying mechanisms of the electrode process.

Two main approaches to the investigation of the metal/solution interface can be distinguished: molecular and thermodynamic. In the first

approach, the interfacial state of the system is studied by various direct methods, usually quite recent. In the thermodynamic approach, the energetics of metal–solvent and metal–adsorbate interactions is investigated on the basis of parameters determined at the equilibrium.

The aim of this review is to present achievements and difficulties of electrochemical research focused on the structure of the metal/solution interface. The literature cited is generally limited to recent reviews and original papers, with relatively little attention paid to the historical background. A more complete list of references on the subject was given by Bockris and Khan in their book.[12]

II. MOLECULAR APPROACH TO THE METAL/SOLUTION INTERFACE

1. Double-Layer Structure: General Considerations

For a long time, the electric double layer was compared to a capacitor with two plates, one of which was the charged metal and the other, the ions in the solution. In the absence of specific adsorption, the two plates were viewed as separated only by a layer of solvent. This model was later modified by Stern, who took into account the existence of the diffuse layer. He combined both concepts, postulating that the double layer consists of a rigid part called the inner—or Helmholtz—layer, and a diffuse layer of ions extending from the outer Helmholtz plane into the bulk of the solution. Accordingly, the potential drop between the metal and the bulk consists of two parts:

$$\Delta\phi = (\phi_M - \phi_{OHP}) + (\phi_{OHP} - \phi_s) = \Delta\phi_i + \Delta\phi_d \qquad (1)$$

where ϕ_M, ϕ_s, and ϕ_{OHP} are potentials of the metal surface, solution in the bulk, and outer Helmholtz plane, respectively; $\Delta\phi_i$ and $\Delta\phi_s$ are the potential drops, correspondingly in the inner and diffuse parts of the double layer.

Assuming that the double layer is composed of two capacitors, the inner and the diffuse one, connected in series, which have the capacitanties C_i and C_d, respectively, the measured total capacitance C can be expressed[13]:

$$\frac{1}{C} = \frac{1}{C_i} + \frac{1}{C_d} = [r/(\varepsilon_i \varepsilon_0) + (a - r)/(\varepsilon_{IHP-OHP}\varepsilon_0)] + (1/\kappa)/(\varepsilon \varepsilon_0) \quad (2)$$

where ε_i is the electric permittivity of solvent at the surface, ε_0 is the electric permittivity of a vacuum ($\varepsilon_0 = 8.854\ 10^{-12}$ F/m), a is the outer Helmholtz layer thickness, r is the inner layer thickness, $\varepsilon_{IHP-OHP}$ is the permittivity of the solvent between the inner and outer Helmholtz planes, ε is the permittivity of the solvent in the bulk, and $1/\kappa$ is the Debye length.

According to this model, and in the absence of specific adsorption, the adsorbed solvent molecules are located in the inner Helmholtz plane, the thickness of which is determined by the radius of the molecule. At the same time, solvated ions define the location of the outer Helmholtz plane. Other ions, charged oppositely to the surface charge, are smeared out in the diffuse layer.

However, in Eq. (2) as many as five parameters (r, ε_0, a, $\varepsilon_{IHP-OHP}$ and $1/\kappa$) are adjustable and their values are not precisely known. For example, the Debye length is calculated assuming that the electric permittivity near the ions has the same value as in the bulk. However, the permittivity of water decreases when it is brought closer to the ions or charged surface because the structure of water is disturbed by the electric field. It was estimated[14] that ε is restored to 90% of the bulk value when the distance from the electrode becomes ca. 6 Å. A similar conclusion is valid for ion–water systems. In a 0.1*M* solution of a 1:1 electrolyte ($1/\kappa = 9.6$ Å), the permittivity of water is regarded as undisturbed, but for higher ion concentrations (e.g., a 1*M* solution of a 1:1 electrolyte, $1/\kappa = 3$ Å), the value of ε is much lower than in the bulk. This may be a source of error in calculating the diffuse layer capacitance when the concentration and the charge of ions increase. It should be stressed that the concentration of ions in the diffuse layer is greater than in the bulk though it is often not taken into account in calculating the diffuse layer capacitance C_d.

The presence of the diffuse layer determines the shape of the capacitance-potential curves. For a majority of systems, models describing the double-layer structure are oversimplified because of taking into account only the charge of ions and neglecting their specific nature. Recently, these problems have been analyzed using new theories such as the modified Poisson–Boltzmann equation,[15] later developed by Lamperski.[16,17] The double-layer capacitanties calculated from these equations are

generally higher than those obtained using a simple Gouy–Chapman theory, the values of the inner layer capacitanties calculated from Grahame model, and the results of an estimate of the metal and solvent contributions to the double-layer capacitance proposed by Amokrane and Badiali.[9]

The problem of influence of the electric field intensity on the permittivity of solvents has been discussed in many papers. The high permittivity of water results from the intermolecular forces and is a cumulative property. The electric field intensity is the lowest at the potential of zero charge (pzc), thus allowing water molecules to adsorb in clusters. When the electrode is polarized, the associated molecules, linked with hydrogen bonds, can dissociate due to a change in the energy of their interaction with the electrode. Moreover, the orientation of water molecules may also change when the potential is switched from one side of the pzc to the other.

The value of the electric permittivity of water in the inner part of the double layer is commonly accepted as equal to 6. A much higher capacity of the inner layer at the Ga/solution interface was explained by the weak interaction of gallium with water, leading to a high value of ε_i.[18] As shown by high-frequency measurements of the electric permittivity ($\nu = 10^8$ Hz), the value of ε decreases from about 80 to 5.9. This is brought about by lack of the dipole correlation effects, which at low frequencies are responsible for the high permittivity values of polar solvents.[19]

A similar conclusion arises from the capacitance data for the mercury electrode at far negative potentials ($q << 0$), where anions are desorbed. In this potential range, the double-layer capacitance in various electrolytes is generally equal to ca. 0.17 F m^{-2}.[20] Assuming that the molecular diameter of water is 0.31 nm,[21] the electric permittivity can be calculated as $\varepsilon_i = Cd/\varepsilon_0 = 5.95$. The data on thiourea adsorption on different metals and in different solvents have been used to find the apparent electric permittivity of the inner layer. According to the concept proposed by Parsons,[22] thiourea can be treated as a probe dipole. It has been calculated for the Hg electrode that at $\sigma_M = 0$, ε_i is equal to 11.4,[22] 5.8,[23,24] 5.1,[25] and 10.6[26] in water, methanol, ethanol, and acetone, respectively.

In the presence of ions, the permittivity of a solvent changes not only in the bulk but also at the interface. The energy of the dipole–dipole interaction can be approximated by the relation $U_{d-d} = -2\mu^2/r^3$, and for water is equal to 0.25 10^{-19} J. The energy of the charge–dipole interaction, $U = -ze_0\mu/r^2$, is much higher and for water reaches 1 10^{-19} J. The fact that

the charge–dipole interaction is stronger than the dipole–dipole interaction results in a change of the solvent structure and dielectric properties of solvents at the interface.

Another problem is an uncertainty involved in the estimation of the double-layer thickness. This thickness is often calculated from the size of the solvent molecule, using macroscopic data (e.g., the molar volume) under a doubtful assumption about the shape of the molecule, which is often taken as spherical. There are some indications, also provided by modern experimental techniques (X-ray spectroscopy, quartz crystal microbalance, QCM), that the density of water near the interface can change drastically (see later discussion).

The contribution of the metal to the capacitance of the double layer was neglected for a long time. It was considered that electrons in the metal are uniformly distributed and assumed that the capacitance of the double layer in the absence of specific adsorption is the sum of capacitanties of the metal and the solvent connected in series

$$C_i^{-1} = C_M^{-1} + C_s^{-1} \tag{3}$$

Since the metal can be treated as a nearly perfect conductor, C_M is high compared with C_s and cannot influence the value of the measured double-layer capacitance. The role of the metal in the double layer structure was discussed by Rice,[27] who suggested that the distribution of electrons inside the metal decides the properties of the double-layer. This concept was later used to describe double-layer properties at the semiconductor/electrolyte interface. As shown later, the electron density on the metal side of the interface can be changed under the influence of charged solution species (dipoles, ions).[28]

According to Bockris and Habib,[29] the potential difference at the metal/solution interface at pzc is a result of the contribution of two components: the surface potential (electron overlap) of the metal g_0^M and solvent dipoles oriented at the electrode surface, g_0^s. The value of g_0^s cannot be experimentally measured because the absolute value of the electrode potential is not known. However, the value of g_0^M can be estimated from the relation

$$g_0^M = \chi^M + \delta\chi_0^M \tag{4}$$

where χ^M is the surface potential of the metal in a vacuum

$$F\chi^M = \Phi + \mu_e^M \tag{5}$$

Here Φ is the work function, μ_e^M is the chemical potential of electrons in the metal, and $\delta\chi_0^M$ is the change of the metal surface potential upon contact with the solution. Hence, the modification of electronic distribution in the metal is due to the adsorbed solvent molecules, which change the surface potential of the metal, $\delta\chi_0^M$. A similar concept was developed in numerous works of Trasatti (e.g., Ref. 30). The value of $\delta\chi_0^{Hg}$ at $\sigma = 0$ was estimated as equal to –0.31 V and assumed to be independent of the kind of the solvent.[30] For Cd and Zn, the $\delta\chi_0^M$ values were estimated to be –0.45 V and –0.37 V, respectively.[29]

Another approach to the double-layer structure is based on the jellium model of the metal.[10,31] Owing to the small mass of electrons, they can spill over the metal surface, which can be no longer treated as a rigid wall. The electronic density decreases from a nonzero value in the bulk of the metal down to zero in the double layer. The surface region of jellium is a few angstroms thick. The electronic density in the metal as well as the distance between the metal and the solvent molecule change with charge. The effective potential acting on solvent molecules at the interface is the mean of mutual interactions of the metal and the solvent and determines the closest approach of the solvent molecule to the surface. The location of the outer Helmholtz plane is described by $D = d + r_0$, where d is the closest approach of the solvent molecule to the surface and r_0 is the radius of the molecule. The variation of d with the charge[31] and the contribution of C_m to C_i[32] were calculated for an Ag electrode. The contribution of C_s could be estimated from the calculated C_m and experimental C_i values. It was further assumed[33] that C_s has a constant value independent of the metal (at pzc). Hence, the contribution of C_m could be calculated for different metals from experimental values of C_i.

Application of the model for various solvents adsorbed on an Hg electrode[34] showed that the plots of C_s vs. electrode charge have similar shapes. It was concluded[34] that the value of C_s near the maximum is determined by the size of the solvent molecule whereas the position of the maximum depends on the orientation of the molecule induced by nonelec-

trostatic interaction specific to each metal–solvent couple. The molecular and orientational parts cannot be separated experimentally.

The role of the metal electrons in determining properties of the metal/electrolyte solution interface was reviewed by Kornyshev, who presented and discussed an alternative approach to the jellium model.[35] As stated by Kornyshev, the jellium model, which is correct for the interpretation of capacity measurements, appears to be too rough to explain the data obtained with modern techniques, such as many spectroscopic and microscopic techniques (see later discussion).

2. Solid Metal/Electrolyte Interface

The structure of the solid electrode/electrolyte interface is more complex than in the case of the liquid mercury electrode. The reason is that the range of potentials of the so-called ideal polarizability is usually much narrower on solids, due to hydrogen evolution and surface oxidation at the negative and positive ends of the polarization range, respectively. Another problem is related to the influence of the crystallographic structure of the metal on the double-layer structure and the electrochemical reactions. At a given applied potential, the metallic electrode surface is equipotential, but as a result of different surface irregularities, the charge density can vary to a great extent and the double-layer structure becomes only a resultant of the "double-layers" of individual kinks, steps, and terraces. Voltammetric curves, which are very sensitive to the surface structure, depend on orientation of the monocrystalline electrode and the surface roughness. Hence, the preparation of the electrode is of great importance when studying the properties of the interface.

(i) Polycrystalline Electrodes

The structure of a polycrystalline electrode depends on its preparation. Usually the rough electrodes are prepared by electrochemical deposition of a given metal onto a suitable substrate. Microcrystals present in polycrystalline samples are randomly oriented on the surface. Most likely, not only basal but also higher Miller-index planes should be considered in anticipating the final structure of the electrode surface.[36] It was shown that the structure of the platinized platinum surface depends strongly on the platinization conditions, e.g., on the concentration of the platinization solution and current densities used.[37] Cyclic voltammetry in the hydrogen

adsorption-desorption range of potential was used as a sensitive probe of the state of the platinum surface. The range of polarization potentials and the scanning rate may favor the appearance of certain planes on the surface of a polycrystalline electrode.

It has been demonstrated by Arvia and his co-workers that surfaces of preferred crystallographic orientation can be obtained by fast repetitive potential perturbations.[38] After a very fast cyclic polarization in the range 0.04 to 1.50 V, peaks characteristic of Pt(111) and Pt(100) become more pronounced, whereas a peak typical for Pt(110) disappeared.[39] Voltammetric curves indicating the change of the Pt polycrystalline electrode structure are shown in Fig. 1.

The changes in reorientation of surface atoms were explained using the dynamic model of the crystal space lattice. It was assumed that during anodic polarization, when the oxidation of adsorbed water is taking place, atoms oscillate mainly in a direction perpendicular to the electrode surface. This process leads to periodic separation of atoms in the first surface layer. Thus, the location of atoms in different orientations is possible. It was stated that various techniques of electrode pretreatment used for

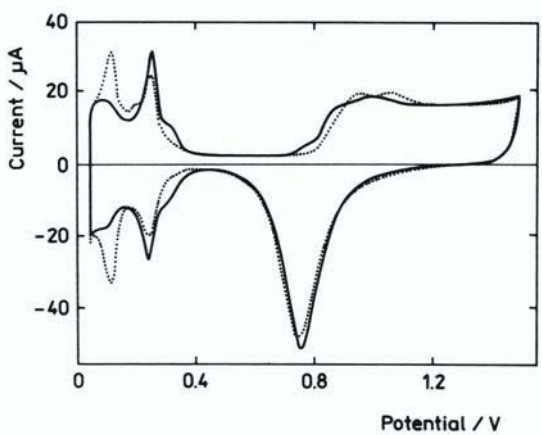

Figure 1. Voltammograms of Pt electrodes at 0.1 V s^{-1} in 0.5*M* H_2SO_4 at 25°C. (. . . .), untreated polycrystalline platinum; (—) polycrystalline platinum after 6 min of repetitive triangular potential sweeps.[39]

cleaning the electrode surface (electrochemical polarization, flame annealing, ion sputtering), affect the distribution of the crystalline surface sites.[40]

There are two types of roughness of the electrode surface: the macro- and microroughness. The macroroughness can be eliminated by mechanical polishing of the surface. A highly reflective surface ensures the absence of macroroughness. The microroughness can be partly reduced by annealing the electrode at high temperatures in an inert gas atmosphere. The real surface area of an annealed electrode is smaller than the freshly polished one. Though the formation of different structures of the electrode surface is possible, the long-lasting cyclic anodic–cathodic polarization leads to reproducible voltammograms of the polycrystalline platinum and gold electrodes. Hence, the results of studies of the double-layer structure and electrosorption on polycrystalline surfaces of platinum and gold should be viewed as reliable.

(ii) Determination of Electrode Roughness

The lack of knowledge of precise values of the roughness factor makes it difficult to compare data reported from different studies. This applies in particular to the double-layer capacity data, the values of surface concentration of the adsorbates, and the rates of electrochemical reactions. Therefore, the question of how to determine the real surface of the electrode is of crucial importance. A survey of various methods for determining roughness was given by Trasatti and Petrii.[41] For noble metal electrodes, the charges of hydrogen deposition and surface oxide formation can be utilized in real-surface determination.[42]

In the case of platinum electrodes, the charge of hydrogen deposition is usually used. The assumption that one hydrogen atom is adsorbed on one adsorption site of platinum was verified experimentally by checking hydrogen desorption charges, obtained from the charging curves, against the Brunauer, Emmett and Teller isotherm measurements.[43] The determination of the real surface area of a polycrystalline gold electrode from the reduction charge of the anodically formed oxide is generally accepted. The situation is not so simple for other noble metals because voltammetric peaks are often poorly separated.

Capacity measurements are frequently used to determine real surface area. In the measurements, alternating current signals are employed, with

rough solid electrodes usually showing a frequency dispersion. The influence of electrode roughness and electrolyte concentration on the frequency dispersion was studied for the **Pt–$HClO_4$** system by Bidoia *et al.*[44] The impedance of a resistance-capacitance (RC) circuit in series and an ideally polarizable solid metal/solution interface is given by the equation

$$Z(\omega) = R + (j\omega C)^{-1} \tag{6}$$

Here j is the imaginary unit, ω is the angular frequency, and C is the capacitance. For solid electrodes, however, the impedance response deviates from a purely capacitive one and the empirical equation should be used

$$Z(\omega) = R + Q(j\omega)^{-n} \tag{7}$$

Here Q and n are constants and the term $Q(j\omega)^{-n}$ is "the constant phase element." The value of n represents how much the real system deviates from the ideal one. It was shown that the value of n increases with increasing electrolyte concentration until a constant value is reached at 0.5 mole L^{-1}.[44] The value of n decreases with the surface roughness of a Pt electrode, which was determined by measuring the charge of hydrogen adsorption. It was found that in some cases polishing with a coarser abrasive gives a less rough surface than a fine-grade abrasive.[44] According to the authors' opinion, the particles of the coarser abrasive may open larger grooves, thus causing a large number of smaller grooves to disappear and the roughness factor to drop.

The electrode roughness factor can be determined by using the capacitance measurements and one of the models of the double layer. In the absence of specific adsorption of ions, the inner layer capacitance is independent of the electrolyte concentration, in contrast to the capacitance of the diffuse layer C_d, which is concentration dependent. The real surface area can be obtained by measuring the total capacitance C and plotting C^{-1} against C_d^{-1}, calculated at pzc from the Gouy–Chapman theory for different electrolyte concentrations. Such plots, called Parsons–Zobel plots, were found to be linear at several charges of the mercury electrode.[45]

The procedure can be further simplified by plotting C^{-1} **vs.** $c^{-1/2}$ (c is the concentration of a nonadsorbing electrolyte) because for a 1:1 electrolyte $C_d^{-1} = 3.73\ 10^{-4}\ c^{-1/2}$ at pzc and 25°C.[46] The real surface area

of the electrode A and the total inner-layer capacitance $A C_i$ can be calculated from the slope and the intercept of such a plot, respectively. The method is valid for homogeneous surfaces for which the measured capacitance is frequency independent. It can be used for single-crystal electrodes with a small number of surface defects. For polycrystalline electrodes, a curvature of the plot C^{-1} vs. C_d^{-1} is observed[47] because of the surface inhomogeneity. For metals of low melting point, characterized by relatively high mobility of surface atoms, the use of the method may be acceptable.[41] A proper choice of the nonadsorbing supporting electrolyte is of key importance and may depend on the electrode used. For example, fluoride-based electrolyte ions are suitable for studies on mercury but not on silver because F^- ions tend to adsorb on the latter metal.[48]

Determination of the real surface area of electrodes may be carried out using underpotential deposition of metals. The method is applied for metals for which there is no satisfactory separation between the potentials of hydrogen desorption and surface oxidation. The method, often used to determine the roughness factor of silver and copper, gives the number of surface-active sites rather than the true area. Moreover, it is necessary to assume that the deposited ion is discharged completely (a partial charge transfer is neglected). The charge of either deposition of ions or stripping of the metal is determined voltammetrically. For single-crystal surfaces, the shape of a voltammogram depends strongly on the crystallographic orientation of the plane. For instance, the desorption of lead from terraces of the flat (111) plane of gold gives rise to a narrow peak whereas a broad and positively shifted peak is observed on the stepped (110) plane.[49] Moreover, the narrow peak on the (111) plane splits at high sweep rates due to limitations in the charge transfer rate. Generally, cyclic voltammetry is very sensitive to the surface structure, especially in the potential range where no electron transfer across the interface takes place, i.e., in the potential range of the ideal polarizability of the electrode.*

*A voltammetric curve can be viewed in electrochemistry as the emission or absorption spectra in spectroscopy. The current density (i.e., the number of charges per unit of time and area) corresponds to the emitted or absorbed light intensity (the number of quanta per unit of time and area). Finally, when multiplied by the Faraday constant, the potential defines the energy of the system and can thus be treated as an analog of the light frequency, which can also gives energy when multiplied by the Planck constant.

(iii) Monocrystalline Electrodes

Observations of the effect that the state of the electrode surface had on the structure of the double layer and adsorption and electrochemical reactions focused the attention of electrochemists on studying electrode processes on well-defined surfaces of single crystals. A strong effect of the plane orientation of platinum on the shape of voltammetric curves was shown by Will and Knorr long ago.[50] Polycrystalline electrodes can be viewed as a sum of different planes, not necessarily the basal ones, randomly distributed on the surface. This is the reason why there is no clear relation between the properties of the polycrystalline and single-crystal electrodes. In the early stages of single-crystal electrochemistry, the procedures of surface preparation were different and the experimental results were barely reproducible. Dramatic differences in the voltammograms of the Pt(111) electrode given by Clavilier[51] and Ross[52] may serve as an example (see Fig. 2).

Further studies showed how the method of surface preparation, including polishing, annealing, and cyclic polarization, influences electrochemical properties of the electrode. Moreover, the preparation of a single-crystal plane depends on the metal studied and calls for not only professional knowledge but a dose of artistry as well. It seems that the procedure proposed by Clavilier[51] that involves accurate orientation of the monocrystal; fixing it in a desired position; polishing, annealing, and quenching in extra-pure water, followed by a quick transfer of the electrode under protection of a drop of water into the electrolytic cell, has actually become a standard method in many laboratories. To fulfill the requirement that only the studied face remain in contact with the solution, it is necessary to mount the monocrystal in a proper holder made from a material that will not contaminate the system. No such material is needed in the so-called meniscus method[53] in which, owing to the surface tension of the solution, only the face of interest touches the solution.

Pretreatment of electrodes by cyclic polarization needs special care because the surface structure depends on the number of cycles and the potential range of polarization. It was shown that during the polarization of Au and Pt electrodes, up to ca. 1.5 V (vs. Normal Hydrogen Electrode) in $1M\ H_2SO_4$, the quantities of dissolved metals corresponded to the anodic charges of 3.6 and 8.9 $\mu C\ cm^{-2}$ per cycle, respectively.[54] The

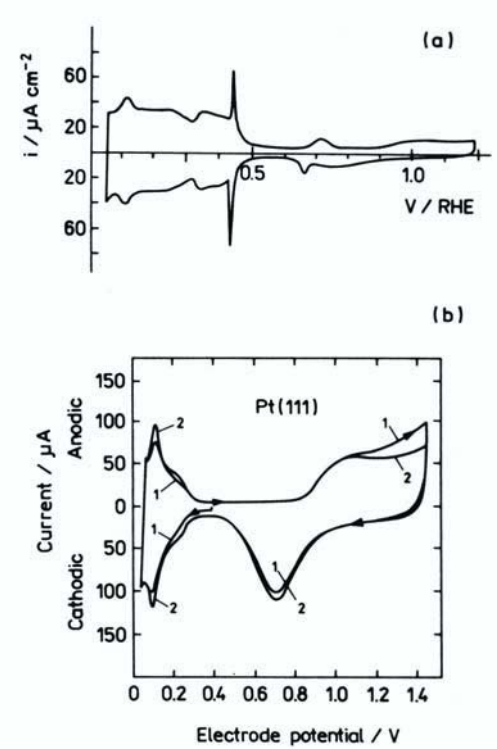

Figure 2. Comparison of voltammograms for the Pt(111) electrode in 0.5*M* H_2SO_4 given by (a) Clavilier *et al.*[51] and (b) by Ross.[52] Sweep rate 50 mV s^{-1}.

dissolution and redeposition of surface atoms greatly affect the electrode surfaces. Even when the polarization potential does not exceed the onset potential of surface oxidation, a high number of pretreatment cycles may completely change the shape of the voltammograms.[55]

The sensitivity of the planes of single crystals to cyclic polarization depends on the kind of the metal and the crystallographic orientation of the plane itself. Metals melting at low temperatures (e.g., Sb, Pb, and Zn), with mobile surface atoms, are less prone to surface reconstruction than metals melting at high temperatures (e.g., Pt, Au, Cu, and Ag). This is

reflected by the strong dependence of the potential of a zero charge on the crystallographic orientation in the case of the latter metals. For example, the pzcs of silver planes (100) and (110) in KPF_6 solution, which is considered a nonadsorbing electrolyte, are equal to –0.865 and –0.975 V vs. Saturated Calomel Electrode, respectively.[48]

The surface reconstruction of Au and Pt monocrystals has been intensively studied by Kolb (see Ref. 56). For example, the structural transition of Au(100) with fourfold symmetry to a hexagonal close-packed structure was observed during heat treatment as well as during cathodic polarization.[56] The reconstructed plane, similar to the (111) surface, shows little deformation due to the interaction with the underlying bulk atoms of Au(100) crystal. Though the reconstructed surface is thermodynamically more stable than the unreconstructed one, the reconstruction can be removed by the adsorption of anions as well as by anodic polarization. Since the concentration of atoms on a reconstructed surface is higher than that on the unreconstructed one, such a transition leads to an increase in the electrode roughness.

The more densely packed reconstructed surface has a higher work function and a more positive pzc than the unreconstructed one.[57] During cyclic polarization, the shape of voltammograms changes markedly if the scan enters higher positive potentials. The current charge associated with the removal of the reconstruction must be accounted for in the electrochemical studies on reconstructing surfaces.

3. Methods Used to Study Properties of the Metal/Solution Interface: Role of the Solvent and the Metal

Fundamental issues facing modern interfacial research are as follows:

- the orientation of solvent molecules on the electrode surface,
- the energy of the solvent–metal bond and its variation with the electrode potential,
- the correlation of the metal–solvent interaction with the solvent–solvent and solvent–ion interactions in the bulk,
- the role played by a metal's surface properties, such as roughness factor and crystallographic orientation,

the effect of an electric field of high intensity (existing in the double-layer region) on the properties of the solvent (e.g., electric permittivity, dipole moment, deformation of the adsorbed species, and donor–acceptor features), as well as on the properties of the metal (e.g., electronic structure and surface reconstruction).

Most earlier papers dealt with the mercury electrode because of its unique and convenient features, such as surface cleanness, smoothness, isotropic surface properties, and wide range of ideal polarizability. These properties are generally uncharacteristic of solid metal electrodes, so the results of the solid metal/electrolyte interface studies are not as explicit as they are for mercury and are often more controversial. This has been shown by Bockris and Jeng,[58] who studied adsorption of 19 different organic compounds on polycrystalline platinum electrodes in 0.01*M* HCl solution using a radiotracer method, ellipsometry, and Fourier Transform Infrared Spectroscopy. The authors have determined and discussed adsorption isotherms and the kinetics of adsorption of the studied compounds. Their results were later critically reviewed by Wieckowski.[59]

Of all the solvents used by electrochemists, water is the most important for understanding the metal/solution interface. Therefore, it is the behavior of water molecules at the interface that is mainly discussed in the following section. The role of other solvents in the determination of properties of the metal/solution interface is described in detail in Section 2.

Information about the metal/solution interface can be obtained by different electrochemical methods or, in a more direct fashion, by using a number of nonelectrochemical techniques. The application of different techniques in studying the metal/solution interface is briefly discussed below, mainly for aqueous solutions.

(i) The Work Function

According to a proposed definition,[60] the electron work function Φ of a metal M is the minimum work needed to extract an electron from the Fermi level of the metal across a surface carrying no net charge, and to transfer it to infinity in a vacuum. The work function for polycrystalline metals cannot be precisely determined because it depends on the surface structure; it is different for smooth and rough surfaces, and for different

monocrystalline planes. Hence, the measured work function of a polycrystalline metal is a superposition of work functions of various patches of the metal surface of different morphologies and orientations.[61] It was shown[62] that the work function of Pt, Au, and Ag electrodes changes following polarization at different potentials in an $HClO_4$ solution and subsequent transfer to an ultrahigh vacuum (UHV) system. However, despite these limitations, the measurements of the work function provide important information about the interface structure.

Since the work function is very sensitive to contaminants, the most reliable measurements are done in ultrahigh vacuum conditions. From the determination of the electron work functions of Fe, Co, Ni, Cu, Au, and other metals in the presence of water adsorbed from the gas phase, it follows that water molecules are oriented with oxygen atoms toward the metal surface.[63] The method is very sensitive to the presence of water. For example, upon adsorption of 3×10^{13} molecules of water per square centimeter of Co film (4% of a monolayer), the work function value is decreased by ca. 0.3 eV.[64] However, these measurements were done at 77 K, meaning that adsorbed water was likely to be in a crystalline or amorphous ice form. Hence, the quoted results are of limited value to understanding the metal–water system in electrolyte solutions.

In electrochemical conditions, the electrons are transferred from the metal to the solution rather than to a vacuum. Moreover, the metal/solution interface is charged and the potential difference between the metal and the solution should be taken into account. The situation is simplified when the work function and uncharged interface are considered. The relationship between the work function and potential of zero charge was proposed nearly 30 years ago by Bockris and Argade[65] and by Frumkin (see e.g., Ref. 66) and later intensively discussed by Trasatti (e.g., Refs. 5, 21, 67). The relationship is given by the equation

$$E = \Phi^M/e + \delta X_0^M - g^s(\mathrm{dip})_0 - K \tag{8}$$

Here K is a constant depending on the reference electrode and the solvent (for a study of the dependence of $E_{\sigma=0}$ on Φ^M, knowledge of the term K is not necessary). Equation (8) was checked several times for different metals and solvents.[67] General rules regarding the dependence of the pzc on the electrode structure are as follows: (1) a more densely packed face

has more positive pzc because of a higher work function value and (2) the rougher the surface on the atomic scale, the more negative the pzc because of a lower work function value.[6]

The orientation of molecules at the interface depends on an interaction with both the surface and the molecules in the liquid phase, and also on the interaction within the adsorbed layer. The interaction of molecules with the electrode is stronger the weaker their interaction with other molecules in the bulk. The correlation between $E_{\sigma=0}$ and Φ^M is linear but different for the transition metals and the *sp* metals. Owing to the tendency to form chemisorption bonds, transition metals bind water molecules more strongly than the *sp* metals.

Expression $\delta X_0^M - g^s(\text{dip})_0 = X$ was given the name "interfacial parameter" by Trasatti.[68] This parameter is not amenable to direct experimental determination; instead, a relative value of X^M can be estimated from a plot of the potential of zero charge vs. the electron work function. If mercury is taken as a reference metal ($E_{\sigma=0}$ and Φ for mercury are known with high accuracy), then

$$\Delta X^M = X^M - X^{\text{Hg}} \tag{9}$$

The X^M values for all metals studied are more negative than for Hg. A higher value of X indicates a stronger interaction of water with the metal surface.[68] The interfacial parameter strongly depends not only on the kind of metal but also on the structure of the electrode surface.

Since water molecules interact with a metal surface through their oxygen atoms, the enthalpy of the metal oxide formation ΔH_{M-0} should be a measure of the energy of the metal–water interaction. Hence, the ΔX values should correlate well with the enthalpy of metal oxide formation, corrected for metal–metal bond breaking: $\Delta H'_{M-0} = \Delta H_{M-0} - \Delta H_{M-M}$.[68] Linear $\Delta H'_{M-0}$ vs. ΔX plots of different slopes have indeed been found for various metals. The data supported a general tendency that $\Delta H'_{M-0}$ is lower for metals characterized by higher ΔX values. The rule did not apply to Au, Ag, and Cu. Therefore, it was suggested that for the latter metals, high values of ΔX are mainly due to the polarizability of their surface electrons and that the orientation of water molecules plays only a minor role.[68]

A similar correlation was found between the Gibbs energy of adsorption $\Delta G°_{ads}$ and the interfacial parameter ΔX at $\sigma = 0$.[67] $\Delta G°_{ads}$ includes the adsorbate–solvent in the bulk (B–S), the adsorbate–metal surface (B–M), and the solvent–metal (S–M) interactions

$$\Delta G°_{ads} = \Delta G°(B–S) + \Delta G°(B–M) - n\Delta G°(S–M) \tag{10}$$

where n is the number of solvent molecules displaced from the surface by one molecule of the adsorbate. It was stated that $\Delta G°_{ads}$ should decrease as $E_{\sigma=0}$ becomes less positive, i.e., from the more compact (111) to the more open (100) face.[67]

The structure of the interface should be reflected by the temperature coefficient of the pzc, according to the equation

$$dE^{M}_{\sigma=0}/dT = (1/e)\, d\Phi^{M}/dT + dX^{M}/dT \tag{11}$$

Because both right-hand terms in Eq. (11) are of comparable magnitude and most likely two bear opposite signs ($d\Phi^{M}/dT$ may be less than zero), one cannot judge unequivocally what the orientation and surface structure of water molecules on the metal surface may be.[67] The situation appears simpler in the case of single-crystal electrodes, although experimental results obtained with such electrodes are not always consistent. For example, values of $dE^{Ag}_{\sigma=0}/dT$ reported for single crystals of silver differ even in sign: the $dE^{Ag}_{\sigma=0}/dT$ values were found to decrease[69] on going from the (111) to (100) face, whereas the opposite values were reported in Ref. 70. Moreover, the differences apply not only to the experimental results but also to the interpretation of the data.[67]

Similar discrepancies can be found in regard to the inner-layer capacitance at $\sigma = 0$. For instance, the value of C_i reported by Vitanov *et al.*[71] is lower for Ag(111) than for Ag(100), the opposite of what was reported by Valette.[72] The reason for such discrepancies is not clear but they may be due to different roughness of the electrode surface, different supporting electrolytes used, and various methods of preparing the single crystals. Valette showed[73] that fluorides are specifically though weakly adsorbed on silver electrodes, an effect not observed by Vitanov *et al.*[71]

In a very extensive and thorough study of silver electrodes in a nonadsorbing KPF_6 electrolyte, Valette determined the inner-layer capacities of Ag(111), Ag(100), and Ag(110) to be equal to 77, 92, and 112 μF

cm^{-2}, respectively.[74] From the calculated values of $\delta\chi_0^{Ag}$ and $g_0^{H_2O}$ (dip), it follows that the Ag(111) face is the most and Ag(110) the least hydrophilic face.[74] This is linked to the surface structure of the electrode, i.e., the expected highest hydrophilicity of the most compact surface layer. According to the opinion of one author,[74] when the surface has a loose structure, as is the case for the (110) face, water molecules can come closer to the surface, positioning themselves between surface atoms. This results in a higher capacitance for such a face than the more compact ones.

A comparison of data obtained for different metals but the same adsorbate and the same solvent (constant energy of the adsorbate–solvent interaction) allows one to create a hydrophilicity scale. The chosen adsorbate should be neutral and should not react chemically with the electrode surface. Aliphatic compounds, especially alcohols, are the most suitable adsorbates. Alcohols adsorb on metals with their hydrocarbon tail toward the electrode and the functional group surrounded by the hydrophilic liquid phase. Hence, the energy of the metal–adsorbate interaction can again be considered as approximately constant. Still, the reported data obtained for different alcohols and the resulting hydrophilicity scale are controversial. It appears that an additional element influencing the scale of hydrophilicity is the supporting electrolyte. Certain ions that are inactive on some metals may undergo specific adsorption on other metals (see Section III).

(ii) The Contact (Volta) Potential Difference

Some information about the metal–solvent interaction can be obtained from measurements of the contact (Volta) potential difference at the metal/solvent interface

$$\Delta\psi_s^M = \psi^M - \psi^s = \delta\chi^M - \delta\chi^s - g_s^M(\text{ion}) \tag{12}$$

Here, $\delta\chi^M$ is the change in the surface potential of the metal brought into contact with the solvent and represents a modification of the electronic distribution in the metal; and $\delta\chi^s$ is the change of the surface potential due to solvent reorientation after contact with the metal; and $g_s^M(\text{ion})$ is the contribution of ions to the potential drop in the presence of free charges on the metal. At the potential of zero charge, $g_s^M(\text{ion}) = 0$, and

$$(\Delta\psi_\sigma^M)_{\sigma=0} = \delta\chi_0^M - \delta\chi^s \tag{13}$$

The value of $\delta\chi^s$ is equal to

$$\delta\chi^s = g_M(\text{dip})_0 - \chi^s \tag{14}$$

where $g_M^s(\text{dip})_0$ is the contribution of solvent dipoles to the potential of the inner part of the double layer and χ^s is the potential of the solvent at the free surface. The values of $g_M^s(\text{dip})_0$ and χ^s cannot be determined directly. $g_M^s(\text{dip})_0$ depends on the interaction of solvent dipoles with the metal as well as the mutual interaction of solvent molecules. The value of $\delta\chi^s$ at the pzc was estimated to be low and negative on Hg, thus indicating that the interaction of water molecules with mercury is weak.[30] Low values of $\delta\chi_{\text{Hg}}^s$ are likely to be caused by a strong interaction of water molecules in the bulk phase.

Trasatti[30] assumed that the value of $\delta\chi^{\text{Hg}}$ at $\sigma = 0$ is constant (–0.31 V) and independent of the nature of the solvent. Therefore, if the contact potential difference $\Delta\psi_s^M$ at $\sigma = 0$ is known, the values of $\delta\chi^s$ for a given metal can be calculated. It should be noted that the idea that the potential shift due to the interaction of metal electrons with solvent is independent of the nature of the solvent is open to criticism.[75] For example, the local solvent field can interfere with electron distribution in the metal in the vicinity of the interface. The data obtained for a mercury electrode and different solvents show that the contact potential difference is mainly determined by the orientation of solvent dipoles at the interface.[30] The positive values of $g_M^s(\text{dip})_0$ are due to orientation of the solvent dipoles with their negative ends directed toward the mercury surface.

The metal–solvent interaction is expected to depend on the donicity of the solvent: the higher the donor number of the solvent, the stronger the solvent–metal interaction should be. Hence, a correlation between the contact potential difference $\Delta\psi_\sigma^M(\sigma = 0)$ and the donor number of the solvent should be observed. However, this correlation for the Hg electrode is rather poor, with the most deviant point having been found for water, that is, for the case of the strongest dipole–dipole interaction in the bulk.[30] The correlation is better when acceptor numbers of solvents are taken into account.[76]

It was shown earlier that the acceptor number can be treated as a measure of disorder of the solvent structure around the ion, reflecting the changes of $\delta\chi^M$ caused by the solvent–solvent interaction.[77] The contact

potential difference shifts negatively with an increase in the donor number and a decrease in the acceptor number. This is reasonable because reorientation of the solvent dipoles at the interface should increase with the strength of the solvent–solvent interaction and decrease with increasing energy of the metal–solvent interaction. It was shown that the plot of the experimental $(\delta\psi_s^M)_{\sigma=0}$ values vs. the function of donor (DN) and acceptor numbers (AN) is linear for seven solvents, with the correlation coefficient equal to 0.95.[76] The plots of contact potential difference vs. the donor number and vs. a function of both donor and acceptor numbers are shown in Figs. 3a and 3b. The contribution of DN and AN to the observed solvent

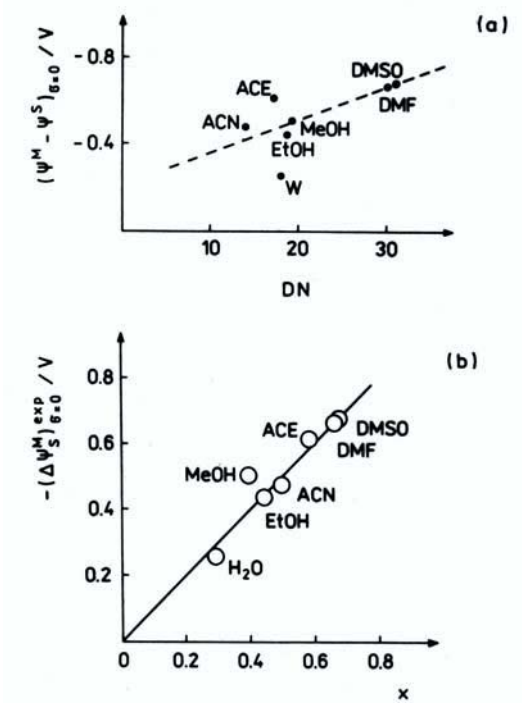

Figure 3. Comparison of the Volta potential differences at the Hg/solvent interface vs. (a) donor number[30] and (b) donor and acceptor numbers.[76] $x = 0.007$ AN – 0.011 DN – 0.485[76]

effect depends on the type of metal. The stronger the metal–solvent interaction, the greater the contribution of solvent donicity.[76]

(iii) Thermal Desorption Spectroscopy

Valuable information can be obtained from thermal desorption spectra (TDS) spectra, despite the fact that electrochemists are somewhat cautious about the relevance of ultrahigh vacuum data to the solution situation, and the solid/liquid interface in particular. Their objections arise from the fact that properties of the double layer depend on the interaction of the electrode with ions in the solution. Experiments in which the electrode, after having been in contact with the solution, is evacuated and further investigated under high vacuum conditions, can hardly reflect the real situation at the metal/solution interface. However, the TDS spectra can provide valuable information about the energy of water adsorption on metals and its dependence on the surface structure. At low temperatures of 100 to 200 K, frozen molecules of water are fixed at the metal. This case is quite different from the adsorption at the electrode/solution interface, which usually involves a dynamic equilibrium with molecules in the bulk.

However, the data on the H_2O/D_2O isotope exchange on Pt(111) at low temperatures show that the mobility of hydrogen is greater on the surface than in the bulk ice.[78] TDS spectra indicate that the temperature of water desorption from all of the group VIII metals is similar (150–170 K), with the activation energy of desorption as 42–48 kJ/mol, which is close to the heat of ice sublimation[79] (51 kJ/mol at 273 K). Because the energy of the metal–water interaction is comparable to the energy of the hydrogen bond in the bulk, the clusters of water molecules are usually formed on the surface.

The desorption spectra depend on the surface structure. For some metals having a face-centered cubic structure, the activation energies of desorption from the (100) and (110) faces are higher than from the (111) face. The spectra of water desorption from the surfaces of gold and silver show only one peak, which means that the surface monolayer of water desorbs together with the multilayers present on top of it. For other phases, [e.g., Pt(111), Rh(111), and Ni(111)], the TDS spectra are more complex: a single peak of monolayer desorption is observed at higher temperatures than the multilayer desorption. It was found for Ni(111) that the activation

energy of water desorption slightly increased with the surface coverage.[64] The value of 42–43 kJ/mol is at present accepted as the heat of desorption of a monolayer of water from metal surfaces.[78] Because the adsorption of water from the bulk has to be followed by the rupture of hydrogen bonds in the bulk (energy equal to ca. 20 kJ/mol), the energy of water adsorption on metals should amount to ca. 20 kJ/mol (a weak chemisorption).

On many metals, such as Ni, Pt, Ag, Cu, and Pd, when a submonolayer of oxygen is present on the surface, the reaction $H_2O + O_{ads} \rightarrow 2\ OH_{ads}$ may take place. For some noble metal planes [e.g., Ru(001)], adsorbed oxygen is responsible for the dissociation of water. Experimental data on the metal–water interaction have been reported and extensively discussed in a review by Thiel and Madey.[79]

TDS data can be compared with the results of quantum calculations for adsorption of single water molecules and water associates on different metals and faces that were presented by Kuznetsov *et al.*[80] The calculations showed that the chemisorption of a single water molecule in a hollow position via the oxygen atom is energetically most favorable. The calculated chemisorption energies are much higher than those determined from the TDS spectra. Water molecules are much more strongly chemisorbed on the (110) face than on the (111) or (100) faces of Cu, Ag, and Au. The chemisorbed water molecule lies almost flat on the mercury surface (bent angle 26°). For Au, Ag, and Cu electrodes, the bent angles of adsorbed water on the (111) face are 67°, 56°, and 63°, respectively. Adsorption of water associates is also possible. Hydrogen bonds between the adjacent monolayers are shortened. The results of calculations for different metals show that the water structure near the metal surface depends on its hydrophilic properties.[80]

(iv) Spectroscopic Methods

(a) Infrared spectroscopy

Infrared (IR) spectroscopy with modulation of the electrode potential was used by Bewick and Kunimatsu[81] to study the change of water structure at the Pt/H_2SO_4 and Au/NaF interfaces. They observed several sharp bands within the OH region, superimposed on a broad absorbance background. The absorption increased at a higher field strength. The observed bands were similar to the bands recorded for small clusters of

water molecules, using matrix methods. It was concluded that at a potential of zero charge, the water structure near the electrode surface is the same as in the bulk. The polymeric structure of water is disrupted at high surface field strength, and small clusters are formed.

Using a similar technique, Bockris and Habib[82] studied water adsorption on a smooth platinum electrode in 50% H_2O + 50% D_2O + 0.1*M* NaF solution. Due to the O–H vibration in the adsorbed water molecule, the intensity of spectra increased with the change of potential in the positive direction, i.e., with the increase of the water–platinum bond energy. According to one of the surface selection rules, the amplitude of the observed band shifts from zero to a maximum when the adsorbed water molecules change their orientation from parallel to perpendicular to the surface (only dipoles perpendicularly oriented to the surface interact with the incident light). Hence, the increase of the absorbance with potential could be interpreted as evidence of the change of water position from a parallel to perpendicular one. The change in orientation of water molecules with the electrode potential is shown in Fig. 4.

(b) Surface-enhanced Raman spectroscopy

Surface-enhanced Raman spectroscopy (SERS) has been widely used to study the interaction of solvent molecules with the electrode surface, including orientation at the interface. The first observation of the Raman

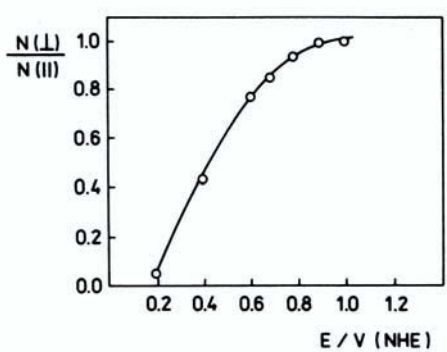

Figure 4. The change of adsorbed water orientation as a function of Pt electrode potential.[82]

spectrum of pyridine on a silver electrode from KCl solution was reported by Fleischmann *et al.*[83] Later, the SERS spectra on other metals such as Au and Cu were also observed. The theory and practice of SERS spectra have been described in numerous monographs (e.g., Ref. 84).

The main advantage of SERS is its selectivity and the fact that the enhancement of spectra is the greatest for the first monolayer and decreases dramatically with the distance from the surface. The measurements can be done *in situ*, at constant potential (no potential modulation is needed), and on bulk electrodes. However, there are some drawbacks to the use of SERS in studying electrosorption. The surface enhancement coefficient of SERS spectra depends on many factors, including the electrode potential. A contribution of short-range interactions of adsorbate with metal to the total enhancement coefficient is about two orders of magnitude lower than the potential-independent electromagnetic contribution. The resonance contribution is responsible for instability of SERS spectra in time. The electrochemical roughening of the surface creates different active sites that can form complexes with adsorbed molecules of different stability. Their instability is the reason SERS spectrum intensity is time dependent. During anodic-cathodic polarization, hysteresis of the spectra is observed, depending on the range of potentials and sweep rate.

The spectra of interfacial water molecules are characterized by the presence of the O–H stretch and bond vibrational modes, the O–H bend mode and the Fermi resonance mode, superimposed on the continuum background scattering.

SERS spectra of adsorbed water were observed during cyclic polarization of an Ag electrode in H_2O, D_2O, and HDO using KCl and KBr as supporting electrolytes.[85] The kind of anion and the solution concentration greatly affect the spectra of adsorbed water. The SERS signal of H_2O decreases when the electrode potential becomes more negative, which is due to the decrease in concentration of anions at the surface. It was stated that the interfacial water molecules exist as monomers following a disruption of the hydrogen bond.[86] Spectra of H_2O are very sensitive to the nature of cations and can be correlated with their hydration energies.[87]

It was surprising that SERS spectra of adsorbed water were observed in the presence of halide ions but not weakly adsorbing anions, like F^- or ClO_4^-. Hence, these spectra could be ascribed to water molecules coadsorbed with specifically adsorbed halide ions.[86]

In contrast to earlier work,[85–87] the SERS signal from the bending vibration of water, in either 0.1*M* Na_2SO_4 or NaF alone (without halide present), was observed at potentials negative of the pzc.[88] No stretching modes were detected in the quoted study, although in recent work SERS spectra containing both the stretching and bending modes were recorded for a silver electrode in a concentrated solution of $NaClO_4$.[89] The maximum stretching mode intensity and the greatest change in the band intensity were observed at –1.1 V vs. SCE. This was considered as evidence of a change in orientation of adsorbed water molecules. It was concluded that in the potential region near pzc, the electrode coverage by adsorbed water is higher than in other regions of the potential. This is likely to be due to the decreased interaction of ions with the surface.[89]

(v) Surface X-ray Scattering

Contrary to optical methods, such as IR, SERS, and second harmonic generation (SHG), which are all inherently indirect, X-ray scattering provides direct information on the location of atoms at the interface. The weak interaction of X-rays with matter and low scattering cross sections of atoms require long acquisition times and typically limit the studies to bulk samples. The use of the synchrotron has improved radiation intensity and extended the application of the method, which now can be used to study the structure of water at the interface. *In situ* X-ray scattering spectra were recorded for Ag(111) in aqueous 0.1*M* NaF solution.[90,91] The intensity distribution of spectra for specular and nonspecular Ag(111) rods was measured at potentials shifted by 0.52 V positive and 0.23 V negative of the pzc of the Ag(111) electrode. The orientation of water molecules was found to be perpendicular to the interface, assuming that the adsorption of Na^+ and F^- ions can be neglected.

For a specular rod, the spectrum intensity depends on the structure of both the electrolyte and the electrode, whereas for a nonspecular rod, the intensity depends only on the electrode surface structure, because in the plane parallel to the interface, the water is not ordered well. It was concluded that water is ordered in a layer extending about three molecular diameters (9–10 Å) from the electrode. The extent of the order depends on the potential, and the distance between the electrode and the layer of oxygens is shorter at positive than at negative potentials. The latter result can be regarded as evidence of the reorientation of water molecules within

the double-layer. The areal density of water in the inner layer is much higher than in the bulk, i.e., the water is greatly compressed in the double-layer—by a factor of 2. Oxygen distribution near the Ag(111) electrode at two different potentials is presented in Fig. 5. The high density of water in the double-layer is inconsistent with the icelike structure of the double layer structure accepted in many models and as such calls for a change in the interaction potentials used in theoretical calculations of the water–electrode system.[91]

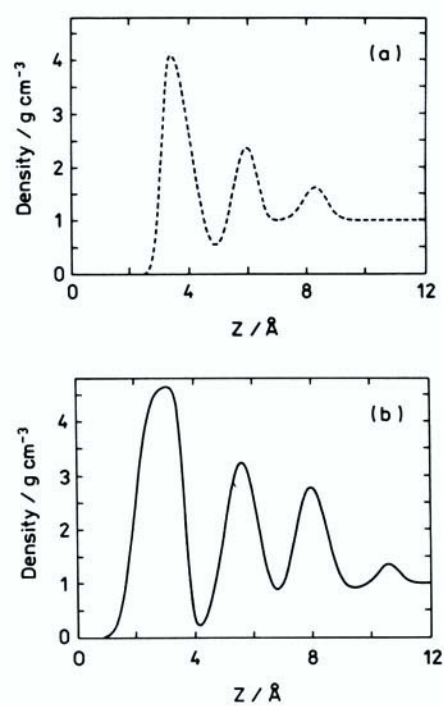

Figure 5. Oxygen distribution near Ag(111) electrode at (a) –0.23 V and (b) + 0.52 V, relative to pzc. Z is the distance from the center of the Ag atoms in the top Ag plane. Unit density corresponds to the density of bulk water.[90]

Data obtained on the electrode–oxygen distances and the reorientation of water in the inner layer are consistent with the results of computer simulations. The relative density profile for oxygen at the water/platinum interface shows two distinct maxima at 2.5 and 5.4 Å, respectively.[92] The first maximum corresponds to water directly bound to the surface whereas the less pronounced second maximum can be ascribed to the second layer of water linked through hydrogen bonds to the first layer.

The experimental results mentioned above as well as computer simulation data confirm the earlier concept of Bockris *et al.*[93] about the reorientation of water molecules with a change of electrode potential.

(vi) Scanning Tunneling Microscopy

The arrangement of water molecules at the Pt(100) face was observed using the scanning tunneling microscope (STM).[94] The tunneling process is affected by the surface water and occurs within the range that corresponds to the thickness of one layer of water. The water layer electrically shields the surface and decreases the tunneling current. This indicates that oxygen atoms in water molecules are oriented toward the platinum surface. However, in the experiment described, the potential of the electrode was not controlled and the system was open to atmospheric oxygen.

A tunneling junction device was used to determine the water structure at the mercury electrode in an aqueous solution of $0.25M$ $Hg_2(NO_3)_2$ + $0.3M$ HNO_3.[95] It was found that the structure of water domains is the same as that of hexagonal ice. Hydrogen bonding is a dominant, structure-determining factor in liquid water near the mercury electrode surface.[95]

It should be remembered that STM data refer to a small segment of the surface whereas electrochemical data describe the properties of the integral surface/electrolyte interface. Hence, for a precise comparison of data obtained with both methods, the surface should be scanned by STM at many places and the results averaged.

(vii) Electrochemical Quartz Crystal Microbalance

The changes in the mass of the surface during cyclic polarization of the electrode provide information on the amounts of deposited or stripped substances, adsorption, and surface hydration. The first report on the *in situ* use of quartz crystal microbalances for determination of the mass change of an electrode was given by Nomura and Iijima.[96] The experimen-

tal aspects of the application of QCM in electrochemical studies have been described by Bruckenstein and Shay.[97] A detailed description of the method and a review of the data obtained have been published by Buttry.[98]

An application of an electrochemical quartz crystal microbalance (EQCM) in the study of the Au/$HClO_4$ system shows that even at a potential about 0.5 V more negative than the onset of AuO formation (the so-called preoxide region), the resonant frequency of the Au-covered quartz crystal decreases as that of the surface mass increases.[99] A comparison of a voltammogram with the potential dependence of the microbalance frequency for an Au electrode is shown in Figs. 6a and 6b.

This increase of the mass was ascribed earlier to the adsorption of perchlorate ions,[100] a conclusion that found no confirmation in work published later.[99] It turns out that other weakly adsorbing anions of different masses (NO_3^-, $CF_3SO_3^-$) give the same values of frequency decrease as was observed for C1O4. Ultimately, the increase of the electrode mass in the preoxide region was explained in terms of the three-dimensional hydration of AuOH, which is present in small amounts at the gold surface. The mass increase was consistent with the surface hydration for a cluster of about 32 water molecules per one AuOH site.[99]

(viii) Radiometric Methods

Radiometric methods are unique for their ability to provide directly the surface concentration of the adsorbate. A method for *in situ* study of electrochemical reactions on solid electrodes was invented by Joliot.[101] He used a thin gold foil as an electrode which at the same time served as the window of the radiation counter. Joliot determined the kinetics and the effect of tartaric acid on polonium electrodeposition on gold. The method was later further developed and improved (e.g., Refs. 102,103).

Two different methods are usually used. The first one, described in detail by Wieckowski,[104] is used to measure the surface concentration on rough electrodes. Solute is labeled with a low-energy β^- emitter in order to decrease, owing to self-absorption, the counting coming from the bulk of the solution. Adsorption of the labeled substance gives rise to a signal in the radiation detector, e.g., in the glass scintillator placed directly under the electrode surface. The counting rate is proportional to the amount of adsorbed species, which can easily be converted into the surface concentration provided that the roughness factor of the electrode is known.

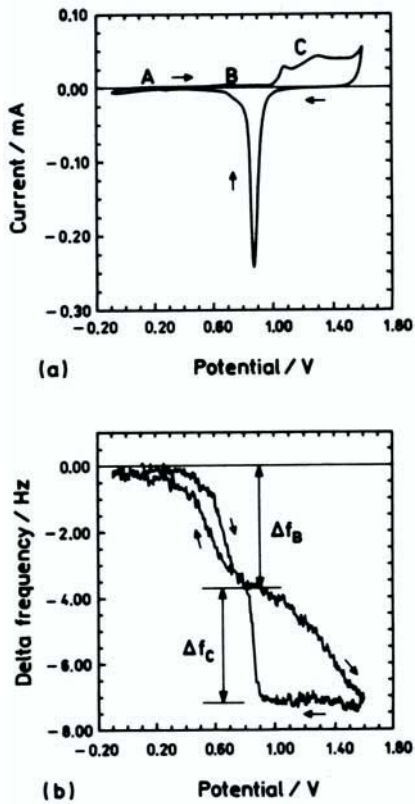

Figure 6. Correlation between the current-potential (a) and frequency-potential (b) curves for the Au EQCM film in 0.1*M* $HClO_4$. Sweep rate 75 mV s^{-1}.[99]

Radiometry is often combined with electrochemical techniques, such as cyclic voltammetry and coulometry. In this way, the number of electrons involved in the oxidation of adsorbed species can be obtained.

The second radiometric method, proposed by Kazarinov,[105] is based upon a different principle. At the beginning of an experiment, the electrode is placed far from the detector, which is situated at the bottom of the cell,

and the counts are only due to labeled adsorbate in the bulk of the solution. When the electrode is lowered onto the detector, the surface counts begin to contribute to the overall counts measured. If counts at a situation of no adsorption are also known, the surface concentration of the adsorbate can be determined. The first method is used with rough electrodes and compounds labeled with β^- emitters of low energies. It is somewhat more accurate and easier to use than the second one. However, the electrode-lowering method has the great advantage of being suitable for smooth electrodes, including monocrystals, and can be used with high-energy emitters. The method has been reviewed in detail by Zelenay and Wieckowski.[106]

The adsorption of water on a platinum electrode was studied on rough Pt electrodes from nonaqueous solutions. It was shown that the interaction of water with the electrode depends on the nature of the solvent. The process is a competition of both components for the surface sites. A comparison of the voltammogram in dilute solution of dimethylsulfoxide (DMSO) in water and water in DMSO[107] shows that DMSO molecules are much more strongly adsorbed on platinum than water molecules. When a small amount of tritium-labeled water is added to a solution of $KClO_4$ in DMSO, an increased radiometric signal is observed. The recorded counts are due to the presence of labeled water molecules on the top of the primary layer of DMSO that completely covers the electrode. When unlabeled water is then added in excess, the radiometric signal decreases as a result of the exchange of tritium-labeled water molecules by the unlabeled ones. This indicates that water molecules adsorbed on top of the DMSO layer are labile and weakly bound to the substrate.[107] Figure 7 shows this experiment.

The situation is quite different in the case of an acetic acid–water system.[108] The energy of acetic acid adsorption on platinum is low and therefore the voltammetric curves taken in the absence and in the presence of acetic acid in the supporting electrolyte are nearly the same. However, radiometric data show that ^{14}C-labeled acetic acid is adsorbed on the electrode surface. Most likely the acetic acid molecules are adsorbed on the top of the water molecules populating the electrode surface. Simultaneously recorded voltammetric and counting rate data are shown in Fig. 8.

Propylene carbonate (PC) weakly interacts with a platinum surface. The cyclic voltammetry of Pt electrodes is not significantly altered upon

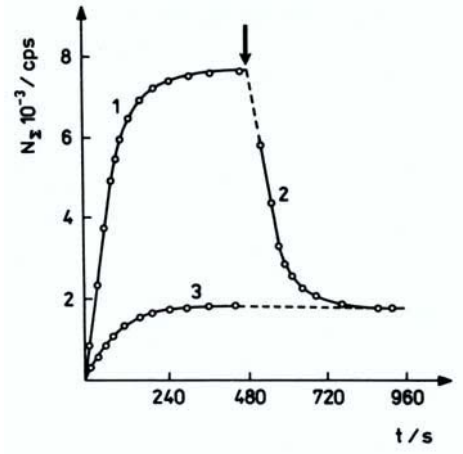

Figure 7. Counting rate vs. time plots for Pt electrode in anhydrous solution of $KClO_4$ in DMSO containing 0.025 cm^3 of HTO before (curve 1) and after (curve 2) an addition of unlabeled H_2O in large excess (0.5 cm^3). The moment of addition is marked with a vertical arrow. Curve 3 shows the counting rate dependence recorded after 0.5 cm^3 of H_2O was added first to the solution, followed the addition of 0.025 cm^3 HTO. (Note that, as expected, the same final counting rate is reached with both procedures.) E = 0.30 V vs. SCE.[107]

addition of PC to the supporting electrolyte.[109] Conversely, even a small amount of water added to a tetrabutylammonium perchlorate solution in anhydrous PC markedly changes the voltammetric curve. Radiometric measurements with tritium-labeled water show that the adsorption is a reversible process and only slightly depends on the electrode potential. As follows from these data, water exhibits higher affinity to the platinum electrode than PC and even at low concentration in the bulk, it can displace the PC molecules from the electrode surface.

Quite different behavior is observed when an isotope exchange of hydrogen atoms between water and the adsorbate can take place. A typical example is an acetone–water system. As follows from the voltammetric

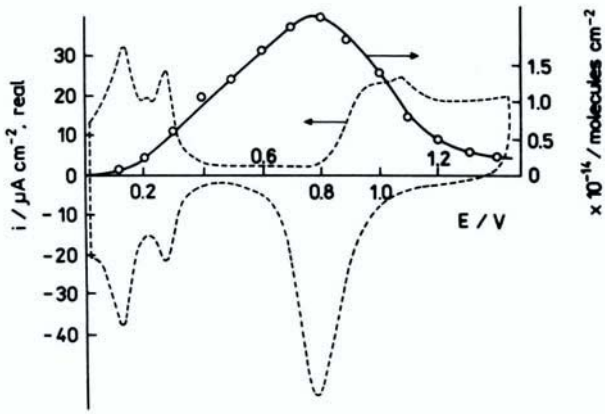

Figure 8. The cyclic voltammogram of polycrystalline Pt electrode in $10^{-2}M$ acetic acid + $0.5M$ H_2SO_4 solution, and simultaneously recorded surface concentration of HAc. Sweep rate 40 mV s^{-1}.[108]

as well as radiometric measurements, acetone is adsorbed on the platinum electrode surface.[110] The addition of unlabeled acetone to a tritium-containing solution of H_2SO_4 gives a surprising result: an increase in the counting rate. This means that tritiated species are accumulated at the interface. As soon as adsorbed acetone is electro-oxidized and removed from the surface, the counting rate drops back to its original value. Also, when tritium-labeled water is added to the acetone solution at open circuit, an increase of the counting rate is observed. These observations are interpreted in terms of a heterogeneous isotope exchange between acetone and water (despite the fact that no homogeneous exchange of hydrogen between both molecules is observed). The exchange of hydrogen atoms between heavy water, D_2O, and hydrogen in the methyl groups in acetone during electrolysis on a platinum electrode was observed earlier.[111]

These examples show that adsorption of water molecules on platinum electrodes depends on the solution components. If the energy of the solute adsorption is higher than that of water molecules, water tends to adsorb on the top of the primary solute layer, which is directly bound to the platinum adsorption sites. If the interaction of organic molecules with platinum is weak, water adsorbs directly onto the electrode surface. In the

latter case, adsorption of water is irreversible, linearly dependent on the bulk concentration of water, and only slightly dependent on the electrode potential. The exchange of hydrogen atoms between water and organic molecules cannot be excluded in labile systems that may undergo substantial structural changes, especially in the strong electric field existing in the interfacial region.

III. THE THERMODYNAMIC APPROACH TO THE METAL/SOLUTION INTERFACE

Though thermodynamics cannot provide direct insight into the metal/solution interface on a microscale, it generates important information about the energies of interaction of metals with the solvent and the solute. Adsorption parameters are of great value to understanding mutual interactions of the system components at the interface.

1. The Standard Gibbs Energy of Adsorption, ΔG°

(i) Choice of the Standard-State Conditions

Very often thermodynamic parameters of adsorption, calculated from different isotherms and reported in the literature, can scarcely be compared because the standard-state conditions used in the calculation are not specified.

Frequently, the adsorption of solutes on electrodes is considered as a substitution process in which "n" solvent molecules in the adsorbed layer S_{ads} are replaced by one solute molecule B that arrives at the surface from the bulk of solution

$$B + nS_{ads} = B_{ads} + nS \tag{15}$$

The relation between the surface concentration of the adsorbate Γ_B and the concentration in the bulk a_B can be described by an adsorption isotherm in the general form

$$f(\Gamma_B) = \beta a_B \tag{16}$$

where $f(\Gamma_B)$ is a configurational term due to the entropy of mixing of the adsorbate particles and β is an equilibrium constant of adsorption and is related to the standard Gibbs energy of adsorption

$$\beta = \exp(-\Delta G^\circ/RT) \tag{17}$$

The form of the isotherm [Eq. (16)] can be derived from the equations of the chemical potentials, i.e., taking into account the relation

$$\beta = \exp[(\mu_B^\circ - \mu_{B(\text{ads})}^\circ) - n(\mu_S^\circ - \mu_{S(\text{ads})}^\circ)/RT] \tag{18}$$

(where $\mu^\circ s$ are the chemical potentials in their standard states), or from the equation of state used for a description of the adsorbed layer at the electrode. At a molecular level, the value of the size ratio parameter n determines the model of the interface. A detailed discussion of that issue is available in the literature.[67,112,113]

The use of different models of the adsorbed layer leads to various values of ΔG° based on the various standard states.[114–119] The problem of choice of appropriate standard states in measurements of adsorption at electrode interfaces was discussed, in relation to solvent displacement, by Conway *et al.*[114] In the case of the Langmuir isotherm used for the adsorbed phase in gas/solid adsorption, it was concluded that the appropriate standard state is $\Theta_B^\circ = 0.5$, which reduces the $\ln[\Theta_B^\circ/(1-\Theta_B^\circ)]$ term to zero. When the solvent displacement is taken into account, the $\Theta/(1-\Theta)$ term no longer represents the configurational chemical potential of the adsorbate alone because of the presence of two components on the surface. If one molecule of B displaces n water molecules as in the Flory–Huggins isotherm, the corresponding configurational quotient $\Theta/n(1-\Theta)^n$ should be equal to 1 in the standard state. Unfortunately, such a choice of standard state has the disadvantage of being dependent on the size of the molecule adsorbed and would thus be different for different adsorbates. This approach has been applied by Zelenay *et al.*[115,116] to Flory–Huggins-type isotherms and the Bockris–Swinkels isotherm in particular. If n is assumed equal to 3 in the latter case, the value of Θ_B° becomes 0.582.[115]

Conway *et al.*[114] described the most convenient conditions defining standard chemical potentials for adsorption with solvent displacement. First, for $n = 1$, the conditions are the same as in binary solution thermo-

dynamics: $\Theta_B^\circ = 1$ and $\Theta_S^\circ = 1$ for the adsorbate and solvent, respectively. Second, for $n > 1$ (e.g., the Flory–Huggins isotherm), the condition for the adsorbate is $\Theta_B^\circ = 1$, so that

$$\mu_B = \mu_B^\circ + RT \ln[\Theta/\exp(n-1)(1-\Theta)] = \mu_B^\circ \tag{19}$$

and for the solvent $\Theta_S^\circ = 1$, so that

$$\mu_S = \mu_S^\circ + RT \ln\{(1-\Theta)/\exp[\Theta/(n-\Theta)]\} = \mu_S^\circ \tag{20}$$

It was shown earlier that the choice of a standard state can be based on the analysis of the adsorption equilibrium. Assuming that adsorption is a substitution process of a solvent molecule by the solute, that the adsorbate and solvent have the same size ($n = 1$), and that the adsorption layer can be treated as a separate phase, the equilibrium constant can be written as

$$\beta = a_S a_{B(\text{ads})}/(a_B a_{S(\text{ads})}) \tag{21}$$

where a_S is the activity of the solvent. Since in the adsorption process discussed there is no variation in the total number of moles, β is dimensionless and independent of selection of the standard state.

If the adsorption process is written as

$$B \rightleftarrows B_{(\text{ads})} \tag{22}$$

where the solvent is not explicitly considered (the isotherm is based on the continuous solvent model), the equilibrium constant

$$\beta' = a_{B(\text{ads})}/a_B \tag{23}$$

has a specific dimension, and the value of β' depends on the choice of units in which the activities are expressed.

From Eqs.(21) and (23) it follows that

$$\beta' = \beta a_{S(\text{ads})}/a_S \tag{24}$$

If the experimental data of adsorption are fitted into the virial isotherm, the equilibrium constant β^v is given by the equation

$$\beta^v = \beta \Gamma_S/a_S \tag{25}$$

where for $n = 1$, $\Gamma_S = \Gamma_{B(max)} - \Gamma_B$ (Γ_S is the surface concentration of the solvent).

In the case of a Frumkin isotherm, the equilibrium constant β^F is given by

$$\beta^F = \beta / a_S \tag{26}$$

Thus $\Delta G^\circ = -RT \ln\beta$, calculated at zero surface coverage, implies that the standard state for adsorbed "S" is pure solvent and for the adsorbate "B" is the ideal $x_B = 1$, i.e., the pure solute with lateral interactions corresponding to an infinite distance between the molecules (i.e., the physical state corresponds to infinitely diluted solution of *B*).

Assuming this standard state, the ΔG° value expresses a change in the Gibbs energy of adsorption of one molecule *B* upon being moved from the hypothetical ideal solution onto the electrode surface. This enables the particle–particle interactions on the surface to be separated from any other interactions and to be included in the term $f(\Gamma_B)$.

In many works in which the adsorption process is described using the Frumkin isotherm, the solvent activity is considered as constant for every value of a_B in view of the fact that the ratio of the molar fractions X_B/X_S is small. Hence,

$$\Theta/(1 - \Theta) \exp(A\,\Theta) = (\beta^F a_S) a_B \tag{27}$$

where $\Theta = \Gamma/\Gamma_{sat}$, and A is the interaction parameter, having negative and positive signs when the interaction between the adsorbate molecules is attractive and repulsive, respectively.

On the other hand, the data for some organic compounds are often fitted into the Frumkin isotherm equation in a modified form

$$[\Theta/(1 - \Theta)] \exp(A\,\Theta) = \beta^F a_B \tag{28}$$

In this case, the value of $\Delta G^\circ = -RT \ln\beta^F$ is referred to the standard state Θ° which gives the left side of Eq. (28) equal to 1 and $a_B^\circ = 1$. Another form of the Frumkin isotherm is

$$[\Gamma_B/(1 - \Theta)] \exp(A\,\Theta) = (\beta^F \Gamma_{B(sat)}) a_B \tag{29}$$

in which the value of $\Delta G^\circ = -RT \ln(\beta^F \Gamma_{B(sat)})$ corresponds to the standard state $\Gamma^\circ = 1$ molec./cm^2 and $a_B^\circ = 1$ mol/dm^3 ($\Gamma_{B(sat)}$ is the maximum surface concentration of B, which can be determined experimentally).

The problem of standard states as well as a comparison of ΔG° values obtained from different isotherms was discussed by Torrent *et al.*[120,121] Using the Guggenheim model of the interphase,[122] they derived a relation between the chemical potentials of all components in the interphase and in the bulk that are required to describe the equilibrium state.

The relation between a "universal" Gibbs energy of adsorption $\Delta G^\circ (= -RT \ln\beta)$ and the energies calculated from different isotherms can be expressed as follows [121]:

a. Frumkin isotherm

$$[\Theta/(1-\Theta)] \exp(A\,\Theta) = \beta\, a_B/a_S \tag{30}$$

$$\Delta G^\circ_{\Theta=0} = (\Delta G_F^\circ)_{\Theta=0} + RT \ln a_S \tag{30a}$$

$$\Delta G^\circ_{\Theta=0} = (\Delta G_F^\circ)_{\Theta=1} + RT\,(A/2) \tag{30b}$$

b. Henry isotherm

$$\Theta = \beta'\, c_B/c_S \tag{31}$$

$$\Delta G^\circ = \Delta G_H^\circ - RT \tag{31a}$$

and

$$\Delta G^\circ_H = -RT \ln\beta' \tag{31b}$$

c. virial isotherm

$$\Theta \exp(-2B\Theta) = \beta_v\, a_B \tag{32}$$

where B is the second virial coefficient (in this factor, size effects and energetic interactions are both included).

$$\Delta G^\circ = \Delta G_v^\circ - RT\,(1+B) \tag{32a}$$

and

$$\Delta G_v^\circ = -RT \ln\beta_v \tag{32b}$$

d. Temkin isotherm

$$\exp(-2f\Theta) = \beta(a_B/a_S) \tag{33}$$

where f is an inhomogeneity factor,

$$\Delta G^\circ = \Delta G_T^\circ - fRT \tag{33a}$$

Generally, one can choose either a symmetrical standard-state system[113,123–126]

1. $\gamma_S^S \to 1$ when $x_S^S \to 1$ and $\gamma_B^S \to 1$ when $x_B^S \to 1$, and
2. $\gamma_S^b \to 1$ when $x_S^b \to 1$ and $\gamma_B^b \to 1$ when $x_B^b \to 1$

or an unsymmetrical one:

3. $\gamma_S^S \to 1$ when $x_S^S \to 1$ and $\gamma_B^S \to 1$ when $x_B^S \to 0$, and
4. $\gamma_S^b \to 1$ when $x_S^b \to 1$ and $\gamma_B^b \to 1$ when $x_B^b \to 0$

where γ_S and γ_B are the activity coefficients of solvent and solute, respectively. Depending on the choice of the standard-state conditions for B on the surface ("S") and in the solution ("b"), the equilibrium constant assumes different values. Nikitas and Sotiropoulos[113] presented various equations for the calculation of ΔG° at different standard states given above.

According to the above definitions, $\Delta G_F^\circ\ (\Theta = 0)$ calculated from Eq. (30a), refers to the unsymmetrical standard-state system at the surface (system 3). In order to refer ΔG_F° values to a symmetrical standard-state system 1, the following correction ought to be made[121]:

$$\ln\beta_F^{\text{corr}} = \ln\beta_F - (A/2) \tag{34}$$

Therefore the determination of the standard Gibbs energies of adsorption at various symmetrical or unsymmetrical standard states leads directly to derivation of the particle–particle interaction parameter. The same result may be obtained from the difference of ΔG° values calculated at zero surface coverage $(\Theta = 0)$ and at saturated surface coverage $(\Theta = 1)$, using Eqs. (30a) and (30b).

A physical sense of some isotherm parameters depends on the adsorption model and may change from one isotherm to another. Information on the main parameters of adsorption, such as the adsorption constant β, saturation surface concentration Γ_{sat}, the number of solvent molecules displaced by one adsorbate molecule n, and either the interaction parameter A or the surface heterogeneity coefficient f, are reliable if the isotherm is determined precisely. The question of interdependencies of parameters in the isotherms most often used to describe adsorption processes (Langmuir, virial, Frumkin, Temkin, Flory–Huggins) was discussed by Gawlowski *et al.*[127] It was shown that adsorption parameters calculated using Langmuir and virial isotherms carry the lowest error because of the simple form of the isotherm equations. The strongest interdependence of parameters was found for the Flory–Huggins isotherm. The biggest error corresponds to parameter A in the Frumkin isotherm. Parameters Γ_{sat} and f in the Temkin isotherm are so strongly interdependent that an unambiguous determination of f requires Γ_{sat} to be obtained in a separate experiment.

The interdependence of the Gibbs energy of adsorption and the molecular interaction parameter was recently discussed in detail by Karolczak,[128] who used a six-parameter model. Contrary to the rather general Damaskin model,[2] no relation between the molecular interaction parameter A and ΔG°_{ads} was assumed. It was suggested[128] that this is an arbitrary relation dependent on the theoretical model used in fitting experimental data within acceptable experimental errors.

(ii) Examples of the Standard-State Selection

The Gibbs energy of adsorption is a measure of adsorbate–metal interactions. Its values depend, however, on the choice of standard states for the chemical potentials of the components involved in the process. Therefore ΔG° values determined for different systems can only be compared if they refer to the same standard-state conditions. ΔG° values of adsorption of thiourea (TU) on several metallic electrodes, calculated for the most often used standard states, are presented in Table 1.

As indicated by the data in Table 1, the conclusions dealing with the influence of solvents on the ΔG° may differ, depending on the choice of the standard state. Selection of the standard state from column (a) results in relatively high ΔG° values of the TU adsorption on Hg in water,

Table 1
Gibbs Energy Values for Adsorption of Thiourea on Some Metallic Electrodes
(kJ/mol)

Solution	(a) $-\Delta G^{\circ}_{F(\theta=0)}$ $[x^{\circ}_B = 1; \Theta^{\circ} = 1]$	(b) $-\Delta G^{\circ}_{F(\theta=1)}$ $[x^{\circ}_B = 1; \Theta^{\circ} = 1]$	(c) $-\Delta G^{\circ}_{F(\theta=0)}$ $[\Gamma^{\circ} = 1$ molec/cm^2, $a^{\circ}_B = 1\ M]$	(d) $-\Delta G^{\circ}_{F(\theta=0)}$ $[\Theta^{\circ} = 0.5$, $a^{\circ}_B = 1\ M]$
Hg				
Water + 0.1 NaF Ref. 22	21.6	11.3	95.7	11.6
MeOH + 0.1 KF Refs. 23, 24	21.6	13.9	92.2	9.0
ETOH + 0.1 KF Ref. 25	13.5	16.1	90.0	6.1
ETOH + sat. KPF_6 Ref. 129	13.3	5.6	88.3	5.9
EG + sat. KPF_6 Ref. 130	12.0	1.7	86.3	4.2
Ac + sat. KPF_6 Ref. 26	13.9	11.7	91.3	7.5
NM + sat. KPF_6 Refs. 131, 132	20.1	12.4	92.9	12.0
Ag				
Water + 0.1 KF Ref. 133,134	15.0	1.8	85.5	4.6
MeOH + 0.1 KF Ref. 135	—	—	81.5	—
Au				
Water + 0.1 KF Ref. 136	26.5[137], 43.0[138]	—	90.1	16.2
MeOH + 0.1 KF Ref. 139	21.5	—	86.3	14.0
Bi				
Water Ref. 140	—	—	91.1	—
MeOH Ref. 141	—	—	85.9	—

methanol, and nitromethane. Much lower values are obtained for the remaining solvents. If the standard states from column (b) are chosen, the highest value of ΔG° of the TU adsorption is observed for the KF + ethanol system. Interestingly, ΔG° drops to the third lowest value if KF is replaced by KPF_6 as a supporting electrolyte in the same solvent (both F^- and PF_6^- are considered as nonadsorbing anions on the Hg electrode). If standard states from column (c) are selected, the effect of the solvent is rather small. In this case, the error of the calculated ΔG° value mainly depends on the involved error in determination of $\Gamma_{B,sat}$ [see Eq. (29)]. The latter error is usually quite high, hence a considerable error may be associated with ΔG° values in this column. In conclusion, the choice of the standard-state conditions not only changes the values of ΔG° but may also influence the order of the ΔG° values calculated for different electrolyte–solvent systems.

For the sake of consistency, all ΔG° values given in the text of this review refer to the standard-state conditions $x^\circ = 1$, and $\Theta^\circ = 1$, and the reference state $\Theta = 0$.

(iii) Influence of the Electric Field on ΔG°

The determination of the Gibbs energy of adsorption at zero surface coverage $\Delta G^\circ_{\Theta=0}$ and of the interaction parameter A as a function of an electrical variable, may become a valuable source of information on the interactions at the interface. The value of ΔG° can be considered as the energy required to replace n monomolecularly adsorbed solvent molecules from a fully solvent-covered electrode surface by one monomeric molecule of the solute

$$\Delta G^\circ = \Delta G^\circ_B - n\Delta G^\circ_S \tag{35}$$

ΔG°_B includes both the solute–solvent interaction in the bulk and the solute–metal interaction at the interface.[112,142] The change of all interactions with the change of the electric field strength should be taken into account.

Parsons[143] described the influence of the electric field on ΔG° with the general equation

$$\Delta G^\circ = \Delta G^\circ_{ch} + a\chi + b\chi^2 = \Delta G^\circ_{ch} + \Delta G^\circ_{el} \tag{36}$$

where ΔG°_{ch} and ΔG°_{el} refer to the chemical and electrical parts of the Gibbs energy, respectively. Depending on the choice of electrical variable, χ is defined by either $\chi = 4\Pi\sigma_M/\varepsilon$ or $\chi = \phi^{M-2}/x_2$, where σ_M and ϕ^{M-2} denote the charge and the potential drop in the inner part of the double layer of the thickness x_2, respectively. The term $a\chi$ accounts for adsorption of ions, polar molecules at fixed orientation, and/or nonpolar molecules with induced dipole moment. The term $b\chi^2$ represents adsorption of polar molecules of undetermined orientation, and adsorption of nonpolar molecules.

According to the capacitor model of the double layer, assuming constant thickness and electric permittivity, the dependence of ΔG° on σ_M should be linear.[143] Deviations from linearity can be viewed as resulting from changes of x_2 and/or ε in the inner part of the double layer. A linear plot of ΔG° vs. χ is observed for adsorption of ions and thiourea.[22,23]

From an adsorption study of aliphatic compounds on an Hg electrode,[112] it follows that ΔG° is a quadratic function of the charge density and applied potential. The value of ΔG° reaches minimum (the most negative value) at σ_{max}, i.e., at the charge of maximum solute adsorption, which is usually in the vicinity of the potential of zero charge.

Cross-differentiation of the Gibbs equation gives the relation

$$(\delta E/\delta \ln c)_{\sigma} = -RT(\delta\Gamma/\delta\sigma_M)_c \tag{37}$$

As a result, the plots of σ_M vs. E for different bulk concentrations of the solute intersect at the same point (σ_{max}, E_{max}), which corresponds to the adsorption maximum. This implies that at the adsorption maximum ϕ^{M-2} does not vary with increasing Γ. Consequently, the surface dipole potential due to the adsorbing molecules exactly matches that of the desorbed solvent molecules,[112] provided that the solvent and solute molecules assume only one orientation at the surface. In practice, however, a single point of intersection of the σ_M vs. E plot for different bulk solute concentrations is observed rather rarely.[144,145] For example, a gradual increase in the surface concentration of 2-propanol on mercury in aqueous solution brings about a small positive shift of σ_{max}. A much bigger shift has been observed for hexafluoro-2-propanol (HFP).[146] It has been ascribed to the reorientation of the HFP molecules in such a way that both $-CF_3$ groups are directed toward the electrode, which in turn results in

further displacement of adsorbed water molecules from the surface. Thus the single-orientation assumption for both solvent and solute is not fulfilled in this case.[146]

The correct quadratic form of the dependence of $\Delta G°$ upon charge is due to the assumed reorientability of water molecules. This permits water dipoles to take the energetically most favorable orientation, depending on the magnitude and sign of the external electric field. The solute molecules, which do not change orientation with varying σ_M, are then preferentially adsorbed in the proximity of the potential of zero charge, where electrostatic interactions between the external electric field and the water dipoles are the weakest.

However, most experimentally obtained $\Delta G°$ vs. σ_M curves do not have a regular parabolic shape. The plots of log β vs. $(\sigma_M - \sigma_{max})^2$ for nicotinamide (NcA) adsorption show (Fig. 9) that the positive branch $(\sigma_M > \sigma_{max})$ is steeper than that for the negative branch $\sigma_M < \sigma_{max}$). This

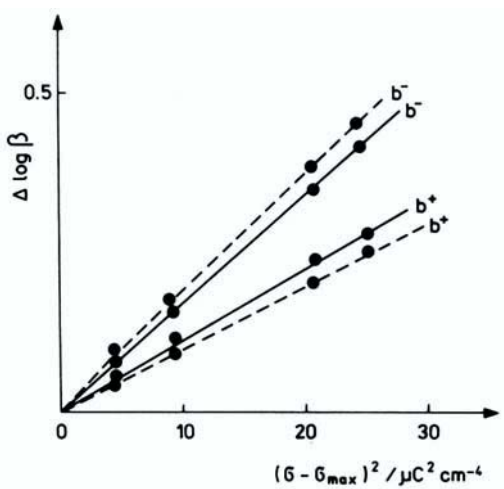

Figure 9. Log β as a function of $(\sigma_M - \sigma_{max})^2$ for NcA solution containing 0.1 mol/dm^3 (—) and buffer at pH = 9 (- - -) as the supporting electrolyte. b^+ and b^- correspond to the positive and negative charge densities of the electrode, respectively. Data from Ref. 147.

is because a gradual increase in the positive value of σ_M causes a progressive increase in interactions between the electrode and the water molecules. This makes water molecules more difficult to displace by the adsorbing solute molecules.[147] This conclusion has been supported by the adsorption data for various alcohols.[148] The charge of maximum adsorption σ_{max} was almost the same for all alcohols studied but the slope of the branches of the parabolic plots increased with an increase in the hydrocarbon chain length.

The value of σ_{max} for the Hg electrode is most often in the range from -1 to -3 $\mu C/cm^2$.[145–153] Positive values of σ_{max} are observed only for organic molecules with polyfunctional groups and for perfluorinated organic compounds, for which structural effects prevail over the hydrophobicity.

An exception among organic molecules is the adsorption of thiourea since that gives no maximum on the $\Delta G°$ vs. σ_M plot. It was suggested[148] that such atypical behavior can be expected for any neutral molecule that has the normal to the surface component of the dipole moment μ_N sufficiently positive compared with the resulting dipole moment of n displaced water molecules. In the case of a TU molecule oriented with the sulfur atom toward the metal surface, the ratio of μ_N/n is approximately equal to 2.5 D.[151] This value is greater than the dipole moment of water, thus fulfilling the condition of "atypical" behavior. The anomalous behavior of thiourea is probably due to the fact that only a few solute molecules satisfy this condition.

The plots of $\Delta G°$ vs. σ_M for different μ_N/n ratios, calculated from the model proposed in Refs. 148, 151, and 152 are presented in Fig.10. The calculation was made for $n = 2$, the area occupied by one water molecule equal to 0.09 nm^2, and for other double-layer parameters that best fit the experimental data on differential capacity of the Hg/water interface. As follows from these plots, no σ_{max} of adsorption can be reached if the μ_N/n ratio is greater than the dipole moment of water (1.84 D).

As mentioned earlier, the Gibbs energy of adsorption can be analyzed using one of two independent electrical variables: potential or charge density. The problem was discussed by Parsons[154] and others,[126,155–157] but it was not unequivocally solved because both variables are interconnected. Recent studies of the phase transition occurring at charged interfaces, performed at a controlled potential, show that if the potential is

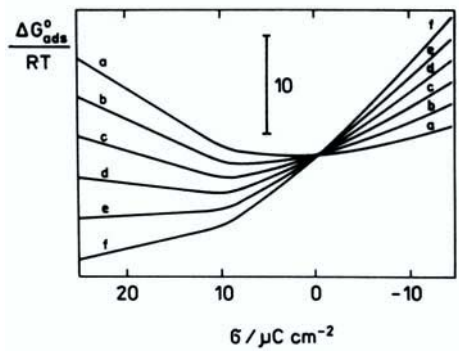

Figure 10. ($\Delta G^\circ/RT$) vs. σ_M plots at n = 2 and μ_N/n equal to (a) 0, (b) 0.5, (c) 1, (d) 1.5, (e) 2 and (f) 2.5. Data from Ref. 148.

replaced by a charge density in the description of the interphase, the phase transition cannot be detected.[158,159] This shows that the two electrical variables are not always equivalent in describing the double-layer properties and that the potential should be selected as the independent electrical variable.

(iv) Effect of the Metal on ΔG°

The contribution of various interactions to the Gibbs energy of adsorption can be described by an equation proposed by Trasatti[67,68]

$$\Delta G^\circ = \Delta G^\circ(B - S) + \Delta G^\circ(B - M) - \Delta G^\circ(S - M) \qquad (38)$$

Here, $\Delta G^\circ(B - S)$, $\Delta G^\circ(B - M)$, and $\Delta G^\circ(S - M)$ represent the energies of the solute–solvent, solute–metal and solvent–metal interactions, respectively. The term $\Delta G^\circ(B - S)$ accounts for the squeezing out of solute molecules from the solution. The original work by Bockris *et al.*[160,161] led to the relationship between the Gibbs energy of adsorption of the organic compounds on mercury and their solubility in water. Based upon studies of adsorption of *n*-decyloamine[161] and naphthalene[162] on five solid metal electrodes (Ni, Fe, Cu, Pb, and Pt), the authors suggested that adsorption arises largely from the metal–adsorbate dispersive interaction differences

between water and the organic while varying only a little with the kind of the metal.

Hence, if adsorbed molecules interact only weakly and nonspecifically with the metal surface, the term $\Delta G°(B-M)$ can be treated as being independent of the nature of the metal. If, simultaneously one assumes that for organic compounds the $B - S$ interactions are approximately the same, then

$$\Delta(\Delta G°) = -\Delta\,[\Delta G°(S-M)] \tag{39}$$

Equation (39) indicates that the difference in the Gibbs energies of adsorption on two different metals is approximately equal to the difference in the energies of the solvent desorption from these metals. This applies, for example, to the adsorption of aliphatic alcohols on different metals. The sequence of energies of adsorption of aliphatic alcohols with different numbers of carbon atoms in the chain is similar at the solution–air interface and on the mercury–solution interface. This is viewed as evidence of the absence of specific interactions between the molecules of alcohols and the metal surface. Also, it seems that the differences in $\Delta G°$ values are determined mainly by the change in the metal–solvent interactions. The $\Delta G°$ data for *n*-pentanol adsorption on different metals are –15.0,[163] –13.4,[164] and –19.1 kJ/mol[165] for Ag, Au, and Hg, respectively. Hence, the lower the Gibbs energy of adsorption, the weaker the metal–solvent interaction. These data allow one to order the metal hydrophilicities in the following sequence: Hg > Ag > Au. A similar sequence (Hg > Au) has been found for *n*-butanol adsorption from 0.02*M* NaF aqueous solution.[155,166]

According to Valette,[167] the hydrophilicity sequence of metals is Cu > Hg > Ag > Au, which is in agreement with the data presented earlier. The problem of hydrophilicity of metal has also been discussed in many other papers (e.g., Refs. 163 and 168).

Lipkowski *et al.*[169] determined the Gibbs energy of diethylether adsorption on single-crystals of gold in aqueous NaF solution and compared the data with the $\Delta G°$ value for a mercury electrode.[155] The results are presented in Table 2.

Using Eq. (39) and these data, one can propose the following hydrophilicity sequence of gold faces: Au(111) > Au(100) > Au(110). It is worth

Table 2
Adsorption of Diethylether from Aqueous Solution of NaF[169]

	Au(111)	Au(100)	Au(110)	Hg[155]
$\Delta G°$ (kJ/mol)	−15.5	−13.5	−10.0	−14.4

Standard state $x° = 1$, $\Theta° = 1$.

noting that this sequence is altered in the case of adsorption of *t*-pentanol, for which $\Delta G°$ [Au(100)] > $\Delta G°$ [Au(111)].[169] The data in Table 2 show that the difference in hydrophilicity of various planes of a given metal can be greater than that of different metals.

The influence of the surface structure on the metal–water interaction has also been determined for silver electrodes (Table 3). There are discrepancies in the $\Delta G°$ values given by different authors for silver electrodes. For example, Vitanov and Popov[170] obtained the same hydrophilicity sequence as for gold: Ag(111) > Ag(100). Another sequence based on the "interfacial parameter x,"[67,168] was given by Trasatti. The interfacial parameter includes electronic and solvent effects and measures the degree of coupling between the metal surface and the solvent. Trasatti showed that for Ag, Au, and Cu, the value $\Delta X = X_M - X_{Hg}$ varies with the crystal face and increases in the sequence (111) < (100) < (110), which agrees with the energy of the water–metal bond.

Foresti *et al.*[171] determined the sequence of hydrophilicity of different metals from the $\Delta G°$ vs. ΔX plot for adsorption of *n*-hexanol from aqueous solutions: Hg > Bi, Sn > In(Ga) > Cd > Ag(111) > Ag(100) > Ag (110),

Table 3
Adsorption of *n*-Hexanol from Aqueous Solution with Na_2SO_4[170] (1) and $KClO_4$[171] (2)

	Au(111)		Au(100)		Hg[155]
	(1)	(2)	(1)	(2)	
$\Delta G°$ (kJ/mol)	−24.7	−18.4	−23.0	−17.7	−22.6

Standard state: $x° = 1$, $\Theta° = 1$.

Ga. The order for the basal planes of silver is opposite to that reported by Trasatti.[172]

The observed discrepancies in experimental results is most likely caused by the ions of the supporting electrolyte. For example, fluoride ions do not adsorb on the mercury electrode but adsorb on the silver electrode.[173] The adsorption on the latter metal strongly depends on the face orientation.[174] The sequence of $\Delta G°$ values for *n*-hexanol adsorption from Na_2SO_4 and $KClO_4$ solutions is $\Delta G°$ [Ag(111)] > $\Delta G°$ [Ag(100)] (see Table 3). However, the sequence of $\Delta G°s$ of *n*-pentanol adsorption from KF solution is just the opposite: $\Delta G°$ [Ag(110)] > $\Delta G°$ [Ag(111)].[163] The fact that different data have been reported by various authors indicates that some additional, not exactly identified, factors influence the order of hydrophilicity of single-crystal faces of the *sd* metals.

Taking into account the hydrophilicity sequence presented above, i.e., Hg > Ag > Au, and the $\Delta G°$ values of TU adsorption from the aqueous KF solutions [see Table 1, column (a)], it can be estimated that the contribution of $\Delta G°(M - B)$ to the overall energy of the TU adsorption is about 6.6 kJ/mol higher on an Hg electrode than on an Ag electrode. From the comparison of the TU adsorption on Ga and Hg,[175] it follows that absorbability of TU on Ga is higher than on Hg, even at the negative surface charge, where the specific adsorption of anions, the oxidation of metal, and the chemisorption of water can be altogether neglected. The opposite effect was observed for aliphatic alcohols that adsorb more weakly on Ga than on Hg. Unlike the TU dipoles, the molecules of alcohols assume an orientation with their positively charged ends toward the metal.[148] The electron density in Ga is about twice as large as in Hg and hence the extent of the electron spillover at a given charge is greater on Ga than on Hg. The observed opposite effects for TU and aliphatic alcohols suggest a coupling between the water orientation and the electron spillover, which appears to be greater for Ga than for Hg.[151]

Adsorption of TU on active and passive iron electrodes was studied by Bockris *et al.* using radiotracer and Fourier Transform Infrared Spectroscopy techniques.[176] The high values of $\Delta G°$ (the standard states: $\Theta° = 0.582$ and $c° = 1$ mol l^{-1}) equal to –17.20 kJ/mol and –18.98 kJ/mol have been obtained for the active and passive iron electrodes, respectively. They are markedly higher than those obtained for other metals (Table 1).

The influence of the metal on electrosorption was also considered in the adsorption of aromatic compounds. Extensive studies of adsorption of different aliphatic and aromatic compounds on a polycrystalline Pt electrode in 0.01*M* HCl solution were done by Bockris *et al.*[58] Using different techniques (radiotracer, FTIR, and ellipsometry), they were found that aromatic molecules are adsorbed parallely to the electrode surface and that the potential dependence of adsorption is symmetrical around the pzc. It was concluded that the dependence of adsorption on the potential is mostly determined by the interaction of water with the Pt surface.

Adsorption of benzoic acid (BA) was studied on four face-centered cubic (FCC) metals—Pt, Au, Ag, and Cu[177]—and on Hg.[178] It was observed that the $\Delta G°$ value for BA adsorption on Hg is a little lower than on Au and Cu, and much lower than on Pt. Such a difference can be explained in terms of the change of the *d* character of the studied metals. Neutral molecules are more weakly bound to the *sp* metals (e.g., Hg) than to typical *d* metals (e.g., Pt). As follows from the sequence of the $\Delta G°$ values of BA adsorption (Pt > Cu > Au > Hg), the group IB metals, for example, Au, Ag, and Cu, should be placed between the two limiting cases.

(v) Solvent Effect on $\Delta G°$

In the process of adsorbing neutral organic compounds from aqueous solutions, the adsorbed water molecules play an important role for they interact via H bonds with other water molecules, and also with the polar groups of the surfactants. Since the hydration energy of ions of the supporting electrolytes is high, their specific adsorption on electrodes is insignificant. Therefore, organic compounds are easily adsorbed from water solutions. This pertains especially to those compounds that are characterized by low polarity and therefore small value of donor–acceptor numbers. Owing to different solvation effects and different structures, adsorption of an organic solute can be changed in the nonaqueous solvent.

(a) Adsorption of thiourea

The role of nonaqueous solvents in adsorption processes can be exemplified by the adsorption of thiourea. A number of systematic studies of TU adsorption on Hg electrodes from protic as well as aprotic solvents have been published. The results of TU adsorption from water,[22] methanol,[23,24] ethanol,[25,129] ethylene glycol,[130] acetone,[26] and ni-

tromethane[131,132] suggest that the chemical nature and donor–acceptor properties of the solvent play an essential role in the adsorption process (Table 1). In general, the surface excesses of TU on the Hg electrode in protic solvents, with KPF_6 as the electrolyte, are smaller than in aprotic solvents. This is a fact likely to result from the stronger interaction of TU with protic than aprotic solvents, in the bulk or/and on the surface. The effect of TU interaction with solvents is particularly visible in water[179] or ethanol.[180,181] In these solvents, a special role in the formation of a condensed phase played by the hydrogen bonds between the functional groups of TU and other components of the solution was discussed.

The situation is different with aprotic solvents. The strength of interaction between the solvent and the metal, particularly at the positively charged electrode, may be significant in the aprotic solvent. For example, in the case of TU adsorption in acetone solution, the weaker the interaction of the metal with the solvent, the greater the TU adsorption observed.[26] In spite of some differentiation of the $\Delta G°$ values (Table 1) for different solvents, for every one, $\Delta G°$ is greater than –10 kJ/mol, indicating the enhanced contribution of a specific interaction of TU with the metal. Nevertheless, the data in Table 1 show that the $\Delta G°$ value in water is always greater than in methanol for all metals studied.

(b) Adsorption of acetone

Another example of the solvent effect in interfacial processes has come from the investigation of the adsorption of acetone on the mercury

Table 4
$\Delta G°$ for Acetone Adsorption at the Hg Electrode

	$\Delta G°$ (kJ/mol), σ_{max} (10^{-2} mC/m^2)		
	H_2O + Ac + 0.1 HCl Ref. 182	MeOH + Ac + 0.1 LiCl Ref. 183	NM + Ac + 0.1 KPF_6 Ref. 144
$\sigma_M = 0$	–5.6	–2.1	–0.2
	–7.2	–2.5	–1.7
	(σ_{max} = –5.0)	(σ_{max} = –4.0)	(σ_{max} = –7.5)

Standard state: $x° = 1$, $\Theta° = 1$

electrode using aqueous solutions,[182] methanol,[183] and nitromethane.[144] The values of ΔG° at $\sigma_M = 0$ and σ_{max} are given in Table 4.

The ΔG° values of acetone adsorption decrease slightly in the sequence H_2O, MeOH, NM. They are indicative of a weak physical adsorption at the Hg/solution interface. It is also evident that the Gibbs energy of adsorption is enhanced by the electric field, particularly at the point of adsorption maximum. Small values of ΔG°, similar to those determined at the solution/air interface,[184] attest to the absence of specific interactions cf acetone with the mercury surface (which is opposite to the TU adsorption case). Hence, the solute–solvent interaction in the solution is an important factor in the adsorption of acetone, as shown for the zero charge on the Hg electrode in Fig. 11.

Acetone adsorption changes significantly, depending on whether the electrode charge is positive or negative. Adsorption from nitromethane solutions is small at zero charge but increases as the charge becomes negative. The opposite happens at positive σ_M (Fig. 12), which means that nitromethane molecules dominate on the positively charged surface. These effects result from the absence of specific interactions between

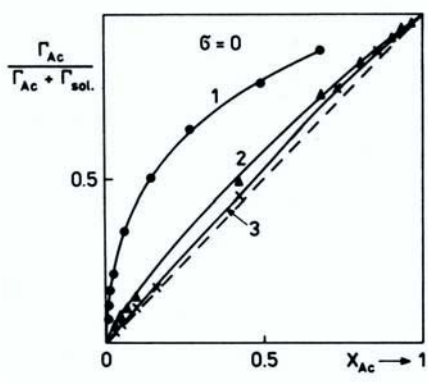

Figure 11. Surface mole fraction of Ac at $\sigma = 0$ as a function of the bulk mole fraction of Ac. (1) Ac + H_2O + HCl ($\mu = 0.1M$).[182] (2) Ac + MeOH + 0.01M LiCl[183] and (3) Ac + NM + 0.001M KPF_6.[144]

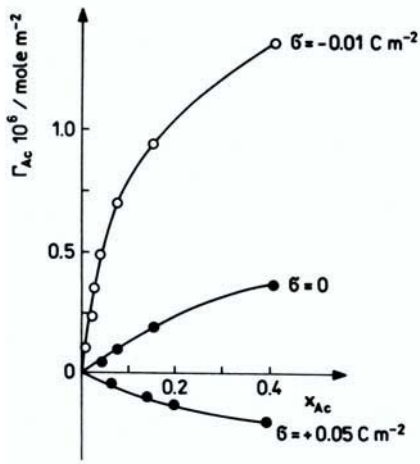

Figure 12. Surface excess of Ac at different Hg electrode charges, against the mole fraction of acetone in the bulk. Adsorption from NM + Ac mixtures saturated with KPF_6. Data from Ref. 185.

mercury and the solvents. This situation is also in good agreement with the observation on the opposite orientations of the Ac and NM molecules at the mercury surface (Ac molecules adsorb with the positive end toward the mercury,[182] but NM molecules adsorb with the negative end facing the metal).[185]

2. Effect of Supporting Electrolyte on Electrosorption

In any study of electrosorption of neutral molecules on metallic electrodes, the ions of supporting electrolytes should not be specifically adsorbed. Nevertheless, the interaction of the electrolyte ions with the electrode surface may depend on the interaction of the ions with the solvent. Usually, the stronger the ion–solvent interaction, the weaker the adsorption of the ion. Since the ions are more weakly solvated in nonaqueous solvents than in water, the ions that are not adsorbed from aqueous solutions may still be adsorbed from organic solvents. However, even in the absence of

specific adsorption, the ions of the supporting electrolyte are likely to influence the adsorption of organic molecules through the following effects:

1. Salting out of the substance near the electrode surface (e.g., the adsorption of alcohols from the Na_2SO_4 solution).[186]
2. Electrostatic interaction with polar groups of the adsorbate that may lead to the coadsorption of the ions and the organic adsorbate.[129]
3. Screening by the ions of the diffuse layer, decreasing the mutual repulsion of the dipoles and leading to an increase in adsorption (e.g., the change in adsorption and reorientation of coumarin[187]).
4. Enhanced formation of the condensed layer observed during the adsorption of thiourea[179,180] and uracil.[188]

The role of supporting electrolyte in adsorption processes is sometimes unclear. The adsorption of mannitol[189] and sucrose[190] on the Hg electrode from NaF and NaCl solutions shows that Cl^- ions exert small, though observable, effects on the differential capacity curves (the saturation coverage and surface excess are slightly different in both solutions). Unexpectedly, at low surface excess of sucrose, the adsorption of sucrose is greater in the NaCl than in the NaF solution. At high surface excesses, the opposite situation is observed.

A change in ionic adsorption in the presence of organic molecules was also observed by Parsons and Zobel.[191] They found that in the presence of acetanilide in the inner layer, the surface concentration of specifically adsorbed phosphate ions decreases. In another work it was suggested that specific adsorption of nitrate ions is markedly reduced in the presence of thiourea in the solution.[192] Thiourea alters the properties of the mercury electrode, affecting even the adsorption of iodides.[193]

These observations lead to a general conclusion that the same supporting electrolyte should be used for a valid comparison of parameters obtained for various organic adsorbates on the same electrode. The situation becomes more complex when different electrodes are to be studied, because some ions (e.g., fluorides) which are not adsorbed on the Hg electrode do adsorb on Ag[172,194] and probably also on the Au electrodes.[195] Large ions of small charge density, such as PF_6^-, BF_6^-, and ClO_4^-, seem to be more weakly adsorbed on solid electrodes than small F^- ions. All the

above factors impede comparison of the experimental data obtained for different metals and supporting electrolytes.

(i) Dissociative Effects in the Electric Double Layer

The electrical field effect on the degree of dissociation of solutes has been the subject of theoretical[196–199] and experimental work.[199–202] The theoretical approach has pointed to the decrease of dissociation caused by the polarization of the solvent in the electric field whereas the experimental one has revealed the increase of dissociation, particularly in the solvents of low electric permittivity. In such solvents ions tend to form ionic pairs, with the strong electric field in the double layer changing their dissociation constants. This effect becomes important when the capacity of the diffuse layer is to be calculated from the Gouy–Chapman theory.

It was shown that the field effect exists in the case of organic compounds dissolved in glacial acetic acid.[203,204] A small dissociative effect is observed even at $\sigma_M = 0$. It manifests itself in the increase of diffusion layer capacitance, which is about 25% higher than that calculated from the Gouy–Chapman theory. An analogous method[204] used in studying the acetone/Hg interface in a KPF_6 solution[205] showed that at higher concentrations of KPF_6 (e.g., $10^{-1}M$), the degree of dissociation is about two times higher than in the absence of the double-layer electric field. The effect was not found in dilute KPF_6 solutions, e.g., at a concentration of $10^{-3}M$. For an Hg/acetone LiCl system and at the charge density $\sigma_M = -10\ \mu C/cm^2$, the dissociation constant of LiCl at the interface increases about 740 times. This agrees with the calculation based on the Onsager theory[206] that gives the ratio of dissociation constants in the presence ($\sigma_M = 10\ \mu C/cm^2$) and in the absence of an electric field equal to 660.

In conclusion, the dominant effect of the increasing strength of the electric field in the double layer is an increase in the dissociation of salts dissolved in nonaqueous solvents, and this behavior is similar to that observed in aqueous solutions.[200,201]

(ii) Influence of the Supporting Electrolyte on the Differential Capacity Curves

For a majority of systems involving pure or mixed solvents, direct measurements of the capacity curves on Hg demonstrate characteristic

humps on the anodic branch. This effect has been observed in aqueous solutions of polyatomic nonadsorbing anions (PF_6^-, BF_4^-, ClO_4^-)[207] as well as in several aprotic solvents.[184,205,208–212] The nature of the capacitance humps has been discussed in many papers.[213–216]

To explain the nature of the hump, the ion–solvent molecule competition model[217,218] can be applied. According to this model, the solvent dipoles oriented with their positive ends toward the electrode are displaced by the anions (for example PF_6^-) that enter the inner layer at the point of maximum double-layer capacity (C_{max}). The value of C_{max} is similar in different solvents (Table 5) if the activity of the PF_6^- ions is the same and the adsorption of these anions can be neglected. Thus it is the PF_6^- anions rather than solvent molecules that are responsible for the formation of the

Table 5
Capacity Maximum C_{max} and Corresponding σ_M on Hg Electrode in Various Solvents for KPF_6 and $LiClO_4$

Solvent	C_{max} (10^{-2} μF/m^2) KPF_6	C_{max} (10^{-2} μF/m^2) $LiClO_4$	σ_M (at C_{max})[a] (10^{-2} μC/m^2)
Ethylene glycol (EG) Ref. 130	26	31	8
Dimethylsulfoxide (DMSO) Ref. 208	24–29	36	8
Acetone (Ac) Ref. 206	28–30	—	10
Tetramethylsulfolane (TMS) Ref. 210	26–27	—	13
Ethylene carbonate (EC) Ref. 209	25	36	13
Propylene carbonate (PC) Ref. 212	24–25	33	15
Nitromenthane (NM) Ref. 211	25–26	33	18

[a]Taken from experimental data for KPF_6 solutions.

hump. The value of C_{max} decreases with an increase in the radius of a polyatomic anion. For example, C_{max} in $LiClO_4$ solutions is higher than in KPF_6 (Table 5).

A higher value of the electrode charge at the capacitance maximum indicates a stronger interaction between the solvent and the electrode. Therefore, absorbability of solvents on the Hg electrode, with KPF_6 used as a supporting electrolyte, can be arranged as follows: DMSO < Ac < EC, TMS < NM. The same order was found for Ac and TMS, when their adsorption in aqueous solutions was investigated.[219,220] However, in the case of organic solvent–water systems, the interaction between different molecules can play an important role in the adsorption process. This effect may account for a difference in the sequence shown above (DMSO < Ac) and that suggested by Fisher for adsorption from aqueous solutions (Ac < DMSO).[221]

(in) Specific Effects of Ions on the Solvent Contribution to the Capacitance C_s

Amokrane and Badiali proposed a semiempirical approach to the determination of the solvent contribution C_s to the capacitance of the double layer in aqueous[32,33] and nonaqueous[34] solutions. They used the relation $C_s^{-1} = C_i^{-1} - C_M^{-1}$, where C_i is the experimentally determined capacity of the inner layer and C_M is the contribution of the metal. The plots of C_s vs. σ_M were presented for various solvents and correlated with their properties.[222] However, the problem of the supporting electrolyte was entirely neglected in the quoted papers. It was shown recently[223] that the height and position of the maximum on the C_s vs. σ_M plots depend on the type of the supporting electrolyte. Experimental differential capacity data obtained on the Hg electrode in methanol and ethanol containing various electrolytes with nonadsorbing anions (F^-, PF_6^-, ClO_4^-) indicate that the type as well as concentration of the electrolyte influences the position and the height of the maximum on the C_s vs. σ_M plots (Fig. 13).

The increase in the anion concentration results in higher values of C_s at the maximum and in the shift of the maximum toward the zero charge density. The shift of the peak with increasing concentration is caused by the screening effect of the anions, accumulated in the diffuse layer and linked to the positive ends of the solvent dipoles. However, the changes in the shape of the C_s vs. σ_M plots are greater on the negative than on the

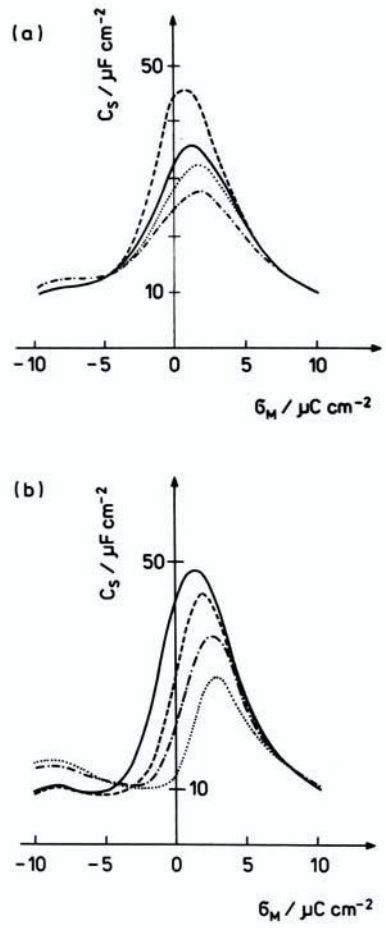

Figure 13. The C_s vs. σ_M plots obtained in (a) methanol solutions containing various salts: - · - · - 0.1*M* KPF_6, ... 0.1M $NaClO_4$, — 0.5M $LiClO_4$, - - - 0.1*M* $LiClO_4$; and in (b) ethanol solutions containing . . . . saturated KPF_6, - · - · - 0.1*M* KF, - - - 0.1*M* $LiClO_4$, — 0.5*M* $LiClO_4$.[223]

positive side of the zero charge density. This suggests that the structure of the interfacial layer is modified strongly by the interaction of cations with the hydrophilic groups of the solvent molecules. Similar effects have been observed for ethylene glycol solutions containing different amounts of ClO_4^-.[224]

(iv) Influence of the Supporting Electrolyte on the Thermodynamic Parameters of Organic Adsorption

(a) Thiourea

The study of thiourea adsorption on an Hg electrode from ethanolic solutions[129] shows that different supporting electrolytes can make a comparison of the adsorption parameters more difficult. The data obtained for various electrolytes (KF, KPF_6, LiCl, NH_4NO_3, and KCNS) suggest that coadsorption, size, and polarizability of ions strongly influence the interfacial behavior of TU, at high concentration of the ions in particular.[129] The effect of the electrolyte on ΔG° and parameter A in the Frumkin isotherm is illustrated in Table 6.

Table 6
Adsorption of TU on Mercury

	$\Delta G^\circ_{F(\theta=0)}$ (kJ/mol)							
	Water			Ethanol[129]			Ethylene glycol[130]	
	$-\Delta G^\circ$	A		$-\Delta G^\circ$	A		$-\Delta G^\circ$	A
0.1 NaF Ref. 22	21.6	—	0.1 KF	13.5	−1	Sat. KPF_6	12.0	4
0.1 KNO_3 Ref. 192	20.8	6	Sat. KPF_6	13.3	3	0.05 $NaClO_4$	12.8	10
			0.2 NH_4NO_3	11.5	1	0.125 $NaClO_4$	11.7	16
			0.25 KSCN	11.5	6			
			0.2 LiCl	11.3	−1			

The low values of ΔG° at $\Theta = 0$ and $\sigma_M = 0$ (i.e., when the contribution of charge to the adsorbate–metal bond and to the lateral interaction within the adsorbate can be neglected) indicate a weak physical adsorption of TU from ethanol and ethylene glycol. The values of ΔG°_{TU} are slightly higher in the presence of nonadsorbing anions (F^-, PF_6^-) than the coadsorbing ones (Cl^-, SCN^-). An attractive interaction between adsorbed TU molecules in solutions of KF and LiCl results from the reduction of the repulsion between adsorbed TU dipoles due to the screening of the amino groups in TU by small fluoride and chloride ions.[129]

(b) Acetone

Adsorption studies of acetone on mercury show that the ΔG° values depend not only on the type of supporting electrolyte but also on its concentration.[144,185] The relevant data are given in Table 7. An increase in the KPF_6 concentration in NM + Ac from 0.01*M* to saturation results in a ΔG° drop by a factor of 2, with a simultaneous slight change in σ_{max}, from –7.5 to $-8\ \mu C/cm^2$ (Fig. 14). In the case of an MeOH + Ac system, an increase in the LiCl concentration also leads to a decrease in the ΔG° value but to a lesser extent than in the former case. The change of the σ_{max} is greater, however, from –4 to $-8\ \mu C/cm^2$.

In conclusion, in the presence of a concentrated adsorbing electrolyte, the effect of the electrode charge on ΔG° is greater. Moreover, for both systems, an increase in concentration of the electrolyte leads to the enhancement of the attractive interaction between the Ac dipoles and an

Table 7
Parameters Characterizing Adsorption of Acetone on Mercury

	$1/\Gamma_{sat}$ (nm^2/molec.), σ_{max} (10^{-2} μC/m^2)					
	A	$1/\Gamma_{sat}$	σ_{max}	A	$1/\Gamma_{sat}$	σ_{max}
NM + Ac Ref. 144		0.01 KPF_6			Sat. KPF_6	
	0	0.90	–7.5	–3	0.64	–8.0
MeOH + Ac Ref. 183		0.01 LiCl			Sat. LiCl	
	2	0.45	–4.0	–3	0.33	–8.0

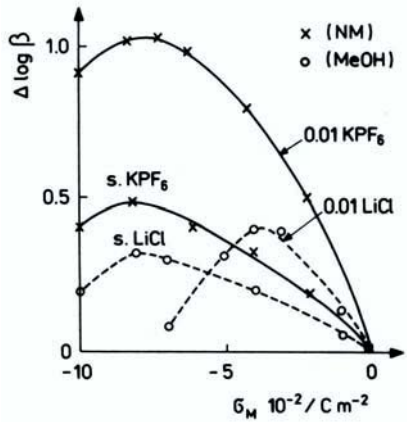

Figure 14. Changes of log β for acetone adsorption, as a function of the charge density on the Hg electrode, from Ac + NM[185] and Ac + MeOH mixtures.[183]

observed increase in Γ_{sat} (Table 7). The anions may act as bridges between the CH_3 groups in Ac on the solution side, lowering the energy of the dipole–dipole repulsion (screening). The data presented in Table 4 show that the $\Delta G°$ values are very low for all systems. Still, they depend on both the kind and the concentration of the supporting electrolyte, which plays a significant role in the adsorption process of acetone.

(c) Ethylene glycol and n-butanol

A systematic study of the effect of halides on EG adsorption on Hg from aqueous solutions[225,226] has given the following sequence of the $\Delta G°$ values: –8.65 in NaF, –8.44 in KC1, –8.36 in KBr, and –8.02 kJ/mol in KI.[225] Thus, the stronger the halide adsorption, the lower the Gibbs energy of the EG adsorption. The effect can be explained in terms of lowered effective surface charge in the presence of more strongly bonded ions. Similar effects of halide ions have been observed in the adsorption of *n*-butanol on mercury from aqueous solutions.[155,165] As before, greater adsorptivity of anions has resulted in lower $\Delta G°$ values of *n*-butanol. Despite that, the changes in the value of the interaction parameter *A*

indicate an increase in the attractive forces operating between butanol molecules in the adsorbed layer in the presence of the more strongly adsorbing anions.[165]

ACKNOWLEDGMENTS

Financial support by the Committee for Scientific Research (KBN) grants 2 P303 058 07 (J.S.) and 3 T09A 038 08 (M.J.-H.) is acknowledged. The authors are very grateful to Dr. Piotr Zelenay for his valuable comments. We would also like to thank Professor John O'M. Bockris for careful reading of the manuscript and many critical remarks.

REFERENCES

[1]R. Parsons, in *Modern Aspects of Electrochemistry*, Vol. 1, Ed. by J. O'M. Bockris and B. E. Conway, Butterworth, London, 1954.
[2]A. N. Frumkin and B. B. Damaskin, in *Modem Aspects of Electrochemistry*, Vol. 3, Ed. by J. O'M. Bockris and B. E. Conway, Butterworth, London, 1964.
[3]R. M. Reeves, in *Modern Aspects of Electrochemistry*, Vol. 9, Ed. by B. E. Conway and J. O'M. Bockris, Plenum Press, New York, 1974.
[4]M. A. Habib, in *Modern Aspects of Electrochemistry*, Vol. 12, Ed. by J. O'M. Bockris and B. E. Conway, Plenum Press, New York, 1977.
[5]S. Trasatti, in *Modern Aspects of Electrochemistry*, Vol. 13, Ed. by B. E. Conway and J. O'M. Bockris, Plenum Press, New York, 1979.
[6]A. Hamelin, in *Modern Aspects of Electrochemistry*, Vol. 16, Ed. by B. E. Conway, R. E. White, and J. O'M. Bockris, Plenum Press, New York, 1985.
[7]M. A. Vorotyntsev, *in Modern Aspects of Electrochemistry*, Vol. 17, Ed. by J. O'M. Bockris, B. E. Conway, and R. E. White, Plenum Press, New York, 1986.
[8]J. Goodisman, in *Modern Aspects of Electrochemistry*, Vol. 20, Ed. by J. O'M. Bockris, R. E. White, and B. E. Conway, Plenum Press, New York, 1989.
[9]S. Amokrane and J. P. Badiali, in *Modern Aspects of Electrochemistry*, Vol. 22, Ed. by B. E. Conway, J. O'M. Bockris, and R. E. White, Plenum Press, New York, 1992.
[10]W. Schmickler and D. Henderson, *Progress in Surface Science*, Vol. 22, Pergamon Press, New York, 1986.
[11]R. Parsons, *J. Electroanal. Chem.* **150** (1983) 51.
[12]J. O'M. Bockris and S. U. M. Khan, *Surface Electrochemistry. A Molecular Approach*, Plenum Press, New York, 1993.
[13]P. A. Christensen and A. Hamnett, *Techniques and Mechanisms in Electrochemistry*, Chapman & Hall, London, 1994.
[14]J. O'M. Bockris and M. A. Habib, *J. Res. Inst. Catal.* (Hokkaido Univ.) **23** (1975) 43.
[15]C. W. Outwait, L. B. Bhuiyan, and S. Levine, *J. Chem. Soc. Faraday Trans. II* **76** (1980) 1388.
[16]S. Lamperski, *J. Electroanal. Chem.* **379** (1994) 445.
[17]S. Lamperski, *Pol. J. Chem.* **69** (1995) 797.

[18]A. Frumkin, N. Polianovskaya, N. Grigoriev, and I. Bagotskaya, *Electrochim. Acta* **10** (1965) 793.
[19] D. Henderson, in *Trends in Interfacial Electrochemistry*, Ed. by A. Fernando Silva, Reidel, Dordrecht, p. 473, 1986.
[20]A. Frumkin, B. Damaskin, N. Grigoryev, and I. Bagotskaya, *Electrochim. Acta* **19** (1974) 69.
[21]S. Trasatti, *J. Electroanal. Chem.* **123** (1981) 121.
[22]R. Parsons, *Proc. Roy. Soc. (Lond.) A* **261** (1961) 79.
[23]D. Garnish and R. Parsons, *Trans. Faraday Soc.* **63** (1967) 1757.
[24]S. Minc, J. Jastrzebska, and M. Jurkiewicz-Herbich, *J. Electroanal. Chem.* **152** (1983) 223.
[25]M. Jurkiewicz-Herbich and J. Jastrzebska, *J. Electroanal. Chem.* **199** (1986) 201.
[26]M. Jurkiewicz-Herbich, *Electrochim. Acta* **32** (1987) 683.
[27]O. K. Rice, *J. Phys. Chem.* **30** (1926) 1501.
[28]J. O'M. Bockris and A. K. N. Reddy, *Modern Electrochemistry*, Vol. 2, Plenum Press, New York, 1977.
[29]J. O'M. Bockris and M. A. Habib, *J. Electroanal. Chem.* **68** (1976) 367.
[30]S. Trasatti, *Electrochim. Acta* **32** (1987) 843.
[31]S. Amokrane, V. Russier, and J. P. Badiali, *Surface Sci.* **218** (1989) 251.
[32]S. Amokrane and J. P. Badiali, *Electrochim. Acta* **34** (1989) 39.
[33]S. Amokrane and J. P. Badiali, *J. Electroanal. Chem.* **266** (1989) 21.
[34]S. Amokrane and J. P. Badiali, *J. Electroanal. Chem.* **297** (1991) 377.
[35]A.N. Kornyshev, *Electrochim. Acta* **34** (1989) 1829.
[36]C.L. Scortichini and C.N. Reilley, *J. Electroanal. Chem.* **139** (1982) 233.
[37]L. Bakos and G. Horanyi, *J. Electroanal. Chem.* **332** (1992) 147.
[38]A. J. Arvia, R. C. Salvarezza, and W. E. Triaca, *Electrochim. Acta* **34** (1989) 1989.
[39]R. M. Cervino, W. E. Triaca, and A. J. Arvia, *J. Electroanal. Chem.* **182** (1985) 51.
[40]J. Clavilier, K. ElAchi, and A. Rodes, *Chem. Phys.* **141** (1990) 1.
[41]S. Trasatti and A. O. Petrii, *Pure Appl. Chem.* **63** (1991) 711.
[42]R. Woods, in *Electroanalytical Chemistry*, Vol. 9, Ed. by A. J. Bard, Marcel Dekker, New York, 1976.
[43]J. Sobkowski and J. Uminski, *Rocz. Chemii* **44** (1970) 1135.
[44]E. D. Bidoia, L. O. S. Bulhoes, and R. C. Rocha-Filko, *Electrochim. Acta* **39** (1994) 763.
[45]R. Parsons and F. G. R. Zobel, *J. Electroanal. Chem.* **9** (1965) 333.
[46]M. A. V. Devanathan, *Trans. Faraday Soc.* **50** (1954) 373.
[47]L. Blum, D. Henderson, and R. Parsons, *J. Electroanal. Chem.* **161** (1984) 389.
[48]G. Valette, *J. Electroanal. Chem.* **138** (1982) 37; **224** (1987) 226.
[49]A. Hamelin and J. Lipkowski, *J. Electroanal. Chem.* **171** (1984) 317.
[50]F. G. Will and C. A. Knorr, *Z. Elektrochem.* **64** (1960) 258.
[51]J. Clavilier, R. Faure, G. Guinet, and R. Durand, *J. Electroanal. Chem.* **107** (1980) 205.
[52]P. Ross, *Surface Sci.* **102** (1981) 463.
[53]D. Dickertmann, F. D. Koppitz, and J. W. Schultze, *Electrochim. Acta* **21** (1976) 967.
[54]D. A. J. Rand and R. Woods, *J. Electroanal. Chem.* **35** (1972) 209.
[55]C. L. Scortichini, F. E. Woodward, and C. N. Reilley, *J. Electrochem. Soc.* **139** (1982) 265.
[56]D. M. Kolb, in *Structure of Electrified Interfaces*, Ed. by J. Lipkowski and P. N. Ross, Vol. 2, VCH Publishers, New York, 1993.
[57]D. M. Kolb and J. Schneider, *Electrochim. Acta* **31** (1986) 929.
[58]J. O'M. Bockris and K. T. Jeng, *J. Electroanal. Chem.* **330** (1992) 541.
[59]A. Wieckowski, *J. Electroanal. Chem.* **352** (1993) 313.

[60]S. Trasatti and R. Parsons, *Pure Appl. Chem.* **55** (1983) 1251.
[61]J. P. Badiali, M. L. Rosinberg, and J. Goodisman, *J. Electroanal. Chem.* **130** (1980) 31.
[62]R. Kotz, in *Spectroscopic Techniques in Electrochemistry*, NATO ASI Series, Vol. 320, Ed. by E. Gutierez Reidel, Dordrecht, 1990.
[63]J. M. Heras and L. Viscido, *Appl. Surf. Sci.* **4** (1980) 238.
[64]R. H. Stulen and P.A. Thiel, *Surface Sci.* **157** (1985) 99.
[65]J. O'M. Bockris and S. D. Argade, *J. Chem. Phys.* **49** (1968) 1968.
[66]A. N. Frumkin, *Potentials of Zero Charge* (in Russian), *Nauka*, Moscow, 1979.
[67]S. Trasatti, *Electrochim. Acta* **37** (1992) 2137.
[68]S. Trasatti, *Electrochim. Acta* **36** (1991) 1659.
[69]M. Bacchetta, A. Francesconi, S. Trasatti, L. Doubova, and A. Hamelin, *J. Electroanal. Chem.* **218** (1987) 355.
[70]A. Popov, O. Velev, T. Vitanov, and D. Tonchev, *J. Electroanal. Chem.* **257** (1988) 95.
[71]T. Vitanov, A. Popov, and E. S. Sevastyanov, *J. Electroanal. Chem.* **142** (1982) 289.
[72]G. Valette, *J. Electroanal. Chem.* **224** (1987) 285.
[73]G. Valette, *J. Electroanal. Chem.* **269** (1989) 191.
[74]G. Valette, *J. Electroanal. Chem.* **230** (1987) 189.
[75]L. I. Krishtalik, N. N. Alpatova, and E. V. Ovsyannikova, *J. Electroanal. Chem.* **329** (1992) 1.
[76]J. Jaworski, *Electrochim. Acta* **34** (1989) 485.
[77]J. Jaworski, *Monatsh. Chemie* **115** (1984) 415.
[78]F. T. Wagner, in *Structure of Electrified Interfaces*, Vol. 2, Ed. by J. Lipkowski and P. N. Ross, VCH Publishers, New York, 1993.
[79]P. A. Thiel and T. E. Madey, *Surface Sci. Report* **7** (1987) 211.
[80]An. Kuznetsov, R. R. Nazmutdinov, and M. S. Shapik, *Electrochim. Acta* **34** (1989) 1821.
[81]A. Bewick and K. Kunimatsu, *Surface Sci.* **101** (1980) 131.
[82]M. A. Habib and J. O'M. Bockris, *Langmuir*, **2** (1986) 388.
[83]M. Fleischmann, P. J. Hendra, and A. J. McQuillian, *Chem. Phys. Lett.* **26** (1974) 163.
[84]R. L. Birke and J. R. Lombardi, in *Spectroelectrochemistry. Theory and Practice*, Ed. by R. J. Gale, Plenum Press, New York, 1988.
[85]T. T. Chen, J. F. Owen, R. K. Chang, and B. L. Laube, *Chem. Phys. Lett.* **89** (1982) 356.
[86]T. T. Chen, *Ber. Bunsenges. Phys. Chem.* **91** (1987) 296.
[87]T. T. Chen, K. E. Smith, J. F. Owen, and R. K. Chang, *Chem. Phys. Lett.* **108** (1984) 32.
[88]A. M. Funtikov, S. K. Sigalaev, and V. E. Kazarinov, *J. Electroanal. Chem.* **228** (1987) 197.
[89]Z. Q. Thian, K. Sigalaev, S. Z. Zou, B. W. Mao, A. M. Funtikov, and V. E. Kazarinov, *Electrochim. Acta* **39** (1994) 2195.
[90]M. F. Toney, J. N. Howard, J. Richer, G. L. Borges, J. G. Gordon, O. R. Melroy, D. G. Wiesler, D. Yee, and L. B. Sorenson, *Nature* **368** (1994) 444.
[91]J. G. Gordon, O. R. Melroy, and M. F. Toney, *Electrochim. Acta* **40** (1995) 3.
[92]E. Spohr, *J. Phys. Chem.* **93** (1989) 6171.
[93]J. O'M. Bockris, E. Gileadi, and K. Muller, *Electrochim. Acta* **12** (1967) 1301.
[94]G. Nagy, *Electrochim. Acta* **40** (1995) 1417.
[95]J. D. Porter and A.S. Zinn, *J. Phys. Chem.* **97** (1993) 1190.
[96]T. Nomura and M. Iijima, *Anal. Chim. Acta* **115** (1980) 323.
[97]S. Bruckenstein and M. Shay, *Electrochim. Acta* **30** (1985) 1295.
[98]D. A. Buttry, in *Electrochemical Interfaces. Modern Techniques for in-situ Interface Characterization*, Ed. by H.D. Abruna, VCH Publishers, New York, 1991.
[99]J. S. Gordon and D. C. Johnson, *J. Electroanal. Chem.* **365** (1994) 267.

[100]H. Angerstein-Kozlowska, B. E. Conway, A. Hamelin, and L. Stoicoviciu, *Electrochim. Acta* **31** (1986) 1051.
[101]F. Joliot, *J. Chim. Phys.* **27** (1930) 119.
[102]E. A. Blomgren and J. O'M. Bockris, *Nature* **186** (1960) 305.
[103]H. Dahms and M. Green, *J. Electrochem. Soc.* **110** (1963) 1075.
[104]A. Wieckowski, in *Modern Aspects of Electrochemistry,* Vol. 21, Ed. by R. E. White, J. O.'M. Bockris, and B. E. Conway, Plenum Press, New York, 1990.
[105]V. E. Kazarinov, *Electrokhimiya* **2** (1966) 1170.
[106]P. Zelenay and A. Wieckowski, in *Electrochemical Interfaces, Modern Techniques for in situ Interface Characterization,* Ed. by H. D. Abruna, VCH Publishers, New York, 1991.
[107]A. Wieckowski, M. Szklarczyk, and J. Sobkowski, *J. Electroanal. Chem.* **113** (1980) 79.
[108]A. Wieckowski, J. Sobkowski, P. Zelenay, and K. Franaszczuk, *Electrochim. Acta* **26** (1981) 1111.
[109]P Zelenay, M. Szklarczyk, M. Winnicka-Maurin, and J. Sobkowski, *J. Electroanal. Chem.* **308** (1991) 269.
[110]A. Wieckowski, P. Zelenay, M. Szklarczyk, and J. Sobkowski, *J. Electroanal. Chem.* **135** (1982) 285.
[111]X. De Hemptine and K. Schunck, *Trans. Faraday Soc.* **65** (1969) 591.
[112]R. Guidelli, in *Adsorption of Molecules at Metal Electrodes,* Ed. by J. Lipkowski and P. N. Ross, VCH Publishers, New York, 1992.
[113]P. Nikitas and Sotiropoulus, *J. Electroanal. Chem.* **309** (1991) 1.
[114]B. E. Conway, H. Angerstein-Kozlowska, and H. P. Dhar, *Electrochim. Acta* **19** (1974) 455.
[115]P. Zelenay, M. A. Habib, and J. O'M. Bockris, *Langmuir* **2** (1986) 393.
[116]B. R. Scharifker and P. Zelenay, *Acta Cientifica Venezolana* **39** (1988) 315.
[117]J. Jastrzebska, M. Jurkiewicz-Herbich, and S. Trasatti, *J. Electroanal. Chem.* **216** (1987) 21.
[118]P. Nikitas, *J. Electroanal. Chem.* **263** (1988) 147.
[119]M. Rueda, I. Navarro, F. Prieto, and G. Ramirez, *J. Electroanal. Chem.* **379** (1994) 467.
[120]R. Gonzales, J. Torrent, and F. Sanz, *J. Electroanal. Chem.* **244** (1988) 53.
[121]J. Torrent and F. Sanz, *J. Electroanal. Chem.* **286** (1990) 207.
[122]E. A. Guggenheim, *Trans. Faraday Soc.* **36** (1940) 397.
[123]P. Nikitas, *J. Electroanal. Chem.* **170** (1984) 333.
[124]P. Nikitas, *Electrochim. Acta* **34** (1989) 293.
[125]P. Nikitas and A. Pappa-Luisi, *J. Phys. Chem.* **94** (1990) 361.
[126]D. H. Mohilner, H. Nakadomari, and P. R. Mohilner, 7. *Phys. Chem.* **81** (1977) 244.
[127]J. Gawlowski, P. Zelenay, and M. Szklarczyk, *Pol. J. Chem.* **69** (1995) 1046.
[128]M. Karolczak, *J. Electroanal. Chem.* **402** (1996) 37.
[129]M. Jurkiewicz-Herbich, A. Muszalska, and J. Jastrzebska, *Colloids Surfaces,* **41** (1989) 169.
[130]M. Jurkiewicz-Herbich, *Pol. J. Chem.* **66** (1992) 1695.
[131]M. Jurkiewicz-Herbich, *Pol. J. Chem.* **65** (1991) 2271.
[132]M, Jurkiewicz-Herbich, M. Skompska, S. Romanowski, and T. Pietrzak, *Pol. J. Chem.* **67** (1993) 1451.
[133]M. Milkowska, *Electrochim. Acta* **32** (1987) 159.
[134]M. Milkowska, *Electrochim. Acta* **33** (1988) 101.
[135]M. Milkowska, *Electrochim. Acta* **36** (1991)965.
[136]H. Wroblova and M. Green, *Electrochim. Acta* **8** (1963) 679.
[137]M. Brzostowska-Smolska, *Pol. J. Chem.* **68** (1994) 1379.

[138]R. Holze and S. Schomaker, *Electrochim. Acta* **35** (1990) 613.
[139]W. N. Andreev and W. E. Kazarinov, *Elektrokhimiya* **10** (1974) 1736.
[140]U. W. Palm, Yu. I. Erlikh, and T. H. Erlikh, *Elektrokhimiya* **10** (1974) 1180.
[141]E. K. Petyarv and U. W. Palm, *Elektrokhimiya* **9** (1973) 1343.
[142]S. Trasatti, *J. Electroanal. Chem.* **65** (1975) 815.
[143]R. Parsons, *J. Electroanal. Chem.* **5** (1963) 397.
[144]M. Jurkiewicz-Herbich, *J. Electroanal. Chem.* **119** (1981) 275.
[145]M. Jurkiewicz-Herbich and S. Minc, *Pol. J. Chem.* **59** (1982) 769.
[146]M. R. Moncelli, G. Pezzatini, and R. Guidelli, *J. Electroanal. Chem.* **272** (1989) 217.
[147]M. Jurkiewicz-Herbich, R. Slojkowska, and M. Skompska, *J. Electroanal. Chem.* **389** (1995) 191.
[148]M. R. Moncelli, M. L. Foresti, and R. Guidelli, *J. Electroanal. Chem.* **295** (1990) 225.
[149]M. Carla, G. Aloisi, M. L. Foresti, and R. Guidelli, *J. Electroanal. Chem.* **197** (1986) 123.
[150]M. A. M. Gomez, E. Diez, and E. Aldez, *J. Electroanal. Chem.* 165 (1984) 207; **193** (1985) 265.
[151]G. Pezattini, M. R. Moncelli, and R. Guidelli, *J. Electroanal. Chem.* **301** (1991) 227.
[152]R.Guidelli, *J. Electroanal. Chem.* **132** (1981) 59; **197** (1986) 77.
[153]M. Jurkiewicz-Herbich, *J. Electroanal. Chem.* **332** (1992) 265.
[154]R. Parsons, *J. Electroanal. Chem,* **8** (1964) 93.
[115]E. Dutkiewicz, G. Garnish, and R. Parsons, *J. Electroanal. Chem.* **16** (1968) 505.
[156]R. Parsons and S. Trasatti, *J. Electroanal. Chem.* **53** (1974) 335.
[157]S. Trasatti and G. Olivieri, *J. Electroanal. Chem.* **27** (1970) App. 7.
[158]P. Nikitas, *Electrochem. Acta* **36** (1991) 447.
[159]A. Pappa-Louisi, P. Nikitas, and P. H. Andonoplous, *Electmchim. Acta* **38** (1993) 1585.
[160]E. Blomgren, K. Jesch, and J. O'M. Bockris, *J. Phys. Chem.* **651** (1961) 2000.
[161]J. O'M. Bockris and D. A. J. Swinkels, *J. Electrochem. Soc.* **111** (1964) 736.
[162]J. O'M. Bockris, M. Green, and D. A. J. Swinkels, *J. Electrochem. Soc.* **111** (1964) 743.
[163]A. Popov, O. Velev, and T. Vitanov, *J. Electroanal. Chem.* **256** (1988) 405.
[164]R. I. Tucceri and D. Posados, *Electrochim. Acta* **32** (1987) 27.
[165]B. B. Damaskin, A. A. Survila, and L. I. Rybalka, *Elektrokhimiya* **3** (1967) 146, 926, and 1137.
[166]E. Brzezinska-Beltowska, E. Dutkiewicz, and Skoluda, *J. Electroanal. Chem.* **181** (1984) 235.
[167]G.Valette, *J. Electroanal. Chem.* **122** (1981) 285; **139** (1982) 285.
[168]S. Trasatti, *J. Electroanal. Chem.* **172** (1984) 27.
[169]J. Lipkowski, C. Ngugen Van Huong, C. Hinnen, and R. Parsons, *J. Electroanal. Chem.* **143** (1983)375.
[170]T. Vitanov and A. Popov, *Elektrokhimiya* **10** (1974) 1373.
[171]M. L. Foresti, M. Innocenti, and R. Guidelli, *J. Electroanal. Chem.* **376** (1994) 85.
[172]S. Trasatti, *Russ. J. Electrochem.* **31** (1995) 777.
[173]M. Bacchetta, S. Trasatti, L. Dubova, and A. Hamelin, *J. Electroanal. Chem.* **255** (1988) 237.
[174]F. Veggini, S. Trasatti, and L. Dubova, *J. Electroanal. Chem.* **378** (1994) 125.
[173]I. A. Bagotskaya, S. A. Fateev, N. B. Grigorev, and N. G. Bardina, *Elektrokhimiya* **6** (1970) 365.
[176]J. O'M. Bockris, B. R. Scharifker, and J. L. Carbajal, *Electrochim. Acta* **32** (1987) 799.
[177]J. Sobkowski, P. Waszczuk, and P. Zelenay, *Russ. J. Electrochem.* **31** (1995) 920.
[178]J. Dojlido, M. Dmowska-Stanczak, and Z. Galus, *J. Electroanal. Chem.* **94** (1978) 107.
[179]C. Buess-Herman, L. Gierst, and M. Gonze, *J. Electroanal. Chem.* **226** (1987) 267.

[180]M. Skompska and K. Jaszczynski, *J. Electroanal. Chem.* **291** (1990) 217.
[181]S. Romanowski, T. Pietrzak, M. Skompska, M. Jurkiewicz-Herbich, and J. Jastrzebska, *J. Electroanal. Chem.* **345** (1993) 83.
[182]Z. Borkowska, *J. Electroanal. Chem.* **63** (1975) 379.
[183]A. Muszalska and J. Jastrzebska, *J. Electroanal. Chem.* **112** (1980) 77; **318** (1991) 145.
[184]Z. Borkowska, *J. Electroanal. Chem.* **146** (1984) 385.
[185]M. Jurkiewicz-Herbich, Thesis, The University Publishing House, Warsaw, 1988.
[186]D. A. Mouse, H. A.Gualy, M. M. Abou-Ronne, and F. El-Toil Heahal, *Electrochim. Acta* **20** (1975) 489.
[188]T. Wandlowski, *J. Electroanal. Chem.* **213** (1986) 339.
[189]R. Parsons and R. Peat, *Colloids Surfaces* **51** (1991) 49.
[190]R. Parsons and R. Peat, *J. Electroanal. Chem.* **122** (1981) 299.
[191] R. Parsons and F. G. Zobel, *Trans. Faraday Soc.* **62** (1966) 3511.
[192]R. Parsons and P. C. Symons, *Trans. Faraday Soc.* **64** (1968) 1077.
[193]A. M. Morozov, N. B. Grigorev, and I. A. Bagotskaya, *Elektrokhimiya* **3** (1967) 585.
[194]G. Valette, *J. Electroanal. Chem.* **122** (1981) 281; **138** (1982) 37.
[195]A. Hamelin.Z. Borkowska, and J.Stafiej, *J. Electroanal. Chem.* **189** (1985) 85; **209** (1989) 191.
[196]L. Gierst and H. D. Hurwitz, *Z. Electrochem.* **64** (1960) 361.
[197]A. Sanfeld and A. Steinchen-Sanfeld, *Trans. Faraday Soc.* **62** (1966) 1907.
[198]H. D. Hurwitz, A. Sanfeld, and A. Steinchen-Sanfeld, *Electrochim. Acta* **9** (1964) 929.
[199]H.W. Nurnberg, *Disc. Faraday Soc.* **39** (1968) 136.
[200]H. W. Nurnberg and G. Wolff, *J. Electroanal. Chem.* **21** (1969) 99.
[201]K. Takahashi and R. Tamamushi, *Electrochim. Acta* **16** (1971) 875.
[202]M. Szklarczyk, R. C. Kainthla, and J. O'M. Bockris, *J. Electrochem. Soc.* **136** (1989) 2512.
[203]L. Bass, *Trans. Faraday Soc.* **62** (1966) 1900.
[204]G. G. Susbiells and P. Delahay, *J. Phys. Chem.* **72** (1968) 84.
[205]M. Jurkiewicz-Herbich, *Pol. J. Chem.* **52** (1978) 1063.
[206]M. Jurkiewicz-Herbich, *Ann. Soc. Chim. Polonorum* **50** (1976) 515.
[207]L. M. Baugh and R. Parsons, *J. Electroanal. Chem.* **40** (1972) 407.
[208]R. Payne, *J. Am. Chem. Soc.* **89** (1967) 489.
[209]W. R. Fawcett and D. M. Mackey, *J. Chem. Soc. Faraday Trans. I* **69** (1973) 634.
[210]J. Lawrence and R. Parsons, *Trans. Faraday Soc.* **64** (1968) 751.
[211]M. Jurkiewicz-Herbich, *J. Electroanal. Chem.* **92** (1978) 221.
[212]N. H. Cuong, A. Jenard, and H. D. Hurwitz, *J. Electroanal. Chem.* **103** (1079) 399.
[213]D. C. Grahame, *J. Am. Chem. Soc.* **79** (1957) 2093.
[214]R. Parsons, *Electrochim. Acta*, **21** (1976) 681.
[215]J. O'M. Bockris, M. A. V. Devanathan, and K. Muller, Proc. Roy. *Soc. (Lond.) A* **274** (1963) 55.
[216]E. Shvarts, B. B. Damaskin, and A. N. Frumkin, *Zhurn. Fiz. Khim.* **36** (1962) 2419.
[217]D.J. Schiffrin, *Trans. Faraday Soc.* **67** (1971) 3381.
[218]R. Payne, *J. Phys. Chem.* **73** (1969) 3591.
[219]J. E. B. Randles, B. Behr, and Z. Borkowska, *J. Electroanal. Chem.* **65** (1978) 775.
[220]Z. Borkowska, *J. Electroanal. Chem.* **244** (1988) 1.
[221]O. Fisher, unpublished communication.
[222]S. Amokrane, Z. Borkowska, and G. Jarzabek, J. *Electroanal. Chem.* **377** (1994) 9.
[223]M. Jurkiewicz-Herbich, A. Muszalska, M. M. Abdulrahim, and J. Jastrzebska, *J. Electroanal. Chem.* **370** (1994) 165.

[224]M. Jurkiewicz-Herbich, A. Muszalska, and J. Jastrzebska, *Russ. J. Electrochem.* **31** (1995) 846.
[225]S. Trasatti, *J. Electroanal. Chem.* **281** (1970) 257.
[226]M. R. Moncelli and Guidelli, *J. Electroanal. Chem.* **295** (1990) 239.

This Page Intentionally Left Blank

2

Quantum Mechanical Treatments in Electrode Kinetics

Shahed U.M. Khan

Department of Chemistry and Biochemistry,
Duquesne University, Pittsburgh, Pennsylvania 15282

I. INTRODUCTION

In recent years, electrochemical charge transfer processes have received considerable theoretical attention at the quantum mechanical level. These quantal treatments are pivotal in understanding underlying processes of technological importance, such as electrode kinetics, electrocatalysis, corrosion, energy transduction, solar energy conversion, and electron transfer in biological systems.

A quantum mechanical formalism of electron transfer (ET) at a metal electrode to an activated ion (e.g., H_3O^+) in solution was originated by Gurney.[1] This approach was later named *molecular theory* and was further developed by Butler,[2] Gerischer,[3] Christov,[4] and Bockris and co-workers,[5,6] and later by Schmickler,[7,8] Ovchinnikov and Benderskii,[9] Halley and Hautman,[10] and Khan and Zhou.[11] Recently, Rose and Benjamin[12] and Xia and Berkowitz[13] used a molecular dynamics approach to compute the free energy functions and thereby the free energy of activation for the outer sphere ET reactions at electrodes. Straus, Colhoun, and Voth[14,15] also used molecular dynamics to simulate the potential energy functions for the ET transfer reactions at electrodes using the Anderson–Newns Hamiltonian approach.[16,17]

Modern Aspects of Electrochemistry, Number 31, edited by John O'M. Bockris *et al.*
Plenum Press, New York, 1997

Another approach to ET reactions originated in the work of Weiss[18] and Libby,[19] who suggested that activation energy for ET reactions in solution does not arise from the collisional-vibrational or electrostatic interaction of the solvent in the first and second solvation sphere, but rather from continuum solvent polarization fluctuation far out in solution. This approach, called *continuum theory*, was further developed by Kubo and Toyozawa,[20] Marcus,[21] Platzmann and Frank,[22] and by Levich and Dogonadze.[23]

In a recent upsurge of studies on electron transfer kinetics, importance was placed on the outer shell solvent continuum, and the solvent was replaced by an effective model potential or a continuum medium with an effective dielectric constant. Studies in which the electronic and molecular structure of the solvent molecules are explicitly considered are still very rare. No further modern quantum mechanical studies were made to advance the original molecular and quantum mechanical approach of Gurney[1] on electron and proton (ion) transfer reactions at an electrode.

In this article, a brief discussion will be given on the relevance of continuum theory in explaining the rate of electron transfer and the activation of species in solution; we will concentrate in particular on *molecular* and quantum mechanical models of ET reactions at the electrode/electrolyte interface that are needed to replace those based on the continuum approach.[21–23]

II. CONTINUUM THEORY OF ELECTRON TRANSFER REACTIONS

Electron transfer reactions, treated by continuum theory,[21–23] suggested that the Franck–Condon barrier (the barrier for the vertical transition of electrons), which is about four times the activation barrier for the isotopic electron transfer in solution, is due to Born continuum solvation processes.[24] Specific contributions for the activation of ions come from the solvent continuum far from the ion; the important contribution from the solvent molecules oriented toward the central ion in the first and second solvation shells is neglected.[21]

The theory of homogeneous electron transfer reactions in solution has been formulated in terms of models in which the transferring electron is localized at a donor site in the reactant and at an acceptor site in the

product. The nuclear modes of the reacting solute and solvent are represented by a set of harmonic oscillators. The complex degrees of freedom are typically modeled using the linear response theory[20] by means of a solvent coordinate. The use of this theory (which involves a Gaussian integral) generates a quadratic expression for the free energy of activation in the electron transfer rate equation[21]

$$k = \kappa \nu_n \exp\left[(\lambda + \Delta G^\circ)^2 / 4\lambda k_B T\right] \tag{1}$$

where κ is the electronic transmission coefficient which has been used as unity by assuming the reaction to be adiabatic, ν_n is the nuclear frequency factor, ΔG° is the standard free energy of the electron transfer reaction between the donor D and the acceptor A. The total reorganization energy λ is initially considered only as the outer-shell solvent continuum reorganization energy λ_s and is expressed as[21]

$$\lambda_s\,(\text{hom}) = (e^2/4\pi\varepsilon_0)(1/2r_D + 1/2r_A - 1/r_{AD})\,(1/\varepsilon_{op} - 1/\varepsilon_s) \tag{2}$$

where ε_0 is the permittivity of a vacuum, r_D and r_A are the radii of donor and acceptor ions, including the solvent (if any) in the inner shell, r_{AD} is the center-to-center distance between electron donor and acceptor, and ε_{op} and ε_s are, respectively, the high-frequency (optical) and static dielectric constants of the solvent. The quantity ε_{op} is equal to the square of the solvent refractive index.

However, for electrochemical electron transfer reactions at a metal electrode, one gets[21,25]

$$\lambda_s\,(\text{het}) = (e^2/8\pi\varepsilon_0)(1/r - 1/2r_{im})\,(1/\varepsilon_{op} - 1/\varepsilon_s) \tag{3}$$

where r is the radius of the acceptor or donor ion in solution, including the solvent in the inner shell, and r_{im} is the distance between the centers of the solvated ions and their images inside the electrode.

The continuum theory expression of the free energy of activation $\Delta G^\#$ (continuum) can be expressed as

$$\Delta G^\#\,(\text{continuum}) = (\lambda_s + \Delta G^\circ)^2/4\lambda_s \tag{4}$$

where ΔG° is the free energy of the reaction. For the rare case (isotopic reaction) in which $\Delta G^\circ = 0$, Eq. (4) yields

$$\Delta G^{\#}\,(\text{continuum}) = \lambda_s/4 \tag{4a}$$

1. Born Equation and the Free Energy of Activation, $\Delta G^{\#}$ (continuum)

The free energy of activation in the continuum theory is based on the prequantal Born continuum solvation equation[24] for ions in solution,

$$\Delta G_{solv}(\text{Born}) = -(z^2e^2/8\pi\varepsilon_0 r_i)(1 - 1/\varepsilon_s) \tag{5}$$

where z is the charge on the ion; e is the electronic charge; r_i is the radius of the ion, including the first layer of solvent; ε_0 is the permittivity of the vacuum; and ε_s is the static dielectric constant of the solvent.

The Born solvation equation is based on the difference in the energy needed to charge a sphere of radius r_i in a solvent of dielectric constant ε_s and in vacuum having a dielectric constant of unity. There are basic flaws in the concept of the Born solvation equation (5) on which the continuum theory of ET reactions is based. First, Born Eq. (5) does not take into account the interaction of ions with a water solvent that has a dielectric constant of approximately 80 at room temperature. Hence, the Born solvation energy will have negligible contribution from solvents with high dielectric constants. Consequently, for solvents of high dielectric constant, Eq. (5) can be written as

$$\Delta G_{solv}(\text{Born}) = -(z^2e^2/8\pi\varepsilon_0 r_i)(1 - 1/80)$$

$$\approx -z^2e^2/8\pi\varepsilon_0 r_i \tag{5a}$$

which is, in fact, the charging energy in a vacuum and not the solvation energy. A simple calculation for the charging energy of $Fe^{3+}(vac)$ in a vacuum yields 19.60 eV, whereas a very close value of 19.36 eV is obtained for the solvation energy of $Fe^{3+}(aq)$ in water. This means that the solvation energy of the $Fe^{3+}(aq)$ ions in aqueous solution $\approx$ charging energy of the $Fe^{3+}(vac)$ ions in vacuum. This result clarifies the fact that the Born solvation equation does not take into account the effect of solvent and hence should not be used to calculate the solvation energy of ions in aqueous solution.

Second, the potential energy of an isolated ion in a vacuum should be zero, not $z^2e^2/8\pi\varepsilon_0 r_i$, because there is no other species present with which

to interact in the vacuum. Third, the concept of Born solvation energy contradicts the way the experimental values of solvation energy are obtained. When an ion is introduced into a solvent, it undergoes solvation by breaking up the structure of the solvent (e.g., hydrogen bonding in an aqueous medium) and orienting its dipoles and induced dipoles. These interaction energies, not the alleged charging energy of a hollow sphere, are responsible for the physical origin of the solvation energy of the ions. Hence, the major contribution to solvation energy should come from the ion–solvent interaction energy with the oriented solvent molecules in the first two or three layers around the ion.

Fourth, the reference state considered in deriving the Born equation (charging energy) is not that by which the experimental values of solvation energy are determined. Experimental solvation energy is obtained by measuring the heat of solution of a salt in the solvent concerned. This value is added to the lattice energy of the salt to obtain the solvation energy. Hence, the experimental solvation energy corresponds to a reference state of lattice energy that is zero in a vacuum. In contrast, in deriving the Born solvation equation, the energy in the reference state in a vacuum is not zero but the huge charging energy in the vacuum, and 98% of this is called the *solvation energy.* Therefore, solvation energies obtained from the Born solvation equation are not related to experimental solvation energy.

These points indicate that the continuum theory expression of the free energy of activation, which is based on the Born solvation equation, has no relevance to the process of activation of ions in solution. The activation of ions in solution should involve the interaction energy with the solvent molecules, which depends on the structure of the ions, the solvent, and their orientation, and not on the Born charging energy in solvents of high dielectric constant (e.g., water). Consequently, the continuum theory of activation,[21] which depends on the Born equation,[24] fails to correlate (see Fig. 1) with experimental results.[26,27] Inverse correlations were also found between the experimental values of the rate constant for an ET reaction in solvents having different dielectric constants[28] with those computed from the continuum theory expression.[21] Continuum theory[21] also fails to explain the well-known Tafel linearity of current density at a metal electrode.[29]

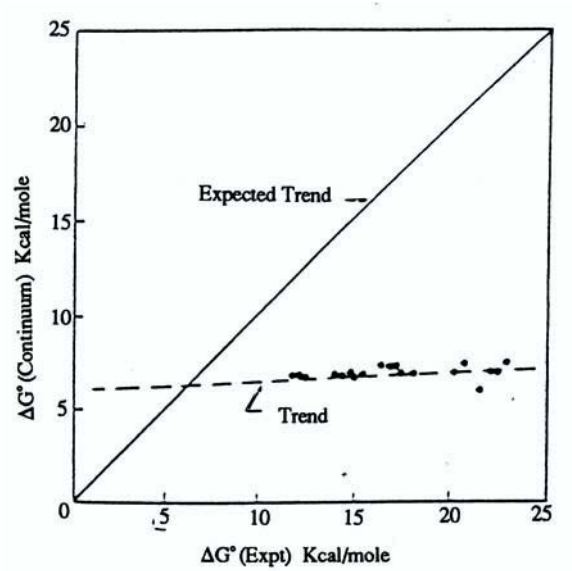

Figure 1. A plot of free energy of activation, $\Delta G^{\#}$ (continuum) vs. $\Delta G^{\#}$ (expt) for electrochemical redox reactions. (Reprinted from Ref. 26.)

2. Reorganization Energy λ_s (Continuum) and the Free Energy of Activation $\Delta G^{\#}$

In the continuum theory, the free energy of activation is obtained as one-fourth of the reorganization energy λ_s (continuum) from geometrical consideration of the harmonic potential, though only for isotopic exchange reactions; the free energy of such a reaction, $\Delta G°$, is zero. It is critical to note that the reorganization energy, as defined in the continuum theory (see Fig. 2), corresponds to a change in the alleged solvation energy just after the electron transfer for a time period on the order of 1.0×10^{-15} s. In this short period, only the charge of the reactant ion changes to the charge of the product ion, but the configuration of the reactant does not change (e.g., no change in the ion–solvent bond or coordinate occurs). Hence, the reorganization energy is defined as the energy of the product ion when its solvent configuration is that of the reactant just after the electron transfer.

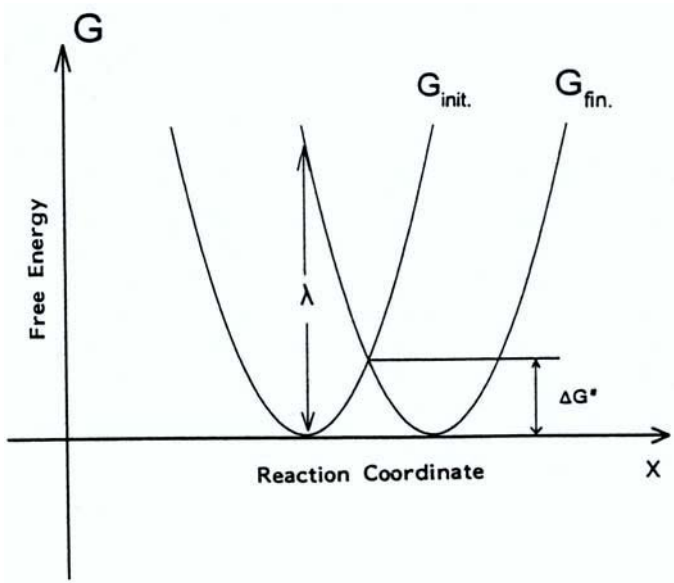

Figure 2. Schematic diagram to show the reorganization energy λ_s for isotopic reactions for harmonic free energy profiles. G_{init} and G_{fin} represent the initial (reactant) and the final (product) system free energy respectively.

This reorganization energy λ_s, which is the energy after the act of electron transfer, is an indirect way (a thought process) to find the free energy of activation $\Delta G^{\#}$ from the geometrical consideration of a parabolic free energy profile. In other words, it is a mathematical construct to obtain $\Delta G^{\#}$ from λ_s. Prior to the act of radiationless electron transfer, ions in solution will have to be activated first to an equal energy state, which involves various molecular-level interactions and passage of the reacting system on the trajectory of the reaction hypersurface.

This method of finding the free energy of activation $\Delta G^{\#}$ in terms of the reorganization energy λ_s suffers the following drawbacks. First, it gives a quadratic form of a rate equation because it uses a parabolic form of a free energy profile and cannot reproduce the experimentally observed Tafel linearity over a larger overpotential range. Second, the λ_s value strongly depends on the shape of the free energy profile. For example, for

the same ET reaction, different λ_s values are expected if the free energy profile is a parabolic or Morse type (see Figs. 3a and 3b). Hence, it will be difficult to obtain the correct value of $\Delta G^{\#}$ from λ_s unless the shape of the potential energy profile is known. Consequently, the free energy of activation obtained from the continuum theory does not agree with experimental values for most systems.[26,27]

Furthermore, the interaction with solvent molecules far outside the ions will be insignificant compared with the various short-range molecular-level interactions during the activation of ions in solution. For example, for the ET reactions involving transition metal ions in aqueous solution, various short-range interactions take place between ions and the water molecules that are responsible for the activation process.[30] First, the solvent (water) molecules that bind directly to the metal ion strongly influence the electronic and geometric structure of the metal complex. These molecules can contribute to the activation energy by short-range electrostatic and chemical interactions. Such contributions from the bonding of solvent or ligand molecules nearest to the ion are relatively easy to

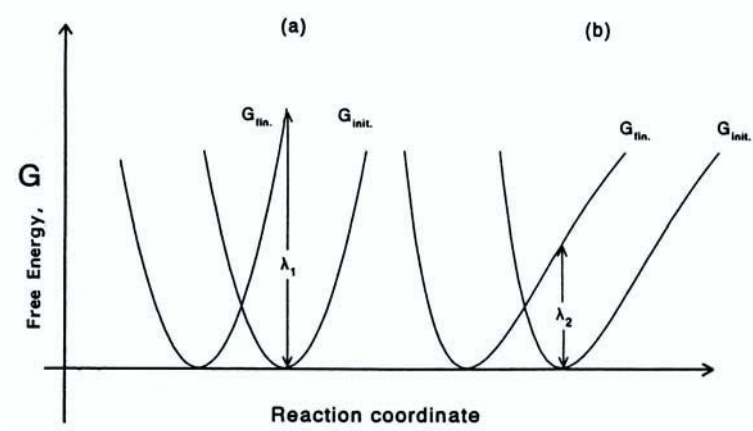

Figure 3. For the same reaction, different values of reorganization energy are found if the free profile is harmonic (λ_1) in (a) or Morse type (λ_2) in (b) where λ_1 (harmonic) >> λ_2 (Morse). G_{init} and G_{fin} represent the initial (reactant) and the final (product) system free energy, respectively. For the Morse free energy profile, $\Delta G^{\#} \neq \lambda_2/4$ for the isotopic reaction in (b).

compute[31] and will be considered further in the discussion concerning the molecular models.

Second, there are water molecules from the second coordination sphere that also contribute strongly to the activation of ions in solution. These interactions are less easy to model accurately due to uncertainty regarding the number of oriented water molecules in the second layer and their degree of orientation toward the central ion; there are some simple classical expressions available, however, to compute the average orientation of these water molecules.[32] Third, there are water molecules that sometimes hydrogen bond to ligands of the complex and these may also contribute to the activation process. These important short-range interactions are neglected in the continuum theory of ET reactions in solution[21] and, as a result, this theory fails to correlate with experimental results and even gives rise to inverse correlations.[28]

III. $\Delta G^{\#}$(CONTINUUM) AND THE INVERTED REGION

1. General

The quadratic rate equation [Eq. (1)] of the continuum theory[21] arises because it implicitly assumed the parabolic dependence of the free energy profile on the solvent coordinate q. One of the consequences of this quadratic equation is the generation of a maximum in the dependence of the rate of reaction on the free energy of reaction and also in current density–overpotential dependence.

Recently, several theoretical[33] and experimental[34–45] studies searched for the existence of a so-called "inverted region" that resulted from the use of the quadratic expression of the rate constant of the continuum theory.[21] By "inverted region" one means that when the free energy of an exothermic reaction is greater than the reorganization energy [i.e., when $-\Delta G^{\circ} > \lambda_s$ (reorganization energy)], the rate of the ET reaction starts to decrease in the inverted region from its maximum position at the activationless ($\Delta G^{\#} = 0$) situation when $-\Delta G^{\circ} = \lambda_s$ (see Fig. 4). It is also shown in Fig. 4 that the activation barrier reappears so that $\Delta G^{\#} > 0$ when the free energy of reaction $-\Delta G^{\circ} > \lambda_s$ and the free energy profile is considered harmonic. However, the activation barrier does not reappear for $-\Delta G^{\circ} > \lambda_s$, when a Morse-type free energy profile is used (see Fig. 5). Consequently, one will

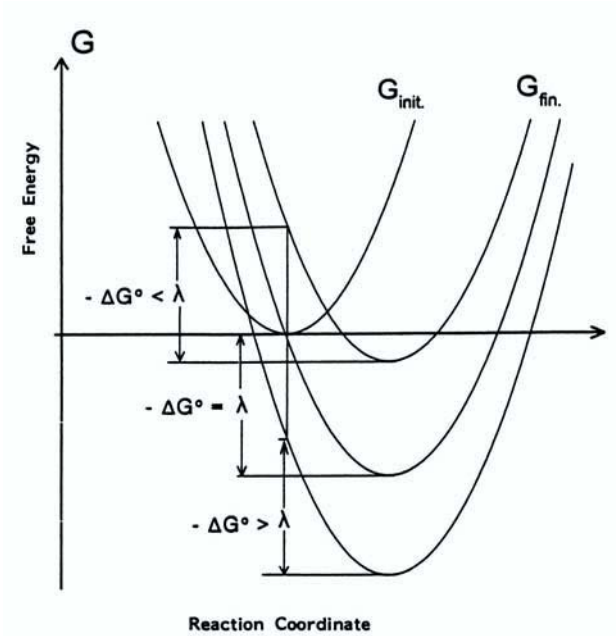

Figure 4. Schematic diagram to show the reorganization energy λ for nonisotopic reactions for harmonic free energy profiles. This figure shows a normal region activation barrier when $-\Delta G^\circ < \lambda$, an activationless situation when $-\Delta G^\circ = \lambda$, and an inverted region activation barrier when $-\Delta G^\circ > \lambda$ for the harmonic potential G_{init} and G_{fin} represent the initial (reactant) and the final (product) system free energy, respectively.

not expect an inverted region if the potential energy profile is a Morse type, which is of course the case for most reactions. It is observed in Fig. 5 that the free energy profiles can never cross each other when $-\Delta G^\circ > \lambda_s$; this indicates that the inverted region does not occur when a Morse free energy profile is used.

To search for the inverted region, experiments were designed so that the donor–acceptor distances were kept fixed by attaching them to a covalent network of rigid spacers,[34–38] frozen media,[38] electrostatic complexation,[39–43] and protein frameworks.[44,45] In all of these cases, the

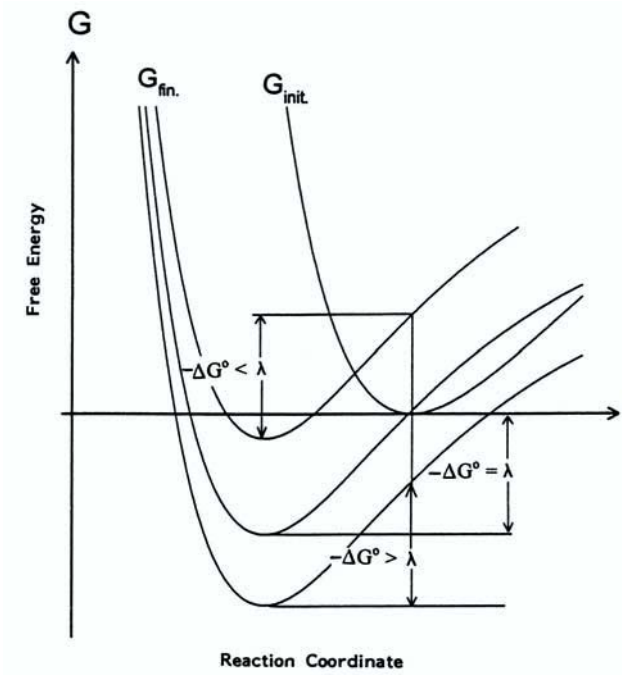

Figure 5. Schematic diagram to show the reorganization energy λ_s for nonisotopic reactions for Morse free energy profiles. This figure shows a normal region activation barrier when $-\Delta G^\circ < \lambda$, an activationless situation when $-\Delta G^\circ = \lambda$, and no inverted region activation barrier when $-\Delta G^\circ > \lambda$. When $-\Delta G^\circ > \lambda$, the two free energy profiles do not cross, G_{init} and G_{fin} represent the initial (reactant) and the final (product) system free energy, respectively.

distance between the donor and acceptor was assumed to remain constant to avoid the diffusion control of ions in solution. However, in the analysis of these experimental results on intramolecular electron transfer reactions in a homogeneous solution, an error was made in interpreting the existence of the "inverted region." The results of rate constants of intramolecular ET reactions having various reactants were used to interpret an "inverted region" using a single value of reorganization energy λ_s.[34] It is not

appropriate to use a single value of reorganization energy for different ET reactions because each reaction having reactants of different sizes and structures will have different reorganization energy (λ_s) values and hence different activation barriers. Consequently, no inverted region is in fact observed, even for the intramolecular ET reactions. Hence, an apparent inverted region for these intramolecular ET reactions is an artifact due to the use of a single value of reorganization energy λ_s for different reactions having reactants of different sizes and structures.

Furthermore, for different ET reactions, it can be easily demonstrated in a schematic diagram that even though, for example, $-\Delta G_1^\circ$ (of reaction 1) is much larger than $-\Delta G_2^\circ$ (of reaction 2), the free energy of activation $\Delta G_1^\#$ (of reaction 1) could be higher than the free energy of activation, $\Delta G_2^\#$ (of reaction 2) in the "normal region" (see Figs. 6a and 6b). Figures 6a and 6b also reveal that it is not essential to use the concept of "inverted

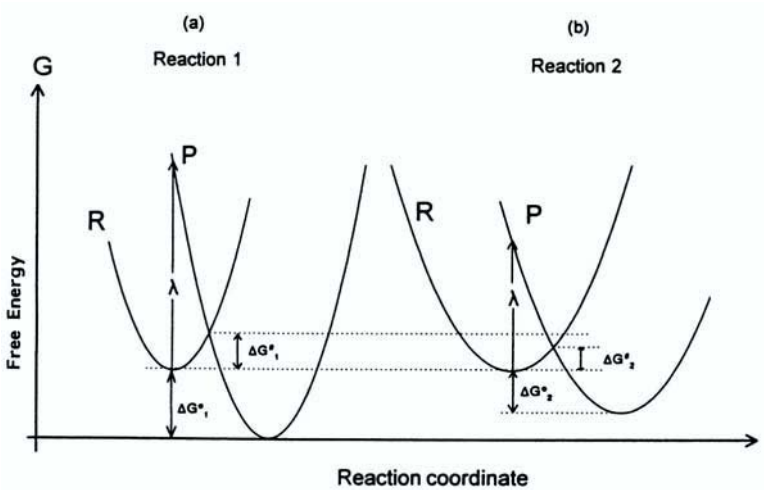

Figure 6. Schematic diagram of free energy-reaction coordinate relationships for exothermic reaction in which the free energy of reaction ΔG_1° of the exothermic reaction 1 in (a) is higher than the free energy of reaction ΔG_2° of the exothermic reaction 2 in (b). It shows that the free energy of activation $\Delta G^\#_1$ for reaction I is higher than $\Delta G^\#_2$ of reaction 2, even though $-\Delta G_1^\circ$ for reaction 1 is higher than ΔG_2° of reaction 2. The concept of "inverted region" is hence redundant to explain higher $\Delta G^\#$ values even though $-\Delta G^\circ$ is larger when different reactions are compared. R and P represent the reactant and the product system, respectively.

region" to explain a higher activation barrier for a reaction that has a higher value of $-\Delta G°$ than another reaction. Hence, the lowering of rate with higher $-\Delta G°$ values for different exothermic reactions can be easily explained in the normal region without the use of an inverted region.

2. ET Reactions at Electrodes and the Inverted Region

The best way to search for the existence of an inverted region (if any) would be to use a single electrochemical electron transfer reaction in one solvent medium at a particular electrode and determine the effect of high overpotential on the reaction rate or the current density. Many experiments were carried out at organic spacer-covered (~2.0 nm thick) electrodes to search for the inverted region for the outer-sphere ET reactions; however, no inverted region was observed.[46–52]

It should be noted that at organic spacer-covered electrodes, the Tafel line becomes nonlinear and shows the limiting current density at high overpotentials (no inverted region), which is similar to those observed at oxide-covered electrodes. Such nonlinear Tafel lines at an oxide-covered electrode (which show no inverted region behavior) were clearly explained by Schmickler[53,54] as being due to resonance tunneling of electrons via the resonant states in the parabolic-type barrier (see Fig. 7) inside the oxide layer at the interface (see Fig. 8), and were not due to the quadratic activation term of continuum theory.[21,25] The expression of the resonance

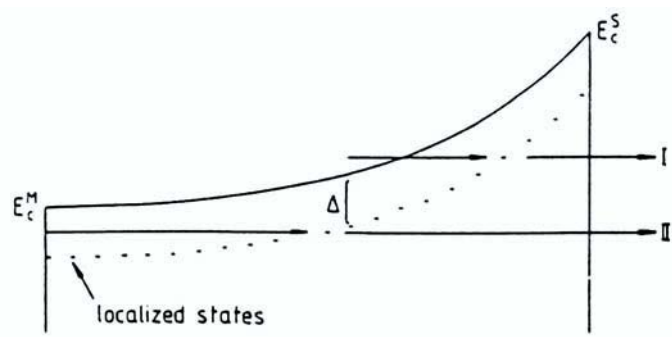

Figure 7. Two different routes of resonance tunneling and the barriers in the oxide layer on a metal surface. E_c^M and E_c^S denote the energy at the bottom of the conduction band of the oxide layer at the metal/oxide and at the oxide/electrolyte interfaces respectively. (Reprinted from Ref. 54.)

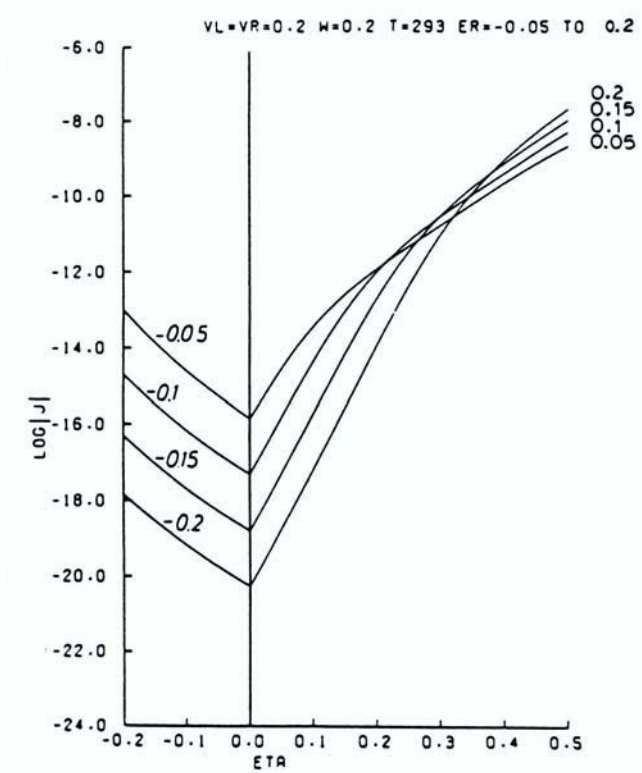

Figure 8. Tafel plots for the cathodic and anodic current densities for various values of the impurity states of energy E_r° for an oxide layer thickness of 20 Å. (Reprinted from Ref. 53.)

current density that was used by Schmickler[53,54] to explain the nonlinear Tafel lines at oxide-covered electrodes did not include the quadratic term and was given as in the following equation,

$$j_r = (1/a)2\pi C c_1 \int_0^a n(E_r)\exp\{-[E^\circ_{act} - (E_r - e\eta)/2]/kT\}\{R_1(l)R_2(l)/[R_1(l) + R_2(l)]\}dl \qquad (6)$$

where a is the width of the oxide layer, C is a constant containing the concentration of the reactants, c_1 is a constant in the tunneling expression, E_r is the energy of the resonance state, E°_{act} is the activation energy, and η is the overpotential. This Eq. (6) should be applicable to organic spacer-covered electrodes to explain nonlinear Tafel lines without the use of a quadratic equation.[21] In the oxide-covered electrode, electron tunneling through the barrier in the oxide layer becomes the rate-determining step over a considerable overpotential range and thus generates the nonlinear Tafel lines (see Fig. 8).

It was suggested[46] that the absence of an inverted region for the ET reactions at spacer-covered metal electrodes is due to the availability of a continuum of electronic states in metal electrodes below the Fermi level. For the same reason, the inverted region is also not expected to be seen for the homogeneous intermolecular ET reactions because a continuum of electronic states are also available below and above the respective ground states of acceptor and donor ions in solutions involved in homogeneous ET reactions.[1,55]

It is important to note that as early as 1931, the density of electronic states in metals, the distribution of electronic states of ions in solution, and the effect of adsorption of species on metal electrode surfaces on activation barriers were adequately taken into account in the seminal Gurney–Butler nonquadratic quantum mechanical treatments,[1,2] which provide excellent agreement with the observed current–overpotential dependence.

Many conceptual inconsistencies of the continuum theory mentioned above and the discrepancy with experiments (see also the appendix of Chapter 4 in Ref. 55) warrant new theories based on molecular models. We focus on molecular models in the following sections.

IV. MOLECULAR MODELS OF ELECTRON TRANSFER REACTIONS AT ELECTRODES

The molecular models of electron transfer reactions are in general much more complicated and do not generate the simple relations of the free energy of activation as in the continuum theory.[21,25] However, it is important to focus on alternative molecular models at this time because of the fundamental flaws of continuum theory and its inconsistencies with experiments, as pointed out earlier.

1. Free Energy of Activation, $\Delta G^{\#}$ and the Molecular Models

(i) George–Griffith Treatment

A simple theory, in terms of molecular models, for the free energy of activation of ions in solution was given by George and Griffith[31] by taking into account the vibrational interactions of solvent or ligand molecules attached to the ion in the first layer. The free energy of activation for the ET reaction in the homogeneous medium was given as[31]

$$\Delta G^{\#}(\text{hom}) = (n/2)[f_A f_D/(f_A + f_D)]\,(\Delta r)^2 \tag{7}$$

In the electrochemical case, it can be expressed as

$$\Delta G^{\#}(\text{het}) = (n/4)[f_A f_D/(f_A + f_D)](\Delta r)^2 \tag{8}$$

where n is the number of solvent molecules or ligands in the inner shell, f_A and f_D are the force constants of inner shell bonds in the acceptor and donor species, respectively, and Δr is the difference between the equilibrium bond distances in inner shell bonds in the reactant and in the product.

The task in using these simple expressions (7) and (8) lies in finding the number of ligands n, the force constants f_A, f_D, and values for the bond length difference Δr. The values of n and Δr are obtained from X-ray crystallographic or extended X-ray absorption fine structure data. The force constants f_A and f_B are obtained from available vibrational spectroscopic data using the equation.

$$f_i = 4\pi^2 c^2 \omega_i^2 (m_L/N) \tag{9}$$

where ω_i is the observed symmetric stretching frequency of the ion–solvent or ion–ligand bond in wave number, c is the velocity of light, m_L is the molecular weight of the solvent or the ligand, N is Avogadro's number, and i represents either the acceptor or the donor state.

Though for some systems experimental stretching vibrational frequencies are available, the paucity of these frequencies for many systems limits the use of the George–Griffith molecular model of the free energy of activation. To overcome this difficulty, one can directly compute the force constants using either a classical improved average dipole orientation (IADO) model[32] or a quantum chemical intermediate neglect of differential overlap (INDO/2) molecular orbital method.[11] Using the

improved average dipole orientation model, the force constant of the ion–solvent or ion–ligand bond can be expressed as[11]

$$f_i = 10ze_0^2\,\alpha/r_z^2 + 6ze\mu/r_z^6 - 3.772(ze\mu kT)^{1/2}/r_z^3 \qquad (10)$$

where e_0 is the electronic charge, α is the molecular polarizability of the ligand or the solvent, μ is the dipole moment of the solvent or the ligand, z is the charge on the ion, and r_z is the radius of the ion having charge z. Using the quantum chemical INDO/2 method, the force constant can be calculated for ions (e.g., transition metal ions) in solution using the relation

$$f_i = -d^2[V(r)]/dr_z^2 \qquad (11)$$

where ion–solvent or ion–ligand interaction potential can be obtained from the relation

$$V(r) = [2H_{ii} + (2J_{ij} - K_{ij})] \qquad (12)$$

where H_{ii} is the average nuclear-electronic attraction energy for the electron in the ith atomic orbital, $\Psi_i \cdot J_{ij}$ and K_{ij} are, respectively, the Coulomb (attraction and the repulsion) and the exchange interaction energies between the ith atomic orbital Ψ_i, and the jth atomic orbital, Ψ_j.

The values of the force constant calculated from classical IADO and quantum chemical INDO/2 methods, along with corresponding experimental values, are given in Table 1. Close agreement with experiments indicates that these two simple methods can be easily used to determine the force constant from ions in solution for which experimental values are not available.

When one compares the computed values of the free energy of activation using the George–Griffith expression, it is observed that it takes into account about three-fourths of the total experimental values[26,27] obtained from the rate constant data or measured directly using the photoemission method.[56] The following corrections may account for the remaining one-fourth contribution of the free energy of activation: (1) incorporation of the contribution from the second layer of solvent molecules, (2) calculation of the correct values of the free energy of activation from the rate constant data using the correct value of the transmission coefficient κ, and (3) the solvent relaxation time-dependent value of the

Table 1
The Force Constants of Ion–Ligand Bonds of Hexaaquo and Amine Complexes

Reactants	w_i (cm^{-1})	Force constants (mdyn $Å^{-1}$)		
		f_i (expt)	f_i (MO)	f_i (IADO)
$[V(H_2O)_6]^{2+}$	389	1.60	1.46	0.85
$[Cr(H_2O)_6]^{2+}$	389	1.60	1.54	0.93
$[Mn(H_2O)_6]^{2+}$	395	1.65	1.56	1.02
$[Fe(H_2O)_6]^{2+}$	389	1.60	1.72	1.12
$[Co(H_2O)_6]^{2+}$	389	1.60	2.03	1.15
$[V(H_2O)_6]^{3+}$	490	2.44	2.39	2.02
$[Cr(H_2O)_6]^{3+}$	490	2.54	2.40	2.18
$[Mn(H_2O)_6]^{3+}$	490	2.54	2.15	2.55
$[Fe(H_2O)_6]^{3+}$	490	2.54	2.16	2.55
$[Co(H_2O)_6]^{3+}$	490	2.54	2.43	2.76
$[Cr(NH_3)_6]^{2+}$	395	1.56	1.21	0.98
$[Mn(NH_3)_6]^{2+}$	321	0.94	1.22	1.08
$[Fe(NH_3)_6]^{2+}$	307	1.03	1.44	1.19
$[Co(NH_3)_6]^{2+}$	327	1.07	1.77	1.25
$[Co(NH_3)_6]^{3+}$	495	2.45	2.60	2.96
$[Cr(NH_3)_6]^{3+}$	475	2.26	1.74	2.32
$[Mn(NH_3)_6]^{3+}$	401	1.50	1.89	2.73
$[Fe(NH_3)_6]^{3+}$	387	1.61	1.98	2.73

nuclear frequency factor ν_n, and (4) the off diagonal contributions that take into account the coupling interactions between the bonds in the inner shell.

(ii) Molecular Dynamic Simulations

Most theoretical studies of outer-sphere (nonbond-breaking) electron transfer reactions at the metal–solution interface involve major simplifying assumptions regarding the molecular and electronic structure of the solvents and the metal. Although the importance of molecular structure and the dynamics of the solvent has been recognized, most of the theoretical work in this area has been based on a highly simplified continuum model.[21]

Rose and Benjamin[12] (see also Halley and Hautman[10]) utilized molecular dynamic simulations to compute the free energy function for an electron transfer reaction, $Fe^{3+}(aq) + e \rightarrow Fe^{2+}(aq)$ at an electrode–solution interface. In this treatment, $Fe^{3+}(aq)$ in water is considered to be fixed next to a metal electrode. In this tight-binding approximation, the electron transfer is viewed as a transition between two states, Ψ_i and Ψ_f. In Ψ_i, the electron is at the Fermi level of the metal and the water is in equilibrium with the Fe^{+3} ion. In Ψ_f, the electron is localized on the ion, and the water is in equilibrium with the Fe^{+2} ions. The initial state Hamiltonian H_i is expressed as

$$H_i = H_{ie} + H_A + q_i U(r) \tag{13}$$

where H_{ie} is the Hamiltonian that represents the electronic contribution, such as the Fermi level in the metal and the energy of the unoccupied ion orbital; H_A includes the solvent molecules and the metal intermolecular and intramolecular potentials, the electrostatic interaction between the solvent molecules and the metal surface, which is considered to switch to zero after 3 water layers (i.e., between 8.5 and 9 Å, and the nonelectrostatic part of the ion–solvent and ion–metal interactions; q_i is the charge on the ion when the system is in the initial state (+ 2e or + 3e), and $U(r)$ is the electrostatic potential at the location of the ion due to the ensemble of water dipoles (where r represents the position and the orientation of all solvent molecules). $U(r)$ can be expressed as

$$U(r) = \Sigma_i q_{i\alpha} / |r_I - r_i^{\alpha}| \tag{14}$$

where r_I is the position of the ion, r_i^{α} denotes the position of the atom α (α = H or O) of a water molecule i, and the partial charge on atoms $q_{i\alpha} = -0.41e$ for α = H atom and $-0.82e$ for α = O atom.

Similarly, the final state Hamiltonian H_f is expressed as

$$H_f = H_{if} + H_A + q_f U(r) \tag{15}$$

where it is assumed that Fe^{+3} and Fe^{+2} interact with the solvent molecules and the metal electrode via the Lennard-Jones potential energy function, V. For an ion–water interaction, it is expressed as

$$V_{\text{ion-water}} = \Sigma_i A / |r_I - r_i^{\alpha}|^9 + q_{\alpha} U(r) \tag{16}$$

where $A = 6392.7$ kcal mol^{-1}, Å^{-9} is used.

The energy difference between the final and the initial state, $\Delta E(r)$ becomes

$$\Delta E(r) = H_f - H_i \simeq \Delta H_e + \Delta q U(r) \tag{17}$$

where $\Delta q = q_f - q_i$ is the total charge transfer during the reaction and ΔH_e is the difference between the electronic energy levels that can be controlled by changing the potential difference between the electrode and the solution.

The ET reactions occur with high probability when $\Delta E(r) \simeq 0$ at the transition state. It is assumed that this condition arises due to an interaction with the solvent that changes $U(r)$. The probability $p_i(u)$ of observing a given value u of U(r) of the initial state is expressed as

$$p_i(u) = \int \delta[U(r) - u] e^{-H_i/kT} dr / \int e^{-H_i/kT} dr \tag{18}$$

where δ is the Dirac delta function and u is a value of $U(r)$ for a specific arrangement of solvent. A similar expression can be used for the probability of observing a given value of u when the system moves to the final state having the Hamiltonian H_f.

$$p_f(u) = \int \delta[U(r) - u] e^{-H_f/kT} dr / \int e^{-H_f/kT} dr \tag{18a}$$

The free energies G of the inital and the final states are expressed as a function of u in terms of probabilities $p_i(u)$ and $p_f(u)$ as

$$G_i(u) = -kT \ln[p_i(u)] \tag{19}$$

and

$$G_f(u) = -kT \ln[p_f(u)] \tag{20}$$

The computed results of free energy as a function of the solvent coordinate, $u - u_0^{\#}$ (where $u_0^{\#}$ is the value of u at the crossing point of the free energy curves at the overpotential, $\eta = 0$) for Fe^{+2} and Fe^{+3} are given in Fig. 9. The free energy of activation $\Delta G^{\#}$ from the crossing point of this plot is found to be 0.6 eV, which correlates well with the experimental result of 0.59 eV.[57] Furthermore, simple calculations using the continuum theory expression[21] show that $\Delta G^{\#}$ (continuum) = 0.23 eV, which is

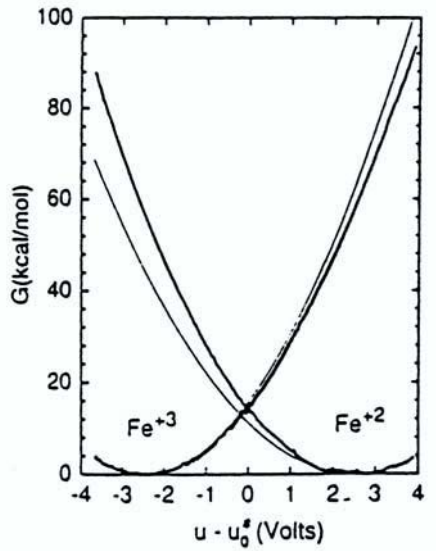

Figure 9. The free energy curves for the Fe^{2+} (aq) and Fe^{3+} (aq) ions. The bold curves represent the result of "umbrella sampling" of the molecular dynamics calculation. Thin solid lines correspond to the best parabolic fit of the region near the bottom of each wall. (Reprinted from Ref. 12.)

approximately one-third of the experimental value,[57] the value obtained from the molecular dynamic simulation[12] or one calculated from the George–Griffith expression.[31] However, this treatment was limited to finding the potential energy profile and the activation barrier at zero overpotential, $\eta = 0$. It is important to note that the rates of ET reactions at electrodes and their dependence on the overpotential are not addressed in this treatment.[12]

(iii) Anderson–Newns Hamiltonian Approach

For the charge transfer between an ion in solution and a metal electrode, several authors[8,14,15,58–60] adapted the Anderson–Newns Hamiltonian,[16,17] which can be expressed as

$$H = H_{solv} + H_{el} \tag{21}$$

where H_{solv} represents the hamiltonian for the solvent–solvent interaction, solvent–surface interaction, and all other interactions that do not include electronic interactions, and H_{el} is the electronic part of the Hamiltonian. It can be written as

$$H_{el} = (\varepsilon_a + \Delta E)n_a + \Sigma_k (\varepsilon_k n_k + V_{ak}c_a + c_k + V_{ka}c_k + c_a) \tag{22}$$

where ε_a is the energy of the ion (with respect to vacuum level) of the electronic orbital $|a\rangle$ in the ion involved in charge transfer, ΔE is the shift of the ion's energy due to interaction with the solvent molecules when the ion undergoes the change in charges during the transition from the initial to final states and V_{ak} or V_{ka} represents the ion–metal interaction energy. The ion orbital is described by an occupancy operator n_a and a metal orbital n_k, each of which can equal either 0 or 1. The sum over k in Eq. (22) is the sum over the electronic energy states ε_k in the semi-infinite metal electrode, c^+ and c are the creation and annihilation operators, respectively.

A molecular dynamic simulation was made by Straus and Voth[14,15] using the Hamiltonian

$$H = H_{solv} + E(\Delta E) \tag{23}$$

which represents the adiabatic ground-state Hamiltonian of Eq. (21). For this, ΔE was assigned to certain classical potential energies in typical molecular dynamics computations. In the Hamiltonian, one can separate all the terms that depend on the Coulombic interaction between the solvent and the ion and can write these terms considering an Fe^{+3} ion with a positive charge $Z = 3$ which has an electronic orbital $|a\rangle$ of occupancy n_a. If the orbital is empty, $n_a = 0$ and the Hamiltonian describes the Fe^{+3} ion. If the orbital is filled, then $n_a = 1$ and the Hamiltonian represents the Fe^{+2} ion near the metal electrode surface. This means that the initial-state Hamiltonian can be changed to the one in the final state via the term n_a. ΔE in the Hamiltonian of Eq. (23) can be expressed in terms of Coulombic potentials as[14,15]

$$\Delta E = -(V_{\text{solvent-ion}} + V_{\text{solvent-ion image}}) \tag{24}$$

where $V_{\text{solvent-ion}}$ is the potential energy between the solvent and the ion and $V_{\text{solvent-ion image}}$ is the potential energy between the solvent and the ion's image in the electrode.

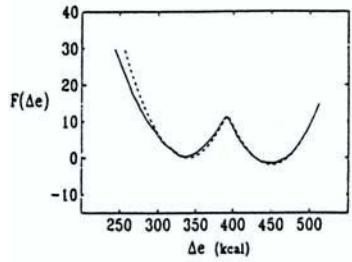

Figure 10. Classical adiabatic free energy curve (solid line) for the Fe^{2+}/Fe^{3+} electron transfer at the water/Pt(111) interface calculated using the Anderson–Newns Hamiltonian and the molecular dynamics umbrella sampling method. Also shown by the dashed line is the parabolic fit of the data. (Reprinted from Ref. 14.)

Like the treatment presented earlier, the free energy function was expressed in terms of the probability $p(\Delta e)$ of having $\Delta E = \Delta e$ where Δe is the particular value of the collective solvent interaction (solvation) energy for the particular value of the charge on the ions and the configuration of the solvent. Thus, the free energy function $G(\Delta e)$ is expressed as[14,15]

$$G(\Delta e) = -kT \ln[p(\Delta e)] \tag{25}$$

where

$$p(\Delta e) = \int \delta[\Delta e - \Delta E] e^{-(H+V)/kT} dx \Big/ \int e^{-(H+V)/kT} dx \tag{26}$$

where V is the biasing electrode potential and x represents the multidimensional coordinate of the entire system.

For a given set of microscopic parameters, Straus, Calhoun, and Voth[14] determined the adiabatic free energy curves as a function of the reaction coordinate Δe using Eqs. (25) and (26). $p(\Delta e)$ was determined using the Anderson–Newns Hamiltonian of Eq. (23) in Eq. (26). The results are shown in Fig. 10. From the crossing point of the free energy curve, the activation free energy $\Delta G^{\#} = 0.49$ eV is found for the reaction $Fe^{+2} \rightarrow Fe^{+3} + e$ at the reversible potential and agrees fairly well with the experimental results of 0.59 eV.[57] Quantum solvent models* were found[15] to more accurately describe the actual physical system, suggesting that the

*The solvent molecules are represented in terms of their wavefunctions in the quantum mechanical model and as dipoles in the classical model.

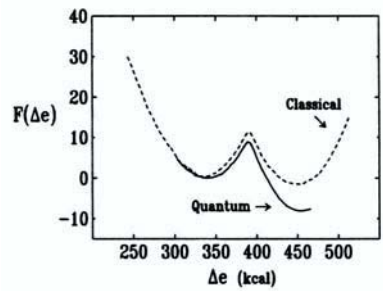

Figure 11. The solid line depicts the quantum adiabatic free energy curve for the Fe^{2+}/Fe^{3+} electron transfer at the water/Pt(111) interface (obtained by using the Anderson–Newns model, path integral quantum transition state theory, and the umbrella sampling of molecular dynamics. The dashed line shows the curve from the classical calculation as given in Fig. 5. (Reprinted from Ref. 14.)

classical simulations are not adequate for the study of electrochemical electron transfer (ECET) reactions. The results of free energy based on classical and quantal treatments are given in Fig. 11.

Calhoun and Voth[61] also utilized molecular dynamic simulations using the Anderson–Newns Hamiltonian to determine the free energy profile for an adiabatic electron transfer involving an Fe^{+2}/Fe^{+3} redox couple at an electrolyte/Pt(111) metal interface. This treatment expands upon their earlier simulation[15] by including, in particular, the influence of the motion of the redox ions and the counterions at the interface.

The difficulty of such treatments are that they do not provide expressions for the rate of die ET reactions at electrodes which can be compared with experiments. They involve complicated computer simulations to determine the free energy profile. Such simulations generally use adjustable parameters to make the results fit experiments. Conversely, these treatments include both short- and long-range ion–solvent interactions and the interaction of the ion and the solvent with the metal electrode at a molecular level.

V. MOLECULAR MODELS OF BOND-BREAKING ION AND ELECTRON TRANSFER REACTIONS

Molecular modeling treatments of electron transfer kinetics for reactions involving bond breaking were developed much earlier than the continuum theories originated by Weiss[18] in 1951. Gurney in 1931[1] published a landmark paper (the foundation of quantum electrochemistry) on a molecular and quantum mechanical model of proton and electron transfer

reactions at an electrode. This was followed by Butler's paper in 1936,[2] which introduced the effect of adsorption of products on charge transfer kinetics at electrodes. Numerical calculations of potential energy curves and electron transfer for proton discharge reactions, based on the Gurney–Butler molecular model, were made by Parsons and Bockris in 1951[62a] and by Conway and Bockris in 1957.[62b]

In the early 1990s a few classical semimolecular[63] and molecular models[64] of electron transfer reactions involving bond breaking appeared in the literature. A quantum mechanical treatment of a unified model of electrochemical electron and ion transfer reactions involving bond breaking was put forward by Schmickler[8] using Anderson–Newns Hamiltonian formalism (see Section V.2).

1. Classical and Semiclassical Treatments

In a classical semimolecular treatment by Saveant,[63] three assumptions were made. First, a Morse potential was adopted to describe the potential energy surface for the bond-breaking reaction. Second, the separability of the contribution from the solvent continuum and from the stretching vibrations corresponding to the bond that is to be broken was assumed. Third, the outer-shell solvent contribution was taken into account using the continuum reorganization concept.[21] The reactions considered are the following:

$$\text{(Homogeneous)} \quad \text{R–X} + \text{A}^{\cdot-} \longrightarrow \text{R}^{\cdot} + \text{X}^{-} + \text{A} \qquad (27)$$

$$\text{(Electrochemical)} \quad \text{R–X} + \text{m(e)} \longrightarrow \text{R}^{\cdot} + \text{X}^{-} \qquad (28)$$

where R–X stands for any molecule of which group X leaves after electron transfer and thus involves bond breaking, R is the remaining group with an unpaired electron (radical), and m(e) represents the electron in the metal electrode. $\text{A}^{\cdot-}/\text{A}$ is a chemically stable redox couple reacting in an outer-sphere manner with no bond breaking. However, in the electrochemical reaction, the contribution from the adsorption of species on the electrode surface* to the free energy of activation was neglected. The potential

*This is an unrealistic assumption to make because it is well known that the halide ions are strongly adsorbed on the electrode surface and contribute to the free energy of activation.[55]

energy of the reactants is assumed to depend on the R–X distance and is expressed like that of Morse, i.e.,

$$U_R = D_{Rx}\,[1 + \exp(-2\gamma_0 Y) - 2\exp(-\gamma_0 Y)] \qquad (29)$$

where Y is the R–X distance minus the equilibrium bond distance in the reactant. D_{Rx} is the dissociation energy of the R–X bond, $\gamma_0 = \nu_0(2\pi^2\mu/D_{Rx})$ with ν_0 as the vibrational frequency of the R–X bond and μ the reduced mass of carbon C in R–X. One approximation was made for the product $(R^{\cdot} + X^{-})$, namely, that the potential energy surface can be expressed as the repulsive part of the reactant Morse curve, i.e., $\exp(2\gamma Y)$. A schematic diagram of the Morse curve for a general R–X system is given in Fig. 12. Saveant[63] found that the contribution of bond breaking to the standard free energy of activation was typically 80% of the total and the

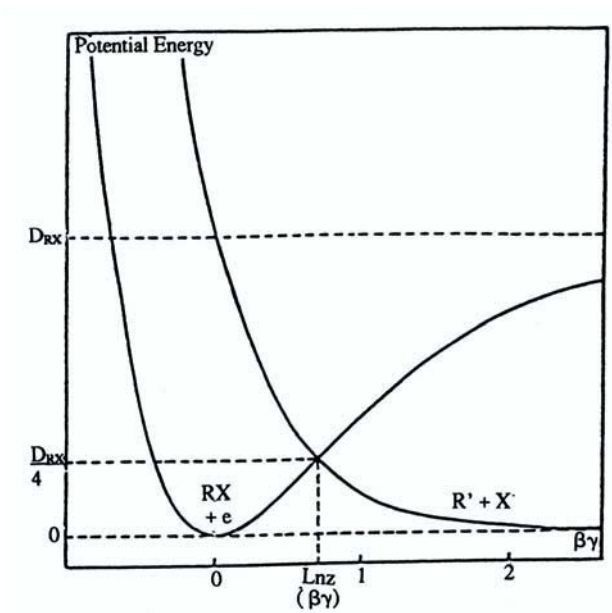

Figure 12. Morse curves for the reactants and products at zero driving force (y, elongation of the R–X distance from the equilibrium; $B = \nu_0(2\pi^2\mu/D_{RX})^{1/2}$; ν_0, vibration frequency; μ, reduced mass; D_{RX}, bond dissociation energy). (Reprinted from Ref. 63.)

remaining 20% was from continuum solvent reorganization. However, it should be noted that the inclusion of electrocatalytic contributions (in the electrochemical case) and the interaction between R–X and A^- (in the homogeneous case) could make up the 20% contribution from outer-shell continuum solvent reorganization. The consideration of electrocatalytic effect would have lowered the activation barrier to a considerable extent and made the continuum solvent contribution redundant.

Perez *et al.*[64] avoided the assumptions used by Savient[63] and performed a Monte Carlo simulation of free energy curves for a dissociative electron transfer reaction in a polar solvent by choosing a simple electrochemical reduction of HF that yielded H and F^-. Perez *et al.*[64] simulated the solute–solvent and solvent–solvent interactions considering the solvent as a point dipole with a dipole moment of 2.15 D for the water solvent. The energies corresponding to the precursor complex (the hydrogen fluoride plus the electron inside the electrode), and the successor complex (the hydrogen fluoride anion) were used to obtain analytic functions for both energy profiles in terms of H–F distance, d_{HF}. Figure 13 shows the interaction energy as a function of distance, d_{HF}.

The solute–solvent interaction was described as charge dipole r^{-6} and r^{-12} terms, i.e.,

$$V_{\text{solute–dipole}} = -q_F |\mu| \cos\theta_{dF}/r_{dF}^2 - q_H|\mu| \cos\theta_{dH}/r_{dH}^2 - B_{dF}/r_{dF}^6 - B_{dH}/r_{dH}^6 + C_{dF}/r_{dF}^{12} + C_{dH}/r_{dH}^{12} \qquad (30)$$

where r_{dF} (or r_{dH}) is the distance between the F atom (or H atom) and a dipole. Conversely, $\cos\theta_{dF}$ (or $\cos\theta_{dH}$) is the cosine of the angle formed by the dipole moment vector μ and the position vector of the dipole; the origin of this position vector is fixed on the F atom (or H atom) while B_{dF}, B_{dH}, C_{dF} and C_{dH} are the constants.

The dipole–dipole electrostatic interaction and a repulsive r^{-12} term that avoids collapsing of dipoles was expressed as[64]

$$V_{12} = -\frac{3|\mu_1||\mu_2| - \mu_1\mu_2}{r_{12}^3} + C_{12}/r_{12}^{12} \qquad (31)$$

where r_{12} stands for the distance between the two dipoles. The parameter C_{12} has been fitted in such a way that by using the V_{12} potential, the interaction energy for the structure of the minimum energy of a pair of point dipoles gives reasonable values for a polar solvent. A C_{12} value of

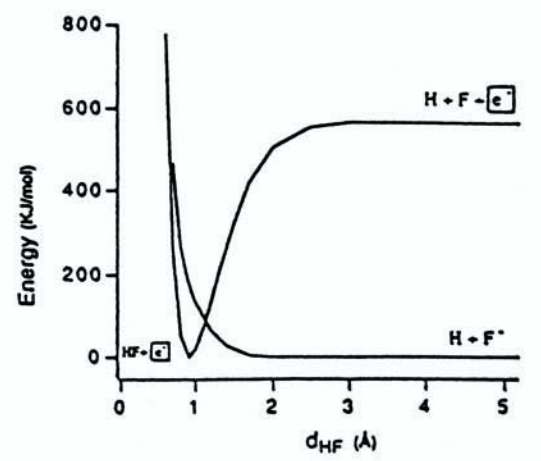

Figure 13. Fitted cubic curves representing solute internal energy with respect to the d_{HF} distance, corresponding to the precursor and the successor complexes, e^- symbol represents an electron inside an electrode. (Reprinted from Ref. 64.)

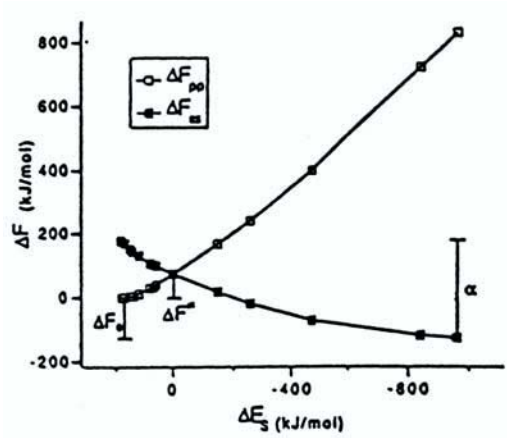

Figure 14. Adiabatic free energy curves for the precursor and successor complexes with respect to ΔE_s values of the reaction coordinate ΔE. (Reprinted from Ref. 64.)

1.65×10^6 bohr hartree was found for $r_{12} = 2.91$ Å with a V_{12} value of -16.78 kJ/mol.

Electron transfer was considered to occur at the intersection region S^* of the potential energy hypersurface $H_{pp}(q)$ and $H_{ss}(q)$ precursor (before electron transfer) and successor (after electron transfer) complexes, respectively. Both energy surfaces were evaluated using the potential function that was built up with an *ab initio* method. For each configuration, the parameter $\Delta E = H_{ss} - H_{pp}$ was calculated. This parameter was used as the reaction coordinate to generate the free energy curves for the reacting system (see Fig. 14) for the situation when the free energy of reaction is not zero. More than 68.34 million configurations have been generated. The separability of continuum solvent reorganization and the reorganization of bonds that were cleaved were tested and it was found that they are not in fact separable, though this is the basic concept in the continuum theory.[25] These authors[64] remarked that the separability assumption may be responsible for the quadratic activation barrier in the continuum expression[21,25] of the rate equation. The main conclusion of the work of Perez *et al.*[64] is that the linear response theory approximation is not valid for the dissociative electron transfer process. Therefore, the quadratic relationship of the free energy of activation that was originally developed for outer-sphere electron transfer reactions fails also for inner-sphere processes.

2. Quantal Treatments

In this treatment,[8] the Anderson–Newns Hamiltonian was utilized to determine the potential energy surface for both ion transfer, $2I^- \rightarrow I_2$ and electron transfer, $Fe^{+2} \rightarrow Fe^{+3} + e$ at a Pt electrode. Here the solvent part of the Anderson–Newns Hamiltonian, H_{solv} of Eq. (21), is expressed as

$$H_{solv} = (1/2)\Sigma_\nu \hbar\omega_\nu (p_\nu^2 + q_\nu^2) + (zn_a)\Sigma_\nu \hbar\omega_\nu g_\nu(x) q_\nu \qquad (32)$$

where the first term denotes the unperturbed solvent having q_ν and p_ν as the dimensionless solvent and momentum coordinates, respectively; ω_ν are the frequencies having ν as the levels of solvent mode. The second term accounts for the reactant–solvent interaction having $g_\nu(x)$ $[= q_\nu/-(z - n_a)]$ as the coupling constant, where q_ν is the solvent coordinate. H_{el} is expressed as in Eq. (22). Using Eqs. (22) and (32) in Eq.

(21), the following expression of potential energy of the ion as a function of distance x is given by Schmickler[8] as

$$E(x) = \varepsilon_a(x)n_a(x) - E_p(x)[z - n_a(x)]^2 + (\Delta/2\pi)\ln[Y^2 + \Delta^2(x)/[Y_p - U_c]^2 + \Delta^2(x)] \quad (33)$$

where

$$Y_p = [\varepsilon_a(x) + 2[z - n_a(x)]E_p(x)] \quad (34)$$

and U_c is the energy of the bottom of the conduction band of the metal electrode with respect to vacuum level.

Note that the important system parameters such as the occupation probability n_a, interaction with polar solvent polarization E_p, strength of interaction of the reactant with the metal Δ, and the electronic energy of reactants ε_a are the functions of position x of the reactant from the electrode surface. These parameters are given below as a function of x.

The occupation probability can be obtained from the self-consistency equation,

$$n_a(x) = (1/\pi)\cot^{-1}[\{\varepsilon_a(x) + 2(z - n_a(x)E_p(x)\}/\Delta(x)] \quad (35)$$

where for the transfer of an iodide ion it can be expressed[8] that

$$E_p(x) = E_p(\infty)\{[1 + p(x/L)]/2\} \quad (36)$$

where $E_p(\infty)$ represents the interaction with the solvent when the ion is far from the electrode surface in the solution, which is considerd here at L = 4 Å; the interpolating function $p(x)$ was used as

$$p(x) = (3 - 2x)x^2, \quad 0 \le x \le 1$$
$$= 1, \quad x > 1$$
$$= 0, \quad x < 0 \quad (37)$$

$$\Delta(x) = \Delta_0 \exp(-x/d) \quad (38)$$

where d is the decay length[65] and Δ_0 is the value of Δ when the ion is adsorbed on the electrode surface.

The energy ε_a involves electronic energy ε_a°, solvent interaction energy E_p, and the image interaction energy ε_{im}. The distance-dependent effective solvent dielectric constant $\kappa(x)$, which appears in the image term, was taken as

$$\kappa(x) = 1 + 3.9\, p(x/L) \tag{39}$$

Utilizing Eqs. (34) to (39) in Eq. (33), the potential energy surface for the iodide ion–iodine system as a function of distance x from the electrode and the normalized solvent coordinate q/g was determined as given in Fig. 15 as a contour plot. It is observed that far from the electrode surface, the ionic and the atomic states are separated by an energy barrier

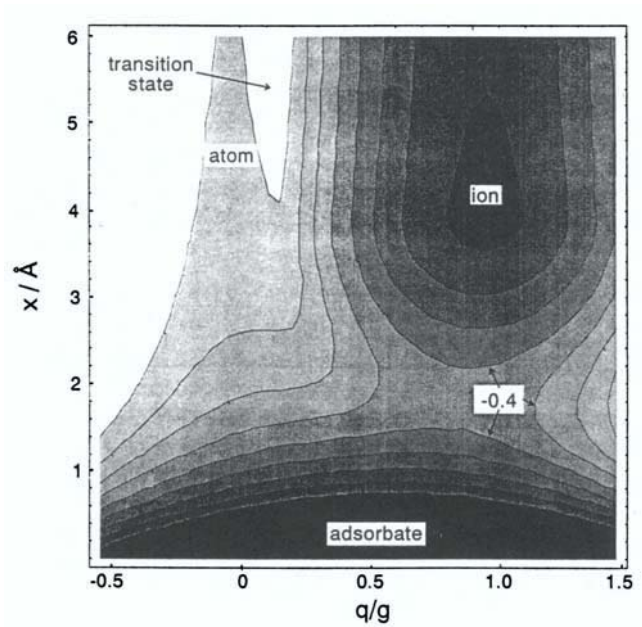

Figure 15. Contour plot of the potential energy surface for the iodide–iodine system as a function of the distance x from the electrode and the normalized solvent coordinate q/g. Contours are drawn for energies from –0.8 to 0 eV in steps of 0.1 eV; darker regions have a lower energy than brighter regions. (Reprinted from Ref. 8.)

that makes the discharge of the ion unfavorable. The adsorption of the ion requires the passing of a saddle point, and the energy of activation is determined mainly by the energy required to shed a part of the solvation sheath. The effective reaction coordinate starts from the minimum of the ionic state and passes to the adsorption site along a path of minimal energy, crossing each contour at right angles. The resulting curved line is directed toward the metal surface, which indicates that the activation process of the reaction is governed by the approach of the ion toward the electrode surface and not by the reorganization energy of the solvent continuum.[21]

For the ion transfer reaction, the energy of activation is determined by the breaking of the inner solvation sheath, interaction with the electrode surface, and the electrode potential. The reaction coordinate is the distance from the electrode surface; the contribution of the solvent continuum is negligible. In contrast, the energy of activation in outer-sphere reactions is determined by the interaction of the ion with the solvent (in the first and second solvation sheath) and the electrode potential. Note that many redox couples reacting via an outer-sphere pathway are surrounded by ligands, which prevent closer approach to the electrode surface. These ligands act as the primary solvation sheath of the bare ion [e.g., Fe^{+3} (aq) ion]. This treatment[8] concluded that the ion transfer reactions differ in fundamental aspects from electron transfer reactions and cannot be interpreted in terms of continuum theory.[21]

VI. ELECTRONIC TRANSMISSION COEFFICIENT κ

In most theories concerning the electron transfer at the electrode/solution interface, the electronic transition probability is generally kept unevaluated or determined in terms of the Wentzel, Kramer, and Brillouin (WKB) tunneling probability.[27] However, it was Khan, Wright, and Bockris[66] who first made the quantum mechanical computation of the electronic transmission coefficient for the electron transfer reaction between the platinum electrode and a redox complex in a solution by using the time-dependent perturbation theory expression of transmission coefficient, i.e., Fermi's golden rule.[27] At the reversible potential, the transmission coefficient $\kappa = 7.2 \times 10^{-3}$ was found.[66] One can also determine the potential dependence of κ_{het} by considering the shift in the value of Fermi energy by $e_0 V$ due to applied potential V. Since the wave function of electrons in metal is

involved in κ_{het}, it will be possible to relate the electrocatalytic property of metal electrodes to it when the species are strongly adsorbed on the electrode surface.

It is important to point out that for the reactions in which the species are chemiadsorbed on the electrode surface (e.g., H_2 and O_2 evolution reactions), the interaction V_{12} is very strong, the value of the transmission coefficient is expected to be close to unity, and the reaction will be mostly adiabatic.

Later, Newton[67] made a quantum chemical computation of transmission coefficient and reported a value of 1.1×10^{-3} for an ET reaction between $Fe(H_2O)_6^{2+/3+}$ redox couple in a homogeneous solution using the Landau–Zener expression,[68,69] i.e.,

$$\kappa = 1 - \exp[-4\pi^2 V_{12}^2 / h v_r |F_1 - F_2|] \tag{40}$$

where V_{12} is the splitting energy of two potential energy surfaces in the transition state; its value depends on the degree of interaction between two reacting systems and is expressed as

$$V_{12} = \langle \Psi_1 | V' | \Psi_2 \rangle \tag{41}$$

where Ψ_1 and Ψ_2 are the wave functions of the electronic states of reactant and product systems and V' is the perturbing interaction potential between them. In Eq. (40) v_r is the relative velocity of approach of the one reactant to the other during the reaction and $|F_1 - F_2|$ is the net force exerted on the system's tending to restore to its original state or take it to the final state.

Recently, the classical improved average dipole orientation and the quantum chemical intermediate neglect of differential overlap methods were utilized to compute the electronic transmission coefficient [using Eq. (40)] for electron transfer reactions involving few transition metal ions in a homogeneous solution[11]; good agreement with experimental values was found. A theoretical model of an energy-dependent transmission coefficient, including various strengths of friction of the solvent, was given by Bader and Berne.[70] The electronic transmission coefficients were computed by several authors[71–74] by preassuming the ET reactions as either adiabatic (strong coupling) or nonadiabatic (weak coupling).

VII. PROTON TRANSFER REACTIONS

Proton transfer is a special case of an ion transfer reaction involving the ion, H_3O^+; such a reaction plays an important role in solution chemistry and electrochemistry. Many recent theoretical studies[75–95] used the method of *ab initio* molecular dynamics to investigate the solvation and dynamics of excess protons and the proton hole (charge defect) in liquid water. In such an approach, the interatomic forces were calculated from the instantaneous electronic structure using the density functional method. For H_3O^+, a continuous oscillation was found between $(H_5O_2)^+$ and $(H_9O_4)^+$ structures as a result of proton transfer. The OH^- ions were of fourfold coordination, forming an $(H_9O_5)^-$ complex. Transport of the charge defect (proton hole) was found to be a concerted dynamic process coupling the proton transfer along hydrogen bonds with the reorganization of the local environment.

However, quantal and molecular treatments of proton transfer reactions at an electrode are rare.[96] This treatment[96] incorporates the major effect of an electric field as well as some of the important concepts reported earlier by Bockris and Matthews[5] concerning proton transfer reactions at an electrode.

In this treatment, the potential energies of the initial state, where the transferring proton is in the solution as a hydronium ion (H_3O^+) and in the final state as an adsorbed hydrogen atom on the metal surface, were given as[96]

$$U_i = E_i + \Sigma_k \hbar\omega_k q_k^2 + (1/2)M\omega_i^2(R - r_i)^2 \tag{42}$$

$$U_f = E_f + \Sigma_k \hbar\omega_k (q_k - \xi_k)^2 + (1/2)M\omega_f^2(R - r_f)^2 \tag{43}$$

where E_i and E_f represent initial and final state energies of the proton corresponding to the minima of the two potential energy surfaces; the index k indicates the modes of the surrounding medium which interact during the reaction, ω_k denotes their frequency, which was assumed to remain unchanged; q_k is their normal coordinates; and ξ_k is the shift in equilibrium position. The third terms in Eqs. (42) and (43) refer to the transferring proton, whose motion is considered to be separable from those around it; ω_i and ω_f represent its frequency in the initial and final states,

M is its effective mass, R is its reaction coordinate, and r_i, r_f are its equilibrium positions in the initial and final states.

This model has obvious shortcomings. For example, the interaction with the solvent in the initial state is straightforward since the proton is in the ionic form, whereas in the final state, the proton is the nonionic adsorbed H atom and its interaction with the solvent should be negligible. No consideration of this fact was made in the potential of the final state U_f in Eq. (43). However, this treatment incorporates the basic feature of the proton transfer reaction: interaction with the solvent, tunneling as well as classical transition of the proton, and the effect of the electric field on the potential energy surfaces of the system.

The cathodic current density i_c for the neutralization of the proton at an electrode was obtained using first-order perturbation theory and was expressed in nonquadratic form as

$$i_c = (|L|^2/\hbar)A \exp[2\varepsilon_p/\hbar(\omega_i + \omega_f)]\exp[-(\varepsilon_{sol}/2 + \Delta G^\circ + \gamma e_0 \eta_c)/2kT] \tag{44}$$

where L is the matrix element of the perturbation operator between the initial and final electronic states; this perturbation causes the electron transfer from the metal electrode to the activated proton at the interface. This equation can explain the experimentally observed Tafel linearity over a wide range of overpotentials.

In Eq. (44) ε_{sol} is the interaction energy of the solvent with the proton; $\Delta G^\circ = (\varepsilon_f - \varepsilon_i)$ is defined as the free energy of reaction; and γ is a symmetry factor $(0 \le \gamma \le 1)$. A is a constant, expressed as

$$A = 2c_p \mathcal{F} \rho(\pi^3 \omega_i \omega_f kT/\varepsilon_{sol})^{1/2} \tag{45}$$

where c_p is the concentration of the proton at the interface, $\mathcal{F}$ is the Faraday constant, and ρ is the electronic density of the states of the metal electrode at the Fermi level.

In Eq. (44), ε_p is the stretching energy of the proton due to its vibrational motion and is expressed (for cathodic overpotential, $\eta_c = 0$) as

$$\varepsilon_p^\circ = (M/2)\omega_i \omega_f (r_i - r_f)^2 \tag{46}$$

and its dependence on the overpotential η_c is then expressed as

$$\varepsilon_p = \varepsilon_p^\circ (1 + p\eta_c)^2 \tag{47}$$

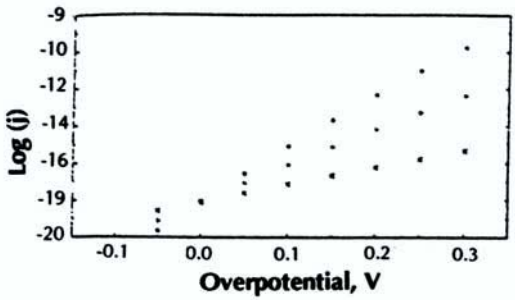

Figure 16. Tafel plots for the hydrogen evolution reaction for various values of the field effect parameter p: (*) 0.8, (+) 0.4, (x) 0. System parameters: $E_p = 0.5$ eV, E_p^* (proton) = 2.0 eV, $\omega_i = \omega_f = \omega = 2 \times 10^{14}$ s^{-1}, $\gamma = 0.5$; $\Delta e_0 = 0$. (Reprinted from Ref. 96.)

where p is a parameter in V^{-1} that takes into account the effect of the field in the double layer on ε_p.

It is important to point out that Eq. (44) is a nonquadratic form of the rate equation and gives rise to linear Tafel plots; the slopes of these plots depend strongly on the interfacial field parameter p (see Fig. 16). The

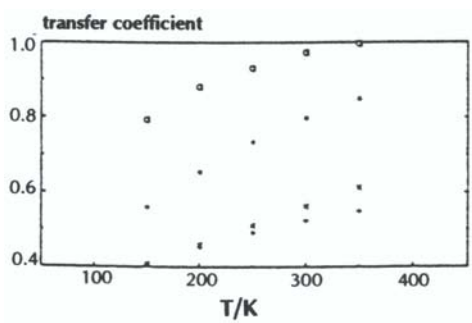

Figure 17. Transfer coefficient α_c for various values of $\omega_i = \omega_f = \omega$ and (*) $p = 0.8$, $\omega = 2 \times 10^{14}$ s^{-1}; (+) $p = 0.4$, $\omega = 2 \times 10^{14}$ s^{-1}; (x) $p = 0.8$, $\omega = 4 \times 10^{14}$; (□) $p = 0.8$, $\omega = 1 \times 10^{14}$. (Reprinted from Ref. 96.)

transfer coefficient α_c and its temperature dependence are given in Fig. 17 at $\eta_c = 0$ using the relation

$$\alpha_c(\eta_c = 0) = \gamma/2 + (kT/e_0)[4p\varepsilon_p^\circ/\hbar(\omega_i + \omega_f)] \quad (48)$$

Note that the temperature dependence arises via the term kT and the temperature-dependent frequencies ω_i and ω_f. Such results are consistent with the strong temperature dependence of transfer coefficients observed by Bockris and Wass.[97]

VIII. SOLVENT DYNAMIC EFFECTS ON ET REACTIONS AT ELECTRODES

In recent years, the effect of solvent dynamics on the kinetics of electron transfer reactions in a solution has received considerable theoretical[98–114] and experimental[115–121] attention. The solvent can influence the ET reactions in a solution mainly in two ways. Statically, it changes the energy of the reactants and the products. Dynamically it exchanges energy and momentum with the reactants by responding to their changing distribution of charge. The static solvent effects are generally taken into account in the free energy of activation, the $\Delta G^{\#}$ term in the exponential part of the rate equation. The dynamic solvent effects appear in the preexponential nuclear frequency factor ν_n as well as in the transmission coefficient κ factor. Solvent dynamics are generally discussed in terms of collisions and dielectric friction in the solvent. Many theoretical studies[122–127] focused on understanding how the solvent dynamics can influence the reaction rate and the rate constant for the ET reactions in a solvent medium. These treatments are mostly limited to the continuum theory[21] approach for the electron transfer reactions in a homogeneous medium.

However, a very limited number of studies focused on the effect of solvent dynamics on electron transfer reactions at electrodes.[128–130] Smith and Hynes[128] introduced the effect of electronic friction (arising from the interaction between the excited electron hole pairs in the metal electrode) and solvent friction (arising from the solvent dynamic [relaxation] effect) in the electron transfer rate at metallic electrodes. The consideration of electron-hole pair excitation in the metal without illumination by light seems unrealistic.

The role of solvent dynamics in the electron transfer reaction at a Pt electrode was discussed[130] utilizing the theory of Zusman.[122,123] In this work,[130] the solvent-dependent rate constant for the electron transfer reaction at an electrode was given as

$$k_s = \nu_n \delta \exp\{-(\pi^2 \delta/h)[2m_e(\Phi_m - 36.0/\varepsilon_{op})]^{1/2}\} \exp[-\Delta G^{\#}/kT] \quad (49)$$

where δ is the distance between the electrode and the reaction plane, OHP (outer Helmholtz plane), ν_n is the nuclear frequency factor, m_e is the mass of electron, $\Delta G^{\#}$ is the free energy of activation, Φ_m is the work function of the electrode expressed in electron volts, and ε_{op} is the optical dielectric constant of the solvent. In Eq. (49), the solvent dependence of the interfacial barrier arises via the solvent-dependent optical dielectric constant ε_{op} of the solvent.

The solvent-dependent frequency factor is generally expressed as[129]

$$\nu_n = \tau_L^{-1}[\lambda_s(\text{het})/16\pi kT]^{1/2} \quad (50)$$

where τ_L is the longitudinal relaxation time that can be extracted from the Debye relaxation time τ_D using the expression,

$$\tau_L = (\varepsilon_\infty/\varepsilon_s)\tau_D \quad (51)$$

where ε_∞ is the high-frequency dielectric constant of the solvent.

An inverse correlation occurs between the experimental value $k_{s,\text{expt}}$ and the theoretical values of the standard rate constant $k_{s,\text{calc}}$ when the latter is computed from Eq. (1) using the adiabatic value of the transmission coefficient (i.e., $\kappa = 1$), the solvent-independent frequency factor $\nu_n = kT/h$ (see solid circles in Fig. 18), and the solvent dependence is taken into account only via continuum λ_s (het) values obtained from Eq. (3).

An improved and direct correlation between the experimental rate constant $k_{s,\text{expt}}$ and $k_{s,\text{calc}}$ [obtained using Eq. (49)] is observed if $\nu_n = 1/\tau_D$ is used instead of $\nu_n = 1/\tau_L$, the solvent-dependent tunneling factor is utilized, and only $\Delta G^{\#}$ (het) of Eq. (8) is used in Eq. (49) (see triangles in Fig. 18). Furthermore, the inverse of the longitudinal solvent relaxation time τ_L is not necessarily the relevant one to use as the frequency factor ν_n (see empty circles in Fig. 18). Similar conclusions were reached by Barbara and Jerzeba[131] for the electron transfer reaction in homogeneous solutions. Barbara and Jerzeba[131] measured the electron transfer time

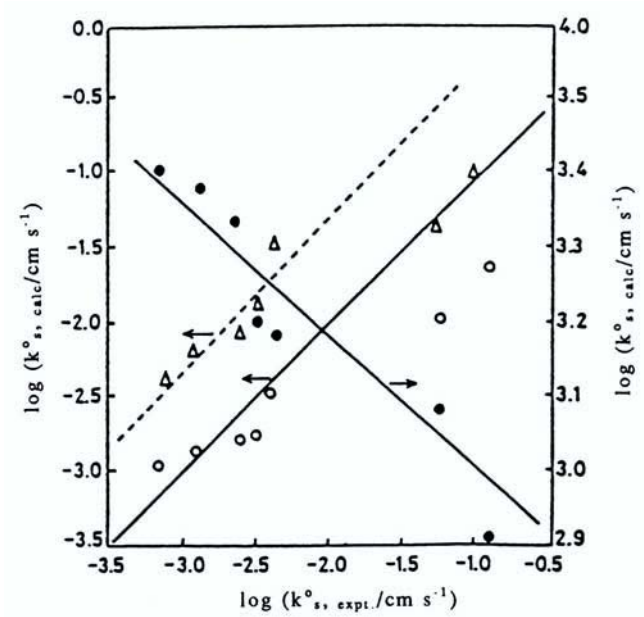

Figure 18. Calculated standard rate constants (a) $k^0_{s,\mathrm{calc}}$ (•), (b) $k^0_{s,\mathrm{calc}}$ (Δ), and (c) $k^0_{s,\mathrm{calc}}$ (°) versus standard rate constant $k^0_{s,\mathrm{expt}}$, for electro-oxidation of ferrocene in *n*-alkanol solvents. (Reprinted from Ref. 130.)

τ_{et} (inverse rate constant) in various polar aprotic solvents. These data showed a better correlation with the microscopic solvent relaxation time τ_s (= τ_D), rather than the longitudinal relaxation time τ_L. It was noted[131] that the lack of correlation between the electron transfer time τ_{et} and τ_L reflects the limitation of the dielectric continuum model in describing the transient solvation accurately because it ignores the molecular interactions and structure of the inner solvation shell.

ACKNOWLEDGMENT

The author gratefully acknowledges the financial support of this work by the Duquesne University President's Writing Award for the summer of 1996. The editorial help of Dr. James Phillips during the preparation of

the manuscript is gratefully acknowledged. The author also gratefully acknowledges useful discussions with Dr. Reyimjan Abdu.

REFERENCES

[1]R. W. Gurney, *Proc. Roy. Soc. (Lond.) A* **134**(1931) 137.
[2]J. A. V. Butler, *Proc. Roy. Soc. (Lond.) A* **125** (1936) 423.
[3]H. Gerischer, Z. *Phys. Chem.* **26** (1960) 223; **29** (1960) 325; **27** (1961) 48.
[4]S. G. Christov, *Electrochim. Acta* **4** (1961) 306; **9** (1964) 575.
[5]J. O'M. Bockris and D. B. Matthews, *Proc. Roy. Soc. (Lond.) A* **292** (1966) 479. *J. Phys. Chem.* **44** (1966) 298; *Electrochim. Acta* **11** (1966) 143.
[6]J. O'M. Bockris and S. Srinivasan, *J. Electrochem. Soc.* **111** (1964) 853.
[7]W. Schmickler, *J. Electroanal. Chem.* **82** (1977) 65; **84** (1977) 203.
[8]W. Schmickler, *Chem. Phys. Lett.* **237** (1995) 152; O. Pecina, W. Schmickler, and E. Spohr, *J. Electroanal. Chem.* **394** (1995) 29.
[9]A. Ovchinnikov and V. A. Benderskii, *J. Electroanal. Chem.* **100** (1979) 563.
[10]J. W. Halley and J. Hautman, *Phys. Rev. B,* **38** (1988) 11704.
[11]S. U. M. Khan and Z. Y. Zhou, *J. Chem. Phys.* **93** (1990) 8808; *Chem. Phys. Lett.* **173** (1990) 37; *J. Chem. Soc. Faraday Trans.* **87**(1991) 535.
[12]D. A. Rose and I. Benjamin, *J. Chem. Phys.* **100** (1994) 3545.
[13]X. Xia and M. L. Berkowitz, *Chem. Phys. Lett.* **227** (1994) 561.
[14]J. B. Strauss and G. A. Voth, *J. Phys. Chem.* **97** (1993) 7388.
[15]J. B. Straus, A. Calhourn, and G. A. Voth, *J. Chem. Phys.* **102** (1995) 529.
[16]P. W. Anderson, *Phys. Rev.* **124**(1961)41.
[17]D. M. Newns, *Phys. Rev.* **178** (1969) 1123.
[18]J.Weiss, *J. Chem. Phys.* **19**(1951) 1066.
[19]W. Libby, *J. Phys. Chem.* **56** (1952) 863.
[20]R. Kubo and Y. Toyozawa, *Prog. Theor. Phys.* **130** (1955) 411.
[21]R. A. Marcus, *J. Chem. Phys.* **24** (1956) 966.
[22]R. Platzmann and J. Frank, *Z. Phys.* **138** (1958) 411.
[23]V. G. Levich and R. R. Dogonadze, *Dokl. Akad. Nauk SSSR* **124** (1959) 123.
[24]M. Born, Z *Physik* **1** (1920) 45, 221.
[25]R. A. Marcus, *J. Chem. Phys.* **43** (1965) 679.
[26]S. U. M. Khan and J. O'M. Bockris, *Chem. Phys. Lett.* **99** (1983) 83; *J. Phys. Chem.* **87** (1983) 4012; *J. Res. Inst. Catal., Hokkaido Univ.* **28**(1983) 249; P. Delahay, *Chem. Phys. Lett.* **99**(1983)87.
[27]J. O'M. Bockris and S. U. M. Khan, *Quantum Electrochemistry,* Plenum Press, New York, 1979.
[28]S. Sahani and M. J. Weaver, *J. Electroanal. Chem.* **124** (1981) 35.
[29]S. U. M. Khan and J. O'M. Bockris, *J. Phys. Chem.* **87** (1983) 2599; *J. Res. Inst. Catal., Hokkaido Univ.* **28** (1980) 249.
[30]P. E. M. Seigbahn, *J. Am. Chem. Soc.* **118** (1996) 4442.
[31]P. George and J. S. Griffith, in *Enzymes* Ed. by P. D. Boyer, H. Lardy and K. Myrback, Vol. 1, Academic Press, New York, 1959, p. 367.
[32]D. R. Bates, *Chem. Phys. Lett.* **82** (1981) 396.
[33]G. King and A. Warshel, *J. Chem. Phys.* **93** (1990) 8682.

[34](a) J. R. Miller and J. V. Beitz, *J. Chem. Phys.* **74** (1981) 6476; (b) G. L. Class and J. R. Miller, *Science* **240** (1988) 440; (c) Liang, J. R. Miller, and G. L. Class, *J. Am. Chem. Soc.* **112** (1990) 5355.
[35]N. E. Katz, S. L. Mecklenburg, D, K. Graff, P. Chen, and T. J. Meyer, *J. Phys. Chem.* **98** (1994) 8959; N. E. Katz, S. L. Mecklenburg, D. K. Graff, and T. J. Meyer, *Inorg. Chem.* **34** (1995) 1282.
[36]E. H. Yonemoto, G. B. Saupe, R. H. Schmehl, S. M. Hubig, R. L. Iverson, and T. E. Mallouk, *J. Am. Chem. Soc.* **116** (1994) 4786.
[37]A. N. Macpherson, P. A. Liddell, S. Lin, L. Noss, G. R. Seely, J. M. DeGraziano, J. M. Moore, T. A. Moore, and D. Gust, *J. Am. Chem. Soc.* **117** (1995) 7202.
[38]S. L. Larson, L. F. Cooley, C. M. Elliott, and D. F. Kelley, *J. Am. Chem. Soc.* **114** (1992) 9504.
[39]I. R. Gould, R. H. Young, L. J. Meuller, A. C. Albrecht, and S. Farid, *J. Am. Chem. Soc.* **116** (1994) 8188.
[40]B. R. Arnould, D. Naukakis, S. Farid, J. L. Goodman, and I. R. Gould, *J. Am. Chem. Soc.* **117** (1995) 4399.
[41]C. Turru, J. M. Zaleski, Y. M. Karabatsos, and D. G. Nocera, *J. Am. Chem. Soc.* **118** (1996) 6060.
[42]N. Gayathri and B. Bagchi, *J. Phys. Chem.* **100** (1996) 3056.
[43]K. Lao, *J. Phys. Chem.* **100** (1996) 4693.
[44]J. R. Scott, M. McLean, S. G. Slinger, B. Durham, and F. Miliett, *J. Am. Chem. Soc.* **116** (1994) 7356.
[45]P. L. Dutton and C. C. Mosser, *Proc. Natl. Acad. Sci. U.S.A.* **91** (1994) 10247.
[46]C. E. D. Chidsey, Science **251** (1991) 919.
[47]J. N. Richardson, G. K. Rowe, M. T. Carter, L. M. Tender, L. S. Curtin, S. R. Peck, and R. W. Murrey, *Electrochimica Acta* **40** (1995) 1331.
[48]J. N. Richardson, S. R. Peck, L. S. Curtin, L. M. Tender, R. H. Terrill, M. T. Carter, *J. Phys. Chem.* **99**(1995)766.
[49]R. W. Murray, G. K. Rowe, and S. E. Creager, *J. Phys. Chem.* **99** (1995) 76.
[50]R. I. Cukierr and D. G. Nocera, *J. Chem. Phys.* **97** (1992) 7371.
[51]J. M. Zuleski, C. K. Chang, and D. G. Nocera, *J. Phys. Chem.* **97** (1993) 13206.
[52]M. T. Carter, G. K. Rowe, J. N. Richardson, L. M. Tender, R. H. Terrill, and R. W. Murrey, *J. Am. Chem. Soc.* **117** (1995) 2896; G. Rowe, M. T. Carter, J. N. Richardson, and R. W. Murre, *Langmuir* **11** (1995) 1797.
[53]W. Schmickler, *J. Electroanal. Chem.* **82** (1977) 65; **100** (1979) 533.
[54]S. U. M. Khan and W. Schmickler, *J. Electroanal. Chem.* **134** (1982) 167.
[55]J. O'M. Bockris and S. U. M. Khan, *Surface Electrochemistry,* Plenum Press, New York, 1993.
[56]P. Delahay, V. Burg, and A. Dziedzic, *Chem. Phys. Lett.* **79** (1979) 57; P. Delahay, *Chem. Phys. Lett.* **87** (1982) 607.
[57]L. A. Curtiss, J. W. Halley, J. Hautman, N. C. Hung, Z. Nagy, Y. J. Rhee, and M. Yonco, *J. Electrochem. Soc.* **138** (1991) 2032.
[58]W. Schmickler, *J. Electroanal. Chem.* **204** (1986) 31.
[59]K. L. Sabastian, *J. Chem. Phys.* **90** (1989) 5056.
[60]B. B. Smith and J. T. Hynes, J. *Chem. Phys.* **99** (1993) 6517.
[61]A. Calhoun and G. A. Voth, *J. Phys. Chem.* **100** (19%) 10746.
[62](a) R. Parsons and J. O'M. Bockris, *Trans. Farad. Soc.* **47** (1951) 914; (b) B. E. Conway and J. O'M. Bockris, *Canad. J. Chem.* **35** (1957) 1124.
[63]J. M. Saveant, *J. Am. Chem. Soc.* **109** (1992) 6788.

[64]V. Perez, J. M. Leuch, and J. Bertran, *J. Computational Chem.* **13 (9)** (1992) 1057.
[65] J. Seitz-Beywl, M. Poxleitner, M. Probst, and K. Heinzinger, *Int. J. Quantum Chem.* **42** (1992) 1141.
[66]S. U. M. Khan, P. Wright, and J. O'M. Bockris, *Electrokhimiya* **13** (1977) 914.
[67]M. D. Newton, *Int. J. Quantum Chem., Quantum Chem. Symp.* **14** (1980) 363.
[68] L. Landau Z. *Phys. Sowjet Union* **2** (1932) 46.
[69]C. Zener, *Proc. Roy. Soc. (Lond.) A* **137** (1932) 696.
[70]J. S. Bader and B. Berne, *J. Chem. Phys.* **102** (1995) 7953.
[71]B. J. Berne, In *Activated Barrier Crossing,* Ed. by G. R. Fleming and P. Haggi, World Scientific, Singapore, 1993.
[72]C. Zhu and H. Nakamura, *J. Chem. Phys.* **102** (1995) 7448.
[73]C. Zhu and H. Nakamura, *J. Chem. Phys.* **101** (1994) 4855.
[74]C. Zhu and H. Nakamura, *J. Chem. Phys*, **98** (1993) 6208.
[75]M. Tuckerman, K. Laasonen, M. Sprik, and M. Parrinello, *J. Phys. Chem.* **99** (1995) 5749; 103 (1995) 150; M. Tuckerman, K. Laasonen, M. Sprik, and M. Parrinello, *J. Phys. Condensed Matter* **6** (1994) A93.
[76]T. Komatsuzaki and I. Ohmine, *Chem. Phys.* **180** (1994) 239.
[77]A. Staile, D. Borgis, and J. T. Hynes, *J. Chem. Phys.* **102** (1995) 2487.
[78]K. Laasonen and M. L. Klein, *J. Phys. Chem.* **98** (1994) 10079; K. Laasonen, F. Csaijka, and M. Parinello, *Chem. Phys. Lett.* **194** (1992) 172; K. Laasonen, M. Parrinello, R. Car, C. Lee, and K. Vanderbilt, *Chem. Phys. Lett.* **207** (1993) 208; K. Laasonen, M. Sprik, M. Parrinello, and R. Car, *J. Chem. Phys.* **99** (1993) 9081; K. Laasonen, A. Pasquarello, R. Car, C. Lee, and D. Vanderbilt, *Phys. Rev. B* **47** (1993) 10142; K. Laasonen, M. Sprik, M. Parrinello, and R. Car, *J. Chem. Phys.* **99** (1993) 9081; C. Lee, D. Vanderbilt, D. Laasonen, R. Car, and M. Parrinello, *Phys. Rev. Lett.* **69** (1992) 462; C. Lee, D. Vanderbilt, K. Laasonen, R. Car, and M. Parrinello, *Phys. Rev. B* **47** (1993) 4863.
[79]F. Sim, A. St-Amant, I. Papai, and D. R. Salahub, *J. Am. Chem. Soc.* **114** (1992) 4391.
[80]R. N. Barret and U. Landman, *Phys. Rev. B* **48** (1993) 2081.
[81]C. Mijoule, Z. Latajka, and D. Borgis, *Chem. Phys. Lett.* **208** (1993) 364.
[82]C. Lee and D. Vanderbilt, *Chem. Phys. Lett.* **210** (1993) 279.
[83]R. V. Stanton and K. M. Merz, *J. Chem. Phys. Lett.* **101** (1994) 6658.
[84]C. Lee, D. Vanderbilt, K. Laasonen, R. Car, and M. Parrinello, *Phys. Rev. B* **47** (1993) 4863.
[85]E. Fois, M. Sprik, and M. Parrinello, *Chem. Phys. Lett.* **223** (1994) 411.
[86]A. Müller, H. Ratajczak, W. Junge, and E. Diemann, Eds., *Electron and Proton Transfer in Chemistry*, Elsevier, New York, 1992.
[87]T. Hynes, H. J. Kim, J. R. Mathis, and J. Juanós i Timoneda, *J. Mol. Liquid* **57** (1993) 53; J. T. Hynes, H. J. Kim, J. R. Mathis, R. Bianco, K. Ando, and B. J. Gertner, in *Reaction Dynamics in Clusters and Condensed Phases,* Ed. by J. Jortner et al., Kluwer, Dordrecht, 1994, p. 289.
[88]T. Fonseca, H. J. Kim, and J. T. Hynes, *J. Mol. Liquid* **60** (1994) 161.
[89]M. Bruehl and J. T. Hynes, *Chem. Phys.* **175** (1993) 205.
[90]R. I. Cukier, *J. Chem. Phys.* **98** (1993) 4548.
[91]G. K. Schenter, M. Messina, and B. C. Garrett, *J. Chem. Phys.* **99** (1993) 1674.
[92]H. J. C. Berendsen and J. Mavri, *J. Phys. Chem.* **97** (1993) 13464.
[93]J. Mavri, H. J. C. Berendsen, and W. F. van Gunsteren, *J. Phys. Chem.* **97** (1993) 13469.
[94]D. Borgis and J. T. Hynes, *Chem. Phys.* **170** (1993) 315.
[95]M. Ferario, D. Laria, G. Cicotti, and R. Kapral, *J. Mol. Liquid* **61** (1994) 37.
[96]W. Schmickler, *J. Electroanal. Chem.* **284** (1990) 269.

[97]J. O'M. Bockris and J. Wass, *J. Electroanal. Chem.* **267** (1989) 325.
[98]J. C. Rasaiah and J. Zhu, *J. Chem. Phys.* **98** (1993) 1213.
[99]J. Zhu and J. C. Rasaiah, *J. Chem. Phys.* **96** (1992) 1435; **101** (1994) 9966.
[100]J. C. Rasaiah and J. Zhu, *ECS Proc. Ser.* **4** (1993) 93–95.
[101]J. S. Bader, ECS *Proc. Ser.* **23** (1993) 93–95.
[102]A. Chandra and B. Bagchi, *J. Chem. Phys.* **99** (1993) 553.
[103]S. Roy and B. Bagchi, *J. Chem. Phys.* **99** (1993) 1310.
[104]H. Resat, F. O. Ranieri, and H. L. Friedman, *J. Chem. Phys.* **98** (1993) 7277.
[105]F. O. Ranieri, H. Resat, B. C. Peng, F. Hirata, and H. L. Friedman, *J. Chem. Phys.* **100** (1993) 1477.
[106]J. Zhu, O. B. Spirina, and R. I. Cukier, *J. Chem. Phys.* **100** (1994) 1.
[107]M. H. Vos, F. Rappaport, J. C. Lambry, J. Breton, and J. L. Mertin, *Nature* **363** (1993) 320.
[108]J. Maddox, *Nature* **363** (1993) 297.
[109]D. K. Phelps, M. J. Weaver, and B. M. Ladanyi, *Chem. Phys.* **176** (1993) 575.
[110]T. Fonseca, B. M. Ladanyi, and J. T. Hynes, *J. Phys. Chem.* **96** (1992) 4085.
[111]A. A. Zharikov, P. O. J. Scherer, and S. F. Fischer, *J. Phys. Chem.* **98** (1994) 3424.
[112]R. I. Cukier and D. G. Nocera, *J. Chem. Phys.* **97** (1992) 7371.
[113]M. J. Weaver, *Chem. Rev.* **92** (1992) 463.
[114]X. Song and R. A. Marus, *J. Chem. Phys.* **99** (1993) 7768.
[115]G. Walker, E. Akeesson, A. E. Johnson, N. E. Levinger, and P. Barbara, *J. Phys. Chem.* (1992) 3728.
[116]A. Papzayan and M. Maroncelli, *J. Chem. Phys.* **98** (1993) 6431.
[117]R. Jiminez, G. R. Fleming, P. V. Kumer, and M. Maroncelli, *Nature* **369** (1994) 471.
[118]J. M. Zaleski, C. K. Chang, and D. G. Nocera, *J. Phys. Chem.* **97** (1993) 13206.
[119]J. T. Hupp and X. L. Zhang, *J. Phys. Chem.* **99** (1995) 853.
[120]X. H. Mu and F. A. Schultz, *J. Electroanal. Chem.* **353** (1993) 349.
[121]D. P. Phelps, M. T. Ramm, Y. Wang, S. F. Nelson, and M. J. Weaver, *J. Phys. Chem.* **97** (1993) 181.
[122]L. D. Zusman, *J. Chem. Phys.* **102** (1995) 2580.
[123]L. D. Zusman, *Z. Phys. Chem.* **186** (1994) 1.
[124]S. Roy and B. Bagchi, *J. Chem. Phys.* **102** (1995) 7937.
[125]S. Roy and B. Bagchi, *J. Phys. Chem.* **98** (1994) 9207.
[126]S. Roy and B. Bagchi, *J. Chem. Phys.* **99** (1994) 973.
[127]R. Jimenez, G. R. Fleming, P. V. Kumaz, and M. Maroncelli, *Nature* **369** (1994) 471.
[128]B. B. Smith and J. T. Hynes, *J. Chem. Phys.* **99** (1993) 6517.
[129]L. D. Zusman, *Chem. Phys.* **112** (1987) 53.
[130]S. U. M. Khan, *J. Chem. Soc., Farad. Trans.* (*I*) **85** (1989) 2001.
[131]P. F. Barbara and W. Jarzeba, *Adv. Photochem.* **15** (1990) 1.

This Page Intentionally Left Blank

3

Molecular Dynamic Simulations in Interfacial Electrochemistry

Ilan Benjamin

Department of Chemistry, University of California, Santa Cruz, California 95064

I. INTRODUCTION

During the past few decades, significant changes have been taking place in the area of electrochemistry. The traditional kinetic approach for elucidating electrochemical phenomena by following voltage and current changes as a result of reactions or ionic transport[1] is being complemented by spectroscopic and other structural techniques[2] borrowed from the area of surface science. The spectroscopic and structural techniques emphasize that modern electrochemistry is a molecular and interfacial science and that a true understanding of electrochemical phenomena must include an understanding of the structure and dynamics of the electrochemical system at the molecular level.

Although the availability of surface-sensitive experimental probes is relatively new, numerous attempts to use a molecular-level description of the electrode/electrolyte interface structure have been reported. In recent years, these efforts have been accelerating due to the availability of powerful computers, advances in the statistical mechanics of inhomogeneous liquids, and new experimental data.

This review examines the new understanding that molecular dynamics computer simulations have provided regarding the structure and dy-

Modern Aspects of Electrochemistry, Number 31, edited by John O'M. Bockris *et al.*
Plenum Press, New York, 1997

namics of several electrochemical systems. Because many excellent reviews of the experimental[1,3–5] and the theoretical[6–8] (nonsimulation) aspects are available, this paper is limited to molecular dynamics methods and results.

Most of the new molecular-level results concern the structure and dynamics of water at interfaces. We begin this review with a brief summary of this area. Several recent review articles and books can be consulted for additional information.[9–12] We then examine in some detail the new insight gained from molecular dynamic simulations of the structure of the electric double layer and the general behavior of ions at the water/metal interface. We conclude by examining recent developments in the modeling of electron transfer reactions.

Electrochemical processes at the interface between two immiscible liquids are less understood and present a challenge to both experiment and theory. We conclude this review with a short summary of recent developments in the microscopic modeling of this system.

II. THE WATER/METAL INTERFACE

1. Preliminary Notes

Despite the fact that the structure of the interface between a metal and an electrolyte solution has been the subject of numerous experimental and theoretical studies since the early days of physical chemistry,[4] our understanding of this important system is still incomplete. One problem has been the unavailability (until recently) of experimental data that can provide direct structural information at the interface. For example, despite the fact that much is known about the structure of the ion's solvation shell from experimental and theoretical studies in bulk electrolyte solutions,[13–15] information about the structure of the adsorbed ion solvation shell has been mainly inferred from the measured capacity of the interface. The interface between a metal and an electrolyte solution is also very complex. One needs to consider simultaneously the electronic structure of the metal and the molecular structure of the water and the solvated ions in the inhomogeneous surface region. The availability of more direct experimental information through methods that are sensitive to the microscopic

structure[2,4] as well as molecular dynamics computer simulations are beginning to provide a more complete picture of this important system.

Because of the complicated way that metal atoms, metal electrons, water molecules, and ions can interact with each other, it is natural to consider simplified situations where only some aspects of the system are treated in detail. For example, significant progress has been made in recent years by considering the distribution of finite-sized ions near a metal surface while the solvent is treated as a continuum dielectric.[6,16] In contrast, we begin our review by considering the way a metal surface modifies the properties of bulk water, and we then consider the problem of ionic hydration. The goal of the studies we describe has been to provide a complete molecular description of the polarized solution/metal interface. Because of the complexity of such a system, only limited aspects of it have been treated using theoretical statistical mechanics methods, and we only briefly mention these. Most of the progress on developing a complete microscopic description has been made using the molecular dynamics method. The necessary ingredient for using molecular dynamics or statistical mechanics methods is the potential energy functions for the interactions between the solvent and the metal, and we begin with these. For a general review of the molecular dynamics method, the reader is referred to the excellent book by Alien and Tildesley,[17] and for general concepts in the statistical mechanics treatment of inhomogeneous systems, the reader can consult a number of books.[18–20]

2. Potential Energy Functions

The study of liquids near solid surfaces using microscopic (atomistic-based) descriptions of liquid molecules is relatively new. Given a potential energy function for the interaction between liquid molecules and between the liquid molecules and the solid surface, the integral equation for the liquid density profile and the liquid molecules' orientation can be solved approximately, or the molecular dynamics method can be used to calculate these and many other structural and dynamic properties. In applying these methods to water near a metal surface, care must be taken to include additional features that are unique to this system (see later discussion).

(i) Water Models

A large number of papers have been written on the potential energy function for describing bulk water, and the reader is referred to excellent recent reviews of this extensively studied topic.[11,12] Here we list only the main features of the models used in the simulation of water near solid surfaces. In these models, each water molecule is represented by a "soft sphere" in which several point charges (corresponding to the oxygen, hydrogens, and in some cases the oxygen's lone pair) are embedded. In some models, the magnitude and the relative intramolecular location of the point charges are constant, and thus the total potential energy function of the system of N water molecules is given by

$$U = \sum_{i<j}^{N} \left\{ 4\varepsilon \left[\left(\frac{\sigma}{r}\right)^{12} - \left(\frac{\sigma}{r}\right)^{6} \right] + \sum_{k,l}^{S} \frac{q_{ik} q_{jl}}{r_{kl}} \right\} \tag{1}$$

where r is the distance between water molecules i and j, and the second sum is over all point charges in these two water molecules, so that r_{kl} is the distance between two point charges in two different water molecules. For example, in the simple point charge (SPC) model of water, one charge is fixed at the location of the oxygen ($q = -0.82$ au) and two charges at the location of the two hydrogens ($q = +0.41$). The OH bond distance is taken to be 0.1 nm, and the HOH angle is 109.47°. The first term in Eq. (1) represents the dispersion attraction between water molecules and the hard core repulsion modeled using the Lennard-Jones potential. For the SPC model, $\sigma = 0.316$ nm and $\varepsilon = 0.650$ kJ/mol. The second term in Eq. (1) represents the dipolar (and higher order) Coulomb interactions between water molecules, which account for most of its internal energy. Despite the simplicity of this model, many structural and dynamic properties calculated using it are in reasonable agreement with experimental results.[21]

This simple model can be improved in two ways. First, the rigid bond constraints may be replaced by an intramolecular potential energy function to account for the vibrational motion of the water molecule. This can be simply done by including harmonic bond stretching and angle bending in the Hamiltonian,[22] or by using a more accurate intramolecular potential energy function selected to fit the water gas-phase infrared (IR) spec-

trum.[23] A second and more significant way of improving the simple model is by properly treating the electronic polarizability of the water molecule. This electronic polarizability is accounted for in the simple model in an average way: The fixed charges used in the nonpolarizable model are chosen to reproduce the effective bulk water dipole moment (2.27 D), which is much larger than that of the gas-phase (single) water molecule (1.86 D). However, this does not take into account fluctuations in the individual dipoles (which could be significant as far as fast dynamic processes are concerned), and the fact that the water effective dipole moment is reduced at an interface. Several methods have been developed to take into account the many-body aspect of water electronic polarizability,[24–26] but only very few applications to water at interfaces have been reported.[27–29] For more details about these, the reader is referred to the above references.

(ii) The Water–Metal Interaction Potential

In early studies of the properties of water near solid surfaces, the water–wall interactions were modeled by a simple single-distance dependent potential energy function.[30–32] For example, a 3-9 Lennard-Jones potential of the form

$$U(z) = 2\pi\varepsilon\left[\frac{2}{15}(\sigma/z)^9 - (\sigma/z)^3\right] \tag{2}$$

can be used to model the interaction of water with a flat structureless wall. Equation (2) is the result of an approximate summation of the Lennard-Jones 6-12 interactions between a single atom and a semi-infinite lattice of atoms.[33,34] A slightly better representation is obtained when the summation over the lateral directions (x, y) is replaced by an integral, but the summation in the normal direction z is kept discrete.[33] This results in a Lennard-Jones 10-4 potential for the interaction between the water molecule and each layer. Potentials of this form have been used by a number of workers to study the interaction of water with solid surfaces, including metal surfaces.[30–32,35,36]

Although Eq. (2) gives a reasonable representation of the packing of the water molecules on a solid surface, it neglects to take into account the following features that are important in modeling water near a metal surface:

(a) Surface corrugation

Even a molecularly smooth single-crystal face represents a potential energy surface that depends on the lateral position (x, y) of the water molecule in addition to the dependence on the normal distance z. One simple way to introduce this surface corrugation is by adding the lattice periodicity. An example of this approach is given by Berkowitz and co-workers for the interaction between water and the 100 and 111 faces of the Pt crystal.[37,38] In this case, the full (x, y, z) dependent potential was determined by a fit to the full atomistic model of Heinzinger and co-workers (see later discussion).

The most straightforward way to take into account surface corrugation effects is to represent the electrode by a finite number of layers constructed from the positions of the individual lattice atoms in the unit cell. Periodic boundary conditions in all three directions, or a nonperiodic arrangement of atoms to simulate specific structures [such as a scanning tunneling microscope (STM) tip] could be used. The lattice atoms may be held rigid in their equilibrium positions. Alternatively, one may use nearest-neighbor harmonic forces between the crystal atoms. In this case, the force constant is selected to approximately reproduce the phonon spectra of the crystal. This type of potential allows for an energy flow between the liquid molecules and the lattice vibrations.

The specific details of the potential energy function for the interaction between a water molecule and a lattice atom depend on the nature of the metal atom. The potential energy function can be determined from quantum mechanical calculations or from available experimental data on the adsorption energy of water. As an example, we consider the water/Pt potential proposed by Spohr and Heinzinger,[39,40] which has been extensively used in the studies reported in this review. This potential is loosely based on the extended Hückel molecular orbital calculations of a single water molecule with a five-atom Pt cluster carried out by Holloway and Bennemann.[41] These calculations show that a water molecule is adsorbed on top of a Pt atom with the hydrogens pointing directly away from the surface, a geometry that is consistent with the lowering of the metal's work function upon the adsorption of water.[42] The mathematical form of the potential suggested by Spohr is given by a sum of oxygen-Pt and hydrogen-Pt pair potentials

$$U_{Pt-O} = [Ae^{-ar} - Be^{-br}]f(x, y) + Ce^{-cr}[1 - f(x, y)]$$

$$U_{Pt-H} = De^{-dr}$$

$$f(x, y) = e^{-\alpha(x^2 + y^2)} \tag{3}$$

where:

$A = 1.1407 \times 10^5$ kJ/mol,
$B = 1.1359 \times 10^5$ kJ/mol,
$C = 6.0220 \times 10^7$ kJ/mol,
$D = 1.0322 \times 10^2$ kJ/mol,
$a = 11.004\ nm^{-1}$,
$b = 10.966\ nm^{-1}$,
$c = 53.568\ nm^{-1}$,
$\alpha = 52.08\ nm^{-2}$.

Figure 1 shows a plot of the total interaction potential between a single water molecule and the 100 face of a platinum slab made of 3 × 6 × 6 unit cells (each containing four Pt atoms). In Fig. 1a, we show a contour plot for the binding energy of a water molecule as a function of the oxygen location (x, y) for the case where the water dipole points away from the surface. The deepest minimum corresponds to the oxygen adsorbing on top of a Pt atom. In Fig. 1b, we show cuts in the potential energy surface for a water molecule approaching an on-top site, with the dipole pointing in four different directions. Figure 1 clearly demonstrates that the potential energy function given by Eq. (3) guarantees that a single water molecule will be adsorbed on the metal surface with the dipole pointing away from the surface and with the oxygen on top of a Pt atom. This orientational preference does not mean that water dipoles will be pointing away from the surface when the surface coverage is a monolayer or more, because of the strong interactions among water molecules and their tendency to maximize hydrogen bonding, as will be discussed later.

A very useful development of water/metal potential energy functions, which takes into account the anisotropic nature of the water/metal interactions, has been recently presented by Zho and Philpott.[43] They used a fit to the *ab initio* binding energy of water on several metal surfaces and applied some simplifying assumptions to develop potentials for the inter-

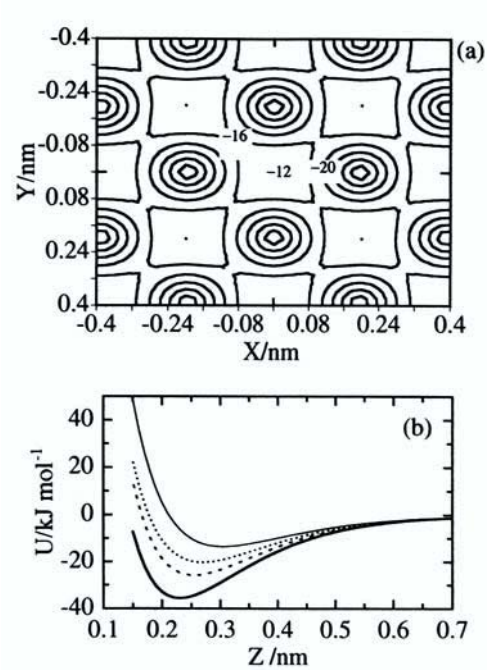

Figure 1. The total interaction energy of a single water molecule and the Pt(100) surface [Eq. (3)]. (a) A contour plot showing the binding energy as a function of the location of the water's oxygen for the case where the water dipole points away from the surface. Contour lines correspond to an energy spacing of 4kJ/mol. (b) The potential energy as a function of the oxygen atom's distance from the surface, for a water molecule approaching an on-top site with its dipole oriented perpendicular to the surface and pointing up or down (thick or thin solid lines, respectively), and oriented parallel to the surface with the HH vector pointing parallel or perpendicular to the surface (dashed or dotted lines, respectively).

actions of water with the 100,110, and 111 surfaces of Pt, Ni, Cu, and Al. The potentials are designed to give the correct orientational preference of a single water molecule on the metal surface.

One of the important electrochemical interfaces is that between water and liquid mercury. The potential energy functions for modeling liquid metals are, in general, more complex than those suitable for modeling solids or simple molecular liquids, because the electronic structure of the metal plays an important role in the determination of its structure.[44–50] However, based on the X-ray structure of liquid mercury, which shows a similarity with the solid α-mercury structure, Heinzinger and co-workers presented a water/Hg potential[51] that is similar in form to the water/Pt potential described earlier. This potential was based on quantum mechanical calculations of the adsorption of a water molecule on a cluster of mercury atoms.[52]

Finally, we mention the approach taken by Siepmann and Sprik,[53,54] which is based on two- and three-body site–site interactions designed to reproduce the correct adsorption of the water molecule. Their model also includes a many-body electrostatic induction of the metal atoms that allows for investigation under applied external field conditions.

(b) The metal electronic structure

Although the water/metal potentials obtained from simplified quantum mechanical calculations on a single water molecule and a few metal atoms are somewhat more reasonable than the simple flat wall-type potential as far as the adsorption structure and energetics are concerned, they neglect the fact that there is a quasi-free electronic density in the metal that could influence the structure and energetics of the pure water and of the double layer. In particular, measurements of the interfacial capacity as a function of surface charge and electrolyte concentration point to the importance of incorporating the metal electronic structure in any model of the metal/solution interface.[55] There is extensive literature on calculations of the metal electronic structure in the presence of an electrolyte solution, treated with various degrees of sophistication, but limited to a fixed solvent configuration.[56–62] Although in some of these treatments the solvent molecules are allowed to respond to the change in the electronic structure of the metal, no attempt has been made to follow the dynamics of the system. Here we briefly mention the attempts that have been made

to combine these approaches with the molecular dynamics description of the liquid phase.

The crudest way to partially account for the fact that the metal surface is an equipotential surface and that the bulk metal electrode has an infinite dielectric constant (ideal conductor) is to have each charged particle on the solution side interact with an image charge of the same size but opposite sign located the same distance inside the metal. An example for this approach was presented by Hautman, Halley, and Rhee.[32] The metal wall in their work is represented by 9-3 Lennard-Jones potentials acting on the oxygen and the hydrogens of each water molecule. Only the repulsive part of the hydrogen–wall interaction is included. This results in the desired preferential adsorption of the water with the oxygen end near the surface. Each atom in the water molecule interacts with an image atom of opposite charge. The total electrostatic interactions are calculated using an Ewald sum (see later discussion), and the effect of an external field due to a fixed potential difference between the metal and the solution is also considered. The results of this model are discussed in the following paragraphs.

Using image charges to take into account the "metallic" nature of the surface can be troublesome at short distances because the quantum mechanical nature of the metal electrons comes into play. A simple model that gives some insight into the nature of this problem is the jellium model.[8,63] In this model, the metal cations are replaced by a constant positive charge density that drops to zero at the metal surface, and the electrons are described by a continuous charge distribution that can penetrate into the solution side. Although this electronic "spillover" decays exponentially outside the metal surface, it produces a net surface dipole that can affect the properties of the pure water and of the ionic distribution in the solution. A very crude way to account for this within the simple model potentials discussed earlier is to position the image plan slightly inside the metal surface, so that the image interaction is given by

$$V_{\text{image}} = -\frac{e^2}{4(z + se^{-3s/2a_0})}, \quad s = \pi a_0/4k_F \tag{4}$$

where z is the distance of the charge from the metal surface, $a_0 = 0.0529$ nm, $k_F = (2m_e\varepsilon_F)^{1/2}/h$ is the Fermi wave vector, and ε_F is the Fermi energy

of the metal. The shift in the image plan is on the order of an atomic unit of distance.

In recent years, dynamic calculations of both the electronic and the molecular structure of complex molecular systems have started to become feasible.[64–69] These methods are based on the general idea that the electronic structure of the system is to be calculated "on the fly" as the nuclei move, while the nuclei respond to the forces determined from the dynamically calculated electronic structure. This assumes that the system moves on the lowest electronic state, and transitions between states are either ignored (because they are well separated in energy) or treated semiclassically.

To date, the only applications of these methods to the solution/metal interface have been reported by Price and Halley,[62] who presented a simplified treatment of the water/metal interface. Briefly, their model involves the calculation of the metal's valence electrons' wave function, assuming that the water molecules' electronic density and the metal core electrons are fixed. The calculation is based on a one-electron effective potential, which is determined from the electronic density in the metal and the atomic distribution of the liquid. After solving the Schrödinger equation for the wave function and the electronic density for one configuration of the liquid atoms, the force on each atom is calculated and the new positions are determined using standard molecular dynamics techniques. For more details about the specific implementation of these general ideas, the reader is referred to the original article.[62]

(iii) The Problem of Long-Range Forces

As is clear from this discussion, the potential energy functions used in the simulation of interfacial electrochemical systems include a Coulomb potential. This potential is a very slowly decreasing function of distance. Since typical molecular dynamic simulations involve systems that include up to a few thousand atoms, and thus have a spatial extent of only a few nanometers, the proper handling of the long-range Coulomb interactions is very important. Increasing the size of the system is extremely inefficient. For example, although doubling the size of the system costs almost four times more in computer time, it increases the largest distance in the system by only a factor of $\approx 2^{1/3} \approx 1.26$ and thus the smallest term in the sum of the electrostatic energy is reduced by only

20%. This explains the very slow convergence of the electrostatic energy of an ionic crystal. For liquids, because the intermolecular correlation decays very rapidly, the electrostatic interactions are relatively well screened and the problem is not so acute, although the complete neglect of any correction due to the long-range interactions can still lead to significant error.

The simplest possible approach that gives reasonable results in some cases is to use the tapered spherical truncation method[17] and to correct the final results by setting the intermolecular correlation function to 1 in the appropriate statistical mechanical integrals.[17] In this method, one uses the minimum image convention to calculate the interactions between atomic centers and to continuously switch the energy (or the forces) to zero near the boundaries. The switching function is taken to be a function of the distance between the centers of neutral groups (and not individual atomic centers). This approach seems to give reasonable results for such properties as the structure of the liquid, the solvation free energy of ions, and the surface tension.

The problem of directly accounting for the contributions of long-range forces in molecular simulations has been the subject of intense activity during the past decade. Two methods that have been used with some success to account for the contributions of the long-range Coulomb interactions are the Ewald sum (ES) and reaction field (RF) techniques.[17] In the ES method (which was originally developed for ionic crystals[70,71]), the Coulomb interactions of a molecule with all of its infinite periodic images are summed by replacing the slowly convergent series with two rapidly converging series, one that is evaluated in real space and one in **k** space. In the RF method,[17,72] the interactions between molecules inside a spherical cavity (tapered appropriately at the boundaries) are supplemented with a contribution from the polarization induced in a dielectric continuum that surrounds the cavity.

There are problems with using both of these methods in the simulation of inhomogeneous systems. Because the periodicity of the system is lost in the direction normal to the interface (unless one uses image charges with the flat wall model, which effectively results in a 3D periodic system[32]), implementation of the ES method is not straightforward for certain type of systems. Hautman and Klein[73] have presented a modified Ewald sum method for the simulation of systems that are periodic in two

dimensions, but of finite thickness in the third dimension (such as monolayers). They also give references to earlier work in this area. Glosli and Philpott[74] described the implementation of the fast multiple method[75] for simulation of electrochemical systems, which is a more efficient way of summing the electrostatic potential than the ES method. Despite this progress, there are more fundamental problems with the ES method. In particular, this method artificially magnifies the instantaneous dipolar fluctuations in the simulation box, which may be particularly large at interfaces, and could result in artificial correlations in the system.[76,77] The RF method is based on the existence of an analytical solution to the problem of the field acting on a dipole at the center of a cavity, due to the polarization induced by the total dipole of the cavity in the surrounding continuum medium. There is no such solution when the medium is inhomogeneous (although an approximate solution based on an expansion of the dielectric tensor has been used to estimate surface potentials of water near its critical temperature[78]). Thus, although much progress has been made in the treatment of long-range forces in molecular simulations, the problem, at least as far as nonhomogeneous systems are concerned, is still very much open.

3. Structure of Water at Metal Surfaces

The microscopic structure of water at the solution/metal interface has been the focus of a large body of literature, and excellent reviews have been published summarizing the extensive knowledge gained from experiments, statistical mechanical theories of varied sophistication, and Monte Carlo and molecular dynamics computer simulations. To keep this chapter to a reasonable size, we limit ourselves to a brief summary of the main results and to a sample of the type of information that can be gained from computer simulations.

The structure of water at interfaces in general, and at the metal surface in particular, is determined by a number of factors:

1. The specific interactions between a water molecule and the metal atoms. The pair interaction H_2O–M is further modified by the metal surface lattice structure and by defects and the electrons in the metal, as discussed earlier.

2. The tendency of water molecules to orient in such a way as to maximize hydrogen bonding with other water molecules at the interface and in the vicinity of the interface.

3. Any external forces due to adsorbed molecules and charges on the metal surface.

The interaction among these factors gives rise to a unique interface structure and dynamics, which we now summarize.

(i) Density Profile

When a liquid is brought into contact with a solid surface, the relatively immobile surface atoms give rise to a dampened oscillation in the density of the liquid, which dies out after 3–5 molecular diameters when the liquid has reached its constant bulk density. This is similar to the oscillations in the pair correlation function of a bulk liquid, except that at the liquid/solid interface the oscillations are generally more pronounced and have a longer decay length. This is a universal feature that reflects the packing of the finite-sized molecules and has been demonstrated for a large number of systems using various types of statistical mechanical theories and simulations.[9,20,33] Interestingly, there is only indirect experimental evidence for these density oscillations, which comes from the measurements of forces between macroscopic surfaces in liquids[34,79,80] and other methods.[5,81]

The results for water are mainly available from computer simulations, although some results of integral equation theories have been reported in recent years.[20,82,83] Despite the varied nature of the intermolecular potential energy functions used, most of these studies give a qualitatively similar picture. As an example, we consider in some detail the results obtained for the potential energy function given above (for the interface between water and Pt).

Figure 2a shows the density of water between two parallel Pt surfaces (the 100 crystal face) at T = 300 K. The distance between the two surfaces is chosen so that the density of water in the middle region (which we consider as bulk water) is near 1 g/cm^3. One can clearly see three peaks near each surface, which represent approximately three disordered layers of water molecules. The data in Fig. 2a are based on an approximately 500-ps molecular dynamics trajectory with the Heinzinger–Spohr poten-

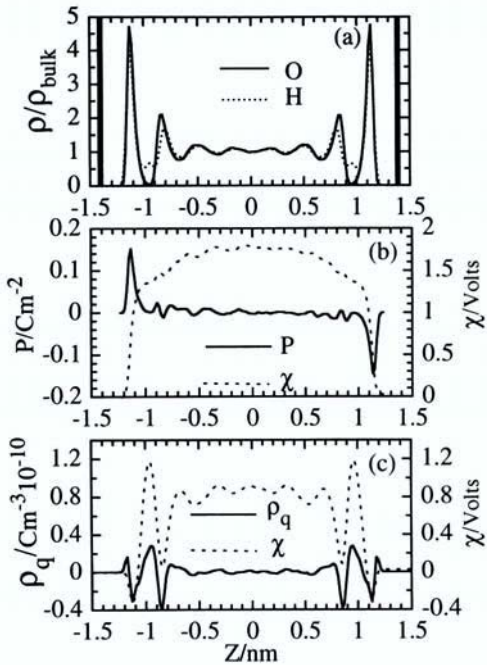

Figure 2. (a) Density of water oxygens and hydrogens. (b) The water dipole density profile and the associated potential drop. (c) The total charge density profile and the potential drop, as a function of the distance between two parallel slabs of the Pt(100) surface at T = 300 K.

tial energy surface and the flexible version of the SPC model of water. The peaks of the density profile are somewhat more enhanced than the results of the 16 ps molecular dynamics trajectory obtained by Heinzinger and Spohr,[40,84] but are quite close in their general features. They are also close to the results obtained by Raghavan *et al.*[37] for water near the 111 surface of Pt. On the other hand, a significantly less defined structure in the density profile has been reported for water weakly interacting with a flat wall,[31,32,36] although the existence of two water layers is quite evident even in these cases.

These results reflect the point made earlier that the structure of water is determined by the competition between the water–metal and water–water interactions. When the former are weak with no underlying lattice structure, the water structure near the metal is similar to the bulk structure. When the water–metal interactions are stronger, the water is much more structured. This was clearly demonstrated by Lee *et al.*,[31] who observed much more pronounced density oscillations when the water hydrogen-bonding interactions were turned off.

The underlying metal lattice structure also has a significant effect on the water structure. As pointed out by Spohr,[40] although the Pt-Pt nearest-neighbor distance is $a_0/\sqrt{2} = 0.277$ nm, which is very close to the O–O distance in ice, the cubic symmetry of the 100 surface is incompatible with the hexagonal symmetry of the ice lattice. As a result, the water molecules cannot form a uniform monolayer and occupy all adsorption sites. On the other hand, Berkowitz and co-workers showed that the hexagonal Pt (111) surface is able to support a more complete layer of adsorbed water molecules,[37] and one can identify patches of an icelike structure in the first layer. This "freezing" is further enhanced by an external electric field, as will be discussed later.

The results for the density profile of water near other metals are also similar to the one discussed above. However, the density profile of water near liquid mercury[85] is significantly less pronounced than that of water near the Pt surface or the solid mercury surface,[51] reflecting the fluidity of the metal, which smears out the profile. The oscillatory density profile of the mercury atoms is consistent with many theoretical[9,46,48,50,86,87] and experimental[81,88] studies of liquid metals and their surfaces.

(ii) Orientational Structure and Surface Potential

The orientation of water molecules at the interface is an important ingredient in understanding the properties of the surface region. A large body of data is available on the structure of water at metal surfaces measured under ultrahigh vacuum (UHV) conditions,[42] but it is expected that the orientation of water molecules under the conditions that exist at the electrode/electrolyte interface is very different. As mentioned earlier, the fact that the minimum energy required to eject an electron from the surface (the work function) is lower when the metal is in contact with water

suggests that, among other effects, there is a net dipole density pointing away from the surface, which indicates orientational ordering.

In addition to the indirect experimental evidence coming from work function measurements, information about water orientation at metal surfaces is beginning to emerge from recent applications of a number of *in situ* vibrational spectroscopic techniques. Infrared reflection-absorption spectroscopy,[89] surface-enhanced Raman scattering,[2,90] and second harmonic generation[91] have been used to investigate the structure of water at different metal surfaces, but the pictures emerging from all these studies are not always consistent, partially because of surface modification and chemical adsorption, which complicate the analysis.

Computer simulations or statistical mechanical theories that are based on isotropic water/metal potential energy surfaces give rise to water dipoles that are oriented parallel to the interface, and thus will not predict the correct potential drop at the interface. The potential energy surface given by Eq. (3) strongly favors the adsorption of water with the dipole perpendicular to the surface, which leads to the correct orientation. This can be seen from Fig. 2a, which shows that the hydrogen density profile does not coincide with the oxygen profile, or more directly in Fig. 2b, which shows the dipole density $P(z)$. This water dipole density is obtained by partitioning the volume occupied by the water molecules into slabs parallel to the metal surface, by summing up the total component of the electric dipole moment normal to the interface in each slab, and then dividing by the volume of the slab. The result is shown by the solid line in Fig. 2b. The main peak near the surface represents the net positive contribution in the direction of the center of the water lamella. This dipole density results in a net surface potential of about 1.7 V calculated using

$$\chi_{\text{dip}}(z) = -\frac{1}{\varepsilon_0}\int_{z_M}^{z} P(z')dz' \tag{5}$$

where $\varepsilon_0 = 8.854 \times 10^{-12}$ C V^{-1} m^{-1} is the vacuum permittivity and z_M is the position of the (left) metal surface. Equation (5) does not include the contribution of higher moments, which can lead to a significant error.[92] A more accurate formula based on the atomic charge distribution is obtained by direct integration of the one-dimensional Poisson equation

$$\chi(z) = -\frac{1}{\varepsilon_0}\int_{z_M}^{z} \rho_q(u)(z-u)du, \quad \rho_q(u < z_M) = 0 \tag{6}$$

The charge density $\rho_q(z)$ and the corresponding potential profile are shown in Fig. 2c. The potential drop is 0.75 V, which is still somewhat larger than the value believed to exist in reality. This may be due to several factors, including the neglect of the electronic density outside the metal surface discussed earlier, and the neglect of the contribution due to long-range electrostatic forces. It is also worth mentioning that because of the pair-wise approximation to the water intermolecular potential, the water dipole moment near the metal surface is probably smaller than the one used in the molecular dynamic simulations. All of these approximations could be the reason for the large value of the potential change. Nagy *et al.*[93] and Glosli and Philpott[94] have recently reported calculations of interfacial electric fields in a system that includes ions and charge on the metal. This work is reviewed in the following paragraphs.

(iii) Pair Correlation

Much more detailed information about the microscopic structure of water at interfaces is provided by the pair correlation function $g_{\mu\nu}(\mathbf{r}_1,\mathbf{r}_2)$, which gives the joint probability of finding an atom of type μ at a position $\mathbf{r}_1$, and an atom of type ν at a position $\mathbf{r}_2$, relative to the probability one would expect from a uniform (ideal gas) distribution. In a bulk homogeneous liquid, $g_{\mu\nu}$ is a function of the radial distance $r_{12} = |\mathbf{r}_1 - \mathbf{r}_2|$ only, but at the interface one must also specify the location z_1, z_2 of the two atoms relative to the surface. We expect the water pair correlation function to give us information about the water structure near the metal, as influenced both by the interaction potential and the surface corrugation, and to reduce to the bulk correlation function when both z_1 and z_2 are far enough from the surface.

The interfacial pair correlation functions are difficult to compute using statistical mechanical theories, and what is usually done is to assume that they are equal to the bulk correlation function times the singlet densities[9,18,20,33] (the Kirkwood superposition approximation). This can be then used to determine the singlet densities (the density and the orientational profile). Molecular dynamics computer simulations can in

principle be easily used to compute the full dependence of the pair correlation function on z_1, z_2, and r_{12}. In practice, however, only a few calculations have been reported, and only for some types of averaged (over z_1 and/or z_2 or the orientation of the $\mathbf{r}_1 - \mathbf{r}_2$ vector) interfacial pair correlation.

Spohr provides a detailed discussion of the water pair correlation function at the water/Pt(100) interface.[40] His results are shown in Fig. 3 for the oxygen–oxygen, oxygen–hydrogen and hydrogen–hydrogen pair correlations when one of the reference atoms is in either the first or the second layer, but otherwise a complete averaging over the locations and orientations of the other atom has been performed. The pair correlations

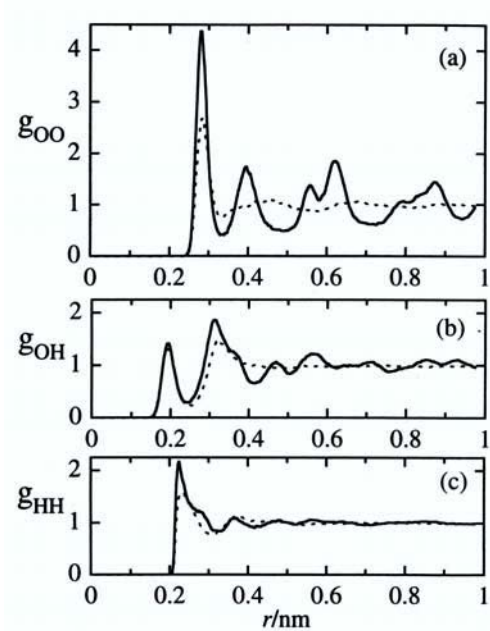

Figure 3. Water pair correlation functions near the Pt(100) surface. In each panel, the solid line is for water molecules in the first layer and the dashed line is for water molecules in the second layer. [Adapted from Ref. 40 (T = 300 K).]

of adsorbed water molecules show that the first solvation peak is enhanced but its location is unchanged relative to bulk water. Thus, despite the strong interaction with the crystal lattice, the surface is able to support a water structure that is similar to the one in the bulk. On the other hand, beyond the first peak, the new peaks (which are absent in bulk water) result from the periodicity of the Pt lattice. The pair correlations of the second adsorbed layer are already very close to the structure of bulk water.

(iv) Hydrogen Bonding

An examination of the number of hydrogen bonds per water molecule in different locations in the system provides additional insight into the interfacial structure of water. This issue has been extensively discussed in the past using lattice models, and the reader is referred to a recent review by Guidelli and Aloisi[95] and to Chapter 2 of the text by Bockris and Khan[4] for details. Molecular dynamics results are available for the water/Pt(100) interface,[40] for the water/Pt(111) interface,[37] and for the water/mercury interface.[51] To study this issue, some definition of hydrogen bonding is necessary, but unfortunately, different workers have used different definitions, which has sometimes led to different conclusions. In addition, some of the calculations were run for only a few picoseconds, which is particularly short given that the lifetime of a hydrogen bond may be on the same order of magnitude. Nevertheless, one can make some general statements about the hydrogen-bonding characteristics of interfacial water molecules compared with those in bulk water.

A widely used definition of hydrogen bonding considers two water molecules to be hydrogen bonded if their interaction energy is more negative than –10 kJ/mol. This seems to be equivalent to a geometric definition in which two water molecules are considered hydrogen bonded if the nonbonded OH distance is less than 0.235 nm (this is the location of the first minimum in the O–H radial distribution function of bulk water). Based on this definition, we show in Table 1 the number of hydrogen bonds per water molecule for water in different locations. The results for the water/Pt(100) interface are obtained from a 500-ps trajectory at T = 300 K.

One notes that there is little change in the hydrogen bonding ability of interfacial water molecules compared with the bulk. This seems to be a general result for the systems mentioned earlier. However, it is in stark contrast to the situation at the other water interfaces, where the number of

Table 1
Hydrogen Bonding Statistics at Water Interfaces

Region	Number[a]	Probability[b]
Bulk water	3.7	0.82
Layer 3	3.7	0.87
Layer 2	3.7	0.88
Layer 1	4.0	0.92
Water/vapor[c]	2.6	0.92
Water/oil[c]	2.4	0.91

[a]Number of hydrogen bonds per water molecule.
[b]Existence probability as defined in the text.
[c]Taken from Ref. 200.

hydrogen bonds decreases to about 2.4–2.6 for the water liquid/vapor and the water/oil interfaces.[10,96] Further insight into this phenomenon can be obtained when one normalizes the number of hydrogen bonds per water molecule by the number of water molecules in the first coordination shell (defined by the location of the first minimum in the O–O radial distribution function, which is 0.32 nm). This is also shown in Table 1. We note that whereas at any time in bulk water 82% of the hydrogen bonds exist, at the interface this rises to around 90%, reflecting a tighter, less fluid structure.

4. Dynamics

Much less attention has been paid to the dynamic properties of water at the solution/metal interface (or other interfaces). Typical dynamic properties that are of interest include the diffusion constant of water molecules and several types of time correlation functions. In general, the time correlation function for a dynamic variable of interest $A(t)$ is defined as

$$C_A(t) = \langle A(\tau)A(t+\tau)\rangle \tag{7}$$

where the angular brackets denote an ensemble average as well as an average over all time origins, τ.[17] An equivalent representation of these data is given by the Fourier transform of the time correlation function, which is just the power spectrum of the dynamic variable $A(t)$. An

important example of this correlation function is when the dynamic variable is the orientation of the molecular dipole (the corresponding power spectrum is proportional to the vibrational spectrum of the molecule). The diffusion constant is given by the zero frequency component of the velocity power spectrum,[97]

$$D = \frac{1}{3}\int_0^\infty C_V(t)dt, \quad C_V(t) = \langle \mathbf{v}(\tau)\cdot\mathbf{v}(t+\tau)\rangle \tag{8}$$

although it is sometimes more efficient to determine it from the equivalent result[97]

$$\Delta R^2(t) = \langle |\mathbf{r}_i(t) - \mathbf{r}_i(0)|^2 \rangle \underset{t\to\infty}{\longrightarrow} 6Dt \tag{9}$$

which states that the ensemble average of the square distance traveled by each molecule is given by $6Dt$ at long times.

(i) Translational Diffusion

The diffusion constant of water molecules at the water/Pt(100) and water/Pt(l 11) interface at different locations is given in Table 2, which is taken from the article by Raghavan *et al.*[38] In this table, the diffusion constants in the direction perpendicular and parallel to the Pt surface are

Table 2
Translational Diffusion Coefficients of Water at Water/Pt Interfaces[a]

		Diffusion coefficient/10^{-5} cm^{2}s^{-1}			
Surface	Type[b]	Layer 1	Layer 2	Layer 3	Bulk
Pt(100)	D_{xy}	0.04	2.02	2.84	2.67
Pt(100)	D_z	0.34	0.46	1.10	1.65
Pt(111)	D_{xy}	0.09	1.58	2.20	2.46
Pt(111)	D_z	0.04	0.14	1.06	1.95

[a]Taken from Ref. 38.

[b]D_{xy} is for the two-dimensional translation parallel to the surface and D_z is for the one-dimensional translation perpendicular to the surface.

shown. In general, the diffusion constant is significantly reduced compared with the value in bulk water, and it is quite anisotropic in the second and third layers from the surface. The diffusion in the direction normal to the surface is slower than the direction parallel to the surface. The diffusion constant in the first layer is very small, suggesting that the first layer is highly immobile. This is explained by the observation that the diffusion in the first layer proceeds by the hopping of water molecules to available adsorption sites, a process which is slow if most of the sites are occupied.[38] Spohr[98] and Heinzinger[99] obtained similar results.

(ii) Rotational Dynamics

Another important dynamic property to consider is the water molecule's reorientation. Given a vector **u** that is fixed in the molecular frame of reference, one is interested in the time-dependent quantities

$$C_l(t) = \langle P_l[\mathbf{u}(\tau) \cdot \mathbf{u}(t + \tau)] \rangle, \quad l = 1,2 \tag{10}$$

where $P_l(x)$ is the lth-order Legendre polynomial. As before, the ensemble average is over all molecules in a given region of space and over all time origins τ. Because molecules can get out of a given region during a sufficiently long period of time, the average over the time origin is limited to times that are shorter than the residence time of the molecule under observation in the specified region.

Rose and Benjamin[100] studied the water dipole and the water H–H vector reorientation dynamics at the water/Pt(100) interface and the results are reproduced in Fig. 4. As in the case of the translational diffusion, the effect of the surface is to significantly slow down the adsorbed water layer. We note that the effect is very short range, and that the rotational motion of water molecules in the second layer is already very close to the one in bulk water.

Spohr found a significant reduction in the dipole reorientation time for a different model of water (but using the same water/Pt potential).[98] In that paper, the reorientation dynamics are characterized by the spectral densities for rotation around the three principal axes of the water molecule. These calculations demonstrated the hindered rotation of water molecules in the plane parallel to the surface. In addition, a reduction in the frequency of rotation about the molecular dipole for water molecules in the adsorbed

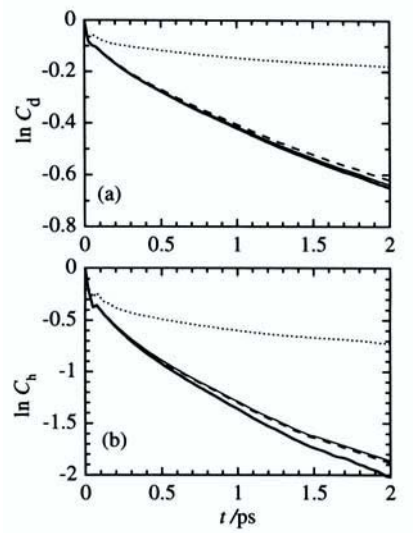

Figure 4. Water dipole (a) and the water H–H vector (b) orientational time correlation functions. In both panels, the dotted line is for the first layer, the solid thick line is for bulk water, the dashed line is for the second layer, and the thin solid line is for the third layer from the Pt(100) surface (T = 300 K).

layer is consistent with a reduced number of hydrogen bonds between water molecules in the adsorbed and second layers.

5. Effect of External Electric Field

An important aspect of the study of water under electrochemical conditions is that one is able to continuously modify the charge on the metal surface and thus apply a well-defined external electric field, which can have a dramatic effect on adsorption and on chemical reactions. Here we briefly discuss the effect of the external electric field on the properties of water at the solution/metal interface obtained from molecular dynamics computer simulations. A general discussion of the theoretical and experi-

mental work on water under external perturbations has been recently presented by Zhu, Singh, and Robinson.[11]

The effect of a homogeneous constant external electric field of magnitude E_0 directed normal to the interface can be incorporated into the molecular dynamic simulations by adding a constant force $q_i E_0 \hat{e}_z$ on every charge q_i in the direction normal to the interface ($\hat{e}_z$ being a unit vector along this direction). This is equivalent to having a charge density of $\sigma = \varepsilon_0 E_0$ or $\sigma(\mu C/cm^2) = 0.885 E_0(V/nm)$ on the left wall, and an opposite value on the right wall. The electrostatic potential energy of the system is modified by an amount $-E_0 \Sigma_i q_i z_i$, where z_i is the position normal to the interface of atom i. The potential drop across the interface is now given by Eq. (5), modified to include the term $-E_0 z$. Hautman *et al.*[32] give a detailed justification of this approach and its implementation when the long-range electrostatic interactions are also included. A different approach for including the effect of an external electric field by incorporating electrostatic induction for the individual metal atoms (using the extended Lagrangian method) has been presented by Siepmann and Sprik.[53,54] Their method is especially suited for studying the effect of a nonhomogeneous field like the one near the tip of a scanning tunneling microscope.

Lee, Rasaiah, and Hubbard[101] presented one of the first molecular dynamic studies of the effect of an external field on the properties of a dipolar fluid between charged walls. They simulated a film of 206 Stockmayer fluid molecules (a Lennard-Jones core in which a point dipole is imbedded) between two flat walls under the influence of external electric fields of intensities ranging from 0 to 4 V/nm. We summarize their results here because they can be used as a reference point for the more complicated case of water.

Without the external field, the Stockmayer fluid near the wall exhibits symmetric density oscillations that die out as they reach the middle of the film. Near the surface, the fluid dipoles are oriented parallel to the walls. Upon turning on the electric field, the density profile of the Stockmayer fluid exhibits pronounced oscillations throughout the film. The amplitude of these oscillations increases with increasing field strength until a saturation point is reached at which all the fluid dipoles are oriented parallel to the field (perpendicular to the walls). The density profile remains symmetric. The dipole–dipole correlation function $\langle \mathbf{d}(t)\cdot\mathbf{d}(0)\rangle$ and its transverse $[\langle d_x(t)d_x(0) + d_y(t)d_y(0)\rangle]$ and longitudinal $[\langle d_z(t)d_z(0)\rangle]$ com-

ponents show that the fluid dipoles move slower in the direction parallel to the walls than in the direction perpendicular to the walls.

The calculations of the structure of water between charged flat walls[32,35] show that the density profile becomes asymmetric and that there is enhanced structuring. This enhanced structuring is intimately connected with the possibility of a continuous phase transition in quasi two-dimensional systems, a subject of recent intense interest.[35,102,103] Most of the molecular dynamics computer simulations on the effects of an external field have been carried out in an attempt to clarify the field-induced restructuring of water molecules at the metal surface, for which recent experimental data have become available.[2,3,104,105]

In the following paragraphs we present results on the restructuring of water at the water/Pt interface under the effect of different external fields using the potentials developed by Heinzinger and Spohr and the flexible SPC model of water. The results are very similar to those published by Nagy, Heinzinger, and Spohr[93,106]; Rose and Benjamin[107]; and Berkowitz and co-workers.[108,109]

Figure 5 shows the density profile of the water oxygens for a system that includes 512 SPC water molecules between the faces of two Pt(100) surfaces for four different values of the external electric field. Each system is simulated for 500 ps. There is a small but noticeable change in the profile as the electric field intensity increases from 0 to 10 V/nm, followed by a dramatic change when the field is further increased to 20 V/nm. These are almost identical to the results reported by Xia *et al.*[108] (their Fig. 6), who used a rigid model of water. This behavior is suggestive of a phase transition to a state where all the water in the lamella is transformed to an ordered form resembling the structure of ice. This phase transition was investigated by Watanabe, Brodsky, and Reinhardt,[35] who showed that as a function of the external field, the water entropy exhibits a maximum at the point of the (continuous) phase transition.

More direct information about the structuring of water is available through an examination of the dipole density profile. Figure 6 demonstrates how the water dipoles align with the external field. These dipoles point slightly away from the metal surface when the field is zero and gradually orient perpendicular to the surface as the field increases. Note the reversal of the water polarization near the right surface (which is negatively charged) for fields of intensity of 5 V/nm and higher. Again, a

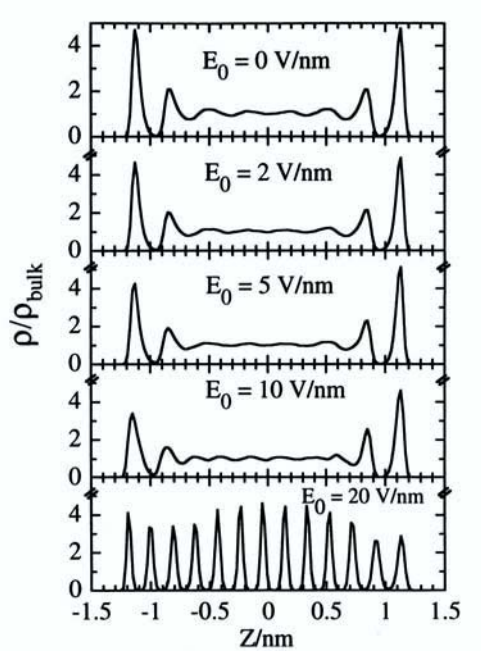

Figure 5. Density of water oxygens as a function of the distance normal to the water/Pt(100) surface for various external electric field strengths. The field is directed normal to the interface (T = 300 K).

dramatic alignment of most water dipoles is achieved when the external field reaches a value of 20 V/nm. A different representation of similar data is given by Xia and Berkowitz,[109] who showed that the average polarization of water molecules reaches saturation when the charge on the electrode is between 8.85 $\mu C/cm^2$ and 26.55 $\mu C/cm^2$, which corresponds to fields between 10 and 30 V/nm. Both Figs. 5 and 6 and the detailed analysis by Xia and Berkowitz demonstrate that the adsorbed layer of water splits into two layers; about half of the water molecules in the first layer move from the on-top positions to interstitial sites and give rise to a (nonperfect) ice-I structure.[109]

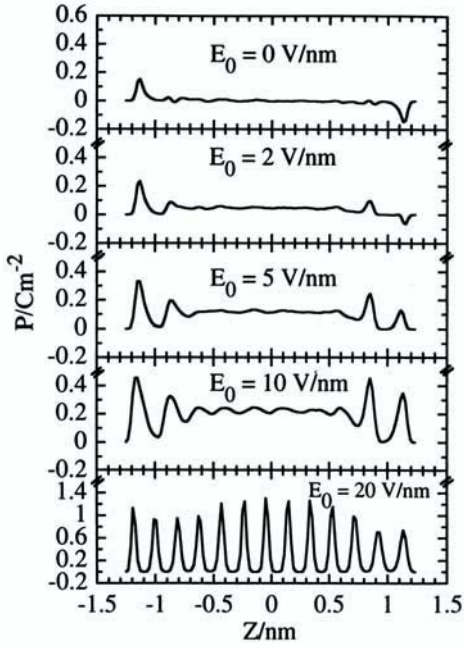

Figure 6. The water–dipole density profile for various external electric field strengths. Other details are as in Fig. 5.

Direct experimental observation of the restructuring of water as a function of an applied field has been reported by several groups. For example, Bockris and Habib used Fourier Transform Infra-Red (FTIR) spectroscopy to show that water molecules "stand up" as the field increases from the potential of zero charge (pzc),[110] and very recently, the same phenomenon has been demonstrated by Ataka *et al.*,[105] who used surface-enhanced IR spectroscopy to study the orientation of water at the Au(111)/solution interface. They showed that water dipoles point toward the surface at potentials below the pzc, are nearly parallel at the pzc, and point away from the surface to form an icelike structure at potentials above the pzc.

Nagy *et al.*[93,106] investigated the effect of the external electric field on the dynamics of water molecules at the water/metal interface. They found

that the dipole relaxation time for water molecules in the middle of the lamella or at the interface is scarcely affected by electric fields up to 10 V/nm, although the dipole correlation function decays to a value that is different from zero and corresponds to the polarization set by the external field. On the other hand, the external electric field seems to make the water diffusion motion more mobile in the direction perpendicular to the surface.[106]

III. IONIC ADSORPTION AND SOLVATION AT THE WATER/METAL INTERFACE

1. Overview

Understanding the behavior of charged atoms and molecules at the electrode/electrolyte interface is of fundamental importance and is the basis for elucidating many electrochemical processes. It is not surprising that this has been one of the most important goals of electrochemistry since at least the beginning of this century. This topic is generally referred to as the problem of the structure of the electric double layer, and many aspects of it are discussed at length in numerous reviews and books.[4,7,8,16,20,111–116] These reviews clearly demonstrate the high degree of understanding achieved about the structure of the electric double layer.

Because of the complexities of the interactions between the solvent and the solid surface, their electronic structure and the need to consider the ion–solvent and the ion–surface interactions, the progress made to date has been based on some simplifying assumptions. In most of the work done to date, the molecular structure of the solvent has generally been neglected, and the solvent has been described using a simple continuum model. Even in the few cases in which the molecular nature of the solvent has been explicitly taken into account, this has been done in a very simplified way. We stress that despite the less than adequate description of the solvent, a significant understanding of the structure of the interface has been achieved. Our goal in this section is to discuss the new insight that has been gained into the structure of the electric double layer and more specifically, into the behavior of ions at the solution/metal interface through the use of molecular dynamics computer simulations. The main motivation for the effort to treat all aspects of the problem at the micro-

scopic level is the recent advances in *in situ* experimental techniques[2,5] and in the theoretical understanding of the molecular structure of water at the metal surface, which we discussed earlier.

In Fig. 7, we show a schematic diagram of the widely accepted structure of the electrolyte-solution/metal interface. Depicted are a single-crystal metal surface represented by the hatched circles, water molecules represented by the dotted circles with an arrow pointing in the direction of the water dipole, and ions represented by solid circles. As discussed earlier, the water molecules near the surface are highly immobile and oriented mostly parallel to the surface. The rest of the water molecules are more mobile, and their dipolar orientation is not shown. Consider now the expected behavior of ions in this system. In bulk water, each ion (at least in a not too concentrated solution) has a structurally well-defined coordination shell containing between 3 and 12 water molecules, depending on the charge and the size of the ion.[13] In general, the higher the charge and the size of the ion, the larger the coordination number. The water molecules in the hydration shell are mobile: there is a constant exchange of molecules between the first shell and the bulk. The lifetime of any given water molecule in the hydration shell can vary between a few picoseconds for singly charged large ions to many nanoseconds for highly charged ions.[117] In a more concentrated solution, interionic correlations develop,

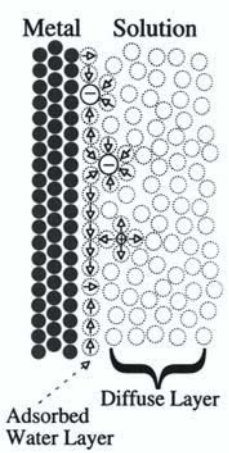

Figure 7. A schematic representation of the microscopic model for the metal/electrolyte solution interface. Shown from top to bottom are an ion that is contact adsorbed with partial loss of its hydration shell, an ion whose hydration shell partially consists of first layer of water molecules, and an ion that is not contact adsorbed.

and each hydrated ion is surrounded by an "atmosphere" of hydrated ions of the opposite charge.

The ion–water interactions are very strong Coulomb forces. As the hydrated ion approaches the solution/metal interface, the ion could be adsorbed on the metal surface. This adsorption may be accompanied by a partial loss of coordination shell water molecules, or the ion could keep its coordination shell upon adsorption. The behavior will be determined by the competition between the ion–water interactions and the ion–metal interactions. In some cases, a partial charge transfer between the ion and the metal results in a strong bond, and we term this process chemisorption, in contrast to physisorption, which is much weaker and does not result in substantial modification of the ion's electronic structure. In some cases, one of the coordination shell molecules may be an adsorbed water molecule. In this case, the ion does not lose part of the coordination shell, but some reorganization of the coordination shell molecules may occur in order to satisfy the constraint imposed by the metal surface, especially when it is charged.

The main goal of the molecular dynamics computer simulation of ionic solvation and adsorption on a metal surface has been to test the above model and to provide more quantitative information about the different factors that influence the structure of hydrated ions at the interface. Unfortunately, most of the experimental information about these issues has been obtained from indirect measurements such as capacity and current-potential plots,[1,8] although in recent years *in situ* experimental techniques have begun to provide an accurate test of the above model. For a recent review of experimental techniques and the theory of ionic adsorption at the water/metal interface, see the excellent paper by Philpott.[118]

2. Potential Energy Functions

In order to study the behavior of ions at the water/metal interface using the molecular dynamics method, the potential energy functions for the interaction between the ions and the water and between the ions and the metal surface must be specified.

A considerable amount of work has been done on the development of water–ion potential energy functions.[117,119] Most of these functions are of the standard Lennard-Jones plus Coulomb form, with parameters selected to give the experimental free energy or enthalpy of solvation.[120]

Although the potential energy functions can be made to reproduce thermodynamic solvation data quite well, they are not without problems. In some cases, the structure of the ion solvation shell, and in particular the coordination number, deviates from experimental data. The marked sensitivity of calculated thermodynamic data for ion pairs on the potential parameters is also a problem.[121–123] Attempts to alleviate these problems by introducing polarizable ion-water potentials (which take into account the induced dipole on the water caused by the ion strong electric field) have been made,[26] and this is still an active area of research.

Much less work has been done on developing ion–metal potential energy functions. One simple approach is to use the Lennard-Jones pairwise additive interactions between the ion and each metal surface (or between the ion and the flat wall[36,124]). The metallic nature of the surface can be introduced by using image interactions.[100] Although this approach seems quite reasonable for a study of the nonspecific adsorption of ions, it will fail for cases where the ions are specifically adsorbed. An excellent account of specific vs. nonspecific adsorption and its experimental manifestation is given in Chapter 2 of the text by Bockris and Khan,[4] but put simply, specific adsorption involves short-range and strong chemical forces that result when the ion electronic orbitals begin to overlap with those of the metal atoms. In this case, a more accurate approach is to use *ab initio* quantum mechanical methods. This has been recently done by Seitz-Beywl *et al.*[125] for the interaction between a Pt surface and Li^+ and I^- ions, and by Tóth, Spohr, and Heinzinger[126] for the interaction between alkali and halide ions with the mercury surface. These calculations involve an SCF solution of the Schrödinger equation for a cluster of a few metal atoms and the ion that are fitted to ion–metal pair potentials. Clearly, much more work is needed in this area.

3. Single Ion Adsorption at the Water/Metal Interface

Although our knowledge of the structure of the electric double layer is based on experimental data collected at finite electrolyte concentrations, understanding the structure of the electric double layer at the microscopic level must begin with knowledge of the structure of a single solvated ion at the interface. This information has been obtained in recent years from molecular dynamics computer simulations.

The molecular dynamics studies of single-ion hydration at the metal/solution interface are able to provide several key properties that are impossible or very difficult to obtain by any other means. These include the molecular structure of the coordination shell, the hydrated ion adsorption sites, the potential of mean force (free energy) for the ion adsorption, and a number of dynamic properties.

(i) Coordination Shell Structure

The structure of the adsorbed ion coordination shell is determined by the competition between the water–ion and the metal–ion interactions, and by the constraints imposed on the water by the metal surface. This structure can be characterized by water–ion radial distribution functions and water–ion orientational probability distribution functions. Much is known about this structure from X-ray and neutron scattering measurements performed in bulk solutions, and these are generally in agreement with computer simulations.[15] The goal of molecular dynamics simulations of ions at the metal/water interface has been to examine to what degree the structure of the ion solvation shell is modified at the interface.

A detailed study of the ionic coordination shell structure at the water/metal interface was performed by Rose and Benjamin,[100] who considered single Na^+ and Cl^- ions at the water/Pt(100) interface, using the water-Pt potentials developed by Spohr and Heinzinger[39,40,98] and an ion–metal image interaction. They found that although the structure of water at the interface is significantly different from the structure in the bulk, the structure of the hydration complex is relatively unperturbed, even for moderate external electric fields.[107] Some data are reproduced in Fig. 8. It can be clearly seen that the location and height of the first peak of the O–Cl and O–Na radial distribution function in the bulk and at the interface is almost the same. The slight enhancement at the interface reflects a tighter structure due to the steric constraints imposed by the solid surface. The main change in the interface radial distribution function is in the appearance of additional peaks at locations consistent with the periodic structure imposed by the metal surface on the position of the water oxygens. The bottom two panels in Fig. 8 show the probability distribution function for the angle between the water dipole and the oxygen–ion vector for water molecules in the first coordination shell. Again, the structure is essentially the same.

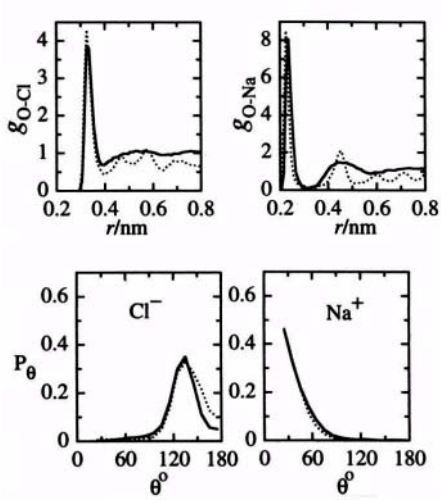

Figure 8. The structure of hydrated Na^+ and Cl^- ions at the water/Pt(100) interface (dotted lines) compared with the structure in bulk water (solid lines). In the two top panels are the oxygen ion radial distribution functions, and in the two bottom panels are the probability distribution functions for the angle between the water dipole and the oxygen–ion vector for water molecules in the first hydration shell. (Data adapted from Ref. 100.)

This behavior suggests that the Na^+ and Cl^- ions keep their solvation shells intact upon adsorption, with only small changes due to the restriction put on the water structure by the metal lattice. For example, when an external electric field is applied, stronger ion–metal interactions are able to strip a small part of the coordination shell, but only for large fields.[107] The electric field is also found to decrease the residence time of water molecules in the ion's coordination shell.

In the study by Rose and Benjamin, the ion–metal interactions were selected to give a weak physisorption. Seitz-Beywl *et al.*[127] and Perera and Berkowitz[128] selected much stronger Li^+ and I^- metal interactions (lowest

minimum of –265 kJ/mol and –319 kJ/mol, respectively). As a result, the equilibrium position of the hydrated ion near the metal is such that the ion seems to be in direct contact with the metal, which is what one expects for I^-, but is contrary to common belief for Li^+ (see later discussion). Nevertheless, the structure of the coordination shell seems to be only mildly affected by the adsorption. Tóth and Heinzinger[129] obtained similar results for the adsorption of Li^+ and I^- at the water/mercury interface. On the other hand, in the study by Glosli and Philpott,[36] the adsorption of hydrated Li^+ and I^- on a flat charged wall seems to be consistent with common ideas about contact vs. noncontact adsorption. The I^- ion is adsorbed with no water between the ion and the surface, whereas Li^+ is adsorbed with the full coordination shell, so that there are water molecules between the ion and the surface. In a later study, Glosli and Philpott[124] considered the adsorption of hydrated halide ions and showed that Br^- and I^{-1} contact adsorb while F^- adsorbs with a full coordination shell and Cl^- represents an intermediate case. Stability of the Na^+ coordination shell upon adsorption was found by Matsui and Jorgensen[130] using a Monte Carlo simulation, which includes ion–wall and water–wall image interactions.

(ii) Ion Density Profiles and Adsorption Free Energies

The issue of contact vs. noncontact adsorption and the location of the adsorbed ion relative to the surface is best handled by an examination of the ion potential of mean force. If we denote by $P(z)$ the probability density for finding an ion at a position z relative to a planar interface, then the free energy profile (or the potential of mean force) is given by

$$A(z) = -kT \ln P(z) \tag{11}$$

so that if one knows the probability of finding the ion in the bulk relative to the probability of finding it near the interface, then the adsorption free energy of the ion can be calculated. In particular, if $A(z)$ exhibits a minimum at a point z_{ad} near the metal surface, then one may have a well-defined adsorbed state, and the issue of contact adsorption and solvent-separated adsorption can be elucidated.

The direct simulation of $P(z)$ is possible in principle by following the motion of the ion in a long molecular dynamics trajectory and binning the observed values of the ion position. This method will give reasonable

results only if the simulation time is long enough to allow the ion to sample each interval a large number of times. It will fail if the free energy difference between any two points along z is much larger than kT; for example, when there is a deep minimum near the surface or a large barrier to adsorption.

Seitz-Beywl *et al.*[127] have determined the I^- and Li^+ ion density profiles near the water/Pt(100) interface. The short simulation time did not allow for calculation of the adsorption free energy, but the issue of contact vs. solvent-separated adsorption could be addressed qualitatively. The Li^+ is not considered contact adsorbed because its density profile is wide and its maximum (corresponding to the minimum of the free energy profile) is shifted away from the surface relative to the minimum of the bare ion–metal potential. A small section of the ion density profiles has recently been calculated by Tóth and Heinzinger[129] for Li^+ and I^- at a water-mercury interface with similar results. The issue of contact vs. solvent-separated adsorption of halide ions has been addressed by Glosli and Philpott,[124] as discussed earlier, and although the ion density profiles have been determined, they are not very accurate despite the relatively long simulation time.

To overcome the problem of poor sampling in calculating the ion density profile and the corresponding free energy, one can use the technique of umbrella sampling.[131,132] Briefly, the interval over which the ion density profile is needed is divided into overlapping subintervals. In each subinterval, the density profile is calculated by a simulation with a Hamiltonian that is modified by adding a potential energy $U_{\text{bias}}(z)$, which is a function of the ion coordinate z only. This potential is selected in such a way as to constrain the ion to the subinterval and to increase the sampling of high free-energy regions. The ion density profile obtained with the modified Hamiltonian $P_{\text{bias}}(z)$ gives rise to a free energy: $A_{\text{bias}}(z) = -kT \ln P_{\text{bias}}(z)$. The correct free-energy profile in the subinterval is found using

$$A(z) = A_{\text{bias}}(z) - U_{\text{bias}}(z) \tag{12}$$

This procedure is repeated for all subintervals. Because the free energy is a continuous function of z, the different sections of the free energy can be matched to produce the final free energy profile over the whole range of

interest. This method has been used in numerous calculations. Anderson[133] gives a detailed general review and a complete reference list of applications. Benjamin[96] provides examples for calculations of adsorption free-energy profiles in interfacial systems.

Using the umbrella sampling method, Rose and Benjamin determined the free-energy profile for Na^+ and Cl^- over the range from bulk water to the water/Pt(100) interface.[100] The results are shown in Fig. 9a. The

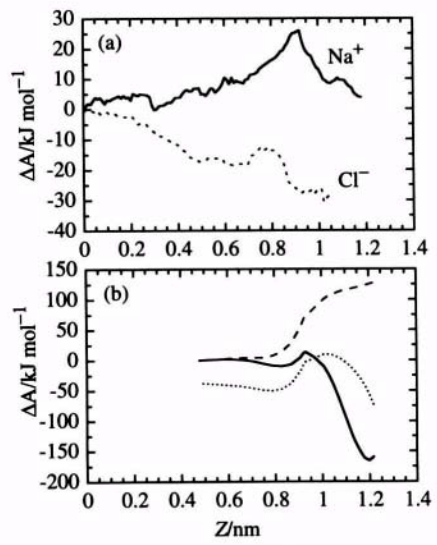

Figure 9. The adsorption free energy profile of several ions at the water/Pt(100) interface at T = 300 K. The metal surface is located at $Z = 1.4$ nm. (a) Free energy of Na^+ and Cl^- calculated using umbrella sampling (data adapted from Ref. 100). (b) Free energy of I^- calculated using direct integration of the average force acting on the ion (data adapted from Ref. 135). Shown are the solvent contribution (dashed line) and the total potential of mean force, calculated using the ion–metal *ab initio* derived potential (solid line), or the ion–metal image potential with the image plan located at $Z = 1.4$ nm (dotted line).

free-energy profile is nonmonotonic and shows a barrier to adsorption. The barrier location seems to coincide with the point where the ion coordination shell molecules would begin to unfavorably overlap with the water-adsorbed layer. The free energy profile is not calculated in the region of the strong repulsion between the ion and the surface because the accuracy of the image model must be very poor there. However, it is expected that the free energy will rise rapidly, generating a local minimum near the surface. Note that the barrier to adsorption of the smaller sodium ion is greater than that of the chloride ion, which is consistent with the tighter solvation shell around the smaller cation.

A different method of calculating the potential of mean force for ion adsorption is based on evaluating the average force acting on an ion in the direction normal to the surface. The ion is constrained to be in a thin slab parallel to the surface (so it is free to move in this direction, but its distance from the surface is kept within a very narrow interval). The average force is then integrated to obtain the free energy.[134] The advantage of this method is that one can independently compute the different contributions from the solvent and the surface.

Using this method, Berkowitz and co-workers computed the free energy profile for the adsorption of Li^+ and I^- at the water/Pt interface,[128] and they found, as in the case of Na^+ and Cl^- discussed earlier, that the barrier to adsorption for Li^+ is greater than that for I^-. The free energy of adsorption of I^- on the water/Pt surface has also been extensively investigated by Spohr,[135,136] who examined the influence of different models of ion–metal and water–metal interactions on the shape of the free-energy profile. Some of his results are shown in Fig. 9b. As in the work by Rose and Benjamin,[100] a significant barrier separating the solvated ion state from the (lower energy) adsorbed ion was found. An important conclusion of Spohr's work is that both the image-based and the quantum mechanically based ion–metal potentials give rise to this barrier (see Fig. 9b). The barrier is due to displacement of adsorbed water molecules, and increasing the strength of the water–metal interaction indeed raises this barrier.[136] Finally, we note that Spohr also considered the adsorption of halide ions and Li^+ at the mercury/water interface,[137] again finding a barrier to adsorption for I^- but not for F^-. It is important to stress that quantitatively the results are sensitive to the potential energy functions used and to the way the long-range forces are treated.[138]

4. Simulations of Electrolyte Solutions at the Water/Metal Interface

The preceding discussion was limited to the artificial case of a single ion. When multiple ions are present, in addition to the issues discussed, there is the problem of ion–ion interactions and correlations. The main motivation for such studies is to come close to the realistic situation in which a finite concentration of ions exists near the metal surface that is in equilibrium with ions in the bulk. Another important specific goal is to investigate the applicability of continuum models, such as the Gouy–Chapman theory.[139,140] Although this has been the subject of several Monte Carlo simulations and statistical mechanical theories,[20,114,116,141,142] the solvent in these attempts has generally been described as a structureless continuum. Very little work has been done on this question using microscopic solvent models.

One of the first studies of multiple ions at the water/solid interface was by Spohr and Heinzinger, who carried out a simulation of a system of 8 Li^+ and 8 I^- ions dissolved in 200 water molecules between uncharged flat Lennard-Jones walls.[143] However, the issues discussed in their paper involved water structure and dynamics and the single-ion properties mentioned earlier. No attempt was made to consider the ions' distributions and ion–ion correlations. This work has recently been repeated using more realistic water–metal potentials.[144]

Philpott and co-workers extensively discuss simulations of electrolyte solutions containing ions at several concentrations, and in some cases they also discuss several neutral species.[94,145–147] In addition to calculating water and ion density profiles, the electrostatic potential drop across the interface is calculated using different methods, and the issue of coadsorption of ions and benzene molecules is addressed. Of most interest to the topic of this section is a simulation involving 1600 water molecules and 32 Na^+ and 28 Cl^- ions (an approximately 1M NaCl solution).[94] The SPCE model of water and the flat-wall potential model were used. The simulations gave information about the diffuse layer and about the screening of the charged electrode,[147] but only a qualitative comparison with the Gouy–Chapman theory was made. In general, the electrostatic drop across the interface contains features that are absent from the Gouy–Chapman theory. Clearly, much more work is needed in this area.

IV. INTERFACIAL ELECTRON TRANSFER REACTIONS

1. Preliminaries

Despite the fact that electron transfer reactions at the electrode/electrolyte interface are of fundamental importance to many chemical processes, a quantitative understanding of the factors that influence the rate of these reactions is still lacking. Although the general theoretical framework was established many years ago by Marcus, Levich, Dogonadze, and others,[148,149] following earlier work by Gurney,[150] the complexity of the inhomogeneous system has limited the calculation of rate constants to very simple approaches, ignoring in many cases significant details that are important for a quantitative treatment. On a more fundamental level, it has become apparent in recent years that solvent dynamic effects could have an important influence on the rate of chemical reactions in general, and of charge transfer reactions in particular.[151–153] These effects are especially significant for fast charge transfer reactions, which are difficult to explore experimentally and thus could be much more readily understood using a microscopic theoretical analysis.

The theoretical modeling of electron transfer reactions at the solution/metal interface is challenging because, in addition to the difficulties associated with the quantitative treatment of the water/metal surface and of the electric double layer discussed earlier, one now needs to consider the interactions of the electron with the metal surface and the solvated ions. Most theoretical treatments have focused on electron–metal coupling, while representing the solvent using the continuum dielectric media. In keeping with the scope of this review, we limit our discussion to subjects that have been addressed in recent years using molecular dynamics computer simulations.

Traditionally, electron transfer reactions have been treated using chemical kinetics concepts.[1] We briefly review the phenomenological treatment to introduce some concepts that will be useful later.

In an electrochemical cell, oxidation occurs on the anode and reduction on the cathode. The measured current density j (current per unit area of the electrode) is proportional to the difference in the rate of the two reactions

$$j = Ne(k_{ox}[R] - k_{red}[O]) \tag{13}$$

where N is Avogadro's number, e is the electron's charge, and $[R]$, $[O]$ are the surface concentrations of the reduced and oxidized molecules (or ions), respectively. The rate constants are given by the phenomenological expressions

$$k_r = A \exp\left(\frac{-\Delta G_r^*}{kT}\right), \quad r = \text{ox, red} \tag{14}$$

where ΔG_r^* is the free energy of activation per molecule, and A is a constant. Experimentally, one measures the current density j as a function of the electrode's potential difference ϕ. If the reaction is at equilibrium, there is no current. We can generate current flow by changing electrode's potential difference from its equilibrium value by an amount η, which is called the overpotential. This reduces the anodic reaction free energy by $e\eta$ and increases the cathodic one by the same amount. Assuming a linear free energy relationship, the activation free energy will be reduced by $\alpha e\eta$ and by $-\alpha' e\eta$ (where α and α' are phenomenological constants) for the anodic and cathodic reactions, respectively. The new current density is

$$j = j_0\left[\exp\frac{\alpha e\eta}{kT} - \exp -\frac{\alpha' e\eta}{kT}\right] \tag{15}$$

where j_0 is the anodic current at equilibrium (which is equal to the cathodic current). Equation (15) is called the Butler–Volmer equation. In practice, it has been found to provide a reasonable fit to experimental data, unless the overpotential is too large. This treatment ignores the dependence of the surface concentration on the electrode potential, and this can be corrected using double-layer theories such as the Gouy–Chapman theory mentioned in the previous section. More details about this and the preceding discussion can be found in many textbooks.[1,7,8]

Early theories of electron transfer attempted to give a theoretical foundation to the phenomenological rate expression (Eq. 15) and the constants A, α, and α'. A brief summary of the history and references to recent reviews have recently been given by Marcus.[154] Marcus' theory has been able to derive an expression similar to Eq. (15), in which the relationship between the activation free energy and the reaction free energy is given in terms of a new quantity called the reorganization free

energy (see later discussion). For electron transfer that involves no change in the equilibrium structures of the molecules, but only changes in the solvent configuration (so called outer-sphere electron transfer), the relationship turns out to be quadratic, but reduces to the linear relation in Eq. (15) under certain conditions. Marcus shows how to compute the reorganization free energy in terms of the microscopic properties of the system using statistical mechanics or continuum models.[155,156] The theory has been found to agree well with experiments and has made important predictions that have been subsequently confirmed.[157]

Marcus' theory is based on certain assumptions that will be discussed later. The main goal of computer simulations of electron transfer is to check some of these assumptions and to provide additional microscopic insight into the mechanism of electron transfer and the microscopic factors that influence the rate of transfer. We discuss these issues in the following section for the simple case of outer-sphere electron transfer reactions.

2. Two-State Models

(i) Background

Most of the work published to date on molecular dynamic studies of interfacial electron transfer involves the simplified assumption of a two-state model for the electronic degrees of freedom. Consider an ion of charge q_i near a solution/metal interface. As a result of electron transfer between the ion and the metal surface, the charge of the ion changes to q_f. We will consider both forward and backward electron transfer and assume that $\nabla q = q_f - q_i = -1$, so that the forward reaction corresponds to a single electron transfer from the metal to the ion, for example: $Fe^{3+} + e^- \rightarrow Fe^{2+}$. In the two-state model, the electron transfer is viewed as a quantum transition between two localized states Ψ_i and Ψ_f. In Ψ_i, the ion with charge q_i is at equilibrium with the interfacial water molecules, and the electron is in the metal. In Ψ_f, the metal has lost one electron, and the ion with charge q_f is at equilibrium with the interfacial water. The total Hamiltonian of the system $\mathbf{H}$, including all nuclear and electronic degrees of freedom, is not diagonal in the basis (Ψ_i, Ψ_f), and so if the system is prepared in the state Ψ_i, it will evolve in time according to:

$$i\hbar\frac{\partial\Psi}{\partial t} = \mathbf{H}\Psi, \quad \Psi(0) = \Psi_i \tag{16}$$

The probability of finding the electron on the ion at time t is given by

$$P_{i\to f}(t) \equiv |\langle\Psi_f|\ \Psi\rangle|^2 = |\langle\Psi_f|\ e^{-iHt/\hbar}|\ \Psi_i\rangle|^2 \tag{17}$$

The difficulty of evaluating the quantity in Eq. (17) is that it requires the time-dependent solution of the Schrödinger equation in which the Hamiltonian is a function of all the solvent, ion, and metal nuclei, as well as of the metal electrons. In the two-state approximation, the Hamiltonian can be written as

$$\mathbf{H} = \begin{pmatrix} H_i & \Gamma \\ \Gamma & H_f \end{pmatrix} \tag{18}$$

where $H_{i,f}$ are the Born–Oppenheimer surfaces for the system localized in the quantum states i and f. We can distinguish two limiting cases that make the evaluation of the transition probability feasible:

1. In the nonadiabatic limit, the coupling Γ between the two electronic states (called the diabatic states) is weak. One can use perturbation theory to calculate the integral in Eq. (17).
2. In the adiabatic limit, the coupling Γ is strong, so that one may consider the transition between the two quantum states a continuous motion of the system on a single Born–Oppenheimer surface (called the adiabatic state) that is the lowest eigenvalue of the 2×2 matrix in Eq. (18).

Case (2) is applicable for ET at the solution/metal interface involving an ion that is contact adsorbed, whereas one may get close to the nonadiabatic limit if the ion is far enough from the metal. In both cases, important concepts that aid in calculating and understanding the nature of electron transfer are those of the reaction free energy profile and the transition state along this profile. Most of the contribution of molecular dynamic simulations to understanding electron transfer has been in the calculation of this free energy, and we briefly examine this next.

(ii) The Free Energy Curves for Electron Transfer

It is easiest to understand the concept of solvent free energy for ET when one works in the diabatic representation. Given a general solvent configuration denoted by **r**, the energy of the two states *i* and *f* is different mainly because the charge of the ion is different. Electron transfer occurs with a high probability in the nonadiabatic limit when (thanks to proper solvent fluctuation) the two states become nearly degenerate. This leads to the following definition of a generalized reaction coordinate

$$\Delta E(\mathbf{r}) = H_f - H_i \tag{19}$$

Because electron transfer occurs when the solvent molecules attain a configuration for which $\Delta E \approx 0$, we are interested in the probability that ΔE will be equal to some number x, $x = 0$ being the transition state. Thus, we have for this probability

$$p_v(x) = \langle \delta[\Delta E(\mathbf{r}) - x] \rangle_v \equiv \frac{\int \delta[\Delta E(\mathbf{r}) - x] e^{-\beta H_v} d\mathbf{r}}{\int e^{-\beta H_v} d\mathbf{r}} \tag{20}$$

where $v = i, f$ and δ is the Dirac delta function. The corresponding free energy functions are given by

$$G_v(x) = -kT \ln p_v(x) \tag{21}$$

The intersection between G_i and G_f gives the activation free energy for the ET, ΔG^*. The intersection between the two free energy curves can be controlled in an electrochemical cell by the application of an external voltage V, which modifies the energy level of the electron in the metal. This is equivalent to changing the energy of the states *i* by V and, as it can be easily shown, shifting G_i by V. The reaction free energy defined by

$$\Delta G_r = -kT \ln \frac{\int e^{-\beta H_f} d\mathbf{r}}{\int e^{-\beta H_i} d\mathbf{r}} \tag{22}$$

is also shifted by $-V$. The three quantities G_i, G_f, and ΔG_r are not independent. It can be shown[158] that

$$G_i(x) - G_f(x) = \Delta G_r + x \tag{23}$$

In Marcus' original formulation of ET theory, the free energy curves G_i and G_f are assumed to be quadratic in x (linear response approximation). Using this assumption, Marcus derives the relationship between the activation free energy and the reaction free energy[148,159,160]

$$\Delta G^* = \frac{(\lambda + \Delta G_r)^2}{4\lambda} \tag{24}$$

where λ is called the reorganization free energy. It is defined along with the other parameters in Fig. 10. [Note that Eq. (24) does not include the reversible work necessary to bring the ion to the surface and to send the product ion to the bulk.[161]] Marcus presents a continuum model calculation of the reorganization free energy[155,160]

$$\lambda = \frac{1}{2}(\Delta q)^2(\varepsilon_{op}^{-1} - \varepsilon_s^{-1})[r^{-1} - (2R)^{-1}] \tag{25}$$

where ε_{op}, ε_s are the optical and static dielectric constants of water, respectively, r is the radius of the conducting sphere used to model the ion, and R is the distance of the ion from the metal surface. Equation (25) gives the outer-sphere contribution to the reorganization energy. The inner-sphere contribution involves a change in the equilibrium position and force constants of the ion ligands, which may be obtained from spectroscopic data.

The main utility of recent molecular dynamics calculations has been first to determine if the assumption of quadratic free energy curves holds and second, to calculate the reorganization free energy in order to test Eqs. (24) and (25). In principle, a molecular dynamic simulation of the free

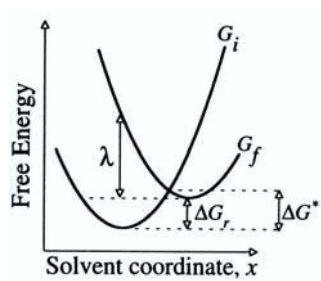

Figure 10. A schematic representation of the free energy curves for an outer-sphere electron transfer reaction.

energy curve for ET can be done by a straightforward application of Eq. (20). By running a molecular dynamics trajectory with the Hamiltonian H_ν, and binning the electrostatic interaction energy of the ion with the solvent, one may obtain the probability distribution $p_\nu(x)$ in the region near the equilibrium value of x

$$x_\nu^{eq} = \langle x \rangle_\nu = \frac{\int e^{-\beta H_\nu} \Delta E d\mathbf{r}}{\int e^{-\beta H_\nu} d\mathbf{r}} \tag{26}$$

(where $\beta = 1/kT$) and thus the values of $G_\nu(x)$ near its minimum. If the assumption of the quadratic dependence of the free energy of each state on the reaction coordinate is correct, then the full free energy curve, and thus the activation free energy, can be obtained with the aid of Eq. (20). However, in order to test the linear response approximation, one must know $G_\nu(x)$ over the whole range of x. This can be accomplished with an umbrella sampling procedure that is described in detail elsewhere.[158,162–165] Using this procedure, the solvent free energies for electron transfer reactions in bulk and in interfacial systems have been calculated by a number of researchers.[163–170]

The results of the free energy calculations for electron transfer in bulk water[158,162] show that the full free energy curves are well approximated by paraboli. The calculations for electron transfer at the solution/metal interface are also, in general, in agreement with the linear response assumption.

Straus and Voth[165] calculated the solvent free energy curves associated with the electron transfer $Na^+ + e^- \rightarrow Na$ at the water/Pt interface using the water–metal potential of Raghavan and Berkowitz.[37] They found that although the solvent free energy in the presence of the ion is well approximated by a parabola, the free energy curve for the neutral atom shows significant deviations in the high free energy region. However, the calculated reorganization free energy was very close to the value obtained when the reaction was carried out in the bulk (as a half-cell reaction).

Rose and Benjamin[163,169] determined the free energy curves for two ET reactions: $Fe^{3+} + e^- \rightarrow Fe^{2+}$ and $Fe^+ + e^- \rightarrow Fe$. They again found that the agreement with linear response theory (parabolic free energy curves) was quite good and that the largest deviation was in the case of the neutral

atom. As an example, Fig. 11 shows the free energy curves for the $Fe^{3+} + e^- \rightarrow Fe^{2+}$ reaction at the water/Pt(100) interface and in bulk water, using the water–ion potentials derived by Kuharski *et al.*[162] Note that the solvent coordinate ΔE is given in units of volts and is shifted so that the transition state for the symmetric reaction is at zero. This choice of the reaction coordinate is especially useful when discussing the effect of overpotential on the rate of the interfacial ET reaction.[163] Rose and Benjamin also investigated the effect of the external field on the diabatic free energy curve, and generally found that the reorganization free energy was only

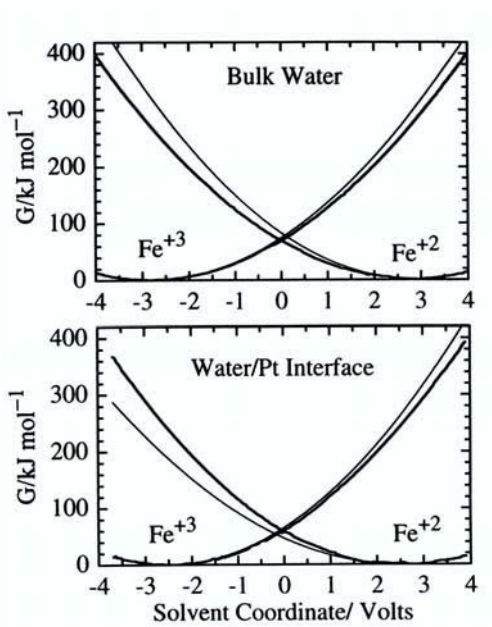

Figure 11. Solvent free energies for the electron transfer reaction $Fe^{3+} + e^- \leftrightarrow Fe^{2+}$ in bulk water (top panel) and at the water/Pt(100) interface (bottom panel) at $T = 300$ K. In each panel, the solid line gives the results of umbrella sampling molecular dynamics, and the thin line is the best parabolic fit to the bottom region of each curve. (Adapted from Ref. 163.)

mildly affected.[169] Of course, the main effect of the external field is to change the reaction free energy and the activation free energy. Simulation studies of this effect are discussed later.

Similar results for the $Fe^{3+} + e^- \rightarrow Fe^{2+}$ reaction were reported by Smith and Halley,[167] who also considered the effect of external field and the distance of the ion from the electrode. They stressed that the transition from diabatic to adiabatic behavior of the ET process varies with the distance of the ion from the electrode.

It is interesting to note that in most of these studies, one finds that despite the fact that the water structure is markedly different in the bulk and at the interface, the shape of the free energy curves is not significantly affected. This can be traced to the fact that the main contribution to the reorganization free energy comes from water molecules that are near the ion whose coordination shell is only slightly affected in these cases. In this regard it is interesting to note that Xia and Berkowitz[168] found that the minimum of the solvent free energy for the contact-adsorbed I^- ion is shifted toward smaller values, reflecting the partial loss of the ion's coordination shell (which reduces the free energy of hydration).

(iii) Rate in the Nonadiabatic Limit

Electron transfer occurs when, due to a proper solvent (or inner sphere molecular) fluctuation, the energy of the system in the two electronic states becomes nearly the same. This situation corresponds to the intersection of the two free energy curves in Fig. 10. Electron transfer is a quantum mechanical process, and actual transfer does not occur every time the system reaches the transition state. Rather, the probability of the transfer must be determined through the solution of the Schrödinger equation. If the coupling Γ is small, most of the passages of the system through the crossing region do not result in a transition between the two states. If the frequency with which the system enters the crossing region is small enough that the system loses coherence (that is, there is no specific phase relation between the wave function of the system in successive visitations of the crossing region), then it can be assumed that the rate of electron transfer can be approximated by the product of the thermal probability of reaching the crossing region and the quantum mechanical probability of changing the electronic state.

Following earlier work by Warshel,[171–173] Halley and Hautman[174] and Curtiss *et al.*[175] presented an approximate numerical scheme to calculate the nonadiabatic electron transfer rate under the above conditions. The method is based on solving Eq. (18) to the lowest order in the coupling Γ by treating the elements H_i and H_f as known functions of time obtained from the molecular dynamics trajectories. The result for the probability of the system making a transition to the final state at time t, given that it was in the initial state at time t_0, is given by

$$P_{i\to f}[t_0;t] = \left| \int_{t_0}^{t} \frac{-i\Gamma}{\hbar} \exp\left[i/\hbar \int_{t_0}^{\tau} [H_f(t') - H_i(t')]dt' \right] d\tau \right|^2 \tag{27}$$

The total rate of electron transfer is calculated by summing over the probability of the transitions for the multiple passes of the system through the crossing region

$$k_{ET}(i \to f) = \frac{1}{T} \sum_{n=1}^{N} P_{i\to f}[t_{in}^{(n)}, t_{out}^{(n)}] \tag{28}$$

where T is the length of the molecular dynamics trajectory, $t_{in}^{(n)}$ is the time of the nth entry of the system into the crossing region and $t_{out}^{(n)}$ is the nth exit time. The transition region is somewhat arbitrarily defined as the region where $|H_i - H_f| \leq \delta_E$. This provides a reasonable estimate of the rate, if one can find a range of values of δ_E for which the calculated rate is independent of the choice of δ_E. The main limitation of this method, besides the assumptions discussed above, is that one is limited to the case where the system makes many passes through the crossing region during the simulation time T. Because the number of times the system gets to the transition state falls off exponentially with the activation energy, this means that the activation free energy needs to be quite low, which corresponds to a high overpotential.

To obtain a reasonable estimate of the nonadiabatic rate for low overpotential ET reactions (typically high activation energy), one may replace Eq. (28) by

$$k_{ET} = \frac{\omega_R}{2\pi} \kappa e^{-\beta \Delta G^*} \tag{29}$$

where ΔG^* is the activation free energy calculated from the intersection of the free energy curves, κ is the average value of the quantum transition probability once the system is in the crossing region, and ω_R is the frequency of the system's motion in the reactant well, which can be obtained from the fluctuations in ΔE calculated from the equilibrium molecular dynamics trajectory with the Hamiltonian H_i

$$\omega_R^2 = \frac{\langle \dot{u}^2 \rangle}{\langle u^2 \rangle}, \quad u(t) = \Delta E(t) - \langle \Delta E(t) \rangle \tag{30}$$

κ can be estimated by assuming that the system passes through the crossing region with a uniform velocity, so that the quantum one-dimensional problem can be solved to obtain the Landau–Zener form[176,177]:

$$\kappa_{LZ} = 1 - \exp\left\{ -\frac{2\pi \Gamma^2}{\hbar |\dot{u}|} \right\} \tag{31}$$

in which $|\dot{u}|$ is the average absolute value of the system velocity through the crossing region, but could be approximated by the value near the reactant well [the same value used in Eq. (30)]. A slightly better approximation to κ is the Holstein form, which takes into account multiple passages of the system through the crossing region[178]

$$\kappa = \frac{2\kappa_{LZ}}{1 + \kappa_{LZ}} \tag{32}$$

Shown in Fig. 12 is an example of the nonadiabatic rate calculated using the full simulation method [Eqs. (27) and (28)] and the approximate formula [Eqs. (29)–(31)] for the $Fe^{3+} + e^- \rightarrow Fe^{2+}$ reaction at the water/Pt(100) interface with $\Gamma = 10\ cm^{-1}$. For the reason discussed earlier, the full simulation method can only be used for the high overpotential case. In this region, the agreement between the two methods is quite good.

(iv) Rate in the Adiabatic Limit

When the coupling Γ is much larger than kT, the diabatic representation is no longer valid. The quantum treatment cannot be limited to

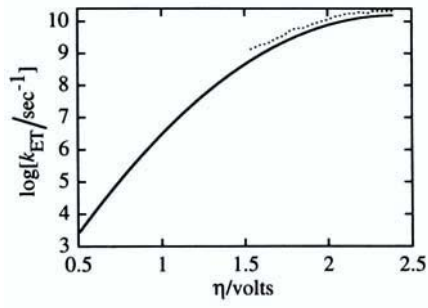

Figure 12. The rate of the electron transfer reaction $Fe^{3+} + e^- \rightarrow Fe^{2+}$ in the nonadiabatic limit. The dotted line is the result of molecular dynamics computer simulations [Eqs. (27) and (28)] and the solid line corresponds to Eqs. (29)–(31). (Adapted from Ref. 163.)

the crossing region. For very strong coupling, the two new basis states obtained by diagonalization of the matrix in Eq. (18) are far enough apart in energy that quantum transitions between them can be ignored. We are thus led to the adiabatic representation. The treatment that follows is discussed in the paper by Rose and Benjamin[163] and follows developments similar to rate calculations in the adiabatic limit in bulk liquids.[179,180]

Diagonalization of Eq. (18) at fixed nuclear coordinates yields

$$H_{ad} = H_i(\mathbf{r}) + \frac{1}{2}(\Delta E(\mathbf{r}) - \{[\Delta E(\mathbf{r})]^2 + 4\Gamma^2\}^{1/2}), \quad \Delta E(\mathbf{r}) = H_f - H_i \tag{33}$$

The system is assumed to be moving classically on the potential energy surface given by Eq. (33). This surface is reduced to the diabatic reactant surface H_i when the coupling Γ is very small and $\Delta E > 0$, or to the diabatic product surface H_f when the coupling Γ is very small and $\Delta E < 0$. It is easy to show that the energy of the system is the same as that of a system having an ion with an effective charge of

$$q = q_i + \frac{1}{2}(q_f - q_i)\left\{1 - \frac{\Delta E}{[(\Delta E)^2 + 4\Gamma^2]^{1/2}}\right\} \tag{34}$$

Note that the effective charge of the ion changes smoothly from q_i to q_f when ΔE changes from positive to negative values, and for $\Gamma = 0$ we get $q = q_i + \frac{1}{2}(q_f - q_i)[1 - \text{sign}(\Delta E)]$, (where sign($\Delta E$) is 1 for positive ΔE and -1 for negative ΔE), so that the charge is equal to either q_i or q_f.

The fact that the adiabatic electron transfer is described by a classical Hamiltonian makes it possible to use the molecular dynamics methodology developed for the study of general condensed-phase chemical reaction dynamics.[151,181] Starting with the ion of charge q_i and running equilibrium trajectories with the Hamiltonian H_{ad} will enable the study of thermally activated electron transfer only for very low activation energies. Calculating the rate for larger activation energies involves an expression similar to that given in Eq. (29), except for two important differences: First, the activation energy must be determined from the adiabatic free energy curve, and second, the parameter κ now represents the fraction of trajectories that successfully cross the transition state, where unsuccessful trajectories reflect the classical recrossings of the transition state due to solvent friction.

The adiabatic free energy curve can be calculated by umbrella sampling using the adiabatic Hamiltonian H_{ad} as discussed earlier. If the coupling Γ is constant (independent of nuclear positions), then it is possible to show[163] that the adiabatic free energy curve can be obtained from the diabatic free energy curve according to

$$G_{ad}(x) = G_i(x) + \frac{1}{2}\left[x - (x^2 + 4\Gamma^2)^{1/2}\right] \tag{35}$$

where the definition of the reaction coordinate includes the value of the overpotential, as explained in detail elsewhere.[163] Examples of adiabatic free energy curves for several values of the overpotential and electronic coupling are shown in Fig. 13.

The calculation of the transmission coefficient for adiabatic electron transfer modeled by the classical Hamiltonian H_{ad} is based on a similar procedure developed for simulations of general chemical reactions in solution.[181] The basic idea is to start the dynamic trajectory from an equilibrium ensemble constrained to the transition state. By following each trajectory until its fate is determined (reactive or nonreactive), it is possible to determine κ. A large number of trajectories are needed to sample the ensemble and to provide an accurate value of κ. More details

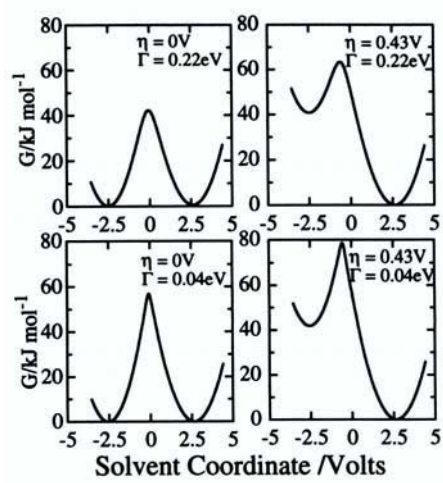

Figure 13. Adiabatic free energy curves for the electron transfer reaction $Fe^{3+} + e^- \leftrightarrow Fe^{2+}$ for selected effective electronic coupling Γ and overvoltage η. (Adapted from Ref. 163.)

about this procedure and its theoretical foundation can be found elsewhere.[151,182] The main issue in the implementation of this procedure is to produce the transition state ensemble. If the ET reaction is symmetric (for example, in the case of the bulk reaction $Fe^{2+} + Fe^{3+} \rightarrow Fe^{3+} + Fe^{2+}$), then the transition state is easily determined by symmetry considerations (in this example it will be a pair of $Fe^{2.5+}$ "ions"). In the electrochemical case, the location of the transition state (in terms of the value of ΔE) is determined by many factors, including the overpotential and the electronic coupling. One way to prepare a transition state ensemble is to determine, with the help of Eq. (34), the effective ion charge and to equilibrate the ion with this charge near the interface. The nonequilibrium dynamic trajectory begins when the Hamiltonian is taken to be H_{ad}. This method has been used in one case to compute the transmission coefficient, and its value has been compared with approximate analytical theories.[163] It should be stressed, however, that this area of research is still in its infancy, and more work is necessary, both simulation and experiments.

3. Multistate Models

The main shortcoming of the molecular dynamics approach discussed in the previous section is that it ignores the fact that an electron transfer at the solution/metal interface occurs between an ion in a well-defined electronic state and a continuum of electronic states in the metal. For example, depending on the ion's orbital energy, the reorganization free energy and the overpotential, the electron could be transferred from, or to, any level around the Fermi level of the metal. Therefore, a sum over all these possibilities must be performed. Analytical theories of electron transfer at the solution/metal interface recognized this issue very early on, and the reader is referred to many excellent expositions on this subject.[149,183–189]

The fact that there are an infinite number of electronic degrees of freedom in the metal, and an analysis of experimental results by Schmickler,[185] suggest that electron transfer at the solution/metal interface is near the adiabatic limit. A particularly useful approach is based on the Anderson–Newns approach to adsorption.[190] When it is adapted to the electron transfer problem, the total Hamiltonian of the system is given by[170,185,189]

$$\mathbf{H} = \mathbf{H}_{\text{nuc}}(\mathbf{r}) + [\varepsilon_I + \Delta E(\mathbf{r})]n_I + \sum_k (\varepsilon_k n_k + V_{Ik} c_I^\dagger c_k + V_{kI} c_k^\dagger c_I) \tag{36}$$

where $\mathbf{H}_{\text{nuc}}$ includes all the solvent–solvent, solvent–surface, and solvent–ion interactions that do not explicitly involve electronic degrees of freedom, and n_I is the quantum occupation operator for the ion's orbital (with eigenvalues of 0 or 1), whose energy is ε_I and whose shift due to the solvent is $\Delta E(\mathbf{r})$. The sum in Eq. (36) is over all the metal electronic states (ignoring the spin), where ε_k, n_k, and c_k are the energy, the occupation operator, and the creation operator of level k, respectively, c_I is the creation operator for the ion's orbital, and V_{Ik} is the coupling between the ion orbital and the electronic level k in the metal.

For a fixed value of the nuclear coordinate, the ground-state energy of the electronic part of the Hamiltonian in Eq. (36) can be found analytically[185,188] to be

$$E_0 = \frac{1}{2}\Delta E + \frac{1}{\pi}(\varepsilon_l + \Delta E - \varepsilon_f)\tan^{-1}\left[\frac{\varepsilon_f - \varepsilon_l - \Delta E}{\Delta}\right] + \frac{\Delta}{2\pi}\ln[(\varepsilon_l + \Delta E - \varepsilon_f)^2 + \Delta^2] \tag{37}$$

where ε_f is the Fermi energy of the metal electrons and Δ is a parameter that describes the strength of the ion–metal interactions

$$\Delta(\omega) = \pi \sum_k |V_{lk}|^2 \delta(\omega - \varepsilon_k) \tag{38}$$

Although Δ is a function of energy, it can be taken to be a constant parameter for energies in the range of interest.

For adiabatic electron transfer, the Hamiltonian of the system is given by adding the nuclear part of Eq. (36) to the ground-state electronic energy given by Eq. (37). The resulting potential energy surface describes, for a certain range of the parameter Δ, a double-well potential similar to the one discussed earlier. Schmickler used a harmonic oscillator model for the solvent to calculate the rate of electron transfer with this Hamiltonian.[185] This was followed by more sophisticated applications, including electronic excitation in the metal.[188,189] The solvent has been described using harmonic oscillators or a generalized Langevin model.[189]

It is clear, however, that one may introduce a microscopic description of the solvent into the above formalism. This was done by Straus, Calhoun, and Voth.[170] The total classical Hamiltonian is given by

$$H_{cl} = H_{\text{nuc}} + E_0 \tag{39}$$

where E_0 is given by Eq. (37) as an explicit function of the nuclear positions, and H_{nuc} is the classical Hamiltonian describing the interaction of an ion of charge $Z - n_l$ with the metal (through image interactions) and the solvent. The classical simulation with the Hamiltonian given by Eq. (39) gives rise to the following average occupancy of the ion orbital:

$$\langle n_l(\Delta E)\rangle = \frac{1}{2} + \frac{1}{\pi}\tan^{-1}\left(\frac{\varepsilon_f - \varepsilon_l - \Delta E}{\Delta}\right) \tag{40}$$

This expression shows that the average occupancy of the ion's orbital takes on values between 0 and 1, depending on the solvent shift of the ion's energy relative to the Fermi level of the metal. For example, if $\Delta E >> 0$, we get $\langle n_l \rangle \approx 0$, and the electron is on the metal, as we find in the case of the two-state model.

The Hamiltonian in Eq. (39) has been used to calculate the adiabatic free energy as a function of the solvent coordinate using the umbrella sampling method, and reactive flux correlation function calculations have been used to determine the adiabatic rate constant.[170] The results were qualitatively similar to the results based on the two-state model.

Voth and co-workers also considered the effect that the quantum nature of the water molecules may have on the adiabatic free energy curve.[170] This was done by using path integral molecular dynamics to quantize the motion of the water's hydrogen atoms. These workers found that the activation free energy and the reaction free energy are significantly affected by the water quantization. Similar results were found earlier for electron transfer in bulk water.[191] These results suggest that classical models of water need to be modified to take this effect into account. However, it is not clear how important the details of the water potential are in contributing to the large quantum effects seen. This is clearly an open area for future work.

V. PROCESSES AT THE LIQUID/LIQUID INTERFACE

Electrochemical processes at the liquid/liquid interface have been another important area in interfacial electrochemistry. Understanding charge transfer processes, such as ion transfer and electron transfer at the interface between two immiscible liquids, is of fundamental and practical importance to many areas of science. Nevertheless, our knowledge of this electrochemical environment is much less developed than our knowledge of the corresponding solution/metal interface. The main reasons are the difficulty of performing simple electrochemical measurements and the even greater difficulty of applying the techniques of modern surface science to this system. Theoretical developments have also been very limited, and only in the past few years have the techniques of molecular dynamics and Monte Carlo computer simulations been used to gain some microscopic insight into this system. As in the case of the solution/metal

interface, the main drive to apply these methods has been the availability of new microscopic-level experimental data. New experimental developments in this area have been extensively reviewed in the past few years.[91,192–195]

Although this chapter would not be complete without a discussion of the contribution of molecular dynamics computer simulation to the study of electrochemical processes at the liquid/liquid interface, this subject has been extensively reviewed recently,[96,196] and so here we limit ourselves to a complete listing of the publications in this area.

Developments in molecular dynamics and Monte Carlo studies of the liquid/liquid interface have followed the general outline of developments in the area of simulations of the solution/metal interface. The first molecular dynamics and Monte Carlo simulations of the interface between two immiscible liquids were concerned with the study of the structure and dynamics of the pure interface and calculating properties such as the density profile of the two liquids, pair-correlation functions, hydrogen bonding (if one of the liquids is water), general structural features of the interface, diffusion constants, and molecular reorientation dynamics. This was done for quite a large number of systems, including the water/benzene,[197] water/hexanol,[198] water/hexane,[199] water/1,2-dichloroethane,[200] water/decane,[201] water/nonane,[202] water/octanol,[203] and water/CCl_4 interfaces.[29] Although most calculations have been for the interface between water and an organic liquid, there have been calculations for simple model liquids.[204,205] Unlike the extensive literature on the effect of the external electric field on the water/metal interface discussed earlier, there has only been one such study on the water/liquid interface.[206]

Following the early studies on the pure interface, chemical and electrochemical processes at the interface between two immiscible liquids have been studied using the molecular dynamics method. The most important processes for electrochemical research involve charge transfer reactions. Molecular dynamics computer simulations have been used to study the rate and the mechanism of ion transfer across the water/1,2-dichloroethane interface[207,208] and of ion transfer across a simple model of a liquid/liquid interface, where a direct comparison of the rate with the prediction of simple diffusion models has been made.[209,210] Charge transfer of several types has also been studied, including the calculations of free energy curves for electron transfer reactions at a model liquid/liquid

interface[164] and at the water/1,2-dichloroethane interface,[166] and the calculations of solvent dynamic response to a solute electronic transition.[196,211]

In addition to charge transfer processes, calculations of adsorption free energy[212,213] and of isomerization reaction equilibrium and dynamics[214] have been reported. Detailed accounts of all these calculations are provided in the two reviews mentioned earlier[96,196] and in another one that has been recently published.[215]

VI. CONCLUSIONS AND OUTLOOK

The use of molecular dynamics and Monte Carlo simulations to study electrochemical processes at the interface between two phases is only in its preliminary stages. The need to provide a molecular-level understanding of structure and dynamics at the interface to help in interpreting the new microscopic level of experimental data will increase. However, many important basic issues remain to be understood before these computational methods become routine research tools.

One of the fundamental difficulties of using classical molecular dynamics computer simulations in general, and for the electrolyte/electrode interface in particular, is the accuracy and applicability of the model potential energy functions used. Although much progress has been made in recent years, much still needs to be done, especially in the development of solute–metal interactions that take into account both the quantum mechanical nature of the interactions at short range and the classical image-type interactions that result from the extended metal structure. The development of methods that avoid the concept of potential energy function altogether and attempt to directly evaluate the forces from electronic structure calculations is still in its infancy, but it seems quite promising.

A related, relatively unexplored topic is the importance of many-body forces in the simulations of interfacial systems. The development of water-polarizable models has reached some level of maturity, but one needs to explore how these models must be modified to take into account the interactions with the metal surface atoms and the polarizable nature of the metal itself.

Developments in the area of analytical statistical mechanical theories, which we did not discuss in this chapter, will have an important impact on

computational approaches by providing more insight into the importance of different factors in determining the properties of the solution/metal interface. Progress in this area as well as in the development of simple continuum models and new experimental techniques will allow us to have a much better understanding of this important system.

In addition to the development of new methods, new applications of molecular dynamics computer simulation are also needed in order to make comparisons with experimental results. In particular, more complicated chemical reactions, beyond the relatively simple electron transfer reaction, could be studied. Examples include the study of chemical adsorption, hydrogen evolution reactions, and chemical modification of the electrode surface. All of the above directions and opportunities promise to keep this area of research very active!

ACKNOWLEDGMENTS

This work was supported by the Petroleum Research Fund administered by the American Chemical Society (27255-ACS) and the National Science Foundation (CHE92-21580). I wish to thank Dr. E. Spohr, Dr. M. Philpott, Dr. K. Heinzinger, Prof. J. W. Halley, and Prof. M. Berkowitz for providing me with unpublished material and other references.

REFERENCES

[1]A. J. Bard and L. R. Faulkner, *Electrochemical Methods: Fundamentals and Applications*, Wiley, New York, 1980.

[2]C. Gutierrez and C. Melendres, *Spectroscopic and Diffraction Techniques in Interfacial Electrochemistry*, Kluwer, Dordrecht, 1990.

[3]J. O.'M. Bockris and A. Gonzalez-Martin, in *Spectroscopic and Diffraction Techniques in Interfacial Electrochemistry*, Ed. by C. Gutierrez and C. Melendres, Kluwer, Dordrecht, 1990, p. 1.

[4]J. O.'M. Bockris and S. U. M. Khan, *Surface Electrochemistry*, Plenum Press, New York, 1993.

[5]A. J. Bard, H. D. Abruña, C. E. Chidsey, L. R. Faulkner, S. W. Foldberg, K. Itaya, M. Majda, O. Melroy, R. W. Murray, M. D. Porter, M. P. Soriaga, and H. S. White, *J. Phys. Chem.* **97**(1993)7147.

[6]R. R. Dogonadze, E. Kalman, A. A. Kornyshev, and J. Ulstrup, *The Chemical Physics of Solvation*; Part C, Elsevier, Amsterdam, 1988.

[7]J. Goodisman, *Electrochemistry: Theoretical Foundations*, Wiley, New York, 1987.

[8]W. Schmickler, *Interfacial Electrochemistry*, Oxford University Press, Oxford, 1996.

[9]C. A. Croxton, *Fluid Interfacial Phenomena*, Wiley, New York, 1986.

[10]A. Pohorille and M. A. Wilson, *J. Mol. Struct. (Theochem)* **284** (1993) 271.
[11] S.-B. Zhu, S. Singh, and G. W. Robinson, *Adv. Chem. Phys.* **85** (1994) 627.
[12]G. W. Robinson, S. Singh, and M. W. Evans, *Water in Biology, Chemistry and Physics. Experimental Overviews and Computational Methodologies*, World Scientific, Singapore, 1996.
[13]Y. Marcus, *Ion Solvation*, Wiley, New York, 1985.
[14]R. R. Dogonadze, E. Kalman, A. A. Kornyshev, and J. Ulstrup, *The Chemical Physics of Solvation* Part A, Elsevier, Amsterdam, 1985.
[15]*Faraday Discuss. Chem. Soc.* **85** (1988).
[16]S. Trasatti, in *Modern Aspects of Electrochemistry*, Ed. by B. E. Conway and J. O.'M. Bockris, Plenum Press, New York, 1979.
[17]M. P. Allen and D. J. Tildesley, *Computer Simulation of Liquids*, Clarendon, Oxford, 1987.
[18]C. A. Croxton, *Statistical Mechanics of the Liquid Surface*, Wiley, New York, 1980.
[19]J. S. Rowlinson and B. Widom, *Molecular Theory of Capillarity*, Clarendon, Oxford, 1982.
[20]D. Henderson, *Fundamentals of Inhomogeneous Fluids,* Marcel Dekker, New York, 1992.
[21]H. J. C. Berendsen, J. P. M. Postma, W. F. V. Gunsteren, and J. Hermans, in *Intermolecular Forces*, Ed. by B. Pullman, Reidel, Dordrecht, 1981, p. 331.
[22]J.-L. Barrat and I. R. McDonald, *Mol. Phys.* **70** (1990) 535.
[23]K. Kuchitsu and Y. Morino, *Bull. Chem. Soc. Jpn.* **38** (1965) 814.
[24] M. Sprik and M. L. Klein, *J. Chem. Phys.* **89** (1988) 7556.
[25]P. Ahlstrom, A. Wallqvist, S. Engstrom, and B. Jonsson, *Mol. Phys.* **68** (1989) 563.
[26]L. X. Dang, J. E. Rice, J. Caldwell, and P. A. Kollman, *J. Am. Chem. Soc.* **113** (1991) 2481.
[27]A. Wallqvist, *Chem. Phys. Lett.* **165** (1990) 437.
[28]K. Motakabbir and M. Berkowitz, *Chem. Phys. Lett.* **176** (1991) 61.
[29]T. M. Chang and L. X. Dang, *J. Chem. Phys.* **104** (1996) 6772.
[30]C. Pangali, M. Rao, and B. J. Berne, *J. Chem. Phys.* **71** (1979) 2975.
[31]C. Y. Lee, J. A. McCammon, and P. J. Rossky, *J. Chem. Phys.* **80** (1984) 4448.
[32]J. Hautman, J. W. Halley, and Y.-J. Rhee, *J. Chem. Phys.* **91** (1989) 467.
[33]L. L. Lee, *Molecular Thermodynamics of Nonideal Fluids*, Butterworth, Boston, 1988.
[34]J. N. Israelachvili, *Intermolecular and Surfaces Forces*, Academic Press, London, 1992.
[35]M. Watanabe, A. M. Brodsky, and W. P. Reinhardt, *J. Phys. Chem.* **95** (1991) 4593.
[36]J. N. Glosli and M. R. Philpott, *J. Chem. Phys.* **96** (1992) 6962.
[37]K. Raghavan, K. Foster, K. Motakabbir, and M. Berkowitz, *J. Chem. Phys.* **94** (1991) 2110.
[38]K. Raghavan, K. Foster, and M. Berkowitz, *Chem. Phys. Lett.* **177** (1991) 426.
[39]E. Spohr and K. Heinzinger, *Ber. Bunsen-Ges. Phys. Chem.* **92** (1988) 1358.
[40]E. Spohr, *J. Phys. Chem.* **93** (1989) 6171.
[41]S. Holloway and K. H. Bennemann, *Surf. Sci.* **101** (1980) 327.
[42]P. A. Thiel and T. E. Madey, *Surf. Sci. Rept.* **7** (1987) 211.
[43]S.-B. Zhu and M. R. Philpott, *J. Chem. Phys.* **100** (1994) 6961.
[44]J. M. Holender, *Phys. Rev. B* **41** (1990) 8054.
[45]L. E. Gonzalez, D. J. Gonzalez, and M. Silbert, *Physica B* **168** (1991) 39.
[46]J. Theilhaber, *Phys. Fluids B* **4** (1992) 2044.
[47]C. Martin, E. Lomba, J. A. Anta, and M. Lombardero, *J. Phys. Condens. Matter* **5** (1993) 379.
[48]G. Kresse and J. Hafner, *J. Non-Crstal. Solids* **156** (1993) 956.
[49]M. A. Gomez and S. A. Rice, *J. Chem. Phys.* **101** (1994) 8094.
[50]S. Kambayashi and J. Chihara, *Molecular Simulation* **16** (1996) 31.
[51]J. Böcker, R. R. Nazmutdinov, E. Spohr, and K. Heinzinger, *Surf. Sci.* **335** (1995) 372.

[52]R. R. Nazmutdinov, M. Probst, and K. Heinzinger, *J. Electroanal. Chem.* **369** (1994) 227.
[53]J. I. Siepmann and M. Sprik, *Surf. Sci. Lett.* **279** (1992) L185.
[54]J. I. Siepmann and M. Sprik, *J. Chem. Phys.* **102** (1995) 511.
[55]R. Guidelli, in *Trends in Interfacial Electrochemistry*, Ed. by A. F. Silva, Riedel, Dordrecht, 1986.
[56]A. A. Kornyshev, W. Schmickler, and M. A. Vorotyntsev, *Phys. Rev. B* **25** (1982) 5244.
[57]J. P. Badiali, M. L. Rosinberg, and J. Goodisman, *J. Electroanal. Chem.* **150** (1983) 25.
W. Schmickler and D. Henderson, *J. Chem. Phys.* **85** (1986) 1650.
[59]D. L. Price and J. W. Halley, *Phys. Rev. B* **38** (1988) 9357.
[60]D. R. Bérard, M. Kinoshita, X. Ye, and G. N. Patey, *J. Chem. Phys.* **101** (1994) 6271.
[61]C. N. Patra and S. K. Ghosh, *J. Chem. Phys.* **102** (1995) 2556.
[62]D. L. Price and J. W. Halley, *J. Chem. Phys.* **102** (1995) 6603.
[63]J. R. Smith, *Phys. Rev.* **181** (1969) 522.
[64]R. Car and M. Parrinello, *Phys. Rev. Lett.* **55** (1985) 2471.
[65]G. Galli and M. Parrinello, in *Computer Simulations in Materials Science*, Ed. by M. Meyer and V. Pontikis, Kluwer, Dordrecht, 1991.
[66]M. E. Tuckerman, B. J. Berne, G. J. Martyna, and M. L. Klein, *J. Chem. Phys.* **97** (1992) 2635.
[67]D. Marx and M. Parrinello, *J. Chem. Phys.* **104** (1996) 4077.
[68]M. E. Tuckerman, D. Marx, M. L. Klein, and M. Parrinello, *J. Chem. Phys.* **104** (1996) 5579.
[69]M. E. Tuckerman, P. J. Ungar, T. v. Rosenvinge, and M. L. Klein, *J. Phys. Chem.* **100** (1996)12878.
[70]E. Madelung, *Phys. Z* **19** (1918) 524.
[71]P. Ewald, *Ann. Phys.* **64** (1921) 253.
[72]J. A. Barker, in *The Problem of Long-Range Forces in the Computer Simulation of Condensed Matter,* Ed. by D. Ceperley, Vol. 9, NRCC Workshop Proceedings, 1980, p. 45.
[73]J. Hautman and M. L. Klein, *Mol. Phys.* **75** (1992) 379.
[74]J. N. Glosli and M. R. Philpott, in *Microscopic Models of Electrode-Electrolyte Interfaces*, Ed. by J. W. Halley and L. Blum, Vol. 93-5, Electrochemical Society, 1993, p. 80.
[75]L. Greengard and V. Rokhlin, *J. Comp. Phys.* **73** (1987) 325.
[76]J. P. Valleau, in *The Problem of Long-Range Forces in the Computer Simulation of Condensed Matter*, Ed. by D. Ceperley, Vol. 9, NRCC Workshop Proceedings, 1980, p. 3.
[77]J. Alejandre, D. J. Tildesley, and G. A. Chapela, *J. Chem. Phys.* **102** (1995) 4574.
[78]F. H. Stillinger and A. Ben-Naim, *J. Chem. Phys.* **47** (1967) 4431.
[79]R. G. Horn and J. N. Israelachvili, *J. Chem. Phys.* **75** (1981) 1400.
[80]J. N. Israelachvili, *Adv. Coll. Int. Sci.* **16** (1982) 31.
[81]J. D. Porter and A. S. Zinn, *J. Phys. Chem.* **97** (1993) 1190.
[82]D. R. Berard and G. N. Patey, *J. Chem. Phys.* **95** (1991) 5281.
[83]M. J. Booth, D. M. Duh, and A. D. J. Haymet, *J. Chem. Phys.* **101** (1994) 7925.
[84]K. Heinzinger and E. Spohr, *Electrochim. Acta* **34** (1989) 1849.
[85]J. Böcker, E. Spohr, and K. Heinzinger, *Z. Naturforsch.* **50a** (1995) 611.
[86]J. Goodisman, *J. Chem. Phys.* **82** (1985) 560.
[87]M. Iwamatsu, *J. Phys. Soc. Jpn.* **60** (1991) 1272.
[88]L. Bosio, R. Cortes, M. Denoziere, and G. Folcher, *Coll. Phys. C7*, Suppl. 10 **50** (1989) 23.

[89]D. B. Parry, M. G. Samant, H. Seki, M. R. Philpott, and K. Ashley, *Langmuir* **9** (1993) 1878.
[90]T. T. Chen, J. F. Owen, R. K. Chang, and B. L. Laube, *Chem. Phys. Lett.* **89** (1982) 356.
[91]R. M. Corn and D. A. Higgins, *Chem. Rev.* **94** (1994) 107.
[92]M. A. Wilson, A. Pohorille, and L. R. Pratt, *J. Chem. Phys.* **88** (1988) 3281.
[93]G. Nagy, K. Heinzinger, and E. Spohr, *Faraday Discuss.* **94** (1992) 307.
[94]J. N. Glosli and M. R. Philpott, *Electrochim. Acta* **41** (1996) 2145.
[95]R. Guidelli and G. Aloisi, in *Electrified Interfaces in Physics, Chemistry and Biology*, Ed. by R. Guidelli, Kluwer, Dordrecht, 1992, p. 309.
[96]I. Benjamin, *Chem. Rev.* **96** (1996) 1449.
[97]D. A. McQuarrie, *Statistical Mechanics,* Harper & Row, New York, 1976.
[98]E. Spohr, *Chem. Phys.* **141** (1990) 87.
[99]K. Heinzinger, *Pure and Appl. Chem.* **63** (1991) 1733.
[100]D. A. Rose and I. Benjamin, *J. Chem. Phys.* **95** (1991) 6856.
[101]S. H. Lee, J. C. Rasaiah, and J. B. Hubbard, *J. Chem. Phys.* **85** (1986) 5232.
[102]K. J. Strandburg, *Rev. Mod. Phys.* **60**(1988) 161.
[103]A. M. Brodsky and L. I. Daikhin, *Soviet Electrochem.* **25** (1989) 379.
[104]M. F. Toney, J. N. Howard, J. Richter, G. L. Borges, D. G. Weisler, D. Yee, and L. B. Sorensen, *Nature* **368** (1994) 444.
[105]K.-I. Ataka, T. Yotsuyanagi, and M. Osawa, *J. Phys. Chem.* **100** (1996) 10664.
[106]G. Nagy and K. Heinzinger, *J. Electroanal. Chem.* **296** (1990) 549.
[107]D. A. Rose and I. Benjamin, *J. Chem. Phys.* **98** (1993) 2283.
[108]X. Xia, L. Perera, U. Essmann, and M. L. Berkowitz, *Surf. Sci.* **335** (1995) 401.
[109]X. Xia and M. L. Berkowitz, *Phys. Rev. Lett.* **74** (1995) 3193.
[110]J. O.'M. Bockris and M. A. Habib, *Langmuir* **2** (1986) 388.
[111]S. L. Carnie and G. M. Torrie, *Adv. Chem. Phys.* **56** (1984) 141.
[112]L. Blum, in *Fluid Interfacial Phenomena*, Ed. by C. A. Croxton, Wiley, New York, 1986, p. 391.
[113]G. M. Torrie, P. G. Kusalik, and G. N. Patey, *J. Chem. Phys.* **91** (1989) 6367.
[114]L. Blum, *Adv. Chem. Phys.* **78**(1990) 171.
[115]W. Schmickler, *Electrified Interfaces in Physics, Chemistry and Biology*, Ed. by R. Guidelli, Kluwer, Dordrecht, 1992, p. 399.
[116]P. Attard, *Adv. Chem. Phys.* **92** (1996) 1.
[117]R. W. Impey, P. A. Madden, and I. R. McDonald, *J. Phys. Chem.* **87** (1983) 5071.
[118]M. R. Philpott, in *Cluster Models for Surface and Bulk Phenomena*, Ed. by G. Pacchioni, Plenum Press, New York, 1992, p. 359.
[119]P. Bopp, in *The Physics and Chemistry of Aqueous Ionic Solutions*, Ed. by M.-C. Bellissent-Funel and G. W. Neilson, Reidel, Dordrecht, 1987, p. 217.
[120]T. P. Straatsma and H. J. C. Berendsen, *J. Chem. Phys.* **89** (1988) 5876.
[121]M. Berkowitz, O. A. Karim, J. A. McCammon, and P. J. Rossky, *Chem. Phys. Lett.* **105** (1984)577.
[122]B. M. Pettitt and P. J. Rossky, *J. Chem. Phys.* **84** (1986) 5836.
[123]L. X. Dang and B. M. Pettitt, *J. Phys. Chem.* **94** (1990) 4303.
[124]J. N. Glosli and M. R. Philpott, *J. Chem. Phys.* **98** (1993) 9995.
[125]J. Seitz-Beywl, M. Poxleitner, M. M. Probst, and K. Heinzinger, *Int. J. Quantum Chem.* **42**(1992) 1141.
[126]G. Tóth, E. Spohr, and K. Heinzinger, *Chem. Phys.* **200** (1995) 347.
[127]J. Seitz-Beywl, M. Poxleitner, and K. Heinzinger, *Z. Naturforsch.* **46** (1991) 876.
[128]L. Perera and M. L. Berkowitz, *J. Phys. Chem.* **97** (1993) 13803.

[129]G. Tóth and K. Heinzinger, *Chem. Phys. Lett.* **245** (1995) 48.
[130]T. Matsui and W. L. Jorgensen, *J. Am. Chem. Soc.* **114** (1992) 3220.
[131]C. H. Bennett, in *Algorithms for Chemical Computations,* Ed. by R. E. Christofferson, ACS Symposium Series 46, American Chemical Society, Washington, DC, 1977.
[132]G. M. Torrie and J. P. Valleau, *J. Comput. Phys.* **23** (1977) 187.
[133]J. B. Anderson, *Adv. Chem. Phys.* **91** (1995) 381.
[134]G. Ciccotti, M. Ferrario, J. T. Hynes, and R. Kapral, *Chem. Phys.* **129** (1989) 241.
[135]E. Spohr, *Chem. Phys. Lett.* **207** (1993) 214.
[136]E. Spohr, *J. Mol. Liq.* **64** (1995) 91.
[137]E. Spohr, *Acta. Chem. Scand.* **49**(1995) 189.
[138]E. Spohr, "Computer modeling of aqueous/metallic interfaces," Habilitationsschrift, Ulm, Germany, 1995.
[139]G. Gouy, *J. Phys.* **9** (1910) 457.
[140]D. L. Chapman, *Phil. Mag.* **25** (1913) 475.
[141]G. N. Patey and G. M. Torrie, *Chem. Scr.* **29A** (1989) 39.
[142]L. Blum and D. Henderson, in *Fundamentals of inhomogeneous Fluids,* Ed. by D. Henderson, Marcel Dekker, New York, 1992, p. 239.
[143]E. Spohr and K. Heinzinger, *J. Chem. Phys.* **84** (1986) 2304.
[144]K. Heinzinger, *Fluid Phase Equilibria* **104** (1995) 277.
[145]M. R. Philpott and J. N. Glosli, *Surf. Sci.* **335** (1995) 422.
[146]M. R. Philpott, *Chem. Phys.* **198** (1995) 53.
[147]M. R. Philpott and J. N. Glosli, *J. Electrochem. Soc.* **142** (1995) L25.
[148]R. A. Marcus, *Ann. Rev. Phys. Chem.* **15** (1964) 155.
[149]J. Ulstrup, *Charge Transfer Processes in Condensed Media*, Springer, Berlin, 1979.
[150]R. W. Gurney, *Proc. R. Soc. (Lond.) A* **134** (1931) 137.
[151]J. T. Hynes, in *The Theory of Chemical Reactions,* Ed. by M. Baer, Vol. 4, CRC Press, Boca Raton, FL, 1985, p. 171.
[152]M. J. Weaver, *Chem. Rev.* **92** (1992) 463.
[153]P. J. Rossky and J. D. Simon, *Nature* **370** (1994) 263.
[154]R. A. Marcus, *Rev. Mod. Phys.* **65** (1993) 599.
[155]R. A. Marcus, *J. Chem. Phys.* **38** (1963) 1858.
[156]R. A. Marcus, *J. Chem. Phys.* **39** (1963) 1734.
[157]M. D. Newton and N. Sutin, *Ann. Rev. Phys. Chem.* **35** (1984) 437.
[158]G. King and A. Warshel, *J. Chem. Phys.* **93** (1990) 8682.
[159]R. A. Marcus, *J. Chem. Phys.* **24** (1956) 966.
[160]R. A. Marcus, *J. Chem. Phys.* **24** (1956) 979.
[161]R. A. Marcus, *J. Chem. Phys.* **43** (1965) 679.
[162]R. A. Kuharski, J. S. Bader, D. Chandler, M. Sprik, M. L. Klein, and R. W. Impey, *J. Chem. Phys.* **89**(1988) 3248.
[163]D. A. Rose and I. Benjamin, *J. Chem. Phys.* **100** (1994) 3545.
[164]I. Benjamin, *J. Phys. Chem.* **95** (1991) 6675.
[165]J. B. Straus and G. A. Voth, *J. Phys. Chem.* **97** (1993) 7388.
[166]I. Benjamin, in *Structure and Reactivity in Aqueous Solution,* Ed. by C. J. Cramer and D. G. Truhlar, ACS Symposium Series 568, American Chemical Society, Washington, D. C., 1994, p. 409.
[167]B. B. Smith and J. W. Halley, *J. Chem. Phys.* **101** (1994) 10915.
[168]X. Xia and M. L. Berkowitz, *Chem. Phys. Lett.* **227**(1994) 561.
[169]D. A. Rose and I. Benjamin, *Chem. Phys. Lett.* **234** (1995) 209.
[170]J. B. Straus, A. Calhoun, and G. A. Voth, *J. Chem. Phys.* **102** (1995) 529.

[171]A. Warshel, *J. Phys. Chem.* **86** (1982) 2218.
[172]J. K. Hwang and A. Warshel, *J. Chem. Phys.* **84** (1986) 4938.
[173]J. K. Hwang and A. Warshel, *J. Am. Chem. Soc.* **109**(1987)715.
[174]J. W. Halley and J. Hautman, *Phys. Rev. B* **38** (1988) 11704.
[175]L. A. Curtiss, J. W. Halley, J. Hautman, N. C. Hung, Z. Nagy, Y.-J. Rhee, and R. M. Yonco, *J. Electrochem. Soc.* **138** (1991) 2032.
[176]C. Zener, *Proc. R. Soc. (Lond.) A* **137** (1932) 696.
[177]L. D. Landau and E. M. Lifshitz, *Quantum Mechanics: Non-relativistic Theory*, Pergamon, New York, 1977.
[178]T. Holstein, *Ann. Phys.* **8** (1959) 325.
[179]D. A. Zichi, G. Ciccotti, J. T. Hynes, and M. Ferrario, *J. Phys. Chem.* **93** (1989) 6261.
[180]W. P. Keirstead, K. R. Wilson, and J. T. Hynes, *J. Chem. Phys.* **95** (1991) 5256.
[181]R. M. Whitnell and K. R. Wilson, in *Reviews in Computational Chemistry*, Ed. by K. B. Lipkowitz and D. B. Boyd, VCH Publishers, New York, 1993.
D. Chandler, *Introduction to Modern Statistical Mechanics*, Oxford University Press, Oxford, 1987.
[183]R. R. Dogonadze, A. M. Kuznetsov, and M. A. Vorotyntsev, *J. Electroanal. Chem.* **25** (1970)17.
[184]V. G. Levich, in *Physical Chemistry, an Advanced Treatise*, Ed. by H. Eyring, D. Henderson, and W. Jost, Vol. 9B, Academic Press, New York, 1970, p. 985.
[185]W. Schmickler, *J. Electroanal. Chem.* **204** (1986) 31.
[186]K. L. Sebastian and P. Ananthapadmanabhan, *J. Electroanal. Chem.* **230** (1987) 43.
[187]A. M. Kuznetsov, *J. Electroanal. Chem.* **241** (1988) 45.
[188]K. L. Sebastian, *J. Chem. Phys.* **90** (1989) 5056.
[189]B. B. Smith and J. T. Hynes, *J. Chem. Phys.* **99** (1993) 6517.
[190]J. P. Muscat and D. N. Newns, *Progr. Surf. Sci.* **9** (1978) 1.
[191]J. S. Bader, R. A. Kuharski, and D. Chandler, *J. Chem. Phys.* **93** (1990) 230.
[192]G. J. Hanna and R. D. Noble, *Chem. Rev.* **85** (1985) 583.
[193]H. H. Girault and D. J. Schiffrin, in *Electroanalytical Chemistry*, Ed. by A. J. Bard, Dekker, New York, 1989, p. 1.
[194]K. B. Eisenthal, *Ann. Rev. Phys. Chem.* **43** (1992) 627.
[195]H. H. Girault, in *Modern Aspects of Electrochemistry*, Ed. by J. O.'M. Bockris, B. E. Conway, and R. E. White, Vol. 25, Plenum Press, New York, 1993, p. 1.
[196]I. Benjamin, in *Liquid-Liquid Interfaces,* Ed. by A. G. Volkov and D. W. Deamer, CRC Press, Boca Raton, 1996, p. 179.
[197]P. Linse, *J. Chem. Phys.* **86** (1987) 4177.
[198]J. Gao and W. L. Jorgensen, *J. Phys. Chem.* **92** (1988) 5813.
[199]I. L. Carpenter and W. J. Hehre, *J. Phys. Chem.* **94** (1990) 531.
[200]I. Benjamin, *J. Chem. Phys.* **97** (1992) 1432.
[201]A. R. Vanbuuren, S. J. Marrink, and H. J. C. Berendsen, *J. Phys. Chem.* **97** (1993) 9206.
[202]D. Michael and I. Benjamin, *J. Phys. Chem.* **99** (1995) 1530.
[203]D. Michael and I. Benjamin, *J. Phys. Chem.* **99**(1995) 16810.
[204]M. Hayoun, M. Meyer, and M, Mareschal, in *Chemical Reactivity in Liquids*, Ed. by G. Ciccotti and P. Turq, Plenum, New York, 1987, p. 279.
[205]S. Toxvaerd and J. Stecki, *J. Chem. Phys.* **102** (1995) 7163.
[206]K. J. Schweighofer and I. Benjamin, *J. Electroanal. Chem.* **391** (1995) 1.
[207]I. Benjamin, *Science* **261** (1993) 1558.
[208]K. J. Schweighofer and I. Benjamin, *J. Phys. Chem.* **99** (1995) 9974.
[209]I. Benjamin, *J. Chem. Phys.* **96** (1992) 577.

[210]M. Hayoun, M. Meyer, and P. Turq, *J. Phys. Chem.* **98** (1994) 6626.
[211]I. Benjamin, *Chem. Phys.* **180** (1994) 287.
[212]A. Pohorille and M. A. Wilson, *J. Chem. Phys.* **104** (1996) 3760.
[213]A. Pohorille, P. Cieplak, and M. A. Wilson, *Chem. Phys.* **204** (1996) 337.
[214]A. Pohorille and M. A. Wilson, in *Reaction Dynamics in Clusters and Condensed Phases*, Ed. by J. Jortner, R. D. Levine, and B. Pullman, Kluwer, Dordrecht, 1994, p. 207.
[215]I. Benjamin, *Ann. Rev. Phys. Chem.* **48** (1997) 401.

This Page Intentionally Left Blank

4

Underpotential Deposition on Single-Crystal Metals

Akiko Aramata

Catalysis Research Center, Hokkaido Univeristy, Sapporo Japan 060

I. INTRODUCTION

1. Scope of this Chapter

Underpotential deposition is described as less than monolayer metal deposition on a foreign metal substrate, which occurs at more positive potentials than the equilibrium potential of a metal ion deposed on its own metal, expressed by the Nernst equation. Kolb reviewed state-of-the-art Underpotential deposition up to 1978.[1] As Underpotential deposition is a process indicative of less than a monolayer metal on a substrate, it is expected to be quite sensitive to the surface structure of the substrate crystal; a well-defined single-crystal electrode preparation is a prerequisite to the study of Underpotential deposition. In the case of Au and Ag single-crystal electrodes, Hamelin and co-workers extensively studied the necessary crystal surface structure, as reviewed in Ref. 2.

A dipping technique was proposed by Dickermann *et al.* in 1976[3] for the study of single-crystal electrodes, in which only the surface of a well-defined single-crystal is in contact with an electrolyte solution, and without any other pretreatment, the other portion of the crystal metal is not exposed to the solution. In the case of Pt, an annealing-quenching technique was developed by Clavilier *et al.*[4] in 1980. This technique has

Modern Aspects of Electrochemistry, Number 31, edited by John O'M. Bockris *et al.* Plenum Press, New York, 1997

extensively improved the quality of single-crystal surfaces by preventing pollution of the surfaces by impurities in the air and by refreshing the surface structure in a well-defined form. The two techniques of annealing-quenching and dipping are described as being combined for preparation of a well-defined electrode surface in Ref. 4. The technique is simple enough to be adopted by any research group, and seems to present a standard treatment of single crystals for electrochemical measurements. This combined method for obtaining a well-defined condition is called the Clavilier method. It was first employed for Au single-crystal electrode preparations in 1981[5] and then for Ir[6] and Rh.[7]

In order to find the features of a one-atomic-height surface structure, various spectroscopic techniques have been introduced by which only information from electrochemical measurements was tested on single-crystal surfaces and the results interpreted.[8,9] This chapter aims to review recent (post-1978) experimental reports on underpotential deposition, mostly for well-defined surfaces. Electrochemical *in situ* scanning tunneling microscopy (STM) at an atomic scale was used for lead on HOPG in 1989,[10] and for the study of underpotential deposition of copper in 1990.[11] Various reports on the studies of well-defined surfaces are published in *J. Chim. Phys*., Vol. 88, No.7–8 (1991), edited by J. Clavilier *et al.* Various aspects of nanometer-scale electrode interfaces are covered in the *Faraday Discussions.*[12] In *J. Phys. Chem.* (1993), a feature article on the electrode/electrolyte interface by 12 authors discussed not only underpotential deposition but also various modified electrodes at a monatomic level, such as electrodes with LB membranes, molecular adsorption, specifically adsorbed anions, self-assembled monolayer, and polymer films, where STM, AFM, X-ray diffraction, XANES, EXAFS, FTIR, QCM, and SHG are mentioned as investigation tools of *in situ* as well as *ex situ* techniques.[13] Those methods are suggested to be powerful techniques to reveal an atom or molecule monolayer in a clearly well-defined structure. Among the spectroscopies, STM and AFM gave a real image of the structure of the electrode surface and provided the first confirmation that single crystals have well-defined surfaces that are in good order down to an atomic nanometer scale. From those images obtained as a function of electrode potentials, earlier findings and understandings could be tested. However, such images cannot give the chemical identity of a species. Therefore, in addition to the above methods,[13] the radiotracer

technique should be mentioned as a tool for atomic-level observation of the electrode/electrolyte interface,[14–19] which provides information on the kind of atoms at the electrode interface.

Specific adsorption of anions is one of the major subjects for the elucidation of the double-layer structure at the electrode interface,[20] and is treated in a different category from the electrode processes such as hydrogen adsorption/desorption on Pt and underpotential deposition of metal. In the former, specific adsorption and partial electron displacement are considered, and in the latter, adsorption and underpotential deposition processes are as the Faradaic reduction/oxidation reaction with an integral number of electrons transferred. However, Clavilier and co-workers proposed a new concept that involves an elaborate experimental technique of CO adsorption. Specific adsorption is regarded as a redox reaction on the electrode surface. Thus, the cyclic voltammogram feature classified as a hydrogen adsorption wave on Pt is regarded as not only being due to the redox reaction of adsorbed hydrogen formation/desorption, but also to a redox reaction of specifically adsorbed anions, e.g., for sulfuric acid solutions.[21–24]

The process of monolayer deposition of metal ions in underpotential deposition is strongly affected by anion-specific adsorption, and the two processes at the electrode interface must be elucidated if one is to understand underpotential deposition phenomena in a unified way.

2. Preparation and Qualification of Single Crystals

(i) Pt and Pt Metal Single Crystals

The preparation of Pt single-crystal electrodes with well-defined surface qualities achieved by Clavilier and co-workers in 1980,[4] known as the Clavilier method, is schematically shown in Fig. 1.[25] The crystal dipping procedure of Fig. 1d was adopted from the work of Dickermann *et al.*[3] By means of the Clavilier method, characteristic cyclic voltammograms, depending on crystal faces and the kind of electrolytes, were revealed, with the voltammograms of Pt(111) in $HClO_4$ and H_2SO_4 being quite different from each other and totally different from cyclic voltammograms of polycrystalline Pt; these results were reproduced later by many other researchers. Reliable work on Pt single-crystal electrodes can be said to have begun with Clavilier's work described in Ref. 4. The

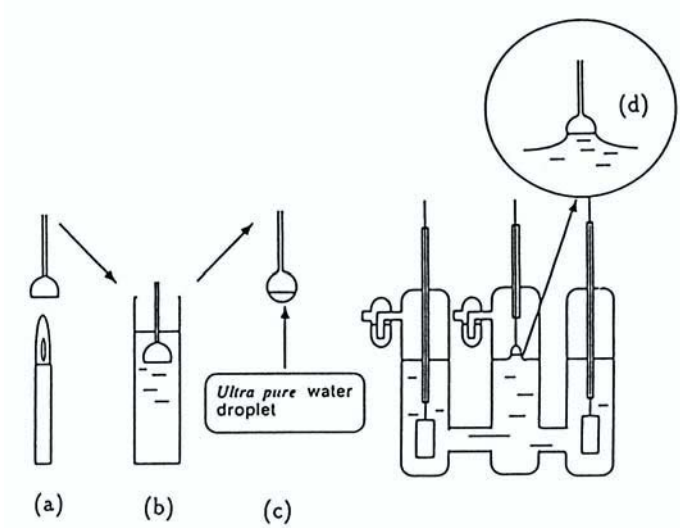

Figure 1. Preparation of a well-defined single-crystal electrode by four steps. (a) Mirror-finished crystal is annealed under gas flame, and (b) quenched in air and then pure water. (c) The crystal is covered with a droplet of pure water to protect it from pollution by impurities in air and (d) is introduced into the cell, where the crystal contacts the meniscus of the electrolyte solution. (From Ref. 25.)

Clavilier method for crystal preparation and flame annealing has been improved since 1980 and is employed as a standard procedure for single-crystal electrode experiments using Pt, Pt metals, and Au.

Clavilier's currently recommended procedure is as follows.[26] Two cooling processes of the crystal after flame-annealing treatment are carried out between steps (a) and (b) in Fig. 1; i.e., air cooling until the temperature of the crystal becomes 200–300°C and cooling in pure water under an H_2 + Ar stream. The transfer of the crystal into the cell in step (c) of Fig. 1 with a droplet of H_2 + Ar-saturated pure water on the crystal face is important for protecting the crystal surface from impurities in air. Then the crystal surface is exposed to the solution by the dipping method of Fig. 1.

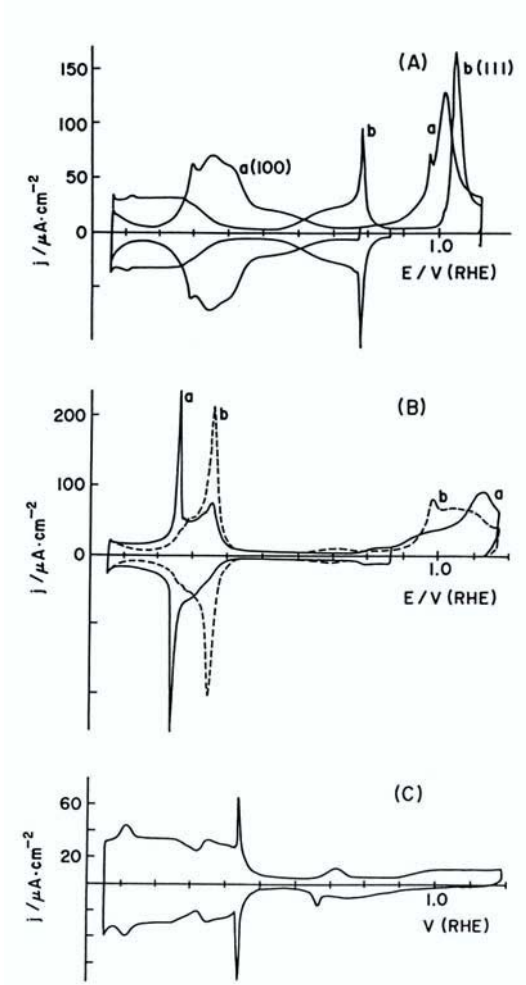

Figure 2. (A) Voltammograms of (a) Pt(100) and (b) Pt(111) cooled in H_2 + Ar and 0.1*M* $HClO_4$. (B) Voltammograms of flame-cleaned Pt(100) in 0.5*M* H_2SO_4; (a) air cooling and (b) H_2 + Ar cooling. (C) Voltammogram of Pt(111) in H_2SO_4. The sweep rate was 50 mV s^{-1}. (From Refs. 4 and 27.)

Cyclic voltammograms on Pt(111),[21] Pt(100),[27] and Pt(110)[26] in perchloric and sulfuric acid solutions are given in Fig. 2. Figure 2A shows voltammograms of Pt(100) and Pt(111) in 0.1*M* $HClO_4$,[27] where the cyclic voltammogram of Pt(111) is a well-recognized curve. The cyclic voltammogram of Pt(100) gives a charge amount of 320 $\mu C\ cm^{-2}$ at the so-called hydrogen adsorption potential region, which is well over 209 $\mu C\ cm^{-2}$ for monolayer coverage of the adsorbed hydrogen on Pt(100). These authors observed that Pt(100) surface is reconstructed in the form of (5 × 20). In sulfuric acid solution, the amount of the charge on Pt(100) was 214 or 217 $\mu C\ cm^{-2}$ for air or H_2 + Ar cooling, as shown in Fig. 2B, which suggests that the Pt(100) surface is not reconstructed in 0.5*M* H_2SO_4.[27] Figure 2C

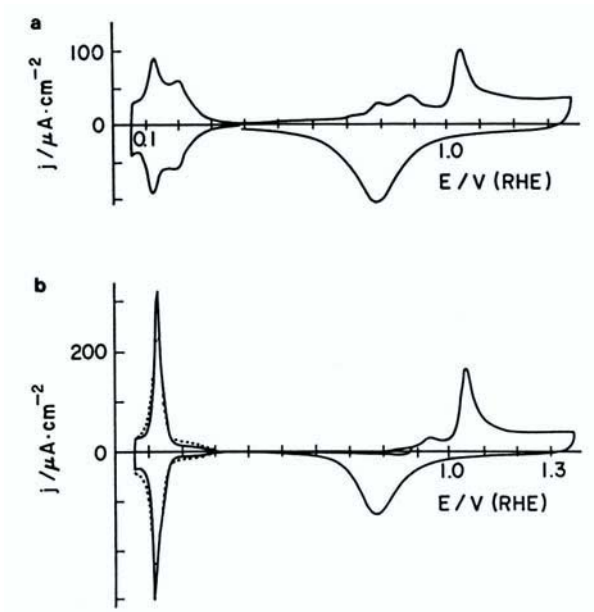

Figure 3. (A) Voltammograms of Pt(110) cooled in H_2 + Ar and 0.1*M* $HClO_4$. (B) Voltammogram of Pt(110) cooled in H_2 + Ar and 0.5*M* H_2SO_4, where the dotted curve was observed after the first oxygen adsorption-desorption cycle. The sweep rate was 50 mV s^{-1}. (From Ref. 26.)

shows a voltammogram of Pt(111) in 0.5*M* H_2SO_4. Figure 3 shows voltammograms of Pt(110) in 0.5*M* H_2SO_4 and 0.1*M* $HClO_4$[26]; the charge densities in the hydrogen region are 218 and 220 $\mu C\ cm^{-2}$, respectively, which suggests that the Pt(110) surface is reconstructed in **Pt(110)(1 × 2)**; in low energy electron diffraction (LEED) observations in vacuum, after electrochemical treatment, the Pt(100) surface was observed to be in the form of **Pt(110)(1 × 2)**.[28] Detailed specification of cyclic voltammograms

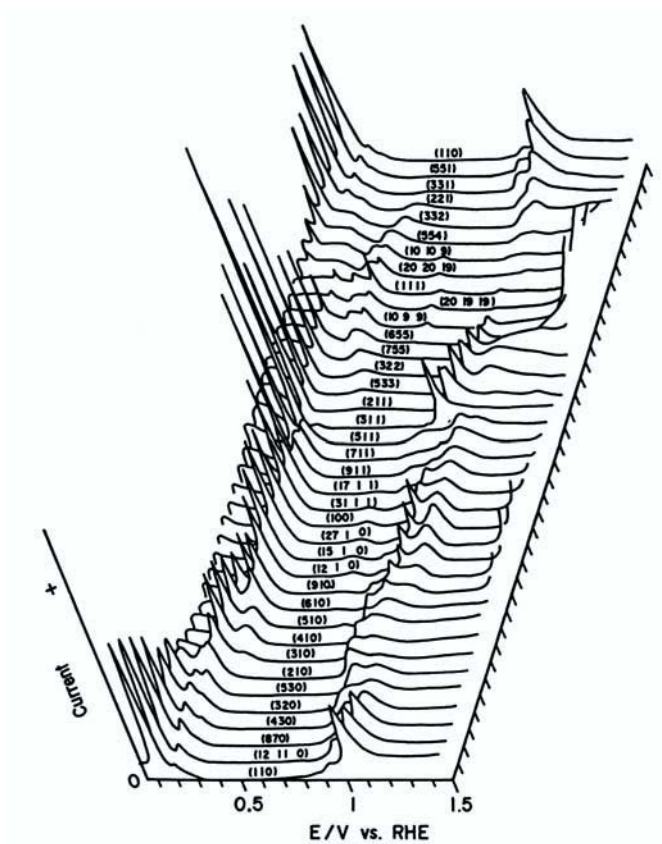

Figure 4. Anodic voltammograms on various Pt single-crystal electrodes in 0.5*M* H_2SO_4. The sweep rate was 50 mV s^{-1}. (From Ref. 30.)

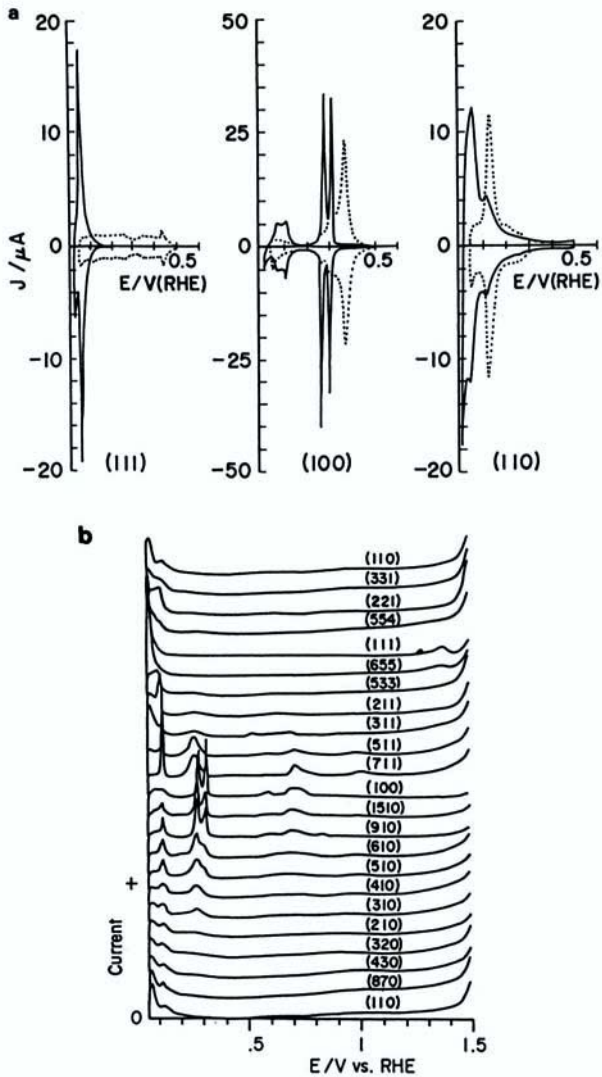

Figure 5. (A) Voltammograms on Ir and Pt low-index single crystals at 50 mV s^{-1} in 0.5*M* H_2SO_4. Solid curves are for Ir and dotted ones for Pt. (B) Anodic voltammograms on various iridium single crystals. (From Ref. 32.)

on Pt(111) and Pt(100) can be found in Ref. 29. Surface structure-sensitive cyclic voltammograms were observed for various high-index Pt crystals in H_2SO_4, as shown in Fig. 4.[30]

A cyclic voltammogram on Rh(111) was observed in 0.1*M* $HClO_4$[7,31] and in 0.5*M* H_2SO_4,[31] where the crystal was prepared according to the Clavilier method. Cyclic voltammograms on various Ir single-crystal faces were also observed in H_2SO_4, being quite surface structure-sensitive,[6,32] as shown in Fig. 5. The preparation of Ir single crystals was conducted under hydrogen-oxygen flame because its melting point is higher than the other Pt metals.

(ii) Au Single Crystals

Gold single-crystal electrodes have been extensively studied by Hamelin and co-workers since the 1960s, as reviewed in Ref. 2. At the beginning of their work, the crystal was not treated by the flame annealing developed by Clavilier and co-workers and then subjected to the Clavilier method developed since 1981,[5] which was found to give excellent performance in cyclic voltammograms for Au crystals also. Cyclic voltammograms on Au(111), Au(100), and Au(110) in perchloric acid solution are shown in Fig. 6.[33] These are now taken to be the standard cyclic voltammograms for respective crystal planes (see Ref. 34). This means that the cyclic voltammogram features of anodic formation of the adsorbed oxygen species (OA) and their cathodic desorption (OC) in Fig. 6 are standards for judging the crystal faces exposed to the solution. Although experimental results for Pt single crystals before the work of Clavilier *et al.*[4] should be carefully viewed, for Au single crystals, the qualities of the crystal and experimental procedures (especially by Hamelin *et al.*) have been progressively improved without any abrupt discontinuity by the new crystal treatments of Ref. 4, as found in Ref. 2.

(iii) Ag, Cu, and Other Single Crystals

Ag, Cu, Bi, Zn, and Pb single crystals were employed as electrodes and their surface characteristics reviewed by Hamelin.[2] Among them, Ag single crystals were mostly investigated, as found in Refs. 35 and 36, in addition to Ref. 2.

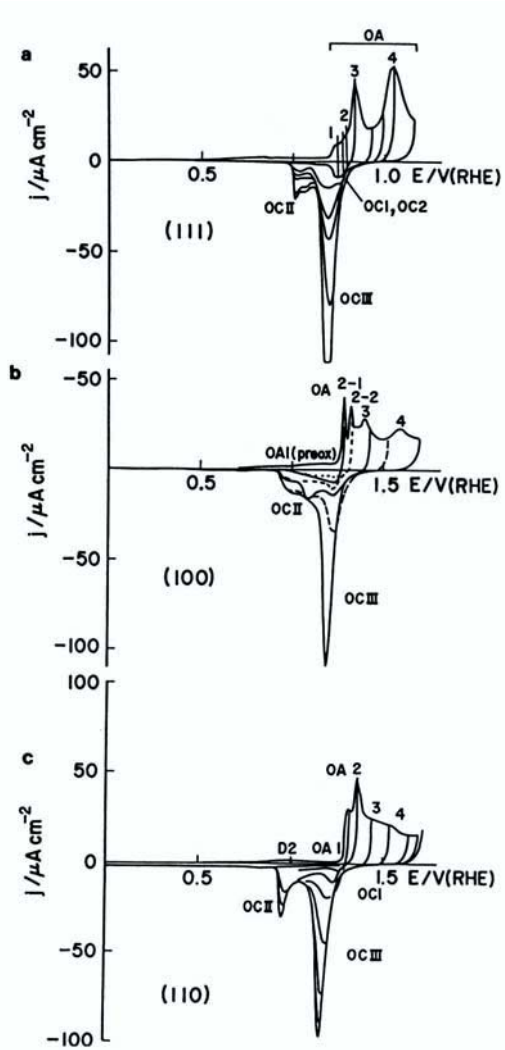

Figure 6. Voltammograms at 20 mV s^{-1} with a change in anodic limit potentials on Au single crystals in 0.01*M* $HClO_4$. (A) (111), (B) (100), and (C) (110). (From Ref. 33.)

3. Well-Defined Surface Structure and Reconstruction of Single-Crystal Surfaces

(i) Voltammogram Observations

In the study of single-crystal electrodes, a real surface exposed to an electrolyte solution should be always qualified to some extent since the surface atom arrangement is not *a priori* oriented along the bulk crystal configuration. It is well known that crystal surfaces are roughened by applying positive potentials to form oxide layers, since the surface area was observed to be increased during positive potential electrolysis. The reconstruction of the electrode surface was suggested by observations of cyclic voltammograms and double-layer capacitance even after the potential was imposed to negative potentials in the case of Au single crystals.[2,37] This was summarized in Ref. 36 and is shown in Fig. 7, where the values

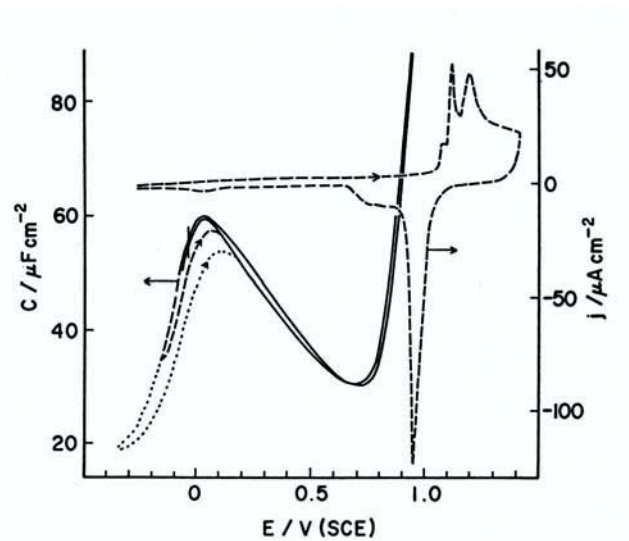

Figure 7. Double-layer capacitance against potentials on Au(100) in 1*M* $HClO_4$ at 10 mV s^{-1} with a change in cathodic limit potentials E_{lim}. Solid curve for $E_{lim} = -0.05$ V, broken curve for $E_{lim} = -0.18$ V, and dotted curve for $E_{lim} = -0.35$ V(SCE). The cyclic voltammogram is given by the broken curve. (From Ref. 37.)

of capacitance at the change of potential sweep direction were changed when the negative potential limit was less than –0.15 V(SCE) on Au(100) in 1*M* $HClO_4$. This reconstruction of gold crystal was later confirmed clearly by STM, as described in the next section. Studies of electroreflectance and SHG seem to reflect surface structure and reconstruction.[38]

In an ultra-high vacuum (UHV) system, single-crystal surfaces of Pt(100) and Pt(110) are known to be reconstructed as Pt(100)-(5 × 20) and Pt(110)-(1 × 2), respectively, but the Pt(111) is believed not to be reconstructed. In electrochemical systems, Pt(111) and Pt(100) do not seem to be reconstructed up to the double-layer region by a positive potential limit as shown by LEED[39] and by STM through CO adsorption.[40] However, Rodes *et al.* claimed that the most carefully treated Pt(100) is

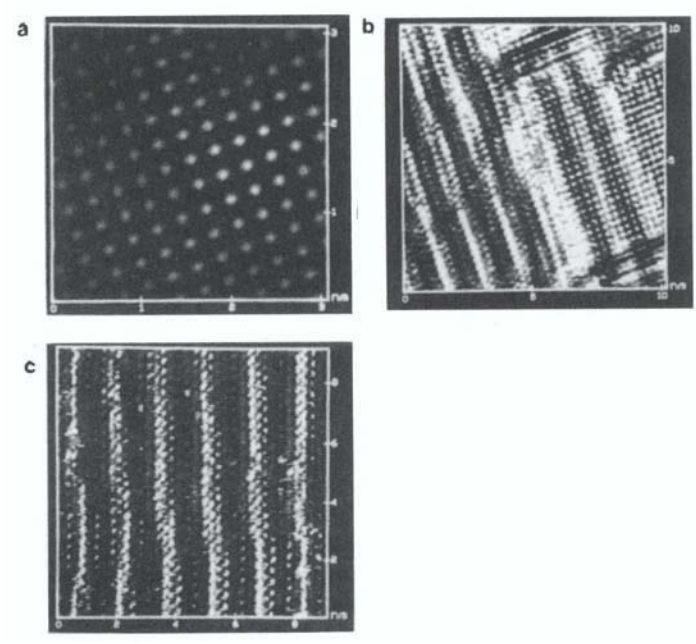

Figure 8. STM images for Au(100) in 0.1*M* $HClO_4$. (a) Filtered image at $E = 0.2$ V(SCE), (b) after 10 min at $E = -0.3$ V, and (c) well-resolved unfiltered image at $E = -0.4$V. (From Ref. 8.)

reconstructed in 0.1*M* $HClO_4$ but not in 0.5*M* H_2SO_4.[27] A Pt(110) surface treated by flame annealing and subjected to a cyclic voltammogram in acidic solution was put into an ultrahigh vacuum (UHV) chamber for LEED pattern observation and gave Pt(110)-(1 × 2),[28] where the evaluation of the so-called adsorbed hydrogen did not give a 1 to 1 ratio of the adsorbed hydrogen to the surface Pt atom of Pt(110)-(1 × 2). Later, it was suggested that each Pt surface of Pt(110)-(1 × 2) accommodated one hydrogen atom according to the amount of the adsorbed hydrogen.[26] It seems likely that the transfer of electrode from solution to vacuum chamber gives some contamination on the surface in the case of the work in Ref. 28, since the observation by simple electrochemical techniques easily reproduced the results of Clavilier *el al*. by many other groups, as indicated in Refs. 41 and 42. Here, we have to remark that these criteria based on the so-called amount of charge densities of "the adsorbed

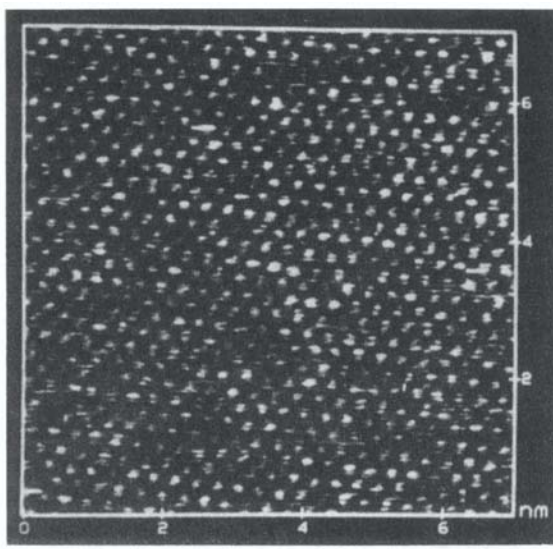

Figure 9. STM image at E = 0.1 V(SCE) on Au(111) in 0.1*M* $HClO_4$. (From Ref. 43 with the permission of the *Journal of Physical Chemistry*.)

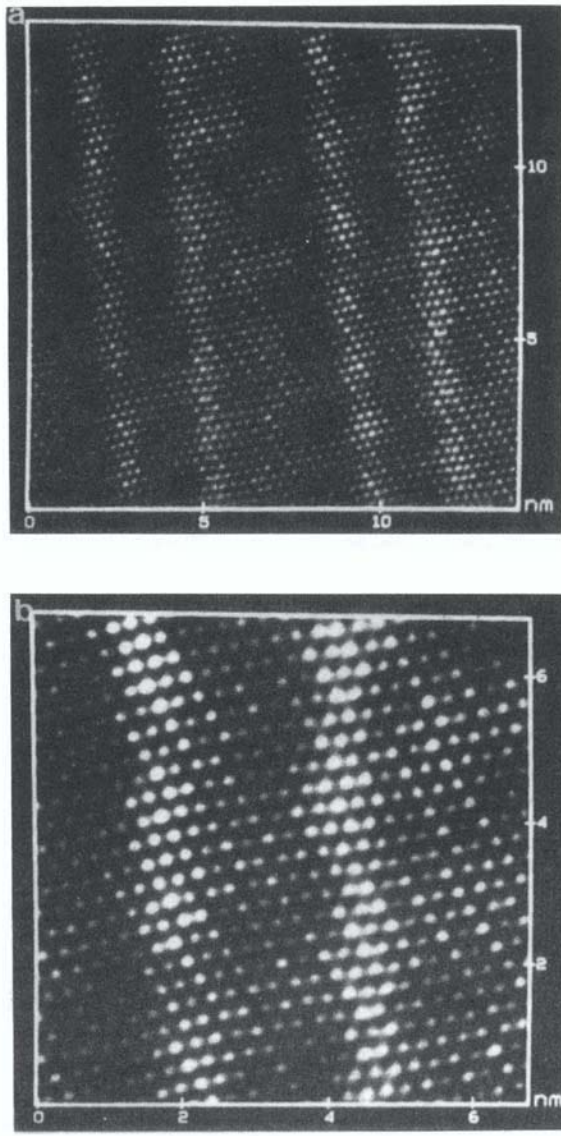

Figure 10. STM images at $E = -0.3$ V(SCE) on Au(111) in 0.1M $HClO_4$. (a) 15 nm × 15 nm and (b) magnified portion of (a). (From Ref. 43 with the permission of the *Journal of Physical Chemistry*.)

hydrogen" seem to fail in interpretation of the surface sites of platinum atoms from work done later by Orts *et al.*, Clavilier *et al.*, and Feliu *et al.* for Pt single crystals,[21–24] which is discussed further in Section I.4.

(ii) Observation by STM

The first confirmation of a plain Au(100) electrode surface by STM was reported in Ref. 8, in which the Au(100) STM image revealed the Au(100)(1 × 1) structure by atomic-scale resolution at a potential of E = 0.2 V(SCE) in 0.1*M* $HClO_4$. The surface was reconstructed at $E = -0.25$ V(SCE), becoming a hexagonal arrangement, which again returned to the (1 × 1) surface at positive potentials after polarization for several minutes, as found in Fig. 8. The atomically resolved STM images on Au(111) were also observed to be reconstructed by the change of electrode potentials; the Au(111)-(1 × 1) structure was observed at E=0.1 V(SCE) on Au(111), which undergoes reconstruction at –0.3 V(SCE), as shown in Figs. 9 and 10.[43] In the case of Au(110), atomically resolved STM images were not

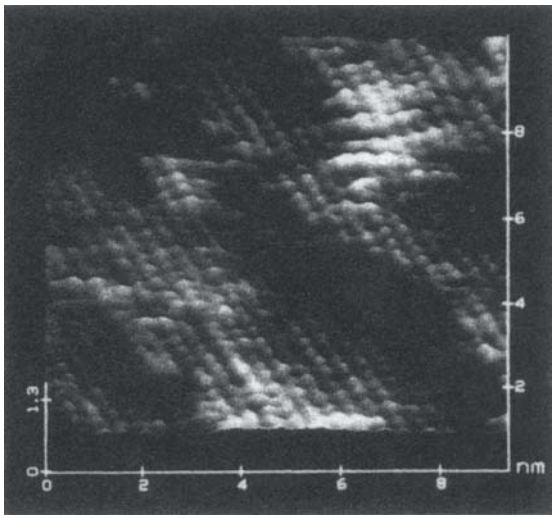

Figure 11. STM images at E = 0 V(SCE) on Au(110) in 0.1*M* $HClO_4$. (From Ref. 44.)

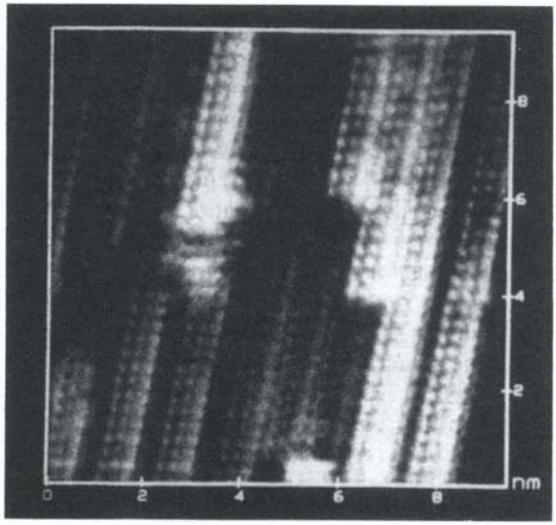

Figure 12. STM images at $E = -0.3$ V(SCE) on Au(110) in 0.1*M* $HClO_4$ Au(110) is reconstructed as (1×2) and (1×3). (From Ref. 44.)

initially observed in the potential region of $E = -0.1$ to 0.2 V. However, by altering the potential from $E = -0.3$ V to 0 V(SCE), the STM image of Fig. 11 was observed at $E = 0$ V(SCE).[44] Figure 12 shows an STM image of reconstructed Au(110)(1×2) and (1×3) at $E = -0.3$ V in 0.1*M* $HClO_4$.[44] Comparison of the electrochemical and STM results clearly demonstrated that the reconstruction of surfaces reflects the potential dependence of double-layer capacitance.[9,45,46] Later, detailed STM observations were conducted not only on low-index surfaces,[47–49] but also on high-index surfaces.[50,51] The effects of anions and cations were also observed.[52–55] In the case of Pt(111), an atomically smooth STM image was observed[56] and later an atomically resolved STM image was found at –0.25 V(SCE) in 0.1*M* $HClO_4$.[57]

4. Anion Adsorption Behavior

In 1992 the cyclic voltammogram feature of Pt single crystals in sulfuric acid solution was examined by CO adsorption.[21,22] Figure 13 shows the effect of CO adsorption on Pt(111) in sulfuric acid solution,[24] where at $E_{ads} = 0.08$, 0.3, and 0.5 V(RHE), CO gas was introduced and the current

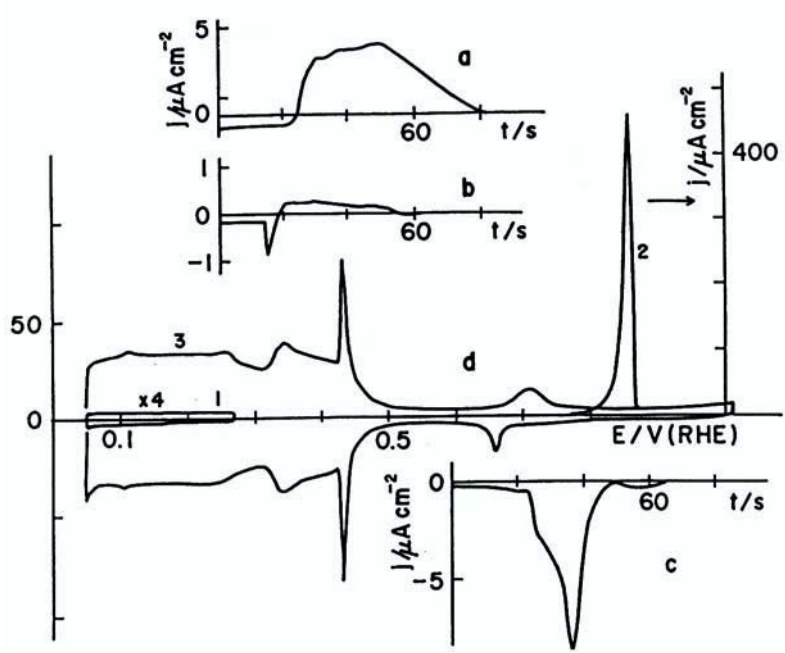

Figure 13. Plot of current against time. (a), (b), and (c) Current-time transients on Pt(111) in 0.5*M* H_2SO_4, when CO was endorsed at potentials of 0.08, 0.3, and 0.5 V(RHE) of curve 3 of (d), respectively. When CO was present in the solution, curves 1 and 2 were observed. The sweep rate was 50 mV s^{-1}. (From Ref. 24.)

associated with desorption of the adsorbed species expelled by CO was observed. At 0.08 V, the adsorbed species is expelled with oxidation current, as expected by processes such as $\mathbf{H(a) \rightarrow H^+ + \mathit{e}}$. At 0.3 V, practically no current was observed, and at 0.5 V, the absorbed species was expelled by reduction current. A similar reduction current had been already observed on polycrystalline Pt.[58] This may be explained by the reductive desorption of sulfate species.[21,22,24] This shows that the cyclic voltammogram current at 0.3 V < E < 0.5 V is due to adsorption/desorption of sulfate species. The effect of sulfate concentration on this wave was observed,[59] showing a change of about 60 mV with one order of change in sulfate concentration, which suggests sulfate-specific adsorption to be a one-electron transfer process.

The adsorption of sulfate was confirmed by radiotracer technique as shown in Fig. 14, which clearly shows that the sulfate adsorption feature depends on crystal faces, as reviewed in Ref. 17.

Sulfate adsorption on Pt(111) was investigated by thermodynamic treatment of the Gibbs excess, which is based on the Frumkin treatment.[60,61] The above cyclic voltammogram feature at Pt(111) in sulfuric acid solution was also thought to be due to the adsorbed sulfate.[59]

The cyclic voltammogram characteristics of Pt(111) in phosphate, sulfate, and perchlorate acid solutions were observed with changing pHs, shown in Fig. 15,[62] where the potential scale is with respect to SHE, and concentrations of sulfate and perchlorate ions were kept constant, as was phosphate ionic strength. Figure 15A shows that the cyclic voltammogram currents at $0.28 < E < 0.5$ V converged into a single curve even with a pH change between 0.8 and 2.1 in sulfate solutions. This tendency of no change of cyclic voltammogram curve by pH at the positive potential in the so-called hydrogen region indicates that the process in this region is not associated with the hydrogen adsorption/desorption process and is in good harmony with the observation that the curve position is dependent on sulfate concentration, but not on pH.[59] The plateau currents at $E < 0.3$ V shifted by *ca.* 60 mV with a unit change of pH in Fig. 15A. Figures 15B and C show the potential shift of the cyclic voltammogram with the

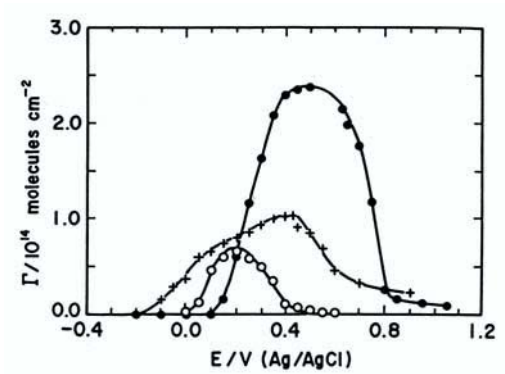

Figure 14. Potential dependence of sulfate adsorption on Pt(100)(○), Pt(111)(●), and polycrystalline Pt(+) in 0.1*M* $HClO_4$ + 1m*M* H_2SO_4. (From Ref. 17.)

change of pH, where the shift of two current peaks is identical by *ca.* 60 mV with a unit change of pH for perchlorate. The 60-mV change by a unit change of pH can be interpreted by a one-electron transfer of hydrogen adsorption/desorption at the negative potential of A, B, and C. At the positive potential of B, the adsorbed hydroxyl species seem to adsorb/desorb at potentials $E > 0.35$ V(RHE), which depends on pH. In the case of phosphate in Fig. 15C, the current peaks negatively shifted with a pH increase. Phosphate species in a solution of $pH \leq 4.6$ of H_3PO_4 and/or

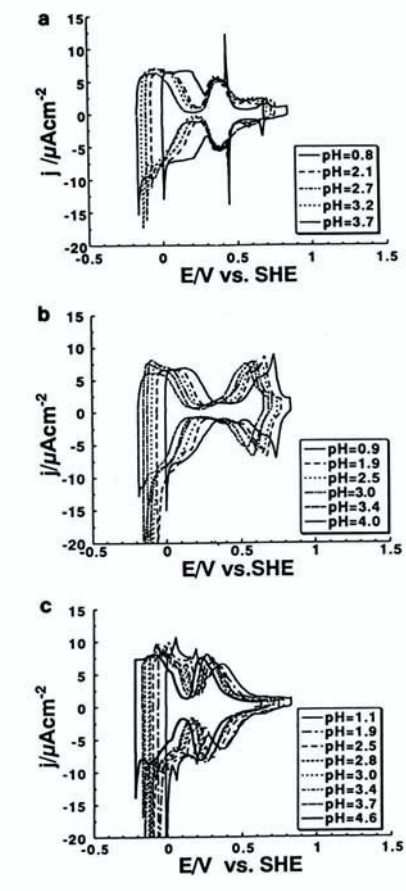

Figure 15. Cyclic voltammogram on Pt(111) at 10 mV s^{-1} for various pH solutions of 0.8 ~ 4.6, when the respective anion concentration was kept at 0.1*M*. (A) Sulfate solutions at [sulfate species] = 0.1*M*. (B) Perchlorate solutions at $[ClO_4^-] = 0.1M$. (C) Phosphate solutions at 0.1*M* ionic strength of phosphate species. (From Ref. 62.)

$H_2PO_4^-$, are suggested to undergo a redox adsorption/desorption process in which H^+ ions are always involved.

II. UNDERPOTENTIAL DEPOSITION ON SINGLE-CRYSTAL ELECTRODES

The electrodeposition/electrodissolution of M^{n+} on metal M is given by

$$M^{n+} + ne \rightleftharpoons M \tag{1}$$

where n is the number of electrons to transfer through the electrode interface and the equilibrium potential of Eq. (1) is given by the Nernst equation of

$$E_{eq} = E_0 + \frac{RT}{nF} \ln \frac{a^{M^{n+}}}{a^M} \tag{2}$$

where E_0 is the standard potential of Eq. (1), $a^{M^{n+}}$ and a^M are activities of M^{n+} and M, respectively, $a^M = 1$, and R, T, and F have the usual meanings. When the potential negative to E_{eq}, E, is imposed, the electrodeposition of the forward reaction of Eq. (1) takes place and the electrodissolution of the backward reaction of Eq. (1) takes place when E is positive to E_{eq}.

The underpotential deposition/dissolution process of metal ions M^{n+} takes place on the substrate metal M' at $E > E_{eq}$, which is expressed by the equation,

$$M^{n+} + ne \underset{\rightleftharpoons}{M'} M/M' \tag{3}$$

where underpotential deposition takes place with an electron transfer number of n by formation of M metal on substrate M', which is described as M^{n+}/M'. The electron transfer number n in Eq. (3) is presumed to be identical to n of Eq. (1) for simplicity. When Eq. (3) is in an equilibrium at a certain potential E^{UPD}, a quasi-Nernst equation can be written as*

$$E^{UPD} = E_0' + \frac{RT}{nF} \ln \frac{a^{M^{n+}}}{a^{M/M'}}, \tag{4}$$

*This definition is modified in Section II.4.

where E_0' is formally defined as potential when the second term of the right-hand side is zero. The *as* are activities of M^{n+} and M/M′, respectively; n is the same as that of Eq. (3), and an underpotential deposition process is observed since E^{UPD} locates at more positive potentials than E_{eq} of the Nernst equation, and the underpotential shift potential of ΔE^{UPD} can be defined as

$$\Delta E^{UPD} = E^{UPD} - E_{eq} \tag{5}$$

In the following section, the position of underpotential deposition is determined at the maximum peak of a cyclic voltammogram peak current, which is expressed as ΔE^{UPD}. Underpotential deposition of M^{n+} on M′ has been mostly observed by voltammograms, which were quite characteristic for various combinations of M^{n+} and M′.

1. Underpotential Deposition on Au Single Crystals

(i) *Electrochemical and* Ex Situ *Spectroscopic Measurements*

(a) Cu underpotential deposition

Cu^{2+} underpotential deposition on low-index single-crystal Au electrodes was observed in $HClO_4$, for which case the crystal dipping method was developed.[3] This method is not only easily handled, but can also provide clean conditions for the electrochemical system, and it became a standard technique for the study of single-crystal electrodes. The cathodic and anodic cyclic voltammogram characteristics were not reversible with respect to potential sweeps at 20 mV s^{-1} for Cu^{2+} on single-crystal Au electrodes in perchloric acid solution. However, a cyclic voltammogram of Cu^{2+} underpotential deposition on Au(111) gives well-reversible waves in sulfuric acid solution, as shown in Fig. 16a, in which two clearly distinguished peaks are found. This suggests a two-dimensional and well-defined structure for Cu underpotential deposition on Au(111). *Ex situ* RHEED and LEED observations gave a $(\sqrt{3} \times \sqrt{3})$ surface structure at potentials between the two peaks of the cyclic voltammogram of Fig. 16a.[38] Figure 16b shows an adsorption isotherm with a monolayer structure of Cu underpotential deposition on Au(111) in $0.05M$ H_2SO_4 + 1 mM $CuSO_4$, where the structure was derived from RHEED.[63] It is interesting that the RHEED pattern at the potential of no Cu underpotential deposition

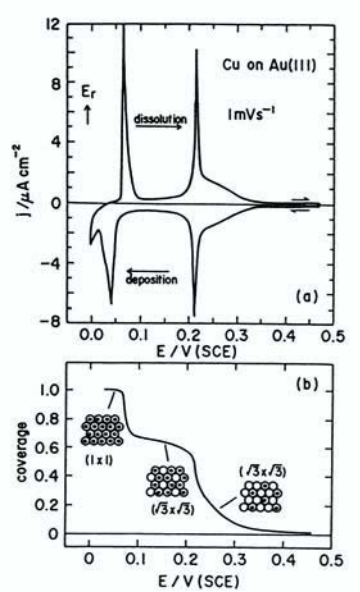

Figure 16. (a) Cyclic voltammograms of Cu underpotential deposition on Au(111). (b) Adsorption isotherm in 0.05*M* H_2SO_4 + 1 m*M* $CuSO_4$ at 1 mV s^{-1}. At potentials < E_r, Cu overpotential deposition occurs. The structure of Cu on Au(111) from RHEED is shown at the respective potentials. (From Refs. 38 and 63.)

is identical to the pattern in the potential region between two underpotential deposition current peaks. Underpotential deposition of Cu on Au(111) was studied by changing the concentration of Cu^{2+}ions, where the shifts of underpotential deposition peaks were 60 mV and 30 mV per $\log[Cu^{2+}]$ for the positive and negative potential side peaks of Fig. 17, respectively. These primarily suggest a one-electron transfer process at the positive potential side and a two-electron transfer process at the negative potential side, where the underpotential deposition monolayer is completed.[64] The number of electron transfers at the underpotential deposition process should be examined with respect to the specific adsorption process of anions in the system, which is discussed in Section 4.

(b) Other underpotential depositions

Cyclic voltammograms of Pb on low-index single-crystal Au were observed in $HClO_4$.[3] Voltammograms of Pb underpotential deposition on various index Au faces were observed in 0.01*M* $HClO_4$ + ImM Pb^{2+} solution.[2] Since the voltammograms of Pb^{2+} underpotential deposition are

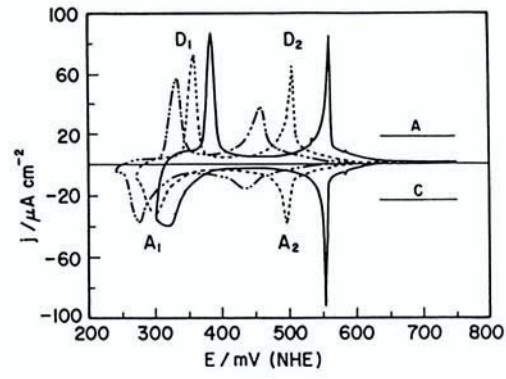

Figure 17. Cyclic voltammograms of Cu underpotential deposition on Au(111) in 90m*M* H_2SO_4 + *x*M $CuSO_4$; *x* = 50m*M*(— —), 5m*M* (- - - -), and 0.5m*M* (—···—). (From Ref. 64.)

quite sensitive to surface structure, the voltammograms may be treated as indicators of single-crystal faces. The Ag underpotential deposition on Au(111), of which the cyclic voltammogram is shown in Fig. 18, was studied by LEED at 0.51 and 0.7 V (Ag^+/Ag) to give $(\sqrt{3} \times \sqrt{3})$R30°. The $(\sqrt{3} \times \sqrt{3})$ R30° is believed to be due to sulfate adsorption with coverage of 0.3. Zn underpotential depositions on low-index Au single crystals were observed in phosphate and chloride solutions, where the electron transfer number was one from Zn^{2+} concentration dependence of underpotential deposition peaks,[34] as was the case for Cu underpotential deposition on Au(111). The underpotential deposition of Zn^{2+} was investigated on polycrystalline Au in alkaline solution.[65] The underpotential depositions of Hg^+, Tl^+, Bi^{3+}, and Cu^{2+} on polycrystalline Au have been recently studied.[66]

(ii) In Situ *STM and AFM*

Atomically resolved STM images of Cu^{2+} underpotential deposition on Au(100) and Au(111) in sulfuric acid solution were first observed by Magnussen *et al.* in 1990,[11] features of which are shown in Figs. 19, 20,

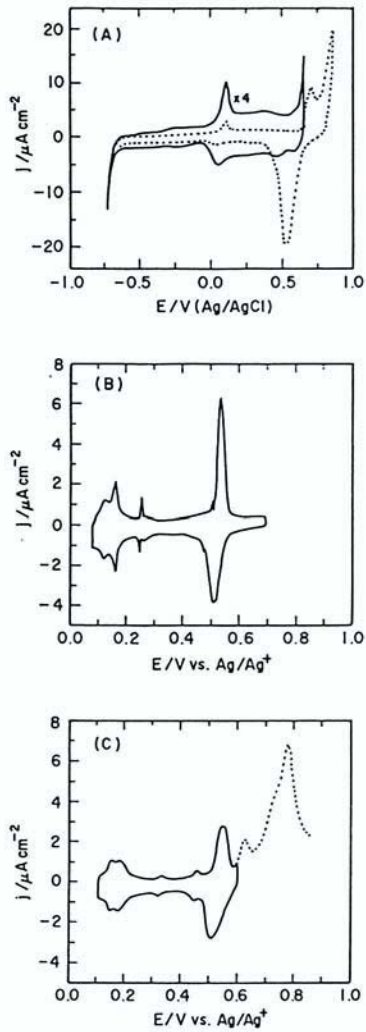

Figure 18. Cyclic voltammograms on Au(111) in sulfuric acid solution. (A) In 0.5m*M* H_2SO_4 at 10m*M* s^{-1}, (B) in 50m*M* H_2SO_4 + 0.1m*M* Ag^+ at 2m*M* s^{-1}, and (C) in 0.5m*M* H_2SO_4 + 0.1m*M* Ag^+ at 2 mV s^{-1}. The dotted curve of (C) represents a cyclic voltammogram in the gold oxidation region. (From Ref. 19.)

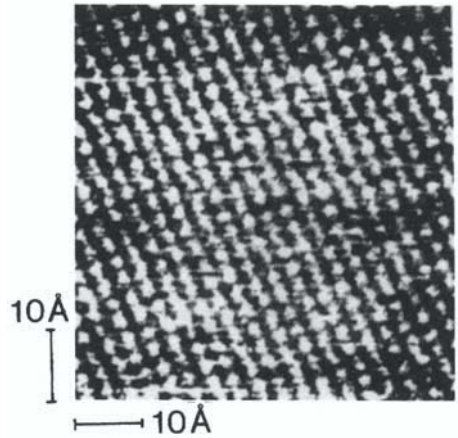

Figure 19. The STM image of Au(100) at 0.3 V(SCE) in 0.05*M* H_2SO_4 + 5m*M* $CuSO_4$. (From Ref. 11.)

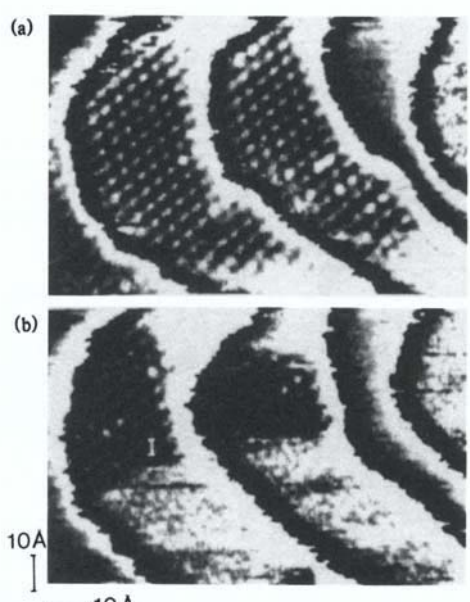

Figure 20. The STM image of Au(111) at (a) 0.215 V(SCE) and (b) 0.20 V(SCE) in 0.05*M* H_2SO_4 + 5m*M* $CuSO_4$. Structures of $(3\frac{1}{2} \times 3\frac{1}{2})R30°$ and (5×5) are found. (From Ref. 11.)

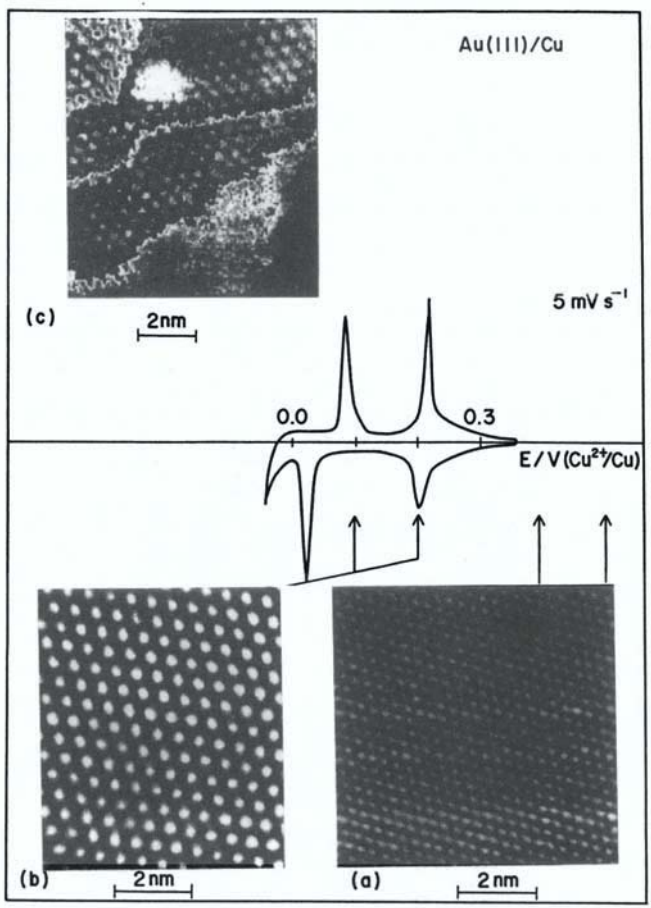

Figure 21. STM images of Au(111) in 0.05*M* H_2SO_4 + 1m*M* $CuSO_4$ at two different potential regions. (a) Bare Au(111), (b) and (c) Au(111) at potentials in the middle of two underpotential deposition peaks. (c) Monatomic steps of the substrate. (From Ref. 67 with the permission of the Royal Chemical Society.)

21, and 22. At potentials between two peaks of Cu underpotential deposition on both Au(100) and Au(111), shown in Figs. 19 and 20, respectively, the STM images were well resolved down to an atomic scale, and Fig. 20 was analyzed to give two phases of phases I and II of $(\sqrt{3} \times \sqrt{3})$ and (5×5), respectively. In Ref. 11, the STM images were considered to be derived from Cu atoms of underpotential deposition on Au single crystals. In 1992, atomically well-resolved STM images of $(\sqrt{3} \times \sqrt{3})$ R30° were observed at various potentials, as shown in Fig. 21.[67] Figure 22 shows STM images with their model for Cu underpotential deposition on

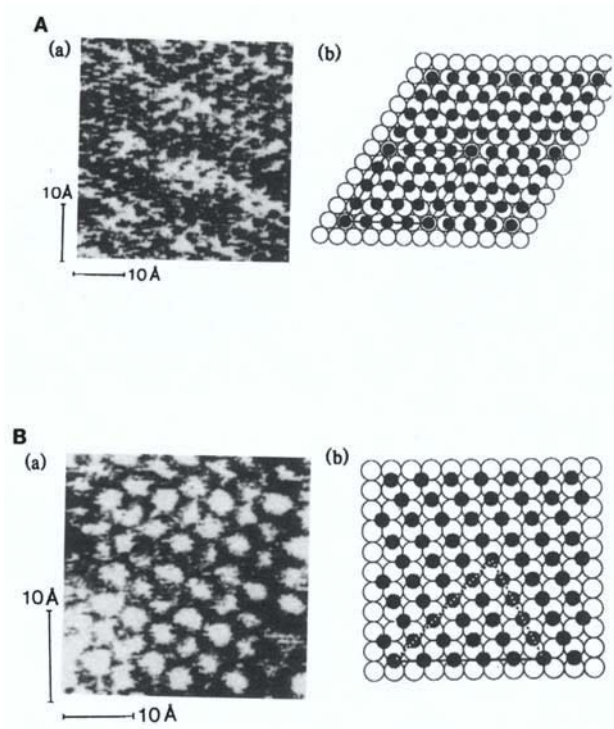

Figure 22. (A) (a) An STM image on Au(111) at 0.2 V(SCE) and (b) model of (a). (B) (a) An STM image on Au(100) at 0.2 V(SCE) and (b) model of (a). (From Ref. 11.)

Au(111) and Au(100). The AFM images of Cu underpotential deposition Cu on Au(111) $(\sqrt{3} \times \sqrt{3})$ and Au(111) (1×1) were observed at the same potential as the $(\sqrt{3} \times \sqrt{3})$ STM image of Ref. 11, and at a potential where Cu underpotential deposition does not take place, as shown in Fig. 23.[68] By adding Cl^- to sulfuric acid solution, an AFM image of (5×5) on Au(111) was obtained at potentials between two underpotential deposition peaks.[69] The AFM image of Cu underpotential deposition on Au(100) was observed to be identical to phase I of Ref. 11. Underpotential deposition of Ag on Au(111) was observed to give an AFM image of p(3×3)-4 at 0.42 V(Ag^+/Ag), as shown in Fig. 24. The amount of charge of the cyclic voltammogram gave 0.52 for Ag coverage, which nearly corresponds to coverage of 0.44 ~ 0.56 for (3×3) and (5×5), observed by LEED on rinsed samples.[19] An STM study of Ag^+ on Au(111) was carried out separately.[70] Later, the STM image at 0.7 V was observed to be

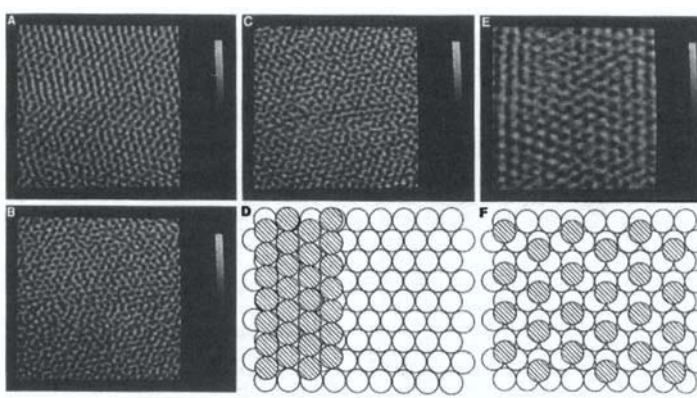

Figure 23. AFM images of Au(111) in 1m*M* Cu^{2+} + 0.1*M* perchloric acid or sulfuric acid solutions. (A) At 0.7 V(SCE), (B) overpotential deposition at –0.1 V, (C) Close-packed overlayer of Cu at 0.114 V in 0.1*M* perchloric acid solution with an atomic distance of 0.29 nm. (D) Scheme of close-packed overlayer of Cu on Au. (E) $(3\frac{1}{2} \times 3\frac{1}{2})$R30° overlayer of Cu on Au(111) at 0.144 V(SCE). (F) Scheme of $(3\frac{1}{2} \times 3\frac{1}{2})$R30° overlayer of Cu (striped circles) on Au (open circles). (From Ref. 68 with permission from the American Association for the Advancement of Science. Copyright 1991, American Association for the Advancement of Science.)

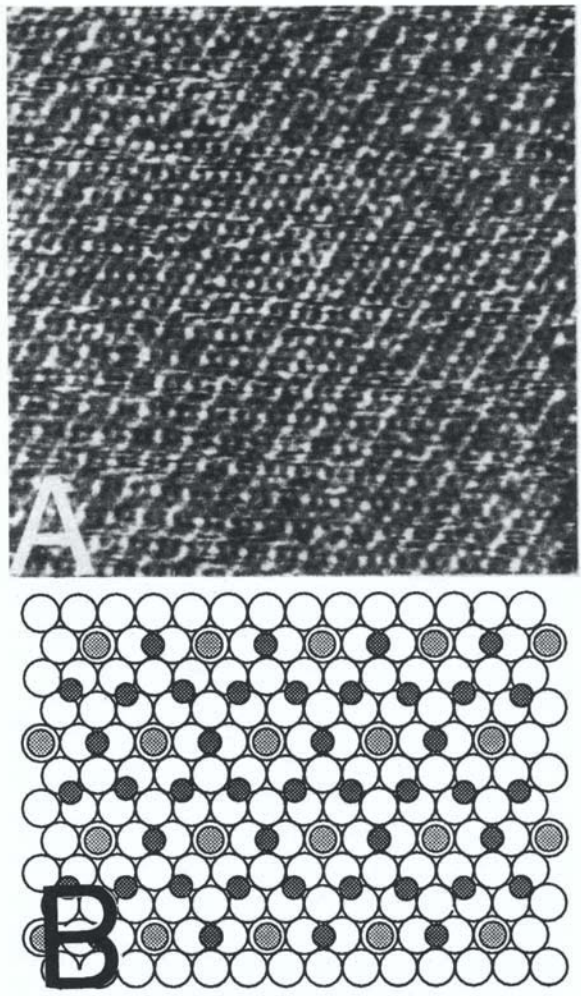

Figure 24. (A) AFM image of the $p(3 \times 3)$-4 Ag underpotential deposition on Au(111) at 0.42 V (Ag/Ag^+) and (B) scheme of the $p(3 \times 3)$-4 Ag. (From Ref. 19 with permission from *Electrochimica Acta.*)

$(\sqrt{3} \times \sqrt{3})$ in sulfuric acid solution, which was now assigned to the adsorbed sulfate species.[67]

In situ STM images were observed in the cases of Zn underpotential deposition on Au(111) with and without I^- in phosphate solutions.[71]

Underpotential deposition of Tl on Au(100) and Au(111) was investigated by X-ray scattering and STM in perchloric acid solution. Both measurements gave $c(p \times 2)$ monolayer structures before bulk deposition.[72]

(iii) In Situ *EXAFS, XANES, and XRD*

An *in situ* X-ray absorption spectroscopic study was carried out for Cu underpotential deposition at Au(111)[73] and Au(100).[74] The 0.3 monolayer of Cu underpotential deposition at Au(111) gave 0.359 nm for Cu-Cu. In the case of Cu underpotential deposition, the distance of Cu-O was observed as 0.197 nm, irrespective of the surface structure of Au(111) and (100).[75] Recently, EXAFS study clearly indicated an atomic arrangement between anion, underpotential deposition metal, and substrate, i.e., that anions are located over the underpotential deposition metal layer.[76] Ag underpotential deposition on Au(111) was studied by EXAFS, and has a (1×1) structure on Au(111).[77] The distance of Ag-O was not dependent on applied potentials, being 0.21 nm. These distances of Cu-O and Ag-O on Au(111) are in contrast to the distance of Pb-O on Ag(111), which changed with the electrode potential from 0.233 to 2.38 nm.[78] XRD observation showed that the distance between underpotential deposition on Au(111) changed with the applied potentials, but the distance between underpotential deposition Tl and Au on Au(111) remained constant against the potentials in the underpotential deposition region.[79] An X-ray scattering study of Tl^+ on Au(100) was also conducted, the results of which were in conformity with those from STM.[72]

Underpotential deposition of Zn^{2+} on Au(100) in 0.1*M* Na_2SO_4 was investigated by *in situ* XANES to obtain an indication of alloy formation.[80]

(iv) In Situ *FTIR*

An *in situ* FTIR study of bisulfate and sulfate adsorption indicated that the coverage of adsorbed sulfate increased in the presence of Cu underpotential deposition on polycrystalline Au.[81]

(v) Electrochemical Quartz Crystal Microbalance Method

The electrochemical quartz crystal microbalance (EQCM) method was first used to study underpotential deposition in 1988 for Pb, Bi, Cu, and Cd on polycrystalline Au.[82] In 1994, the underpotential deposition of Cu on Au(111)-like electrodes was clearly monitored by the EQCM technique, as shown in Fig. 25.[83,84] Figure 25a shows a reversible cyclic voltammogram current increase between 0.3 and 0.7 V, with a change in

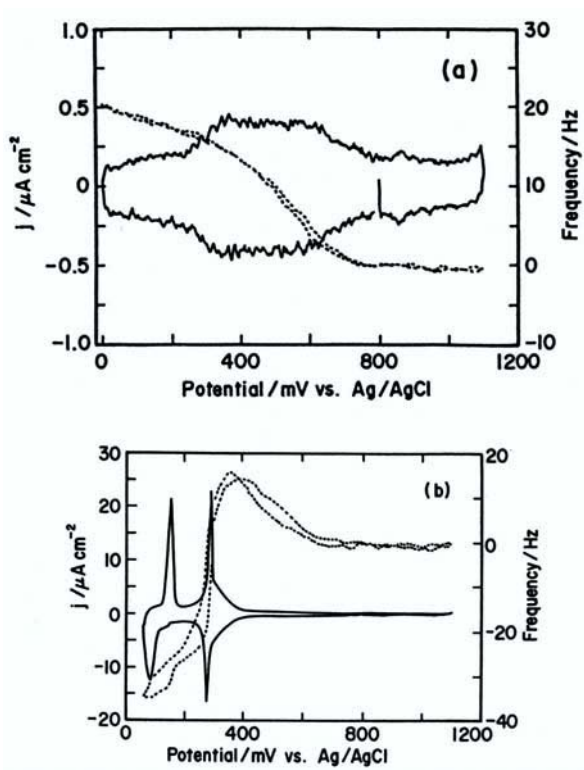

Figure 25. The cyclic voltammogram (solid curve) and frequency response (dotted curve) of a vapor-deposited QCM thin-film Au(111) electrode at (a) 10 mV s^{-1} in 0.1*M* H_2SO_4, and (b) in 2.5m*M* $CuSO_4$ + 0.1*M* H_2SO_4. (From Ref. 83.)

EQCM frequency of 20 Hz, which corresponds to a one-third monolayer of sulfate species adsorption/desorption. However, the electricity from the above cyclic voltammogram current is calculated to be about 1×10^{-5} C cm^{-2}, i.e., 6×10^{13} molecules cm^{-2}, which is about one-tenth of a monolayer. This may indicate that sulfate adsorption on Au(111) is associated with a partial charge transfer process. In Fig. 25b, an increase in EQCM frequency was observed as for (a), and a decrease in the frequency was observed at the Cu underpotential deposition region. The frequency change due to Cu underpotential deposition is determined to be 35 Hz, which is quite close to the 33 Hz of the Cu monolayer value. The total frequency change at the underpotential deposition region is 49 Hz, which shows that sulfate adsorption is associated with Cu underpotential deposition.

2. Underpotential Deposition on Single-Crystal Pt Group Metals

(i) Electrochemical and Ex Situ *Spectroscopic Measurements*

(a) Cu underpotential deposition

Cu underpotential deposition on single-crystal Pt(111) shows two peaks of a cylclic voltammorgram in 0.05*M* H_2SO_4 + 1m*M* $CuSO_4$, as shown in Fig. 26, where the underpotential deposition current peak of the cyclic voltammogram was negatively changed by 0.1 V with the addition of $10^{-4}M$ Cl^-. The two peaks at a positive sweep nearly converge with each other. This underpotential deposition is widely studied by a variety of methods, as described later. The underpotential deposition of Cu on Pt(311), the surface structure of which is equal to ≡ Pt[2(111) × (100)], was investigated and it was found that cyclic voltammogram peaks appeared at different potentials from those of Pt(111) and Pt(100) faces.[85]

Rotating ring-disk electrodes were employed for an anion effect on the Cu underpotential deposition on Pt(111) in fluoric and perchloric acid solutions, the results of which were discussed in comparison with UHV results of AES and LEED.[86–88]

An *ex situ* EXAFS study was conducted for Cu underpotential deposition on polycrystalline Pt in 0.2m*M* $CuSO_4$ + 0.5*M* H_2SO_4.[89] The iodine-treated Pt was subjected to Cu underpotential deposition, the features of which were observed by EXAFS.[90] An EXAFS study of Cu

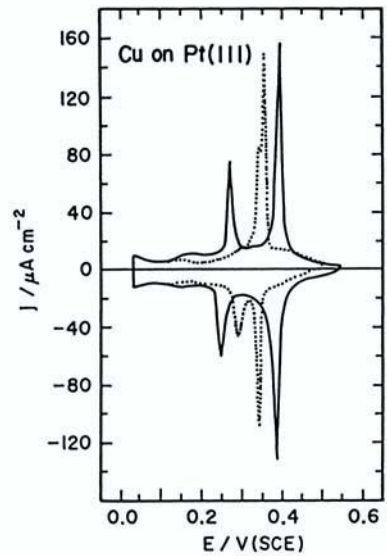

Figure 26. The cyclic voltammogram of Cu underpotential deposition at 10 mV s^{-1} on Pt(111) in 0.1*M* H_2SO_4 + 1m*M* $CuSO_4$ with (—) and without (.....) 10^{-4}*M* Cl^-. (From Ref 38.)

underpotential deposition on Pt(111) showed the distances of Cu-Cu and Cu-O as 0.27 and 0.21 nm, respectively.[91]

(b) Zn underpotential deposition

Underpotential deposition of Zn^{2+} on Pt was seen as adsorption of Zn^{2+} ions in 1970,[92] since ΔE^{UPD} is as high as 1 V, a value that well exceeds the one expected from previous results on various metal combinations of underpotential deposition systems.[1] Recently, Zn underpotential deposition on Pt was reported in acidic solutions,[93] and then in alkaline solutions.[94,95] Zn underpotential deposition on Pd was also found in acidic and alkaline solutions.[94,96] Then cyclic voltammograms of Zn^{2+} underpotential deposition on three low-index, single-crystal Pts were observed in sulfuric and perchloric acid solutions, as shown in Figs. 27 and 28.[41] In comparing Figs. 27 and 28, Zn underpotential deposition on Pt seems to take place only on Pt(110), but not on Pt(111) and Pt(100). Therefore it can be said that a cyclic voltammogram on polycrystalline Pt was observed on a Pt(110)-like surface.

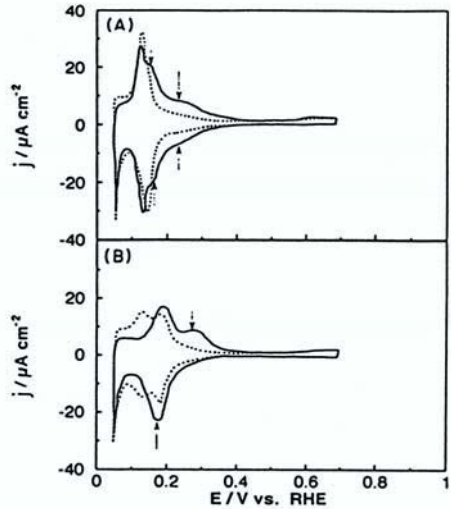

Figure 27. Cyclic voltammograms at 10 mV s^{-1} on Pt(110) in (A) 0.1*M* H_2SO_4 and (B) 0.1*M* $HClO_4$. The solid curves are obtained in the presence of 0.1m*M* Zn^{2+} and the dotted ones in the absence of Zn^{2+}. (From Ref. 41.)

A cyclic voltammogram of Zn underpotential deposition on Pt(110) in sulfuric acid solution is more reversible than that in perchloric acid solution with respect to the change of potentials, as shown in Fig. 27. The ΔE^{UPD} was evaluated as about 1 V. Since Zn underpotential deposition in acidic solutions was observed in the adsorbed hydrogen region, the pH was increased to separate Zn underpotential deposition from the hydrogen adsorption region. At pH 4.6, Zn underpotential deposition was observed, as shown in Fig. 29.[62] The different cyclic voltammogram appearances of Zn underpotential deposition on Pt(111) at different pHs is discussed in Section II.4.

(c) Other underpotential depositions

Ag underpotential deposition in 1*M* $HClO_4$ was observed by LEED, as shown in Fig. 30, where the Pt(111) surface, pretreated by iodine, forms Pt(111) $(\sqrt{7} \times \sqrt{7})$ R19.1°. The LEED patterns are quite dependent on

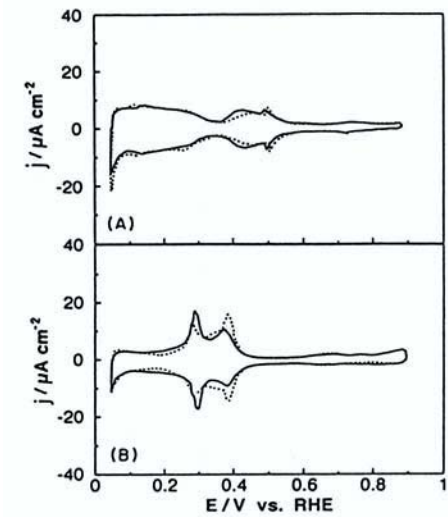

Figure 28. Cyclic voltammograms at (A) 10 mV s^{-1} on Pt(111) and (B) on Pt(100) in 0.1*M* H_2SO_4 with 0.1m*M* Zn^{2+} (solid curves) and without Zn^{2+} (dotted curves). (From Ref. 41.)

potentials and potential sweep direction.[97] Iodine pretreatment was mostly done to avoid contamination before measurement. Ag underpotential deposition on Pt(111) was subjected to electrochemical and UHV studies.[98] The irreversible underpotential depositions of Bi^{3+} and As^{3+} on Pt(111) in sulfuric acid solution were investigated by an *ex situ* adsorption method.[99–101] The irreversible underpotential deposition of Pb on Pt(111), Pt(100), and Pt(110) was studied in acidic and alkaline solutions, where Pb underpotential deposition in alkaline solution was quite substrate-structure sensitive in underpotential deposition potentials and cyclic voltammogram features.[102]

(ii) In Situ *STM*

An $(\sqrt{3} \times \sqrt{3})$ STM image at 0.68 V(RHE) on Pt(111) in the presence of Cu underpotential deposition was first observed in 1991,[103] as shown in Fig. 31, where the electrolyte was sulfuric acid and the applied potential

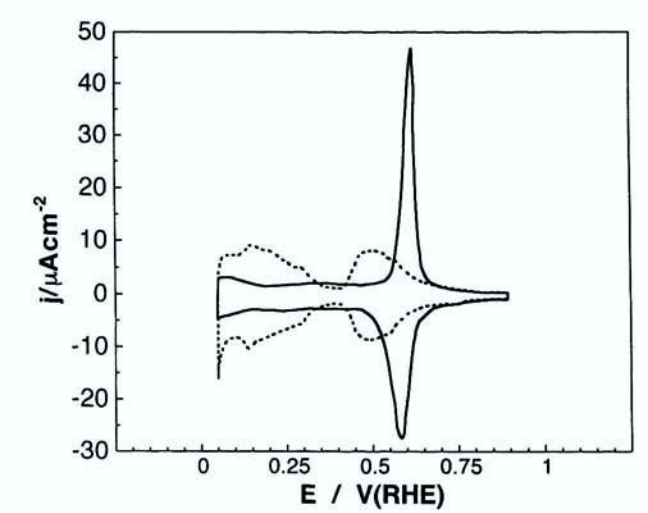

Figure 29. Cyclic voltammograms of Pt(111) in 0.1*M* KH_2PO_4 (pH 4.6) with 1m*M* Zn^{2+} (solid curve) and without Zn^{2+} (dotted curve). The sweep rate was 10 mV s^{-1}. (From Ref. 62.)

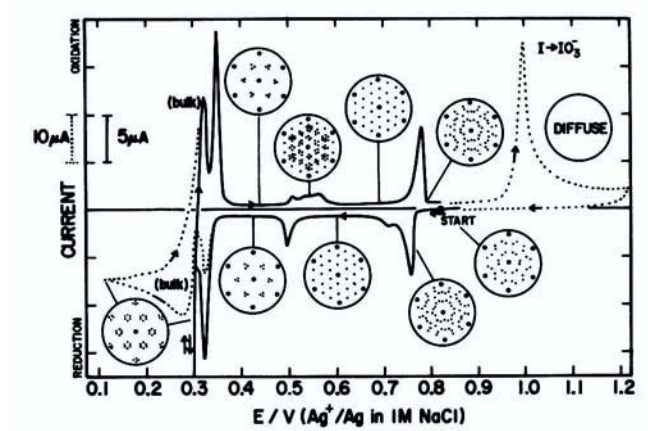

Figure 30. Cyclic voltammograms at 2 mV s^{-1} and LEED patterns. The solution was 10^{-4} *M* Ag^+ + 1*M* $HClO_4$ at I-covered Pt(111)($7^1/_2 \times 7^1/_2$)R19.1°-I surface. (From Ref. 97.)

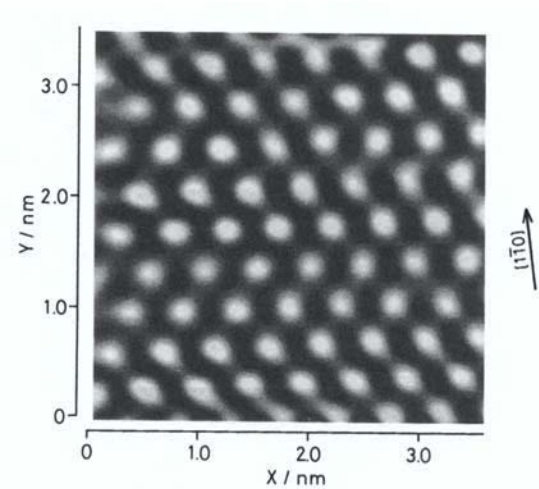

Figure 31. An STM image at 0.68 V(RHE) on Pt(111) in 0.05*M* H_2SO_4 + 5m*M* $CuSO_4$. (From Ref. 103 with permission from the *Journal of Electroanalytical Chemistry*.)

of 0.68 V was located at potentials between the two underpotential deposition peaks of Fig. 32. The charge density of the positive potential-side underpotential deposition peak was $270\ \mu C\ cm^{-2}$, which exceeds the coverage of one-third on the $(\sqrt{3} \times \sqrt{3})$ STM image; at present, the STM image is not attributed to Cu underpotential deposition but to the sulfate species adsorbed as in Cu underpotential deposition on Au(111), as stated in Section II. 1.

STM images of Ag underpotential deposition on Pt(111) were observed as (1×1) and $(\sqrt{3} \times \sqrt{3})$ structures at the potentials of Ag monolayer formation and between two underpotential deposition peaks, respectively.[104] The STM image at Pt(100) was examined for Cu underpotential deposition in the presence of halide ions in sulfuric acid solution by a (2×2) structure at 0.4 V(SHE).[105]

(iii) In Situ *EXAFS and XANES*

Cu underpotential deposition on Pt(100) in 0.1 m*M* Cu^{2+} + 1m*M* $HClO_4$ + 1*M* $NaClO_4$ was studied by *in situ* XANES and EXAFS.[106] The chemical state of copper was taken to be similar to the Cu^+ state. From

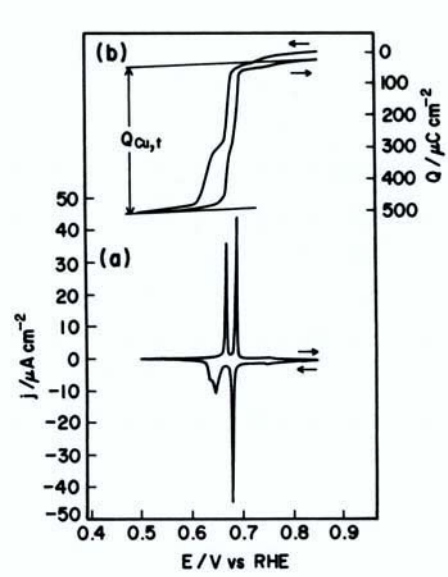

Figure 32. (a) Cyclic voltammogram and (b) Coulometric curve at 1 mV s^{-1} on Pt(111) in 0.05*M* H_2SO_4 + 5m*M* $CuSO_4$. (From Ref. 103.)

EXAFS results, Cu atoms locate on the top of Pt atoms. Experimental and theoretical EXAFS studies were carried out for Cu underpotential deposition on Pt(111) in a 0.1*M* H_2SO_4 + 50μM Cu^{2+} solution, giving the position of copper underpotential deposition at three hollow sites of Pt(111), which is partially positively charged.[91,107,108]

(iv) In Situ *FTIR*

In situ FTIR for Cu underpotential deposition on Pt(111) and Rh(111) was observed in sulfuric and perchloric acid solutions.[42] Both adsorbed sulfate and perchlorate species were found on underpotential deposition Cu. The underpotential deposition of T1 on Pt(111) was observed by FTIR in view of the coadsorption of perchlorate and bisulfate.[109] The IR bands of the adsorbed anions were found to be due to the presence of underpotential deposition metals on Pt(111), and the possibility of the presence of an ion pair of the underpotential deposition metal and an anion is discussed.

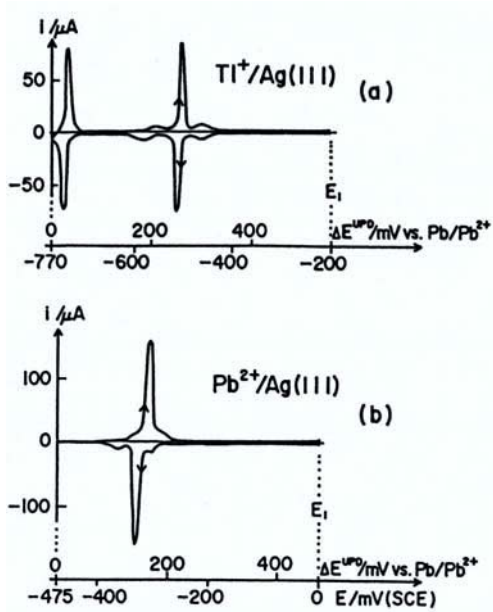

Figure 33. Cyclic voltammogram of (a) Tl and (b) Pb on Ag(111) in 0.5*M* $NaClO_4$ at 10 mV s^{-1}. $[Tl^+]$ = 1.5m*M*; $[Pb^{2+}]$ = 1.43m*M*. (From Ref. 111.)

3. Underpotential Deposition on Ag Single Crystals

Pb underpotential depositions on Ag(111), Ag(100), and Ag(110) were observed by cyclic voltammogram in a 0. 1*M* $HClO_4$+1 m*M* Pb^{2+} solution. The surface structure of the underpotential deposition is suggested from total charge densities of underpotential deposition.[3] Atomically resolved STM images of Pb underpotential deposition on Ag(111) and Ag(100) were observed in 5m*M* $Pb(ClO_4)_2$ + 10m*M* $HClO_4$. The image patterns varied with the potentials[110] applied. Voltammograms of Ti and Pb underpotential depositions on a chemically polished Ag(111) are given in Fig. 33,[111] where the shift in underpotential deposition potential ΔE^{UPD*} of Eq.

*In this section, ΔE^{UPD} is not the underpotential deposition peak potential, but that defined in Eq.(5).

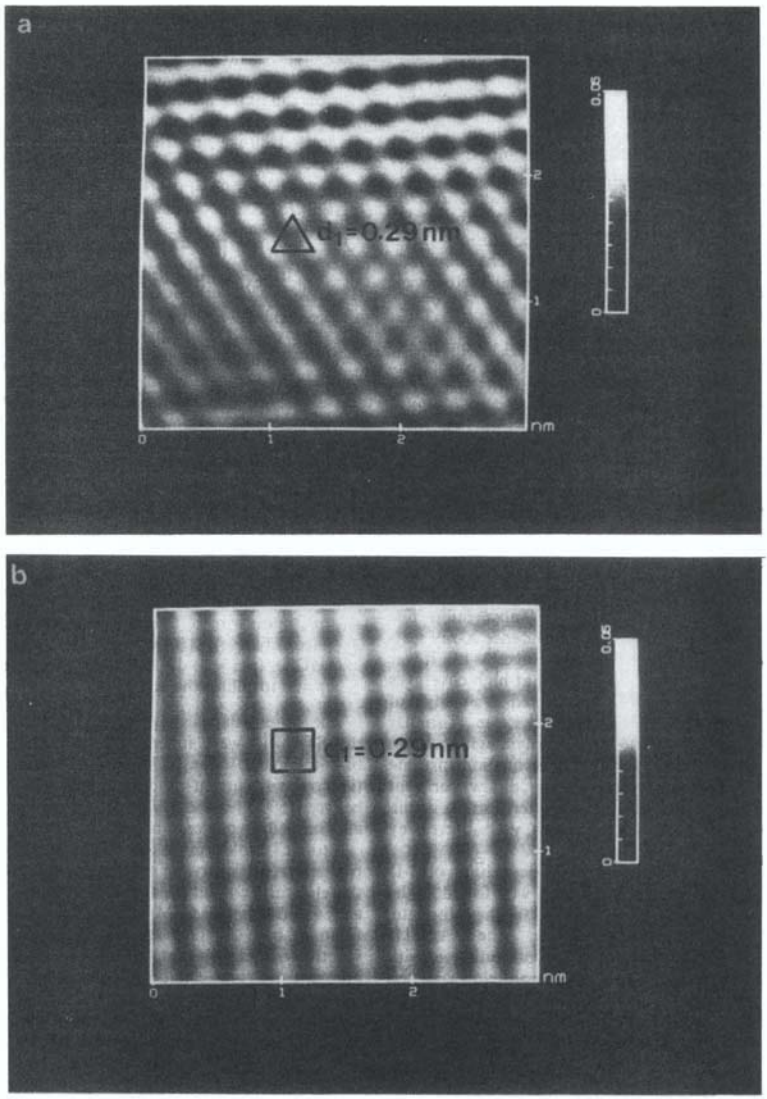

Figure 34. STM image of Pb underpotential deposition on (a) Ag(111) in 0.01*M* $HClO_4$ + 10m*M* Pb^{2+} at ΔE = 0.24 V and (b) on Ag(100). (From Ref. 112 with permission of *Electrochimica Acta*.)

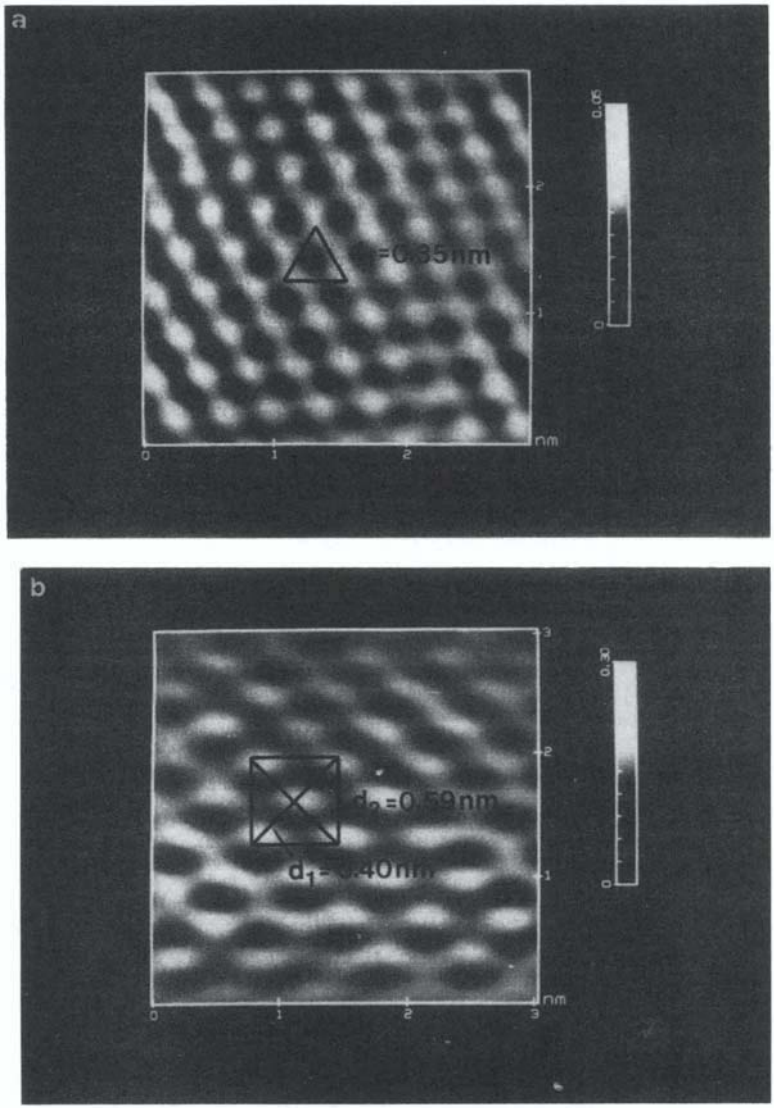

Figure 35. STM images of underpotential deposition Pb on (a) Ag(111) and (b) Ag(100) in 0.01*M* $HClO_4$ + 5m*M* Pb^{2+} taken at ΔE = 0.04 V. (From Ref. 112 with permission from *Electrochimica Acta*.)

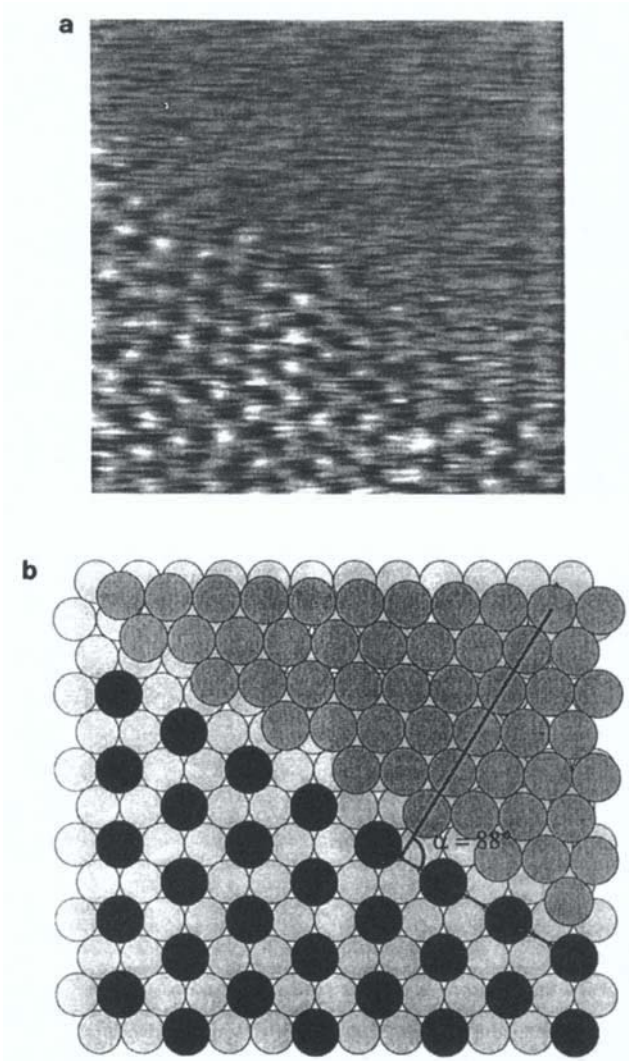

Figure 36. An STM image of underpotential deposition Tl on Ag(111) in 0.01*M* $HClO_4$ + 5m*M* Tl^+ taken at ΔE = 0.359 V. The image size is 6.33 × 6.33 nm and the details are in the text. (From Ref. 113 with permission of *Electrochimica Acta*.)

(5) is presented with respect to the SCE for the ordinate potential scale. STM images of Ag(111) and Ag(100) were observed with atomic-scale resolution of an interatomic distance of $d_1 = 0.29$ nm between nearest neighbors and are shown in Fig. 34 for $\Delta E^{UPD} = 0.24$ V, which is not in the underpotential deposition region.[112] The d_1 value shows the STM image of an unreconstructed Ag substrate in the case of Ag(111). The STM images at $\Delta E^{UPD} = 0.04$ V in Fig. 35 are thought to be due to the monolayer of Pb underpotential deposition in comparison with the potential of Fig. 33. Tl underpotential deposition on Ag(111) seems to be composed of two monolayer structures where the STM images of Tl and Pb underpotential depositions on Ag(111) were observed, as shown in Figs. 36 and 37.[113]

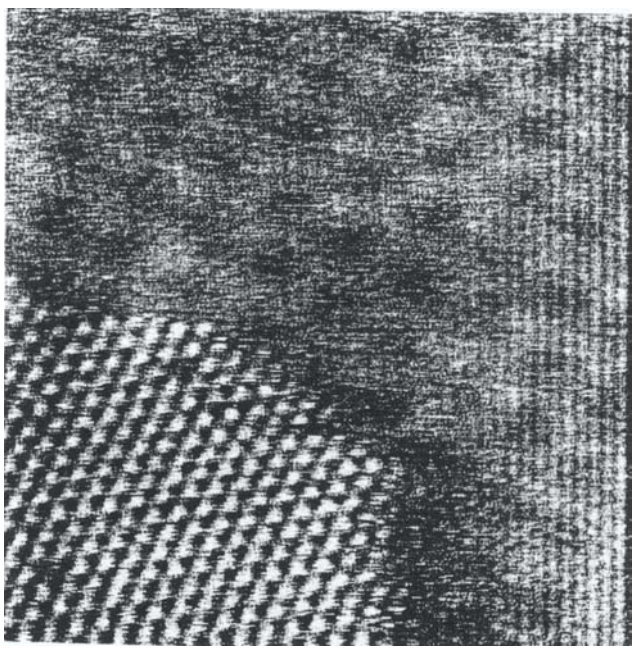

Figure 37. An STM image of Pb underpotential deposition on Ag(111) in 0.01*M* $HClO_4$ + 5m*M* Pb^{2+} taken at $\Delta E = 0.125$ V. The image size is 12.0 × 12.0 nm and the details are in the text. (From Ref. 113 with permission from *Electrochimica Acta*.)

Figure 36a shows an STM image of Tl underpotential deposition on Ag(111) taken at $\Delta E^{UPD} = 0.359$ V during adsorption of the first monolayer peaks of A_1 and A_2 of Fig. 33, and subsequent polarization at potential between the peaks of A_2 and A_3 during 708 s; (b) is the same as scheme a, where black circles represent Tl atoms of the rearranged coverage and dark gray ones are for an initial *hcp* adsorbate layer.[113] Pb underpotential deposition on Ag(111) gave the STM image in Fig. 37, taken at $\Delta E^{UPD} = 0.125$ V after adsorption of an incomplete monolayer at peaks A_1 and A_2 of Fig. 33, and subsequent polarization at a potential between A_2 and A_3 during 600 s. These show that various surface states of underpotential and overpotential deposition can be expected for different pretreatments of the surface.

Underpotential deposition of Zn ions on polycrystalline Ag was investigated in 1*M* KOH to form two kinds of alloys.[114]

4. Underpotential Deposition and Anion Adsorption

(i) Apparent Electron Transfer Number

As found in preceding sections, the underpotential deposition process is strongly influenced by anion adsorption, or controlled sometimes by the presence of the adsorbed anions. Anion-specific adsorption/desorption seems to take place as an electron transfer process[24] and may be accompanied by the underpotential deposition formation/removal process.[62]

Let us consider the case that underpotential deposition takes place at potentials where specifically adsorbed anions depart from the surface, or the removal of underpotential deposition species induces specific adsorption of anions. Then the underpotential deposition process is taken to consist of three consecutive steps: (1) desorption of specifically adsorbed anions from substrate M, (2) adsorption and electron transfer of metal ions M^{n+} to form an underpotential deposition metal layer on the substrate metal M', and (3) readsorption of the anions on the underpotential deposition metal M on M', i.e.,

$$A_{ads}^{\xi-m}/M' + \xi e \xrightarrow{M'} A^{m-} \qquad (6)$$

$$M^{n+} + \gamma e \overset{M'}{\rightarrow} M^{n-\gamma}_{UPD}/M' \tag{7}$$

$$A^{m-} \overset{M_{UPD}}{\rightarrow} A^{\zeta-m}_{ads}/M^{n-\gamma}_{UPD} + \zeta e \tag{8}$$

where A^{m-} is an anion with m as a negative charge in solution, $A^{\xi-m}_{ads}/M'$ is an adsorbed anion on substrate M', which forms by the oxidation of A^{m-} with ξ electrons as the electron transfer number by the reverse step of Eq. (6), M^{n+} is a metal ion in solution, $M^{n-\gamma}_{UPD}/M'$ is the underpotential deposition metal with γ electrons as the electron transfer number on M', which may be different from n, and $A^{\zeta-m}_{ads}/M'$ is an adsorbed anion with ζ electrons as the electron transfer number on M'.

As an overall reaction,

$$A^{\xi-m}_{ads}/M' + M^{n+} + (\gamma + \xi - \zeta)e \overset{M_{UPD}}{\rightarrow} M^{n-\gamma}_{UPD}/M' + A^{\zeta-m}_{ads}/M^{n-\gamma}_{UPD} \tag{9}$$

is a reaction that occurs in the underpotential deposition process, where the above anion redox steps of Eqs. (6) and (8) may partially occur with respect to $M^{n-\gamma}_{UPD}/M'$ or to M'.

When Eq. (9) is at pseudoequilibrium, the pseudo-Nernst equation

$$E^{UPD} = E^0 + \frac{RT}{(\gamma + \xi - \zeta)F} \ln \frac{a^{M^{n+}} \cdot a^{A^{\xi-m}_{ads}/M'}}{a^{M^{n-\gamma}_{UPD}/M'} \cdot a^{A^{\zeta-m}_{ads}/M^{n-\gamma}_{UPD}}} \tag{10}$$

is obtained, where the E^{UPD} is the underpotential deposition potential for Eq. (9), in which the effect of electron transfer of anion-specific adsorption is taken into account, and a^xs are activities of *xs*. The E^{UPD} in Eq. (4) should be replaced by Eq. (10) when the reaction proceeds by Eq. (9). In Eq. (10), the activities of the adsorbed species can be expressed by coverages of θ_M, $\theta_{A/M}$, and $\theta_{A/UPD}$ for underpotential deposition M, the adsorbed anion on substrate M', $A^{\xi-m}_{ads}$, and the adsorbed anion on underpotential deposition M, $A^{\zeta-m}_{ads}/M^{n-\gamma}_{UPD}$, respectively. By differentiation of E^{UPD} with $\log a^{M^{n+}}$ at constant θ_M, and $\theta_{A/M}$, and $\theta_{A/UPD}$,

$$\left(\frac{\partial E^{UPD}}{\partial \log a^{M^{n+}}}\right)_{\theta_M, \theta_{A/M'}, \theta_{A/UPD}} = \frac{0.059}{(\gamma + \xi - \zeta)}\ V \tag{11}$$

at 298 K. In the case that the activity of M^{m+} ions can be replaced by their concentrations, Eq. (11) becomes

$$\left(\frac{\partial E^{\mathrm{UPD}}}{\partial \log C^{\mathrm{M}^{m+}}}\right)_{\theta_{\mathrm{M}},\theta_{\mathrm{A/M}},\theta_{\mathrm{A/UPD}}} = \frac{0.059}{(\gamma+\xi-\zeta)}\ V, \tag{12}$$

The differentiation of E for the electron transfer reaction of Eq. (6) can be written in the same manner as Eq. (12) as

$$\left(\frac{\partial E}{\partial \log C^{\mathrm{A}^{m+}}}\right)_{\theta_{\mathrm{A/M}}} = -\frac{0.059}{\xi}\ V \tag{13}$$

which was first derived by **Adžić** *et al.*[115]

(ii) Anion Adsorption Effect on Underpotential Deposition on Au

The effect of trace amounts of Cl^- on Cu underpotential deposition was studied on Au(111) in $HClO_4$ solution by STM and cyclic voltammogram.[116] Figure 38 shows that the cyclic voltammogram was tremendously changed by the addition of $10^{-4}M$ Cl^- at maximum. Sweep rate dependencies also demonstrate that Cu underpotential deposition on Au(111) in $HClO_4$ is a slow process. The coadsorption of Cu^{2+} underpotential depo-

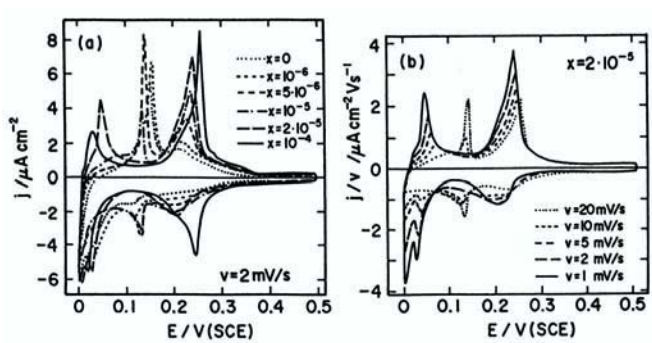

Figure 38. Cyclic voltammograms for Cu underpotential deposition on Au(111) in $0.1M$ $HClO_4$ + $0.01M$ Cu^{2+} + xM HCl. (a) Dependence on Cl^- at a sweep rate of 2 mV s^{-1} and (b) dependence of sweep rates in the presence of $2 \times 10^{-4}M$ Cl^-. (From Ref. 116.)

sition and SO_4^{2-} (or HSO_4^{2-}) on Au(111) was investigated by changing the concentration of sulfate ions in perchlorate solution by thermodynamic treatment.[117] For full coverage of Cu underpotential deposition, the amount of charge was observed to be $360\ \mu C\ cm^{-2}$, which corresponds to 0.75 coverage with a unit atomic ratio of Cu to Au. However, the Gibbs excess of underpotential deposition Cu was 1.37×10^{15} atoms cm^{-2}, which is nearly identical to 1.39×10^{15} Au atoms at Au(111). The STM image of $(\sqrt{3} \times \sqrt{3})$ is thought to be due to the adsorbed sulfate species. The Br^- effect on Cu underpotential deposition on Au(111), which gives quite sharp reversible underpotential deposition peaks in perchlorate solution, was also investigated in terms of the Gibbs excess.[118] The anion effect on Cu underpotential deposition at Au(111) was discussed by evaluation of electrosorption valences of 0.8, 1, and 1 for SO_4^{2-}, Br^-, and Cl^- from the Gibbs excesses of Cu underpotential deposition and anions.[119] The number of electrons transferred at Cu^{2+} underpotential deposition was also estimated as 1.4 ~ 1.8.

For the Cu underpotential deposition peak at the positive potential-side on Au(111) in sulfuric acid solution, the slope of peak potentials with respect to the logarithm of Cu^{2+} concentration was 60 mV,[64] which indicates a one-electron transfer process for Cu underpotential deposition. EQCM measurement[83] shows a weight loss of one-third coverage of sulfate species before Cu underpotential deposition occurs, where the associated charge corresponds to its one-tenth coverage, provided that sulfate species adsorption takes place by one electron transfer process. This discrepancy may be interpreted as the sulfate species on Au(111) adsorbing by a partial charge transfer process. The adsorption of the sulfate on Cu underpotential deposition on Au(111) is expected as specific adsorption by one-electron transfer oxidation, as for the case of Cu underpotential deposition on Pt. Then, ξ of Eq. (11) is nearly zero, and γ is 2 with $\zeta = 1$. These values are put into Eq. (11), giving 60 mV as observed in Ref. 64. For the case of Zn underpotential deposition on Au single crystals, the same argument as for Cu underpotential deposition can be made since the slope of Eq. (11) was 60 mV.[34] Most of underpotential deposition is affected by specifically adsorbed anions in the solution. However, a study in fluoride solution shows that Ag underpotential deposition on Au(111) was found to receive little effect from anion-specific adsorption.[120]

(iii) Anion Adsorption Effect on Underpotential Deposition on Pt

In Eq. (13),[115] ξ was given as 1 for the case of sulfate adsorption on Pt(111). By applying such an argument to the case of Zn underpotential deposition on Pt(111), with the assumption of $\xi = \zeta$ (that the number of electron transfers of anion adsorption on M′ and on M/M′ is identical), γ = about 2.5 from the slope of 25 mV decade^{-1}. As $n = 2$ for Zn^{2+}, γ is found to be nearly identical with n. Since the condition of $\gamma > 2$ is not plausible, the number of electron transfers will be identical to n; $\gamma = n$.[62]

As shown above, the effect of anions on a cyclic voltammogram was characteristic of individual anions. With respect to an anion that is present at the electrode interface, we discussed the behavior of Zn underpotential deposition in different anion solutions, as shown in Fig. 39,[121] in which sulfate solutions (a) and perchlorate solutions (b) do not give sharp underpotential deposition peaks in comparison with phosphate solutions (c), in which quite sharp and high peaks appeared when pH > 3. In close comparison with Fig. 15, we find the potential positions of Zn underpotential deposition and phosphate desorption to nearly coincide in the case of phosphate, but not in cases of sulfate and perchlorate. In the latter two cases, the interface does not accommodate a large enough amount of specifically adsorbed anions in the Zn underpotential deposition region. Therefore, the underpotential deposition process is closely associated with the anion desorption/adsorption process.

When underpotential deposition occurs in the presence of a strongly adsorbable anion, the underpotential deposition process is accompanied by anion desorption. Recently, Horányi and Aramata[122] observed adsorption of sulfate species on polycrystalline Pt by a radioactive S tracer method and found that the amount of the adsorbed sulfate on underpotential deposition Zn is lower than that on Pt at a positive potential range, and that sulfate adsorption is stronger than chloride adsorption on Zn underpotential deposition although chloride adsorbs on Pt at a positive potential range as generally accepted order of adsorption strength of anion specific adsorption. The former findings support underpotential deposition of Zn at specific sites such as Pt(110) as found in Ref. 41. In this reference, the different interaction energies of anion-specific adsorption on underpotential deposition metal and bare substrate metal were first suggested in a study of underpotential deposition. It seems to be anion desorption-

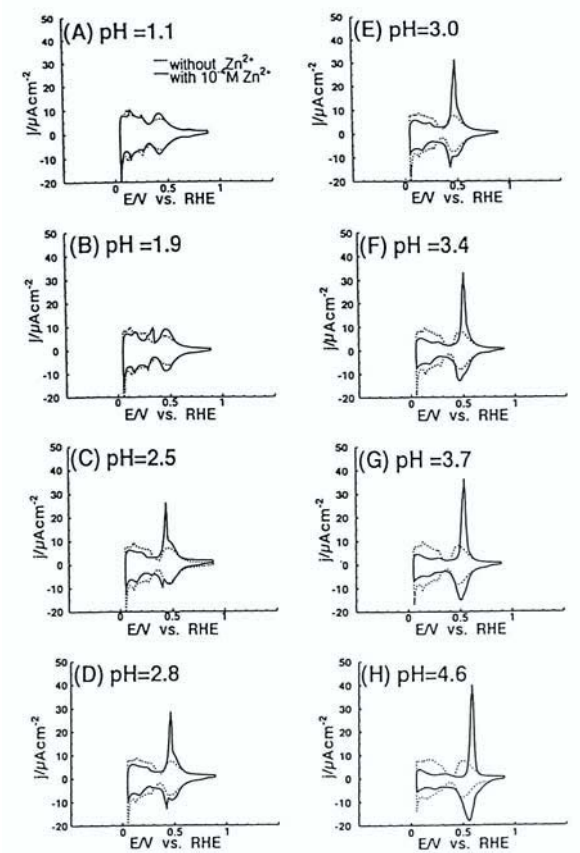

Figure 39. Cyclic voltammogram at 10 mV^{-1} on Pt(111) in a constant anion concentration with 0.1m*M* Zn^{2+} and a change in pH (a) in 0.1*M* phosphate solution. (From Ref. 121.)

assisted underpotential deposition, as if the footprint of the adsorbed anion assists underpotential deposition with two-dimensional nucleation, where the adsorbed anion has formed a two-dimensional phase, as discussed in Section I.

The underpotential deposition cyclic voltammogram peaks of Cu in the presence of Cl^-, Br^-, I^-, and S^{2-} were investigated, and the negative

shift of the peak potentials was observed to be due to the reaction of $CuCl + e \rightarrow Cu + Cl^-$, for the case of Cl^- as an example.[123] The adsorption of Cl^- and Br^- was also observed to be induced by Cu underpotential deposition on Pt(111); adsorbed anions were believed to be in contact with the Pt surface.[124] The effects of Cl^- and Br^- were observed on Pt(311) in sulfuric acid solution, giving complicated cyclic voltammogram features.[85] The effects of Cl^-, thiourea, acetonitrile, and polyethylene glycol on Cu underpotential deposition were investigated by EQCM and visible reflectance spectroscopy.[125] The effect of Cl^- on Cu underpotential deposition at Pt was studied by AES, LEED, RRDE, and X-ray scattering methods. Cu underpotential deposition was found to form by a two-step process: the formation of a Cu-Cl layer and a pseudomorphic Cu monolayer with a Cl adlayer.[88] Different shifts in Cu underpotential deposition potential on Pt(111) and Pt(l00) with the addition of Cl^- are thought to be due to the difference in energies between Cu and Cl^-.[126]

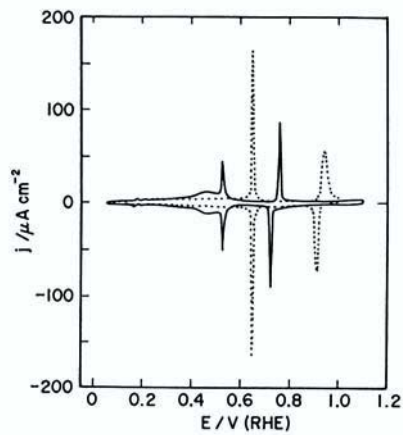

Figure 40. Underpotential deposition of Tl on Pt(111) in 1m*M* Tl^+ + 0.1*M* $HClO_4$ at 20 mV s^{-1}. Solid curve, 10m*M* H_2SO_4; dashed curve, without H_2SO_4. (From Ref. 126.)

Ex situ LEED and XPS studies were conducted to demonstrate the effects of Cl^- and Br^-; these anions form densely packed incommensurate structures on Cu underpotential deposition at the full monolayer.[127]

Ag underpotential deposition on Pt(111)$(\sqrt{7} \times \sqrt{7})$R19.1°-I was observed by STM in $HClO_4$.[128]

Underpotential deposition of Tl on Pt(111) was found to be quite sensitive to anions in perchloric acid solution, as shown in Fig. 40, where the addition of 10m$M$$H_2SO_4$ changed the underpotential deposition peak potential negatively over 100 mV.[129] The effect of Cl^-, Br^-, I^-, and phosphate ions was also shown.[129] The effect of specific adsorption of sulfate ions on Cd^{2+} underpotential deposition was studied in perchloric acid solution by voltammetric and radiochemical methods. In both methods, a part of the deposited Cd is taken to be in an oxidized form at positive potentials, being transformed to an atomic form by the negative-moving potential sweep.[130]

III. MECHANISM OF UNDERPOTENTIAL DEPOSITION

1. Kinetics and Dynamics

(i) *Kinetic Formula for Underpotential Deposition Process*

When underpotential deposition adsorption/desorption takes place randomly at any substrate site M′, the following random adsorption-controlling treatment is to be employed, and when the process is controlled by a two-dimensional nucleation-growth mechanism, the process analysis should be carried out according to Section III.1.(b).

(a) Langmuir or Temkin (Frumkin) random adsorption controlling processes

In the process of underpotential deposition of a metal ion M^{n+} in solution as

$$M^{n+} + ne \xrightarrow{M'} M/M' \tag{14}$$

we assume that the reaction of Eq. (14) is a rate-determining step in the underpotential deposition process. When the underpotentially deposited

M occupies the site on $\mathbf{M}'$ by the coverage $\theta_{\mathbf{M}}$ of Eq. (12), which is abbreviated as θ, the current of Eq. (14), j, is given as[131]

$$j = -nF\left[k_f C^{\mathbf{M}^{n+}}(1-\theta)\exp\left\{\frac{-\beta r\theta}{RT}\right\}\exp\left\{-\frac{\alpha nF(E-E_1)}{RT}\right\} - k_b\theta\exp\left\{\frac{(1-\beta)r\theta}{RT}\right\}\exp\left\{\frac{(1-\alpha)nF(E-E_1)}{RT}\right\}\right] \quad (15)$$

where the current density j is taken as a negative value for underpotential deposition formation, k_f and k_b are forward, and backward rate constants, respectively, $C^{\mathbf{M}^{n+}}$ is the concentration of $\mathbf{M}^{n+}$, $\alpha(0 < \alpha < 1)$is the electron transfer coefficient, E and E_1 are applied potential and the potential where the underpotential deposition process begins, respectively, β is the constant of $0 < \beta < 1$, and r is a lateral interaction parameter between underpotential deposition metals M on $\mathbf{M}'$. The interaction parameter between underpotential deposition metal M on $\mathbf{M}'$, r, is assumed to be given as

$$\Delta H = \Delta H_0 - r \times \theta \quad (16)$$

where ΔH and ΔH_0 are heats of adsorption when $\theta = \theta$ and 0, respectively, and the constant ΔH_0 term is included in k_f or k_b of Eq. (15). In Eq. (16), the interaction is absent when r=0; such a process is called the Langmuir-type adsorption process. When r is constant with $r \neq 0$, the adsorption process is known as the Temkin-(or Frumkin-) type adsorption.* When $r > 0$, the interaction between Ms on $\mathbf{M}'$ is repulsive and when $r < 0$, it is attractive.

When the reaction of Eq. (14) is in a reversible condition, the first and second terms of the right-hand side of Eq. 15 are equated, and

$$E = \frac{RT}{nF}\ln\frac{\theta}{1-\theta} + \frac{r\theta}{nF} + K_0' \quad (17)$$

is given, where K_0' is constant. When the change of coverage θ occurs, the current j to be observed is

*This approximation is also called a linear approximation since r is taken to be constant in Eq.(16).

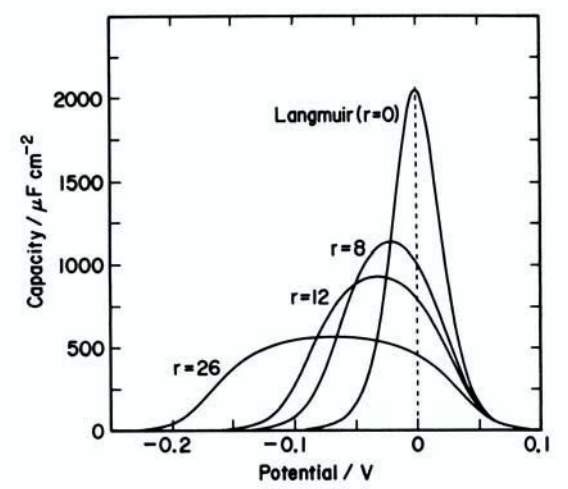

Figure 41. Calculated current-potential curves for various interaction parameters of r for $r > 0$ and $n = 1$.

$$j = -nF\frac{d\theta}{dt} = -nF\frac{d\theta}{dE}\frac{dE}{dt} = -nF\nu\frac{d\theta}{dE} \tag{18}$$

and becomes with Eq. (17)

$$j = -(nF)^2\nu\frac{\theta(1-\theta)}{RT + r\theta(1-\theta)} \tag{19}$$

where $\nu \equiv dE/dt$. From Eqs. (17) and (19), the capacity r is given as a function of electrode potential E, which is given in Fig. 41, where the potential width of half of the current peak, $\Delta W_{1/2}$, is given as

$$\Delta W_{1/2} = \frac{2rS}{nF} + \frac{2RT}{nF}\ln\frac{1/2 + S}{1/2 - S} \tag{20}$$

where

$$S \equiv \left(\frac{1}{4} - \frac{1}{8 + r/RT}\right)^{1/2} \tag{21}$$

The peak current j_p at peak potential E_p, i.e., at $\theta = 0.5$, is given by

$$j_p = -(nF)^2\nu \frac{0.25}{RT + 0.25r} \tag{22}$$

Here, from $\Delta W_{1/2}$, the interaction parameter r can be estimated. When $r = 0$, i.e., the adsorption is expressed by the Langmuir-type adsorption, and $\Delta W_{1/2} \simeq 90/n$ mV at 25°C.

When the potential sweep rate is fast, and the above equilibrium condition is not valid, the current-potential profiles depend on kinetic parameters and sweep rates, which are discussed in Ref. 132.

When the potential step method is employed to elucidate the mechanism of the underpotential deposition process, the current j against time t is readily found to be in the form of

$$j = -nFk_1 \exp(-k_2 t) \tag{23}$$

for the case of the Langmuir adsorption mechanism, i.e., $r = 0$, where ks are constants and $k_2(>0)$ is a function of potential. When $r \neq 0$, a simple mathematical expression was not deduced, and an empirical Elovich equation can interpret the j vs. t relation as a zeroth approximation, as discussed in Ref. 133. The treatment of the case of attractive interaction between adsorbates, i.e., $r < 0$, can be applicable in the sense of a mathematical expression, but its physicochemical explanation will be rather difficult, and the two-dimensional nucleation-growth treatment will replace its position.

(b) Nucleation growth controlling processes

In the treatment by Langmuir and Temkin of adsorption kinetics, a current curve against time is in a monotonic decrease at a given potential as given by Eq. (23) for the former adsorption. However, the curve showed a plateaulike feature in the case of Pb underpotential deposition on an Ag single crystal.[134] The two-dimensional adsorption of underpotential deposition was suggested to induce a two-dimensional phase formation on the substrate metal. The underpotential deposition of Pb on an Ag single crystal was observed to give quite sharp cyclic voltammogram peaks[134–136] and interpreted by phase transformation of nucleus formation with subsequent nucleus growth, which specific adsorption of anions was also reported to strongly influence underpotential deposition potential and the underpo-

tential deposition peaks. The nucleation growth process was examined for two experimentally different conditions: Refs. 137–139 used the potential-step method, and Refs. 139–141 used the potential-sweep method.

A kinetic study of Cu^{2+} underpotential deposition was carried out to determine if it is best described by adsorption processes or by nucleation processes.[142] The nucleation growth process is classified into two categories: instantaneous nucleation growth and progressive nucleation growth.[137–141] In the case of instantaneous nucleation growth, where nucleation site formation is so fast that no other following nucleation sites are created, the number of nucleation sites $N(t)$ is expressed as

$$N(t) = N_0 \tag{24}$$

where N_0 is the number of sites active for nucleation at time $t = 0$. In the case of progressive nucleation growth, where nucleation site formation is slow, the following approximation is employed as

$$N(t) = aN_0t \tag{25}$$

where a is assumed to be a constant. The growth rate r of a single nucleation center is given in the assumption of the Butler–Volmer mechanism for the electron transfer process as

$$\frac{dr}{dt} = k_f C_M^{n+} \exp\left\{-\frac{\alpha nF(E - E_1)}{RT}\right\} - k_b \exp\left\{\frac{(1-\alpha)nF(E - E_1)}{RT}\right\} \tag{26}$$

where the definition of various terms is identical with that of Eq. (15). Likewise, the underpotential deposition removal reaction is also defined. The overlap among the growing centers is also taken into account, and the current observed by the potential-step method against t is given for instantaneous nucleation by

$$j(t) = k_1 t \exp(-k_2 t^2) \tag{27}$$

where k_1 and k_2 are constants. For progressive nucleation, the following variation of Eq. 28 is obtained

$$j(t) = k_3 t^2 \exp(-k_4 t^3) \tag{28}$$

where k_3 and k_4 are constants, including signs of the direction of the current.[142] The summary of the general trends of various processes, in

Table 1
Cyclic Voltammogram Feature for Random Adsorption and Nucleus Formation when the Process is Reversible ($v \rightarrow 0$)

Random Adsorption	
Langmuir random adsorption	
$jJ_p = -(nF)^2 0.25v/(RT)$	E_p = constant
$\Delta W_{1/2} = 90/n$ mV at 25°C	independent of v
Temkin(Frumkin) random adsorption	
$j_p = -(nF)^2 0.25v/(RT + 0.25r)$	$E_p = -0.5r/(nF)$ + constant
$\Delta W_{1/2} = 2rS/(nF) + 2RT/(nF) \cdot \ln\{(1/2 + S)/(1/2 - S)\}$ü	
Nucleation Adsorption	
Instantaneous nucleation growth adsorption	
$j_p = -K(nv)^{1/2}$	$E_p = -k_1 v^{1/2}/n^{1/2}$ + constant
$\Delta W_{1/2} = k_1' v/n^{1/2}$	dependent on v
Progressive nucleation growth adsorption	
$j_p = -k_P v\{k_P' + k_P'' \ln(n^2 v)\}$	
$\Delta W_{1/2} \rightarrow 0$	

Note: According to Ref. 139, S and r are defined in the text. Ks and ks are constant. E_p is here expressed for direction of the formation of underpotential deposition metal.

which monolayer formation takes place under the potential-sweep condition, is given in Table 1.

(ii) Elucidation of the Kinetics of Underpotential Deposition Formation

Zn underpotential deposition on polycrystalline Pt, Pd, and Au was subjected to evaluation of the kinetic parameters of the lateral repulsive interaction constant r.[96] As the underpotential deposition peak width $\Delta W_{1/2}$ changes with pH, a shift in the peak is caused when $\Delta W_{1/2}$ is large, as found in Fig. 41. A correction did not cause a change and the ΔE^{UPD} were *ca.* 1.08, 0.98, and 0.61 V, for Pt, Pd, and Au, respectively, as averages.

Equations (27) and (28) give mountainlike curves of j against t, and js against t of underpotential depositions of Pb on Ag single crystals were

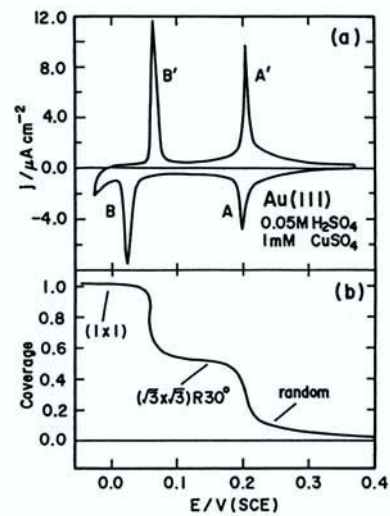

Figure 42. (a) Cyclic voltammogram at 1 mV s^{-1} on Au(111) in 0.05*M* H_2SO_4 + 1m*M* $CuSO_4$. (b) Electrochemically derived Cu underpotential deposition coverage as a function of potential, determined by potential steps in the positive direction. The Cu underpotential deposition structures obtained from LEED and RHEED are also shown. (From Ref. 142.)

observed to have mountainlike curves or plateaus,[134–136] which were attributed to nuclear formation or removal phenomena. In Ref. 142, underpotential deposition of Cu^{2+} on Au(111) was analyzed for elucidation of the mechanism of underpotential deposition for the individual cyclic voltammogram peaks of Fig. 42. The curves of *j* against *t* for peaks of A, A′, B, and B′ of Fig. 42 are given in Fig. 43, where *j* vs. *t* at peak A shows a monotonic decrease with *t*. However, *j*s vs. *t* at peaks A′, B, and B′ show mountainlike shapes, which can be attributed to nucleation growth processes. The cyclic voltammogram current peaks j_{max} and their potentials E_{max} are plotted against the square root of scan rates $\nu^{1/2}$ in Fig. 44, showing a good linear relationship, which is characteristic of instantaneous nucleation. We reexamined the case of Cu underpotential deposition on Au(111) and found that at peak A′, the characteristic feature seemed to be progressive nucleation rather than instantaneous nucleation.[133] The influence of step density on Cu^{2+} underpotential deposition at Au(111) was investigated to enhance nucleation growth rates.[143] In the case of Zn underpotential deposition on Pt(111), the kinetics of underpotential deposition was found to be changed by the addition of Br^- in phosphate solution.[121]

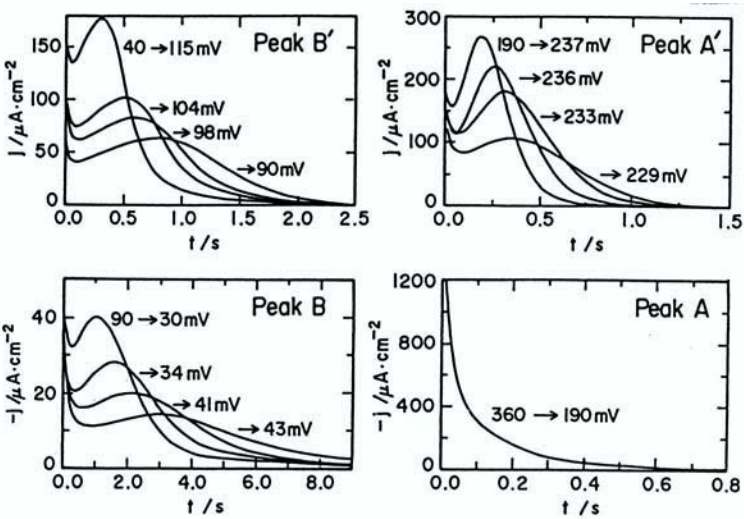

Figure 43. Plot of current against time for peaks A, A′, B, and B′ of the cyclic voltammogram for Cu underpotential deposition. Potential steps are indicated in the figures. Details are in the text. (From Ref. 142.)

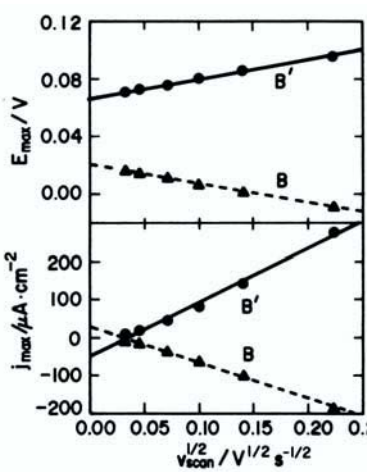

Figure 44. Current maximum j_{max} and their potentials E_{max} of peaks of B and B′ of cyclic voltammogram against $v^{1/2}$. (From Ref. 142.)

(iii) Dynamics of Underpotential Deposition Phase Formation Observed by STM

The characteristics of monatomic height step formation of Cu underpotential deposition on Ag(111) in sulfuric acid solution were observed to be dependent on electrode potentials.[144] At more positive underpotential deposition potential regions, STM revealed the frizzy edges of Cu underpotential deposition at the corners of Cu islands growing on the Ag(111) terrace STM. The kink site mobility was roughly estimated as 3000 nm s^{-1}. Monatomic height steps on Au(111) electrodes did not show any sign of frizziness under the experimental condition.[144]

(iv) Underpotential Deposition, Work Function, and Point-of-Zero Charge

The occurrence of underpotential deposition of various metals on different metal substrates is an interesting subject: Why is it possible? The relation of the underpotential deposition shift potential ΔE^{UPD} was plotted against physicochemical values for differences of the heat of adsorption derived from Pauling's concept, and work function differences of M and M′, $\Delta\phi$. ΔE^{UPD} was found to be in good proportional relation to $\Delta\phi$, since $e\Delta E^{UPD} \simeq 0.5\,\Delta\phi$.[1] Later, the Born–Haber cycle was used to elucidate ΔE^{UPD}; ΔE^{UPD} was expected to be in the form of $e\Delta E^{UPD} = \Delta\phi$.[145] However, the double-layer potential is present at the solution side of the electrode interface, which is expected to affect the evaluation of the energy value by the Born–Haber cycle, as described in Ref. 146 in detail. This argument needs to incorporate an additional correction to describe the difference between outer potentials over substrate metal and underpotential deposition metal at electrode potentials, where the underpotential deposition occurs, since the value and sign of the outer potentials are generally different between both metals at a certain potential. Therefore, the relation

$$e\Delta E^{UPD} = \Delta\phi \tag{29}$$

is present when no anion-specific adsorption needs to be taken into account, since the value of the outer potential is relatively small. In the case of Zn underpotential deposition on Pt, the condition of Eq. (29) is approximately attained because the equilibrium potential of Zn^{2+}/Zn is

located at relatively negative potentials, and the underpotential deposition current can be found in the double-layer region of the Pt electrode.[121] In the case of Tl^+ underpotential deposition on Pt(111) in perchloric acid, $\Delta E^{UPD} \simeq 1.4$ V nearly satisfies the relation of Eq. (29) with $\Delta\phi$, the cyclic voltammogram of which is shown in Fig. 40.[129]

It is interesting that the photoelectronic work functions of Pt, Au, and Ag electrodes changed with electrode potentials E when the electrodes were imposed before they were transferred for measurement in a vacuum; the difference of E, $e\Delta E = \Delta\phi + \text{constant}$, and the work function of the standard hydrogen electrode potential was evaluated as 4.85 eV.[147] This is supported by the work for determination of the point-of-zero charge of the Au single-crystal electrode.[148] Various discussions on the vacuum-scale potential of the standard hydrogen electrode are given in Ref. 146. These results suggest that the relation of Eq. (29) can be expected from an ideal case in which the electrode surface is neither oxidized nor specifically adsorbed by anions.

IV. ELECTROCATALYSIS ON ELECTRODES MODIFIED BY UNDERPOTENTIAL DEPOSITION

Electrodes modified by underpotential deposition of metal were subjected as electrocatalysts to reduction of oxygen,[149] oxidation of formic acid,[150] and other processes in which polycrystalline metal substrates were used (see review in Ref. 151). Electrocatalysis of single-crystal electrodes modified by underpotential deposition was also investigated, as reviewed by Adžić.[152]

Since a well-defined condition of the underpotential deposition metal at a definite coverage is better for studying its modified surface at a definite coverage, an irreversibly adsorbed underpotential deposition metal is desirable: Sb on Pt(111) for CO oxidation,[153] Bi and Te on Pt(l00) for formic acid oxidation,[154] Sb + Bi on Pt(l00) for formic acid oxidation,[155] and others found in these references.

In most of the works referred to in this section, catalytic activities were observed through cyclic voltammograms, which exhibit only primary trends for electrocatalysts. The observation of steady current at certain potentials is quite important because the degree of catalytic activity under the steady-state condition must be known in order to develop

practically applicable processes. The transient phenomena shown on cyclic voltammograms do not always indicate trends of the steady state of catalytic activity. In addition, under steady-state condition, the reaction mechanism can be easily elucidated, as discussed in Refs. 156 and 157.

V. MISCELLANEOUS

1. Bimetallic Underpotential Deposition

For the design of electrode surfaces by binary underpotential deposition layers, Schmidt and Gygax observed ($Bi^{3+} + Pb^{2+}$), ($Pb^{2+} + Tl^{+}$), and ($Pb^{2+} + Tl^{+}$) on Ag at different concentrations of underpotential deposition of metal ions,[158] where the Ag substrate was polycrystalline. Stucki investigated the effect of underpotential deposition on polycrystalline Ag, Au, and Cu substrate with predeposited metal or Underpotential deposition metal.[159] Simultaneous underpotential deposition of Pb^{2+} and Tl^{+} on polycrystalline Ag has also been studied using cyclic voltammograms.[160,161] Underpotential depositions of ($Pb^{2+} + Ag^{+}$) and ($Ag^{+} + Tl^{+}$) on Au(111) and Au(l00) were observed by cyclic voltammogram, where Ag deposition may be in the overpotential region.[162] The system of Bi^{3+} and As^{3+} subsequently and irreversibly adsorbed on Pt(111) was observed by an *ex situ* method on Pt(111).[100] The underpotential depositions of Bi^{3+} and As^{3+} affected each other, giving different cyclic voltammogram features according to the order of the underpotential deposition procedure, and were found to interact with each other by forming individual islands. The *in situ* binary underpotential deposition of Zn^{2+} and Cu^{2+} on Pt(111) in a phosphate solution of pH 4.6 was observed by voltammograms, where the concentration of Zn^{2+} was ten times larger than that of Cu^{2+}. The Cu underpotential deposition seems to expel underpotential deposition of Zn, even in the potential region of Zn underpotential deposition on Pt.[163]

2. Effect of Underpotential Deposition on Overpotential Deposition

The overpotential three-dimensional nucleation process is affected by the change of prepolarization potential in the underpotential deposition region of Pb on Ag. When ΔE^{UPD} is low (potential is close to E_{eq}), the rate of the overpotential nucleation process becomes slow; the Pb underpotential

deposition seems to inhibit the nucleation process in the overpotential region.[112]

Silver deposition on polycrystalline Pt electrodes at potentials positive to the equilibrium potential gave 2.5 atomic layers.[164] Two binding types of Ag layers were found by anodic stripping: the first Ag layer deposited on Pt, which seems to form an alloy of Ag-Pt, on which the second Ag deposition takes place in the Ag underpotential deposition region. STM images from the underpotential to the overpotential deposition region were observed for Cu underpotential deposition on Au(111) in sulfuric acid solution, where Cu underpotential deposition does not affect overpotential deposition, although the latter always takes place on the surface with Cu underpotential deposition and a metal.[67]

3. Effect of Organic Additives on Underpotential Deposition

The electrode interface structure is changed by adsorption of organic additives. Since Grahame's work in the 1940s,[20] their effects have been concisely studied, mostly on liquid Hg electrodes.[165] Recently, the effect of organic additives has also been studied on well-defined single-crystal electrodes.[166–168] A change in the surface structure reconstruction potential with a change in concentration of pyridine and pyrazine was reported. With a concentration increase in these species, a negative shift of surface reconstruction from Au(100)(5 x 20) to Au(100)(1 x 1) was observed in cyclic voltammograms with 0.6 V and 0.2 V for pyridine and pyrazine, respectively, at a sweep rate of $50\ mV\ s^{-1}$.[166]

The effect of acetate, citrate, and thiourea on Pb underpotential deposition on Ag(111) has been studied.[135–136] The effects of the anionic character of the additives were discussed in relation to changes in voltammograms. The two-dimensional phase transformation was also discussed. The influence of various additives such as dimethylfluoride (DMF) and pyridine on cyclic voltammograms of Cu underpotential deposition on Pt(111) was observed.[169] Cu underpotential deposition on Pt(111) was studied in the presence of crystal violet, coumarin, and hydroquinone.[170]

The addition of crystal violet to a Cu underpotential deposition system on Au(111) gave two different STM images at potentials different from the images seen in its absence. One of these was due to the presence of Cl^- as a counteranion in the crystal violet molecule.[67] Thiourea was added to Cu underpotential deposition on Au(111) to investigate the

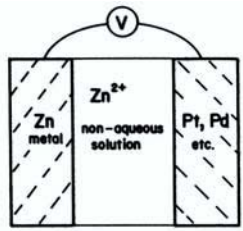

Figure 45. Schematic depiction of possible underpotential deposition supercapacitor.

kinetic mechanism of underpotential deposition as well as Cu overpotential deposition.[171]

4. Underpotential Deposition in Nonaqueous Solvents

Underpotential depositions of Li^+ on Au and Ag in acetonitrile and of Li^+ on Cu, Ag, and Pt in propylene carbonate (PC) were observed at 1.23, 0.96, 1.00, 1.05, and 1.30 V for the underpotential deposition shift potential ΔE^{UPD} where the electrodes were all polycrystalline.[172] The Pb and Cd underpotential depositions on Ag(111) and Au(111) were studied in nonaqueous solvents where the solvents were PC, THF, and DMF.[173] The highest ΔE^{UPD} observed at present is 1.7 V for Cs^+ on Pt in PC.[174] In aqueous solution, it is 1.4 V for Tl^+ on Pt(111).[129] These large values suggest the possibility of an underpotential deposition supercapacitor or a secondary battery of any combination of M^{n+}/M' in nonaqueous media, as shown in Fig. 45, for an example.

VI. CONCLUSION

In this chapter, hydrogen adsorption, particularly observed on Pt electrodes, was not treated as an underpotential deposition phenomenon. However, from a theoretical point of view, it may provide a breakthrough insight into underpotential deposition.[175] Since the underpotential deposition of M on M' is quite characteristic among different combinations of M and M', together with a change in the kind of anions in the solution, a theoretical approach, which requires simplification, is still limited, and more experimental clarification is needed for theoretical work. However, the jellium model was successfully used to describe the lattice contraction of adsorbate Tl and Pb on Ag(111) as underpotential deposition.[176,177]

Other researchers have attempted to simulate the cyclic voltammogram feature from theoretical bases.[178,179]

The under-potential deposition process is one of the simpler electrode processes that have been experimentally studied, not only by electrochemical methods, but also by various *in situ* and *ex situ* spectroscopic methods; the current-potential relation was therefore examined by atomic resolution techniques. Since the underpotential deposition process always involves the substitution reaction at the interface, it receives the strong effect of the species at the interface, i.e., the counterion of the underpotential deposition metal ion at/on the electrode interface may play a crucial role in the underpotential deposition process. The residence of cations and/or anions depends on the double-layer potential, the sign and magnitude of which are determined by the position of the point-of-zero charge (pzc) of the electrode. Primarily, the position of the pzc changes with a change in the crystal face of the metal electrode;[148,180,181] the kind of adsorbed species and its coverage are changed with respect to the pzc. It is likely that the underpotentially deposited metal is directly bound to the substrate metal electrode, while the anions and/or solvent present at the electrode are substituted before the underpotential deposition. Since the underpotential deposition metal's pzc usually locates at more negative potentials than the substrate metals, the anion substituted from the substrate metal is expected to be again pulled over onto the underpotential deposition metal. The underpotential deposition feature on a cyclic voltammogram changes with various combinations of underpotential deposition metal and substrate metal M^{n+}/M', reflecting the interface structure. The current-potential relationship is now revealed at an atomic scale to be correlated with the change of surface state of the underpotential deposition.

Some possibilities of practical application of the system M^{n+}/M' were pointed out in the preceding sections. The underpotential deposition has been studied mostly in aqueous acidic, and, to some extent, in neutral solutions. With an increase in pH, the equilibrium potential of the hydrogen evolution reaction shifts negatively with respect to that of the electron-transfer reaction of $M^{n+} + ne \rightarrow M$ and produces the system M and M', which can operate as an underpotential deposition capacitor, an atomic-scale switching device, and in some other applications, as well as in aqueous alkaline solutions, as shown by a basic set in Fig. 45.

In electroplating industrial iron metals,[182] zinc metal electrodeposition is accompanied by the formation of Zn-Ni, Zn-Co, and Zn-Fe alloys, where zinc electrodeposition is known to be anomalous in some cases. The ratio of zinc metal to iron metal in those alloys is sometimes higher than that of the electroplating bath solution, and zinc ions occasionally deposit at potentials positive to the equilibrium potential of zinc ions on zinc metal E_{Zn}, although E_{Zn} is very negative to the equilibrium potentials of iron metals. It can be seen from the study of underpotential deposition of zinc ions[41,62,93,96] that this is not anomalous, but could be explained as an underpotential deposition phenomenon, to be clarified in further work.

ACKNOWLEDGMENT

Financial support for this work was supplied by the Japan Ministry of Education and Culture for Project No. 072115201 and 08454216. The author appreciates permission to use photos from the American Physical Society, Elsevier S. A., Elsevier Science Ltd, the Royal Society of Chemistry, the American Institute of Physics, and the American Association for the Advancement of Science. I also wish to thank Miss A. Hiratuka of the Catalysis Research Center, Hokkaido University, for tracing the figures and my colleagues for their contribution to this effort. The original figures appeared in and their copy permissions are obtained from Ber. Bunsenges. Phys. Chem., Electrochim. Acta, J. Chim. Phys., J. Electroanal. Chem., J. Electrochem. Soc., and Sur. Sci., to which organizations are acknowledged.

REFERENCES

[1]D. M. Kolb, *Adv. Electrochem. Electrochem. Eng.* **11**, 125 (1978).
[2]A. Hamelin, *Mod. Aspects of Electrochem.* **16**, 1 (1985).
[3]D. Dickermann, F. D. Koppits, and J. W. Schultze, *Electrochim. Acta* **21**, 967 (1976).
[4]J. Clavilier, R. Faure, G. Guinet, and R. Durand, *J. Electroanal. Chem.* **107**, 205 (1980).
[5]A. Hamelin and A. Katayama, *J. Electroanal. Chem.* **117**, 221 (1981).
[6]S. Motoo and N. Furuya, *J. Electroanal. Chem.* **167**, 309 (1984).
[7]J. Clavilier, M. Wasberg, M. Petit, and L. H. Klein, *J. Electroanal. Chem.* **374**, 123 (1994).
[8]X. Gao, A. Hamelin, and M. Weaver, *Phys. Rev. Lett.* **67**, 618 (1991).
[9]A. Hamelin. X. Gao, and M. Weaver, *J. Electroanal. Chem.* **323**, 361 (1992).
[10]M. Szklarczyk, O. Velev, and J. O. Bockris, *J. Electrochem. Soc.* **136**, 2433 (1989).
[11]O. Magnussen, J. Hotlos, R. Nichols, D. Kolb, and R. Behm, *Phys. Rev. Lett.* **64,** 2929 (1990).

[12]A. Hamnett, Ed., *Faraday Disc.* **94**, 1 (1992).
[13]A. J. Bard *et al. J. Phys. Chem.* **97**, 7147 (1993).
[14]P. Zelenay, G. Horányi, C. K. Rhee, and A. Wieckowski, *J. Electroanal. Chem.* **300**, 499 (1991).
[15]P. Zelenay and A. Wieckowski, *J. Electrochem. Soc.* **139**, 2552 (1992).
[16]M. E. G.-Aldeco, E. Herrero, P. S. Zelenay, and A. Wieckowski, *J. Electroanal. Chem.* **348**, 451 (1993).
[17]Y.-E. Sung, T. M. Gamboa-Aldeco, K. Franaszczuk, and A. Wieckowski, *J. Electroanal. Chem.* **378**, 131 (1994).
[18]Z. Shi, J. Lipkowski, M. Gamboa, P. Zelenay, and A. Wieckowski, *J. Electroanal. Chem.* **366**, 317 (1994).
[19]P. Mrozek, Y. Sung, M. Han, M. Gamboa-Aldeco, A. Wieckowski, C. Chen, and A. A. Gewirth, *Electrochim. Acta* **40**, 17 (1995).
[20]D. C. Grahame, *Chem. Rev.* **41**, 441 (1947).
[21]J. M. Orts, A. F.-Vega, J. M. Feliu, A. Aldaz, and J. Clavilier, *J. Electroanal. Chem.* **327**, 261 (1992).
[22]J. Clavilier, R. Albalat, R. Gómez, J. M. Orts, J. M. Feliu, and A. Aldaz, *J. Electroanal. Chem.* **330**, 489 (1992).
[23]J. Clavilier, R. Albalat, R. Gómez, J. M. Orts, and J. M. Feliu, *J. Electroanal. Chem.* **360**, 325 (1993).
[24]J. M. Feliu, J. M. Orts, R. Gómez, A. Aldaz, and J. Clavilier, *J. Electroanal. Chem.* **372**, 265 (1994).
[25]S. Taguchi, dissertation, Hokkaido University (1996).
[26]R. Gómez and J. Clavilier, *J. Electroanal. Chem.* **354**, 189 (1993).
[27]A. Rodes, M. Zamakhchari, K. E. Achi, and J. Clavilier, *J. Electroanal. Chem.* **305**, 115 (1991).
[28]R. Michaelis and D. M. Kolb, *J. Electroanal, Chem.* **328**, 1992 (1992).
[29]J. Clavilier, A. Rodes, K. E. Achi, and M. Zamakhchari, *J. Chim. Phys.* **88**, 1291 (1991).
[30]S. Motoo and N. Furuya, *Ber. Bunsenges. Phys. Chem.* **91**, 457 (1987).
[31]L.-J. Wan, S.-L. Yau, and K. Itaya, *J. Phys. Chem.* **99**, 9507 (1995).
[32]N. Furuya, in *Electrocatalysis: Prospect and Application* Ed. by H. Kita IPC (Tokyo), (1990) 47.
[33]H. A.-Kozlowska, B. E. Conway, A. Hamelin, and L. Stoicoviciu, *Electrochim. Acta* **31**, 1051 (1986).
[34]S. Moniwa and A. Aramata, *J. Electroanal. Chem.* **376**, 203 (1994).
[35]A. Hamelin, T. Vitanov, E. Sevastyanov, and A. Popov, *J. Electroanal. Chem.* **145**, 225 (1983).
[36]A. Hamelin, *J. Chim. Phys.* **88**, 1453 (1991).
[37]A. Hamelin, *J. Electroanal. Chem.* **142**, 299 (1982).
[38]D. M. Kolb, *Ber. Bunsenges. Phys. Chem.* **92**, 1175 (1988).
[39]F. Wagner and P. Ross, *Sur. Sci.* **160**, 305 (1985).
[40]C. M. Vitus, S.-C. Chang, B. C. Schardt, and M. J. Weaver, *J. Phys. Chem.* **95**, 7559 (1991).
[41]S. Taguchi, A. Aramata, M. A. Quaiyyum, and M. Enyo, *J. Electroanal. Chem.* **374**, 275 (1994).
[42]Y. Shingaya and M. Ito, *J. Electroanal. Chem.* **372**, 283 (1994).
[43]X. Gao, A. Hamelin, and M. J. Weaver, *J. Chem. Phys.* **95**, 6993 (1991).
[44]X. Gao, A. Hamelin, and M. J. Weaver, *Phys. Rev. B* **44**, 10983 (1991).
[45]A. Hamelin, L. Stoicoviciu, G. J. Edens, X. Gao, and M. J. Weaver, *J. Electroanal. Chem.* **365**, 47 (1994).

[46]A. Hamelin, *J. Electroanal. Chem.* **386**, 1 (1995).
[47]O. Magnussen, J. Hotlos, R. Behm, N. Batina, and D. M. Kolb, *Sur. Sci.* **296**, 310 (1993).
[48]X. Gao, G. J. Edens, A. Hamelin, and M. Weaver, *Sur. Sci.* **296**, 333 (1993).
[49]X. Gao and M. J. Weaver, *J. Electroanal. Chem.* **367**, 269 (1994).
[50]X. Gao, A. Hamelin, and M. J. Weaver, *Sur. Sci. Lett.* **274**, L588 (1992).
[51]X. P. Gao, G. J. Edens, A. Hamelin, and M. J. Weaver, *Sur. Sci.* **318**, 1 (1994).
[52]X. Gao and M. J. Weaver, *Sur. Sci. Lett.* **313**, 775 (1994).
[53]R. L. McCarley and A. J. Bard, *J. Phys. Chem.* **96**, 7410 (1992).
[54]X. Gao, G. J. Edens, F.-C. Liu, A. Hamelin, and M. J. Weaver, *J. Phys. Chem.* **98**, 8086 (1994).
[55]X. Gao, G. J. Edens, and M. J. Weaver, *J. Phys. Chem.* **98**, 8074 (1994).
[56]K. Itaya, S. Sugawara, K. Sashikata, and N. Furuya, *J. Vac. Sci. Technol. A* **8**, 1291 (1990).
[57]I. Villegas and M. J. Weaver, *J. Chem. Phys.* **101**, 1648 (1994).
[58]H. Kita, K. Shimazu, and K. Kunimatsu, *J. Electroanal. Chem.* **248**, 163 (1988).
[59]W. Savich, S.-G. Sun, J. Lipkowski, and A. Wieckowski, *J. Electroanal. Chem.* **388**, 233 (1995).
[60]A. N. Frumkin and O. A. Petrii, *Electrochim. Acta* **20**, 347 (1975).
[61]R. Parsons, *J. Electroanal. Chem.* **376**, 15 (1994).
[62]S. Taguchi and A. Aramata, *J. Electroanal. Chem.* **396**, 131 (1995).
[63]D. Aberdam, R. Durand, and R. Faure, *J. Chim. Phys.* **88**, 1519 (1991).
[64]I. Omar, H. Pauling, and K. Jüttner, *J. Electrochem. Soc.* **140**, 2187 (1993).
[65]M. G. Chu, J. McBreen, and G. Adzic, *J. Electrochem. Soc.* **128**, 2281 (1981).
[66]G. Salié and K. Bartels, *Electrochim. Acta* **39**, 1057 (1994).
[67]N. Batina, T. Will, and D. M. Kolb, *Faraday Disc.* **94**, 93 (1992).
[68]S. Manne, P. K. Hansma, J. Massie, V. B. Elings, and A. A. Gewirth, *Science* **251**, 183 (1991).
[69]N. Ikemiya, S. Miyaoka, and S. Hara, *Sur. Sci. Lett.* **311**, 641 (1994).
[70]S. G. Corcoran, G. S. Chakarova, and K. Sieradzki, *J. Electroanal. Chem.* **377**, 85 (1994).
[71]M. Nakamura, A. Aramata, A. Yamagishi, and M. Taniguchi, Stm on Au(111) for Zn underpotential deposition (tentative title), to be submitted for publicaton.
[72]J. X. Wang, R. R. **Adžić,** O. M. Magnussen, and B. M. Ocko, *Surf. Sci.* **335**, 120 (1995).
[73]A. Tadjeddine, D. Guay, M. Ladouceur, and G. Tourillon, *Phv. Rev. Lett.* **66**, 2235 (1991).
[74]G. Tourillon, D. Guay, and A. Tadjeddine, *J. Electroanal. Chem.* **289**, 263 (1990).
[75]A. Tadjeddine, G. Tourillon, and D. Guay, *Electrochim. Acta.* **36**, 1859 (1991).
[76]S. Wu, J. Lipkowski, T. Tyliszczak, and A. P. Hitchcock, *Prog. Surf. Sci.* **50**, 227 (1995).
[77]M. G. Samant, G. Borges, and O. R. Melroy, *J. Electrochem. Soc.* **140**, 421 (1993).
[78]M. G. Samant, G. L. Borges, J. G. Gordon II, O. R. Melroy, and L. Blum, *J. Am. Chem. Soc.* **109**, 5970(1987).
[79]E. D. Chabala, B. H. Harji, T. Rayment, and M. D. Archer, *Langmuir* **8**, 2028 (1992).
[80]A. Tadjeddine, M. Ladouceur, A. Lahrichi, D. Guay, and G. Tourillon, in *X-ray Methods in Corrosion and Interfacial Electrode*, Ed. by A. Davenport and J. G. Gordon, *ISE Proc. 92-4*, (1992), 159.
[81]D. B. Parry, M. G. Samant, H. Seki, M. R. Philpott, and K. Ashley, *Langmuir* **9**, 1878 (1993).
[82]M. R. Deakin and O. Melroy, *J. Electroanal. Chem.* **239**, 321 (1988).
[83]G. L. Borges, K. K. Kanazawa, J. G. Gordon II, K. Ashley, and J. Richer, *J. Electroanal. Chem.* **364**, 281 (1994).
[84]J. G. Gordon, O. R. Melroy, and M. F. Toney, *Electrochim. Acta* **40**, 3 (1995).
[85]R. Gómez, J. M. Feliu, and H. D. **Abruña,** *Langmuir* **10**, 4315 (1994).

[86]N. M. Marković, H. A. Gasteiger, C. A. Lucas, I. M. Tidswell, and P. N. Ross, *Sur. Sci.* **335**, 91 (1995).
[87]N. M. Marković, H. A. Gasteiger, and P. N. Ross, *Langmuir* **11**, 4098 (1995).
[88]N. M. Marković, H. A. Gasteiger, C. A. Lucas, I. M. Tidswell, and P. N. Ross, *Sur. Sci.* **335**, 91 (1995).
[89]T. E. Furtak, L. Wang, J. Pant, K. Pansewicz, and T. M. Hayes, *J. Electrochem. Soc.* **141**, 2369 (1994).
[90] G. M. Bommarito, D. Acevedo, J. F. Rodri, and H. D. Abruña, *J. Electroanal. Chem.* **379**, 135 (1994).
[91]H. S. Yee and H. D. Abrúna, *J. Phys. Chem.* **98**, 6552 (1994).
[92]F. Mikuni and T. Takamura, *Denki Kagaku* **38**, 112 (1970).
[93]A. Aramata, M. A. Quaiyyum, W. A. Balais, T. Atoguchi, and M. Enyo, *J. Electroanal Chem.* **338**, 367(1992).
[94]M. A. Quaiyyum. A. Aramata, S. Taguchi, and M. Enyo, *Denki Kagaku* **61**, 847 (1993).
[95]A. A. Dorda, R. R. McLarnon, and E. J. Cairns, *J. Electroanal. Chem.* **364**, 71 (1994).
[96]M. A. Quaiyyum, A. Aramata, S. Moniwa, S. Taguchi, and M. Enyo, *J. Electroanal. Chem.* **373**, 61 (1994).
[97]J. L. Stickney, S. D. Rosasco, D. Song, M. P. Soriaga, and A. T. Hubbard, *Sur. Sci.* **130**, 326(1983).
[98]J. F. Rodríguez, D. L. Taylor, and H. D. Abruña, *Electrochim. Acta* **38**, 235 (1993).
[99]J. Clavilier, J. M. Feliu, and A. Aldaz, *J. Electroanal. Chem.* **243**, 419 (1988).
[100]L. Dollard, R. W. Evans, and G. A. Attard, *J. Electroanal. Chem.* **345**, 205 (1993).
[101] R. W. Evans and G. A. Attard, *J. Electroanal. Chem.* **345**, 337 (1993).
[102]J. Clavilier, J. M. Orts, J. M. Feliu, and A. Aldaz, *J. Electroanal. Chem.* **293**, 197 (1990).
[103]K. Sashikata, N. Furuya, and K. Itaya, *J. Electroanal. Chem.* **316**, 361 (1991).
[104]N. Kimizuka and K. Itaya, *Faraday Disc.* **94**, 109 (1992).
[105]H. Matsumoto, J. Inukai, and M. Ito, *J. Electroanal. Chem.* **379**, 223 (1994).
[106]R. Durand, R. Faure, D. Aberdam, C. Salem, G. Tourilion, D. Guay, and M. Ladouceur, *Electrochim. Acta* **37**, 1977 (1992).
[107]H. S. Yee and H. D. Abruña, *J. Phys. Chem.* **97**, 6278 (1993).
[108]H. S. Yee and H. D. Abruña, *Langmuir* **9**, 2460 (1993).
[109] N. S. Marinkowvić, W. R. Fawcett, J. X. Wang, and R. R. Adžić, *J. Phys. Chem.* **99**, 17490 (1995).
[110]W. Obretenov, U. Schmidt, W. J. Lorenz, G. Staikov, E. Budevski, D. Carnal, U. Müller. H. Siegenthaler, and E. Schmidt, *J. Electrochem. Soc.* **140**, 692 (1993).
[111] E. Schmidt and H. Siegenthaler, *J. Electroanal. Chem.* **150**, 59 (1983).
[112] W. J. Lorenz, L. M. Gassa, U. Schmidt, W. Obretenov, G. Staikov, V. Bostanov, and E. Budevski, *Electrochim. Acta.* **37**, 2173 (1992).
[113] D. Carnal, P. Oden, U. Müller, E. Schmidt, and H. Siegenthaler, *Electrochim. Acta* **40**, 1223(1995).
[114]G. Adzic, J. McBreen, and M. G. Chu, *J. Electrochem. Soc.* **128**, 1691 (1981).
[115]R. R. Adžić, F. Feddrix, B. Z. Nikolić, and E. Yeager, *J. Electroanal. Chem.* **341**, 287 (1992).
[116]J. Hotlos, O. M. Magnussen, and R. J. Behm, *Sur. Sci.* **335**, 129 (1995).
[117]Z. Shi and J. Lipkowski, *J. Electroanal. Chem.* **365**, 303 (1994).
[118]Z. Shi and J. Lipkowski, *J. Electroanal. Chem.* **369**, 283 (1994).
[119]Z. Shi, S. Wu, and J. Lipkowski, *Electrochim. Acta* **40**, 9 (1995).
[120]P. Mrozek, Y.-E. Sung, and A. Wieckowski, *Sur. Sci.* **335**, 44 (1995).

[121] S. Taguchi, T. Fukuda, and A. Aramata, Kinetic study of underpotential deposition of zinc ions on pt(111) in acidic phosphate solution, in press (1996).
[122] G. Horányi and A. Aramata, *J. Electroanal. Chem.* (1997), in press.
[123] J. H. White and H. D. Abruña, *J. Phys. Chem.* **94**, 894 (1990).
[124] R. Gómez, J. M. Feliu, and H. D. Abruna, *J. Phys. Chem.* **98**, 5514 (1994).
[125] M. Wünsche, H. Meyer, and R. Schumacher, *Electrochim. Acta* **40**, 629 (1995).
[126] N. Markovic and P. N. Ross, *Langmuir* **9**, 580 (1993).
[127] R. Michaelis, M. S. Zei, R. S. Zhai, and D. M. Kolb, *J. Electroanal. Chem.* **339**, 299 (1992).
[128] N. Shinotsuka, K. Sashikata, and K. Itaya, *Sur. Sci.* **335**, 75 (1995).
[129] D. R. Wheeler, J. X. Wang, and R. R. Adžić, *J. Electroanal. Chem.* **387**, 115 (1995).
[130] K. Varga, P. Zelenay, G. Horányi, and A. Wieckowski, *J. Electroanal. Chem.* **327**, 291 (1992).
[131] B. E. Conway and E. Gileadi, *Trans. Faraday Soc.* **58**, 2493 (1962).
[132] H. A.-Kozlowska, J. Klinger, and B. E. Conway, *J. Electroanal. Chem.* **75**, 45 (1977).
[133] T. Fukuda and A. Aramata, The kinetic study of adsorption processes of the phosphate species on platinum(111) in aqueous acidic solutions, *J. Electroanal. Chem.*, in press (1997).
[134] A. Bewick and B. Thomas, *J. Electroanal. Chem.* **84**, 127 (1977).
[135] J. N. Jovićević, V.D. Jović, and A. R. Despić, *Electrochim. Acta* **29**, 1625 (1984).
[136] V. D. Jović, J. N. Jovićević, and A. R. Despić, *Electrochim. Acta* **30**, 1455 (1985).
[137] M. Fleischmann and H. R. Thirsk, *Advs. Electrochem. Electrochem. Eng.* **3**, 123 (1963).
[138] H. A.-Kozlowska, B. E. Conway, and J. Klinger, *J. Electroanal. Chem.* **87**, 321 (1978).
[139] M. Noel, S. Chandrasekaran, and C. A. Basha, *J. Electroanal. Chem.* **225**, 93 (1987).
[140] H. A.-Kozlowska, B. E. Conway, and J. Klinger, *J. Electroanal. Chem.* **87**, 301 (1978).
[141] E. Bosco and S. K. Rangarajan, *J. Electroanal. Chem.* **129**, 25(1981).
[142] M. H. Holzle, U. Retter, and D. M. Kolb, *J. Electroanal. Chem.* **371**, 101 (1994).
[143] M. H. Hölzle, V. Zwing, and D. M. Kolb, *Electrochim. Acta* **40**, 1237 (1995).
[144] M. Dietterle, T. Will, and D. M. Kolb, *Sur. Sci. Lett.* **327**, L495 (1995).
[145] S. Trasatti, *Z. Phys. Chem.* **98**, 75 (1975).
[146] J. O. Bockris and S. U. M. Khan, in *Surface Electrochemistry*, Plenum Press, New York (1993) p. 490.
[147] E. R. Kötz, H. Neff, and K. Müller, *J. Electroanal. Chem.* **215**, 331 (1986).
[148] J. Lecoeur, J. P. Bellier, and C. Koehler, *J. Electroanal. Chem.* **375**, 117 (1994).
[140] R. R. Adžić and A. R. Despic, *Z. Phys. Chem.* **98**, 95 (1975).
[150] R. R. Adžić, K. I. Popov, and M. A. Pamic, *Electrochim. Acta* **23**, 1191 (1978).
[151] R. R. Adžić, *Adv. Electrochem. Electrochem. Eng.* **13**, 159 (1984).
[152] R. Adžić, *Mod. Aspects of Electrochem.* **21**, 163 (1990).
[153] E. Herrero, A. Rodes, J. M. Péres, J. M. Feliu, and A. Aldaz, *J. Electroanal. Chem.* **393**, 87 (1995).
[154] E. Herrero, M. J. Llorca, J. M. Feliu, and A. Aldaz, *J. Electroanal. Chem.* **383**, 145 (1995).
[155] E. Herrero, J. M. Feliu, and A. Aldaz, *J. Electroanal. Chem.* **368**, 101 (1994).
[156] A. Aramata, M. Masuda, and T. Kodera, *J. Electrochem. Soc.* **136**, 3288 (1989).
[157] A. Aramata and M. Masuda, *J. Electrochem. Soc.* **138**, 1950 (1991).
[158] E. Schmidt and H. R. Gygax, *Helv. Chim. Acta* **49**, 1105 (1966).
[159] S. Stucki, *J. Electroanal. Chem.* **78**, 31 (1977).
[160] S. Bharathi, V. Yegnaraman, and G. P. Rao, *Electrochim. Acta* **36**, 1291 (1991).
[161] S. Bharathi, V. Yegnaraman, and G. P. Rao, *J. Appl. Electrochem.* **24**, 981 (1994).
[162] H. J. Pauling and K. Jüttner, *Electrochim. Acta* **37**, 2237 (1992).

[163]S. El-Maksoud, S. Taguchi, T. Fukuda, and A. Aramata, *Electrochim. Acta* **41**, 1947 (1996).
[164]A. Vaskevich, M. Rosenblum, and E. Gileadi, *J. Electroanal. Chem.* **383**, 167 (1995).
[165]P. Delahay, in *Double Layer and Electrode Kinetics*, Wiley, New York (1965) p. 17.
[166]U. W. Hamm and D. M. Kolb, *J. Electroanal. Chem.* **332**, 339 (1992).
[167]L. Stolberg, J. Lipkowski, and D. E Irish, *J. Electroanal. Chem.* **322**, 357 (1992).
[168]J. Lipkowski, L. Stolberg, D.-F. Yang, B. Pettinger, S. Mirwald, F. Henglein, and D. M. Kolb, *Electrochim. Acta* **39**, 1045 (1994).
[169]J. H. White and H. D. **Abruña,** *J. Electroanal. Chem.* **300**, 521 (1991).
[170]A. S. Dakkouri, N. Batina, and D. M. Kolb, *Electrochim. Acta* **38**, 2467 (1993).
[171]M. H. Hölzle, C. W. Apsel, T. Will, and D. M. Kolb, *J. Electrochem. Soc.* **142**, 3741 (1995).
[172]D. M. Kolb, M. Przasnyski, and H. Gerischer, *J. Electroanal. Chem.* **54**, 25 (1974).
[173]X. Xing, I. T. Bae, and D. A. Scherson, *Electrochim. Acta* **40**, 29 (1995).
[174]I. Fried and H. Barak, *J. Electroanal. Chem.* **30**, 279 (1971).
[175]H. Kita, *J. Res. Inst. Catalysis* **17**, 77 (1969).
[176]E. Leiva and W. Schmickler, *Electrochim. Acta* **40**, 37 (1995).
[177]E. Leiva. *Sur. Sci.* **335**, 83 (1995).
[178]D. A. Huckaby and L. Blum, *J. Electroanal. Chem.* **315**, 255 (1991).
[179]L. Blum and D. A. Huckaby, *J. Electroanal. Chem.* **375**, 69 (1994).
[180]J. Lecoeur, J. P. Bellier, and C. Koehler, *Electrochim. Acta* **35**, 1383 (1990).
[181]J. Lecoeur, J. P. Bellier, and C. Koehler, *J. Electroanal. Chem.* **337**, 197 (1992).
[182]H. Fukushima, T. Akiyama, K. Higashi, R. Kammel, and M. Karimkhani, *METALL* **44**, 754 (1990).

5

Automated Methods of Corrosion Measurement

Gregers Bech-Nielsen, Jens E.T. Andersen, and John C. Reeve

Department of Chemistry, The Technical University of Denmark

Anne D. Bisgård and Lars Vendelbo Nielsen

Department of Manufacturing Engineering, The Technical Univeristy of Denmark, DK-2800 Lyngby, Denmark

I. INTRODUCTION

Measurements of corrosion rates and other parameters connected with corrosion processes are important, first as indicators of the corrosion resistance of metallic materials and second because such measurements are based on general and fundamental physical, chemical, and electrochemical relations. Hence improvements and innovations in methods applied in corrosion research are likely to benefit basic disciplines as well. A method for corrosion measurements can only provide reliable data if the background of the method is fully understood. Failure of a method to give correct data indicates a need to revise assumptions regarding the basis of the method, which sometimes leads to the discovery of as-yet unnoticed phenomena.

The present selection of automated methods for corrosion measurements is not motivated simply by the fact that a certain measurement can be performed automatically. Automation is applied to nearly all types of

Modern Aspects of Electrochemistry, Number 31, edited by John O'M. Bockris *et al.* Plenum Press, New York, 1997

measurements today. The features of the selected methods are that some could not be applied without automatic devices for control and measurement, and that the automation enables measurements or resolution of measurements, which could not be obtained by manual techniques. Also, even if automation is not essential for applying a given method, it enables numerous measurements to be made in fast succession, possibly at remote locations.

II. CORROSION MEASUREMENTS BY TITRATION

1. General

Corrosion measurements by titration (CMT) were first introduced in 1990.[1] The method is based on the following considerations: When a metal corrodes with no applied current in an aqueous solution, the anodic dissolution reaction

$$Me \rightarrow Me^{z+} + ze^- \tag{1}$$

is combined with cathodic reactions, mostly oxygen reduction

$$z/4O_2 + zH^+ + ze^- \rightarrow z/2H_2O \tag{2}$$

or hydrogen evolution

$$zH^+ + ze^- \rightarrow z/2H_2 \tag{3}$$

This shows that the number of hydrogen ions used in cathodic reactions is equal to the number of charges transferred in the anodic reaction. The pH value in the solution can then be maintained constant by a pH stat, controlling the addition of acid to the solution at such a rate that the loss of hydrogen ions is compensated. Then the following condition is fulfilled:

$$\partial H^+/\partial t = \partial e^-/\partial t = i_c \tag{4}$$

where i_c is the corrosion current. A measurement of the titration rate under pH-static control is thus a direct measure of the corrosion rate. The advantages of the method are

1. The corroding metal electrode is not disturbed by polarization.

2. Because of (1), measurements can be made at short intervals, virtually continuously.

3. The measurements present the rate directly without extended mathematical analysis and interpretation.

Similar advantages can be claimed for a ring-disk electrode system, where the disk electrode corrodes freely, and metal ions arriving at the ring electrode undergo reduction or oxidation reactions and thus also allow a direct measure of corrosion rate via the ring current. However, few stable metal ions can undergo further oxidation, and reduction will often be accompanied by other cathodic reactions, such as those described by Eqs. (2) or (3). Reduction of ions of Al and Mg, for example, cannot take place at the ring electrode. The fabrication of a ring-disk electrode system is rather complicated, and use of the system is restricted to the condition of metal corrosion with a vigorous streaming of solution at the rotating electrode. If corrosion proceeds as a combination of electrochemical dissolution and disintegration of metal (by chunk formation), the metallic particles may dissolve rather fast in the solution, but maybe not before having passed the ring electrode. Detection on the ring electrode will then only relate to contributions from the electrochemical dissolution. In this case, CMT measurements will correspond to the full loss of metal as chunks and by electrochemical dissolution.

2. Restrictions and Limitations of CMT Measurements

The CMT method is based on the direct measurement of chemical change, and a number of restrictions may arise due to the chemistry of the corrosion reactions and the electrolyte solution. The simple relation (4) in accordance with reactions (1)–(3) is not always valid because of complications connected with either the anodic or the cathodic reactions.

The anodic reaction (1) is often followed by hydrolysis

$$Me^{z+} + nH_2O \rightarrow Me(OH)_n^{(z-n)+} + nH^+ \qquad (5)$$

If $n = z$, the loss of hydrogen ions in (2) or (3) is balanced, and there is no need for titration. However, (5) often represents an equilibrium or a number of equilibria associated with various values of n ($< z$). When stability constants for the various hydrolyzed species are known, it is

possible to calculate the effective number of hydrogen ions associated with transfer of one metal ion and thus to arrive at the actual corrosion current.[2,3]

A metal surface that is immersed in an electrolyte solution without prior treatment is often covered by an oxide layer, which can dissolve at the pH of the solution. This gives rise to consumption of acid and is recorded by the CMT measurements in addition to the loss of acid due to electrochemical dissolution. The opposite situation, which could arise during corrosion of an initially film-free metal surface, is the following: At the pH value selected for the experiment, a film of an oxide or hydroxide forms and grows to a certain thickness, after which the thickness remains constant. CMT measurements will then give a zero reading, as long as all oxidized metal is deposited in the film, but when some and finally all of the oxidized metal ions pass the film and enter the solution as simple or partly hydrolyzed ions, the CMT measurements will gradually increase and finally represent the full dissolution rate.[4] The development can be seen more clearly by recording some electrochemical rate measurements during the same period.

A different situation arises when $n > z$. This is the case with metals such as Zn and Al corroding in alkaline solutions. Taking the reaction with aluminum to be

$$Al + 4OH^- \rightarrow Al(OH)_4^- + 3e^- \qquad (6)$$

and combining with (2) or (3) leads to a net loss of one OH^- ion. Hence in such a case it would be necessary to titrate with alkali in order to maintain a constant pH value. This has recently been confirmed experimentally.[5] There is another course of the anodic reaction that can give rise to the need for titration with alkali. This is a fast reaction between the metal ion and a protonated ligand. A recent example is the dissolution of nickel in a solution containing the 1,10-phenanthrolinium ion. At pH values lower than 3.9, more than 90% of the 1,10-phenanthroline is protonated, and the net reaction can be written as

$$Ni + 3HL^+ \rightarrow NiL_3^{2+} + 3H^+ + 2e^- \qquad (7)$$

where L is the 1,10-phenanthroline molecule. The result of (7) combined with (2) or (3) is a gain of one hydrogen ion, so even in an acidic solution

with pH < 3.9, titration with alkali is necessary in order to keep the pH constant. It follows in this case that the corrosion current calculated on the basis of the titration should be multiplied by two in order to fit the number of charges involved in the metal dissolution. Similarly, in the case of aluminum corrosion according to (6), the corrosion current is obtained by multiplying the immediate result from the titration by three.

The anodic dissolution reaction may produce an ion of a lower valence *a*, which is subsequently oxidized in the solution by oxygen or by hydrogen ions to a valence of *b*. Electrochemical measurements will then reflect oxidation to the valence *a*, but CMT measurements will correspond with the final valence *b*. The ratio of the two measurements will be *a/b*.

If cathodic reactions other than (2) or (3) can take place, they should be considered and allowed for with due consideration of their stoichiometry under the conditions of the experiment. It is obvious that partial reduction of some cations, such as

$$Fe^{3+} + e^- \rightarrow Fe^{2+} \tag{8}$$

does not give rise to loss of acid, so CMT measurements cannot detect corrosion combined with this type of reaction. Also, corrosion associated with reduction of the nobler metal ions to metal (galvanic corrosion), such as deposition of copper or silver on steel or other base metals, fails to result in loss of acid.

With various oxidizing anions, reactions such as the following may occur

$$ClO^- + 2e^- + 2H^+ \rightarrow Cl^- + H_2O \tag{9}$$

$$ClO_3^- + 6e^- + 6H^+ \rightarrow Cl^- + 3H_2O \tag{10}$$

both of which involve the same number of charges and hydrogen ions, so that the relation (4) is valid. On the other hand, the reactions of some other anions

$$NO_3^- + 3e^- + 4H^+ \rightarrow NO + 2H_2O \tag{11}$$

$$2NO_3^- + 10e^- + 12H^+ \rightarrow N_2 + 6H_2O \tag{12}$$

$$MnO_4^- + 5e^- + 8H^+ \rightarrow Mn^{2+} + 4H_2O \quad (13)$$

show that there is often not a simple 1:1 ratio between charges and hydrogen ions involved in the reaction, and that reduction of an anion such as nitrate may give different products, each of which results in a particular ratio between charges and hydrogen ions. This means that whenever the cathodic reactions accompanying corrosion include anything but a negligible contribution from reactions of the latter character [in addition to reactions (2) or (3)], there is no safe basis for CMT measurements.

It is readily seen that there are also two types of oxidizing molecular species. The reduction of oxygen according to (2) was included in the basic considerations. Reduction of hydrogen peroxide is of the same type

$$H_2O_2 + 2e^- + 2H^+ \rightarrow 2H_2O \quad (14)$$

but it is obvious that reduction of halogen molecules only involves charges and no hydrogen ions.

CMT measurements should preferably be made in weakly acid or weakly alkaline, unbuffered solutions. In these solutions, a minute loss of acid (or base) results in a measurable change in pH, and the loss is quickly compensated by titration. Each unit of lowering of the controlled constant value of pH from a slightly acid value means a requirement of a ten times greater loss of acid, before titration is triggered. A correspondingly greater amount of acid is then needed to restore pH. The result is increasingly fluctuating measurements when lower pH values are selected. The only way to obtain smoother CMT measurements is by selecting larger intervals between measurements. It is evident that at lower pH values more concentrated acid must be used for titration. In a recent work it was shown that CMT measurements could be made at a pH value of 2.0 when using 0.050 mole/liter HC1 for titration.[6] At pH=4 and higher values, 0.0050 mole/liter HCl can conveniently be used.

Another important point when working at low pH values is the effective concentration of the acid used for titration. Use of 0.0050 mole/liter HCl at pH = 5.0 presents no problems, but at pH = 4.0, the stoichiometric amount of acid is not available for titration. After allowance for the titration required, there must still be enough acid remaining to give the titrant a pH value equal to that of the titrated solution. Taking into account the activity coefficients in a solution of 0.0050 mole/liter HCl and

simultaneously containing 3% NaCl, it could be shown that the effective concentration of acid was 0.0049 mole/liter.[6]

Finally, the gas atmosphere in contact with the solution must be considered. In view of (2) and (3), both oxygen-free and oxygen-containing gas can be used, but the gas must be free of acid or alkaline components, CO_2 must be removed from atmospheric air, and since there is always some CO_2 dissolved in ordinary distilled or otherwise purified water, solutions should be prepared from pure water carefully maintained free from CO_2. Even then it has been observed that when a solution has been titrated to a selected pH value of 5.0, further titration is needed for 15 to 20 min just to keep the pH constant. A recording during this stage, when titration due to corrosion also takes place, makes a false contribution of more than 20 $\mu A\ cm^{-2}$ during the first few minutes.[2] At pH = 6.5, the final adjustment of pH takes even longer due to slow liberation of carbonic acid.[7] It is clearly a shortcoming in the CMT method that it cannot be used to examine the effect of the carbonate system on the corrosion of metals.

3. CMT Measurements with a Polarized Electrode

Although the CMT method was originally developed to measure the corrosion rate at the corrosion potential, it has been demonstrated[6] that it can also be used, with some restrictions, to measure the dissolution rate of a polarized electrode. The device for polarization can be a galvanostat or a potentiostat, the operation of which must not interfere with the pH measurements. Most important, the counter electrode must be in the same cell compartment as the experimental electrode and its content well mixed.

At sufficiently high anodic potentials, only the anodic reaction (1) will proceed at the experimental electrode. Then on the counter electrode the reactions (2) or (3) causing CMT measurements will proceed at the same electrical rate. These CMT measurements should coincide with the value of current measured electrically. The only restriction in this case (other than those discussed in Section II.2) is that dissolved metal ions must not be plated onto the counter electrode in a cathodic reaction in parallel with (2) or (3).

At sufficiently cathodic potentials, metal dissolution according to (1) will be negligible, and again provided that metal deposition does not take place, the reactions on the experimental electrode will be (2) or (3). On the counter electrode, only oxygen evolution is acceptable; being the

reverse reaction of (2), it will compensate for the acid lost in the cathodic reactions, and the result should be no titration and thus a zero reading for CMT measurements. In this case it is important to consider whether unwanted reactions can occur at the anodic potentials (mostly not measured) of the counter electrode. Use of inert electrodes both as the experimental and the counter electrode and a modest concentration of NaCl in the electrolyte solution (3%) demonstrated chlorine evolution at very low current densities.[6] Since this reaction does not generate acid, there was a false titration not relating to metal dissolution.

Significant CMT measurements due to two types of reactions at low cathodic potentials can then be recorded: Dissolution of oxide layers or transfer of metal into solution without charge transfer. Oxide layers are often present, formed by exposure to air or generated in solution as passivating or partially passivating films. At low potentials, these oxides may undergo both electrochemical reduction to metal and dissolution. Electrochemical reduction will release an amount of base equivalent to the corresponding partial current, which is counterbalanced by the anodic reaction at the counter electrode; however, dissolution of oxides will release a base, requiring a separate titration. Oxide layers may persist for rather long periods, but ultimately their contributions to dissolution and reduction reactions should disappear.

The other type of dissolution reaction, metal dissolution without charge transfer, is a subject involving conflicting ideas. It is well known and clearly demonstrated that during uneven anodic dissolution of metals some fragments or "chunks" may simply fall off the metal.[8] In the solution, the less noble metals will then corrode according to (l)–(3), so CMT measurements will include the amount of metal lost in this way, while electrochemical measurements will be unable to detect this loss. Demonstration of any chunk effects could thus be made during anodic polarization, but with cathodic polarization and hardly any anodic dissolution, there is no basis for expecting chunk effects.

Dissolution of some metals can, however, take place at cathodic potentials. Two theories have been advanced to explain the phenomenon,[9,10] and a third one has recently been formulated for a special case.[6] These theories are discussed in connection with the experimental results, but it is obvious that when metal can be transferred into a solution before charge transfer has taken place, then, just as with chunks, subsequent

oxidation in the solution according to reactions (1)–(3) will cause loss of acid and thus allow CMT measurements.

In the vicinity of the corrosion potential, the partial anodic and cathodic currents are of comparable magnitude. The net current flowing through the cell is given by

$$i_{exp} = i_+ - |i_-| = - i_{count} \tag{15}$$

where i_{exp} is the current passing the experimental electrode i_+, and i_- are the partial anodic and cathodic currents due to the reactions on the experimental electrode, and i_{count} is the current passing the counter electrode. Rearranging (15) gives

$$i_+ = |i_-| - i_{count} \tag{16}$$

This shows that for both net anodic and net cathodic currents at the experimental electrode, the sum of the cathodic partial current at this electrode and the current at the counter electrode (anodic or cathodic) is equivalent to the anodic metal dissolution reaction. The combined cathodic reactions will thus give rise to titration corresponding to the metal dissolution rate.

4. Instrumentation and Recording of CMT Measurements

The necessary equipment for a pH stat is easily available, but to obtain highly reliable measurements with a minimum of fluctuations, the greatest care should be used to select instruments of especially high reliability and precision. In all work quoted here the following instruments from Radiometer International A/S were used:

A PHM84 Research pH meter reading pH values with three decimals. In all well-behaving experiments, the pH value could be maintained constant within one or two units in the third decimal place. After an experiment lasting 4 days, the drift in the buffer adjustment was less than 0.02 units.

A combined glass-reference electrode, GK2401C.

A TTT80 Titrator controlling the buret.

An ABU89 autoburet, volume 25 ml, providing a pulse to external units for each microliter delivered.

In addition to these instruments, an interface[2] was required. The interface serves to count the pulses coming from the autoburet. The time it takes to deliver a preset number of microliters (1,2,5,10...) is measured accurately; selection of a higher number of microliters eliminates the effect of mechanical imperfections in the operation of the buret and gives less fluctuating measurements, but also less frequent ones. By the time a CMT measurement has been completed, there is a recording of pH and also of the potential of the corroding metal vs. a separate reference

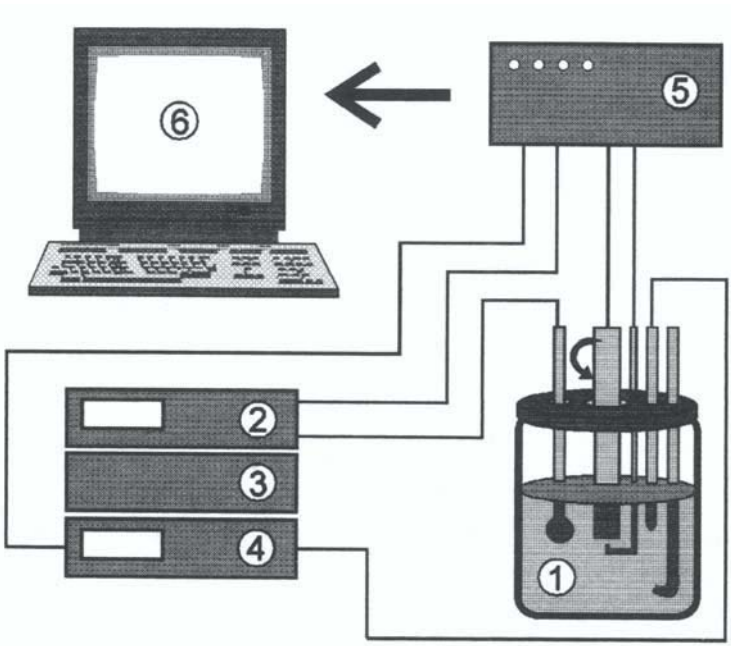

Figure 1. CMT system with rotating disk electrode. 1. Cell containing (left to right) combined glass and reference electrode, rotating disk electrode, reference electrode with Luggin capillary, capillary tip for titration, and glass tube for gas bubbling. 2. Digital pH meter (±0.001 units). 3. Titration controller. 4. Autoburet (±1 μl). 5. Interface reading, as a function of time, outlet from autoburet, pH, potential of the metal electrode vs. the reference electrode and transferring data to 6, personal computer. (Reprinted from Ref. 3, with kind permission from Elsevier Science Ltd., Kidlington, Oxford, UK.)

electrode. These data are then transferred to a personal computer. During an experiment, incoming data are treated continuously, and corrosion potential and the calculated rate of corrosion are plotted on the screen as functions of time. The connections to the electrochemical instruments are shielded from PC signals by optocoupling.

Two types of cell have been described. In Fig. 1 a cell with a rotating disk electrode is shown. Connections to a pH-stat and to the interface are indicated; simultaneously with recording CMT measurements, the metal and reference electrode and a counter electrode (not shown in Fig. 1) can be connected to a potentiostat, so that electrochemical measurements can be recorded intermittently. The volume of solution in the cell is ca. 400 ml. What matters for safe and reliable conditions of measurement is that the disk electrode rotating at a speed of no less than 1000 rpm ensures efficient stirring, so that the effect of alkali formed at the corroding metal (or sometimes at the counter electrode located ca. 1 cm below and parallel to the metal electrode) is immediately sensed effectively by the glass electrode and also the effect of acid supplied from the autoburet is quickly detected.

The use of a rotating disk electrode is convenient in many ways. Cylinders of various metals, of metal plated on other metals, or of variously post-treated metals can readily be made with fixed dimensions. The standardized test material facilitates comparison of results. However, the need for fast rotation for stirring means that corrosion measurements obtained in this way refer to conditions of fast streaming of solution over the surface of the metal. It is possible to calculate the diffusion rate of oxygen arriving at the electrode surface and to see the effect of increasing rotation rates, but it is difficult and risky to extrapolate measurements to lower rotation rates. In some cases a protective layer might form on the metal if the corrosion products were not washed away by the vigorous stirring. In order to overcome these problems, an arrangement with a flow channel cell has been used.

Figure 2 shows the essential parts of such an arrangement. There is a (smaller) cell with provisions for measurement of pH, titration, stirring with an inert stirrer, and gas bubbling through the solution. When the solution in this cell has been titrated to the selected pH value, a peristaltic pump takes the solution to the inlet of the flow cell. Before the solution comes to the metal electrode, it passes two thin holes in the bottom of the

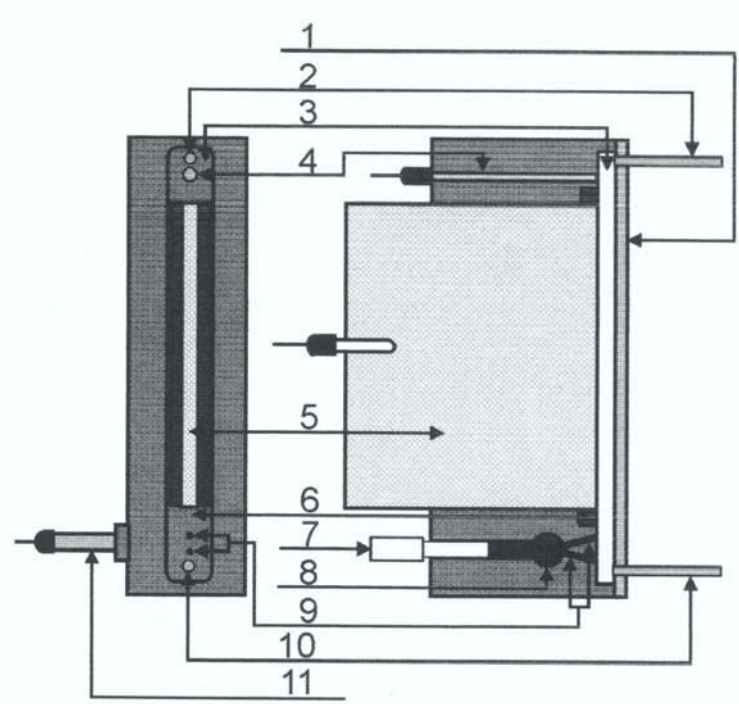

Figure 2. Flow cell (excluding pump and titration cell). Left: Front view. Right: Cross section along center line. 1. Perspex cover. 2. Outlet tube (back to titration cell). 3. Flow channel. 4. Counter electrode (platinum). 5. Metal plate with cut edge exposed in the channel. 6. Seal of molded silicone rubber. 7. Piston for removal of air from reference electrode compartment. 8. Reference electrode compartment. 9. Capillary holes connecting 8 to 3. 10. Inlet tube (from titration cell). 11. Reference electrode (Ag/AgCl, sat. KCl). (Reprinted from Ref. 3, with kind permission from Elsevier Science Ltd., Kidlington, Oxford, UK.)

channel that connect to a reference electrode compartment. The delivery rate of the pump is variable. In one version of the cell, a flow rate in the channel of 0.49 to 5.6 cm/min could be selected. The metal electrode and a counter electrode are mounted so that they form a part of the bottom face of the channel.

At the end of the channel, the solution is returned via a short, thin tube, to the titration cell. Titration of alkali formed by corrosion is thus

delayed by the time it takes the solution to pass from the metal electrode to the titration cell. This is not a serious problem. However, a CMT reading is stored together with a time measurement and a simultaneous reading of the potential. The latter represents the actual value at the time recorded, while the CMT reading refers to this recorded time minus the delay.

In addition to a free choice of flow rate, this cell also allows use of electrodes of shapes other than a circular disk. The cell shown in Fig. 2 was designed for examining the corrosion of only the edge of a 2-mm-thick plate, which had been laser cut.

Recently a new pH-stat instrument (PHM290 with autoburet ABU901) was introduced by Radiometer International A/S. This instrument can be connected directly to a personal computer, so that titration data and pH can be recorded in a Windows-based program. A recording of corrosion potential must then be made by another instrument, but both titration data and potential measurements can be recorded simultaneously using two inputs.

The advantages of the new instrument are the direct communication with the personal computer (so that an interface is not needed) and digital settings for buffer adjustments and end point. It is a limitation that titration data can only be read at fixed time intervals. The intervals chosen must be long enough for at least 25 to 30 pulses (each representing a 1-μl addition of titrant) to be counted, and the significance of a pulse arriving just before or after the end of the interval becomes sufficiently low. A test in the chemistry department of the Technical University of Denmark has confirmed good stability, reliable performance, and a smooth course of the measurements for titration with more than 50 μl during a time interval.

5. Aim and Results of CMT Measurements

There is an obvious need for simple, fast, and reliable corrosion measurements on metallic products, whether use in particular environments is the concern, or whether the application of a particular post-treatment necessitates a control. Various types of chamber tests are used for technical testing. These tests are "accelerated," which means that the metallic items are exposed to more aggressive conditions than they are expected to meet during actual service, but it still takes a long time to obtain a measurement. The measurement indicates the time to failure (to a certain degree or

totally) but gives no details on the development and course of the corrosion processes.

The CMT method was primarily developed to replace traditional corrosion tests with a faster, quantitative test. Since the course of corrosion with time is continuously shown on the screen, it is easy to see if and when a stable situation has been established, resulting in a constant rate of corrosion. The rate of corrosion at that stage can often serve as a safe measure of the lifetime of the object. An assessment of quality on the basis of such a measurement can be made in a much shorter time than by a chamber test. In the latter, a good quality product should typically have a time to failure of more than 100 h, whereas a CMT test of a similar product mostly shows a stable, constant rate of corrosion (on the order of 5–10 $\mu A/cm^2$) after less than 2 h.

In most cases CMT measurements have been supplemented by electrochemical measurements; these measurements were performed at intervals because of the unavoidable disturbance of the corroding metal. It is important that the electrochemical (EC) measurements give reliable values for corrosion current density. In all work quoted here, only one electrochemical measurement method has been used.[3] Data obtained by this method are indicated on diagrams as EC measurements. Reliable results can be obtained with well-behaving systems. In general, the error in a measurement is less than 20% and often no more than ca. 10%. Considering this, and the fluctuations often seen in CMT measurements, it is not easy to discern very modest deviations between EC and CMT measurements, but larger and significant ones are clearly seen.

(i) Observations with Zinc and Alloyed Zinc

A great number of measurements have been reported for articles electroplated with zinc. The various aims have been: evaluation of the corrosion rate of zinc that had been plated in a number of commercial cyanide-free zinc baths,[11] comparison of the corrosion rate of a composite material (zinc with codeposits of various oxides) and of pure zinc deposits,[12] corrosion testing of various alloyed zinc platings (Zn-Ni, Zn-Co, Zn-Fe), with or without subsequent post-treatment. Most of the work in the last category was only recorded in internal reports. The published work consists of an examination of the corrosion behavior of a chromated Zn-Fe

alloy[13] and corrosion testing as a tool for developing a chromate-free post-treatment for zinc and other metals.[14–15]

The work described above provided the technical information for which the CMT method had been developed, while various details of the instrumentation and programming were improved. However, it became obvious at an early stage that there is very rarely agreement between CMT and electrochemical measurements, even if the two are recorded simultaneously. The reliability of the CMT measurements has been tested in several cases (see Refs. 2 and 13, for example), where a sufficient amount of metal had been dissolved during an experiment. Analysis of the cell solution has then in most cases agreed very closely with the result according to the CMT measurements (the total amount of acid used in the experiment is displayed on the autoburet).

The discrepancies between CMT measurements and electrochemical measurements have given rise to some closer examinations revealing a number of different causes ranging from trivial to novel phenomena.

The first striking observation of widely differing CMT and EC measurements was seen with a Zn-Ni alloy with 5% Ni.[16] Because of tensile stress in this particular alloy,[17] cracking and hence loss of particles into the solution caused the CMT measurements to be higher than the EC measurements for some time, until relief of stress brought the cracking to an end. After this, the dissolution apparently took place only by an electrochemical mechanism, and the CMT and EC measurements gave more nearly the same result.

A different pattern of dissolution was seen with a Zn-Sn alloy containing 26% zinc.[2] In this case the stable dissolution situation established after ca. 90 min showed a ratio of EC to CMT measurements of 1:4. As seen in Fig. 3, this remained fairly constant, though the corrosion potential increased by more than 50 mV. Only selective zinc dissolution took place, and analysis by atomic absorption spectroscopy of the amount of dissolved zinc agreed within 10% with the value according to the titration. This pattern is still difficult to understand. The ratio of ca. 1:4 between EC and CMT measurements could be interpreted in terms of formation of the low-valent zinc species Zn_2^+, which seems unlikely, or in terms of dissolution of divalent zinc ions accompanied by loss of chunks consisting of precisely three zinc atoms, each time a zinc ion is dissolved. The latter alternative seems to require a more discrete mechanism of dissolution than

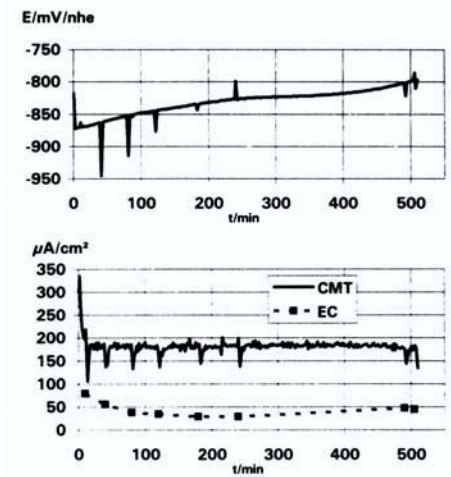

Figure 3. Long-term corrosion measurement of an electrolytic Sn-Zn alloy containing 26% Zn (by weight) in a 3% NaCl solution, pH = 4.000, with argon bubbling through the solution. Upper diagram: corrosion potential vs. time; lower diagram: CMT and EC measurements vs. time. After 80–100 min, the ratio CMT/EC is close to 4. (Reprinted from Ref. 2, with kind permission from Elsevier Science Ltd., Kidlington, Oxford, UK.)

usually seen, when chunk effects appear. There are some similarities between the observations in this experiment and those quoted in the following example.

The most striking results were obtained with a chromated Zn-Fe alloy (0.3% Fe).[13] It was confirmed that the particularly good corrosion resistance of this alloy is due to the properties of the chromating layer,[18] which remained firmly attached to the metal surface until nearly all of the zinc alloy had been dissolved. This feature rules out chunk effects, so that a shift in the ratio of EC to CMT measurements from a little less than one to one half (over a long time and accompanied by an increase in corrosion potential by 120 mV) could best be explained as a result of a shift in

dissolution valence from 2 to 1. A kinetic model combining two dissolution reactions, one forming divalent zinc ions and the other forming a relatively short-lived monovalent species, Zn_2^{2+}, predicted the same development of corrosion potential and apparent dissolution valence as that observed. The model explained at the same time a typical pattern of etching observed with pure and alloyed zinc that had not been chromated. A recent publication[19] dealing with inhibition of zinc corrosion by suspended inert particles in the solution gives further support to the above model.

(ii) Observations with Nickel

It was found at an early stage that there is an anomalous dissolution reaction for nickel in oxygen-containing solutions.[16,20] However, it was difficult to prove that CMT measurements exceeding the simultaneous EC measurements were not just the result of dissolution of oxides or of chunk effects. Lately a convincing and simple demonstration of the phenomenon has been given.[6] Shifting between an oxygen-containing and an oxygen-free atmosphere appeared to be the only factor giving rise to (a) CMT measurements some three to four times higher than the simultaneous EC measurements in the presence of oxygen, but (b) CMT and EC measurements becoming equal in the absence of oxygen (at a constant potential) (Fig. 4).

Several other important features of the anomalous dissolution reaction were revealed by the CMT measurements, but they seemed to support the following general interpretation: Dissolution of nickel can take place without charge transfer and under conditions where chunk effects or effects of trapped hydrogen can be excluded. It has been suggested[6] that a complex of nickel ad-atoms and anions of the solution can attach an oxygen molecule and thus form a soluble species. Many other metal complexes are capable of forming such complexes with undissociated oxygen molecules,[21] in some cases reversibly, as with hemoglobin. After the complex has passed the electrochemical double layer, a normal nickel ion is formed in a redox reaction, resulting in CMT measurements that exceed the EC measurements.

Under the conditions of the experiments revealing the effect of oxygen (with solutions of chloride, sulfate or perchlorate ions at pH 4 or lower), it was not possible to observe the potential-independent dissolu-

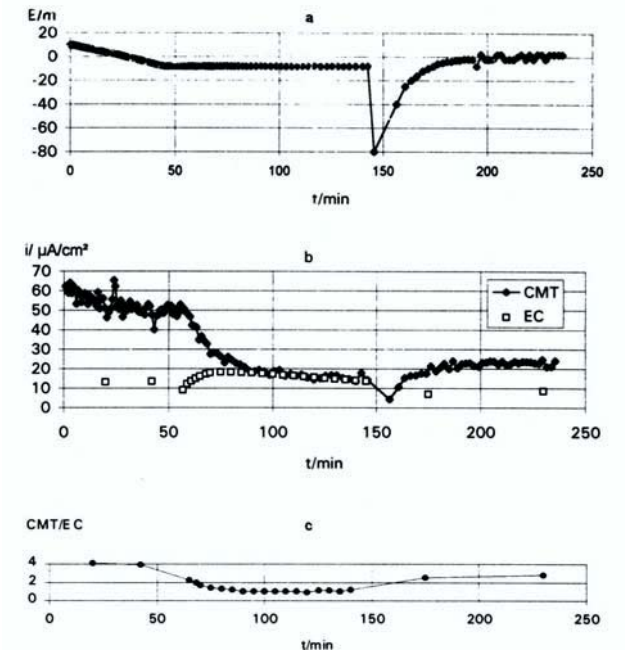

Figure 4. Recording of an experiment with a wet-ground (100)-oriented single-crystal nickel electrode. Rate of rotation: 1000 rpm, 2.0*M* NaCl solution, pH 4.000, 25.0°C. A CO_2-free air was bubbled through the solution for 45 min, Ar between 45 and 146 min, then again CO_2-free air. The electrode was left at its corrosion potential for 45 min, then potentiostatically controlled until 146 min, then left at its corrosion potential. Diagram a. Potential. Diagram b. EC and CMT measurements. EC measurements give the calculated corrosion cd before 45 min and after 146 min. From 45 to 146 min, cd readings at the fixed potential. Diagram c. The ratio of CMT to EC measurements. (Reprinted from Ref. 6, with kind permission from Elsevier Science Ltd. Kidlington, Oxford, UK.)

tion reaction of nickel reported earlier by Penov and co-workers.[22] However, when nickel dissolution was studied using the same set of solutions at pH 3.7 or 6.3, but now containing a strong complexing agent (1,10-phenanthroline), it was found that also in the absence of oxygen the net dissolution reaction was much faster than the electrochemical dissolution

reaction.[5] Kolotyrkin has stated that most metals are capable of dissolving via nonelectrochemical reactions.[23] The work quoted above seems to indicate that such reactions may be significantly enhanced by various substances, forming relatively stable, soluble complexes with metal ad-atoms.

6. Concluding Remarks

It is likely that combined CMT and EC measurements can contribute to further information about the basic details of several other corrosion processes and provide more reliable data for corrosion rates than EC measurements alone. Concerning the possible use of CMT measurements as a routine test of technical products, some of the limitations (it can't be used with iron and steel in aerated solutions or with other metals in bicarbonate solutions) are rather serious. However, there are still many applications where the fast and quantitative results obtained by CMT measurements would seem advantageous.

III. IMAGING CORROSION BY SCANNING PROBE MICROSCOPY

1. General

Scanning probe microscopy (SPM) techniques rely on computer recordings of interactions between the tip of a minute probe and the surface of the small specimen as a function of position; the measurements are used to depict an image of the atomic-scale surface topography on the computer screen. Mechanical control, recording, and data processing must therefore be automated to a high level of precision and reliability. These general techniques and the apparatus involved have been described extensively.[24–35] The automated methods of such high-resolution microscopy coordinated with computerized electrochemical measurements as well as elemental analysis look very promising for elucidating corrosion reaction mechanisms. The study of initial surface reactions at the atomic or submicron level is becoming an important field of research in the understanding of corrosion processes. At present, mainly two scanning microscope techniques are employed investigating corrosion processes, and usually *in situ*: *in situ* scanning tunneling microscopy (*in situ* STM) and *in situ* atomic

force microscopy (*in situ* AFM). It is these techniques to which attention is directed here.

2. Use of STM and AFM in Corrosion Studies

As a rule, *in situ* STM is applied to conducting surfaces and *in situ* AFM to insulating surfaces.[30] In order to minimize faradaic currents at the tip surface, except for the sensing extremity, the tip must be coated by an insulating material such as epoxy resin, glass, or electropaint.[31–33] The electric insulation limits faradaic currents to the tip because these currents would otherwise introduce a significant error by making the tip current deviate notably from the actual tunneling current; such an error would, of course, give an error in the image generated.[33]

In addition, a bipotentiostat is used to control the tip potential with respect to the surface and independent of control of the surface potential with respect to the reference electrode.[30] The tip potential E_t is given by $E_t = E_B + E_w$, where E_B is the bias potential that generates the tunneling current between tip and surface, and E_w (a vital variable not typical of other applications of STM and AFM) is the potential of the surface relative to the reference electrode.

This experimental setup has a dual purpose. First, it enables further reduction of tip faradaic currents during recording of images, thus improving image clarity. Second, if the faradaic contribution to the total tip current is not too large, it allows the tip to be used actively to examine the electrochemical processes that are simultaneously occurring on the surface being imaged. Although, as explained earlier, such an involvement of the tip in faradaic processes is undesirable, it is sometimes advantageous to be able to use the tip as an independent electrochemical probe. In this mode and with a coated carbon fiber tip, the technique is called scanning electrochemical microscopy (SECM).[27–28] For *in situ* AFM, a more usual three-electrode potentiostat is sufficient to control the electrochemistry of the system while the surface is being imaged. When the scanning techniques are used to study dynamic changes occurring at the surface, there are some limitations to be considered that are defined by the scanning speed and the sensitivity of the electrochemical equipment. In the lower limit, metal deposition followed atom by atom requires a highly stable surface with little drift and a low (nA) electrochemical current. When fast changes on the surface are to be followed, the upper limit for electrochemi-

cal current lies in the vicinity of $30\ \mu A/cm^2$, depending on the scan speed and the desired image quality.[36]

Although oxides are generally considered to be insulators, it is sometimes possible to monitor the surface of an oxide film by STM. Basically two mechanisms that explain the imaging of oxide surfaces by *in situ* STM are considered:

1. Oxides may exhibit conductivity or semiconductivity, depending on the lattice oxygen content. Oxides of the transition groups of metals especially can exhibit conductivity as a result of a deficiency of lattice oxygen. In oxides, electronic conduction proceeds by the hopping of electrons between sites of oxygen depletion to which they are attracted and where electron density is low. The electronic structures of such oxides have considerable electron density in the band gap. Electrons close to the top of the valence band may consequently be excited to the conduction band by thermal excitation.[37] Demonstrating this effect, excellent *ex situ* images have been obtained with atomic resolution of TiO_2 [38] and V_2O_5 [39] surfaces.

2. The oxide film may be very thin, involving only a few monolayers, so that electron tunneling through the film may occur.

Surfaces of transition metals that have been passivated by electrochemical oxidation or by the action of chemical oxidizing agents have been extensively investigated by *in situ* STM/AFM; these investigations have yielded a wealth of new and interesting information.[36] Figure 5[40] illustrates atomic resolution obtained by *in situ* STM of chromium oxide on aged passivated Fe-25Cr surfaces; the unit cell of chromium oxide can be recognized. After Ni(111) was passivated in $0.05M\ H_2SO_4$, an epitaxial layer of nickel oxide was imaged by *ex situ* STM also with atomic resolution (Fig. 6).[41] The images of Figs. 5 and 6 were obtained after passivating the metallic surface in the potential region below the pitting potential, and they demonstrate that it is indeed possible to image oxide layers on metal surfaces. Aging of the thin film of oxide under potential control increases the stability of the passive film in air, which is explained by the formation of an interfacial oxide layer grown below the top surface layer.[43,44]

Most of the early corrosion studies by *in situ* methods were directed toward elucidation of the mechanism of pitting corrosion, the nature of the transition from the potential region for passivation to the pitting

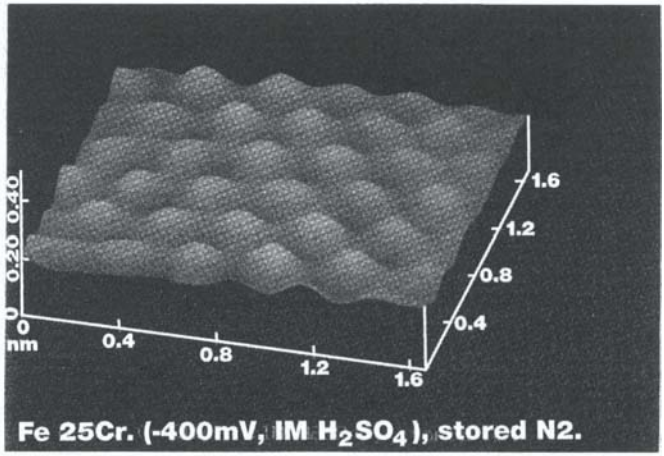

Figure 5. Filtered 3D representation of the triangular lattice on passivated and aged Fe-25Cr. (Reprinted from Ref. 40 by permission of The Institute of Materials, London.)

potential, and the mechanism of pit formation. These results confirmed the current ideas but also provided valuable new insights. In the following sections corrosion processes have been collected under four main headings, all related to processes occurring in the anodic range of potentials.

1. Potential excursions provoking surface oxidations and surface reconstructions of crystalline surfaces. These phenomena can be monitored on noble metal surfaces over a wide range of potentials. With the unique atomic resolution of *in situ* STM/AFM, it is possible to follow corrosion processes in real time at the atomic level.

2. The low overpotential regions with metal dissolution and inhibition. The results from these investigations include information concerning aspects of metal dissolution, mobility of surface atoms, and the blocking actions of both noble metal atoms and organic inhibitors.

3. Potential regions involving passivation. The passivation of the surfaces of metals of the transition metal series has been followed by *in situ* STM, which at first was expected to be usable only on unoxidized metal surfaces. Passivation has been followed on stainless steel, nickel, and titanium in various buffers and chloride-containing electrolytes.

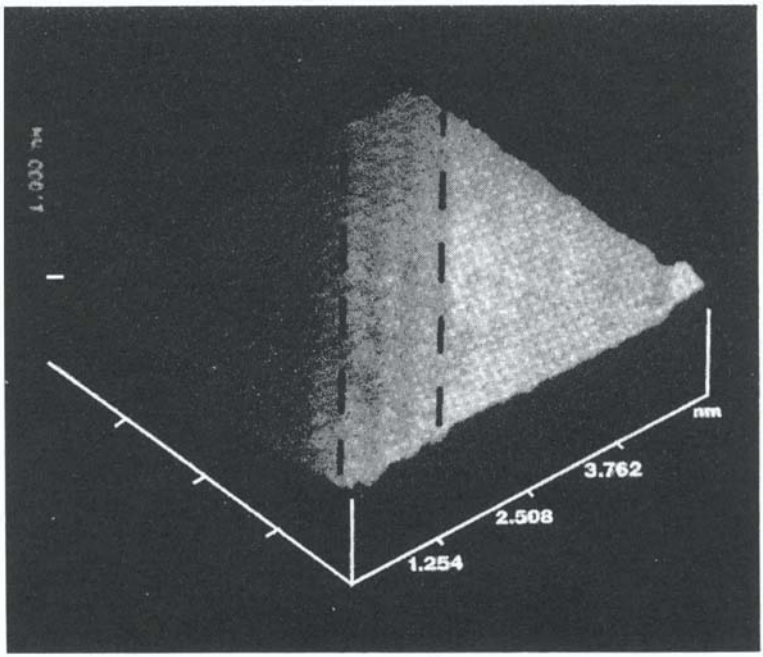

Figure 6. A 5×5-nm^2 topographic image of the fine structure of a step edge along the [−101] direction of the Ni surface passivated at +750 mV/SHE, V_t = +113 mV, I_t = 0.5 nA. The lines indicate a two-stage transition between the upper terrace (right) and the lower terrace (left). (Reprinted from Ref. 41 by permission of The Institute of Materials, London.)

4. Regions characterized by large anodic overpotentials. Under such conditions, complete passivation and severe oxidation of most metal surfaces occurs. A breakdown of passive oxide layers and pitting corrosion is observed for transition-metal model systems. In this section are considered also the surfaces of electropositive metals such as aluminum.

(i) Stability and Reactivity of Crystalline Surfaces

Owing to the inherent capability of obtaining atomic resolution by *in situ* STM/AFM, much effort has been devoted to its application in studies of crystalline surfaces, including their stability and chemical

reactivity as a function of potential.[35] It has been shown that, depending on the potential, specific adsorption of anions (e.g., OH^-, ClO_4^-, HSO_4^-, and Cl^-) occurs, and this may initiate the surface reconstruction of the model crystalline systems provided by gold and platinum.[35]

The bond strength of substrate surface atoms is diminished by anion adsorption, thus causing significant surface relaxation. The bonds may become so weak as to induce mobility in the surface atoms. Surface atom mobility has been studied in detail at atomic resolution or near atomic resolution in model systems.

Vitus and Davenport[25] showed that upon anodic oxidation of Au(111), a monolayer of AuO was formed on the surface, maintaining the surface crystallinity. Subsequent electrochemical reduction of the oxide formed a characteristic wormlike structure that coarsened in a matter of hours to restore the original terrace structure of the substrate surface. This result shows that repeated potential cycling performed in the anodic region may destroy or roughen the surface owing to a lack of coalescence of surface atoms after oxide reduction.

(ii) Metal Dissolution and Inhibition

Consideration of surface mobility of gold atoms in a Cu_3Au alloy is important in understanding the presence of a critical potential E_c above which corrosion currents increase by orders of magnitude.[29] Moffat *et al.*[29] showed that the gold atoms are highly mobile on the surface, and at low overpotentials they block the dissolution of copper atoms. At potentials above E_c, the gold atoms are held less firmly and become unable to protect the copper; this results in a general roughening of the surface (Fig. 7). The influence of the blocking action of gold atoms owing to the surface tension of the gold film leads to some points of resemblance with the behavior of systems in which inhibitors have been introduced.

Inhibitors form a film on the surface that blocks the dissolution of the substrate. Adsorption of an alkyl-thiol to the surface of the Cu_3Au alloy resulted in an increased surface tension of the gold film; this is observed as an increase in the value of E_c, which depresses dissolution of copper. This behavior resembles inhibition of copper corrosion on a pure copper surface where benzotriazole increases the potential to start significant copper dissolution; this was demonstrated by Cruickshank *et al.*[45] using *in situ* AFM. However, when the critical potential for benzotriazole film

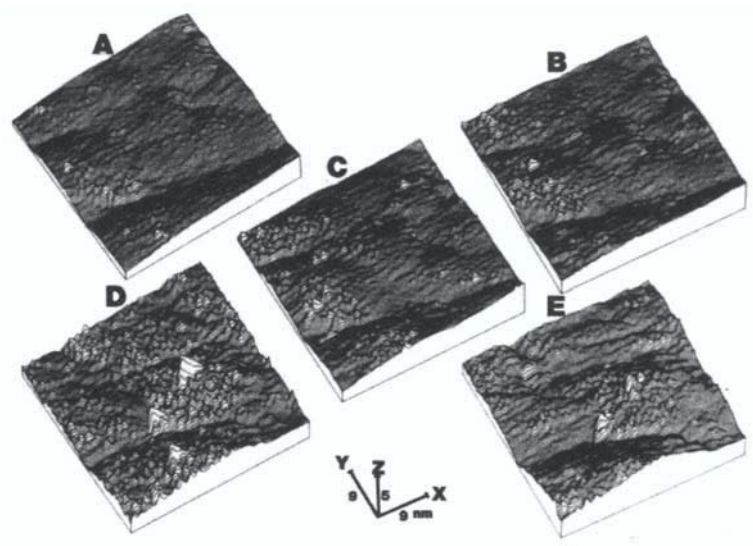

Figure 7. A sequence of constant-current STM images of disordered Cu_3Au following polarization above the critical potential, $E_c = -0.250$ V; (A) at 0.0 V for 30 min, (B) at 0.3 V for 2 min, (C) 0.3 V for 4 min, (D) at 0.4 V for 4 min (E) reverse potential step to 0.0 V after 4 min. (Reprinted from Ref. 29 by permission of the publisher, The Electrochemical Society, Inc.)

breakdown was exceeded, the corrosion in this case was vigorous and resulted in pit formation. This type of film protection of the substrate also resembles passivation of transition metal surfaces.

(iii) Passivation of Surfaces

Below the pitting potential, in the passivation region of potentials, a complete and coherent oxide film protects the surface against metal dissolution. With the aid of both *ex situ* STM and *in situ* STM, Ryan *et al.*[40] showed that images displaying atomic corrugation could be obtained with a passivated and nitrogen-aged film on Fe-25Cr. The periodicity of the image features corresponded to unit cell dimensions, probably displaying a chromium(III)-oxide lattice (Fig. 5). Atomic corrugation on Ni(111) passivated in 0.05*M* H_2SO_4 was obtained by Maurice *et al.*[41–42] using *ex*

situ STM imaging. The NiO surface displayed a kinked and stepped structure with rows of oxide atoms aligned along the edges (Fig. 6).[41–42]

At high potentials in the passive region, the imaging of nickel surfaces proves difficult owing to the formation of thick oxide layers.[46] It was shown by Bhardwaj *et al.*[47] that on polycrystalline iron in a borate electrolyte, oxide formation starts as patches on the surface that gradually fuse together to establish a surface oxide film. Also, clusters of the hydroxide were seen[48] on a polycrystalline iron surface observed by *in situ* STM and after potential cycles in an NaOH electrolyte.

Stainless steel (SS) is protected against corrosion by a passivating oxide layer, but corrosion may be initiated by addition of chloride ions. In buffered chloride electrolytes, corrosion of SS surfaces is initiated at surface defect sites or edges, and the surface is slowly roughened, with steps formed at random across the surface.[49] Upon addition of a pitting corrosion inhibitor such as *N*-lauroylsarcosine (NLS), Fan and Bard[49] showed that the inhibition mechanism is different from the film formation mechanism discussed earlier for copper surfaces exposed to benzotriazole. The addition of NLS to SS in chloride electrolytes leads to the buildup of an insulating interfacial layer with a disordered structure and of more than monolayer thickness. The precise composition and growth of this layer needs further investigation to be fully understood.[49]

(iv) Pitting Corrosion

On a clean surface of an $Fe_{17}Cr$ alloy in a 0.5*M* NaCl electrolyte, corrosion is accelerated as pitting corrosion when a potential pulse of 1 s duration extending from the passive region and above the pitting potential is applied.[50] Gugler *et al.*[50] showed by *in situ* AFM that in this case the pitting corrosion was initiated close to an inclusion on the surface (Fig. 8). Such a surface defect may act as a center for pit nucleation, as was

---

Figure 8. An Fe-17Cr stainless steel surface near a handle-shaped inclusion observed by AFM in 0.5*M* NaCl. (a) Surface at the corrosion potential of −240 mV (SCE). (b) Surface after application of a potential pulse of 1 s to 650 mV to initiate pitting, then anodically polarized at 150 mV (SCE). The pitting potential is approximately 350 mV. (Reprinted from Ref. 30 by permission of The Institute of Materials, London.)

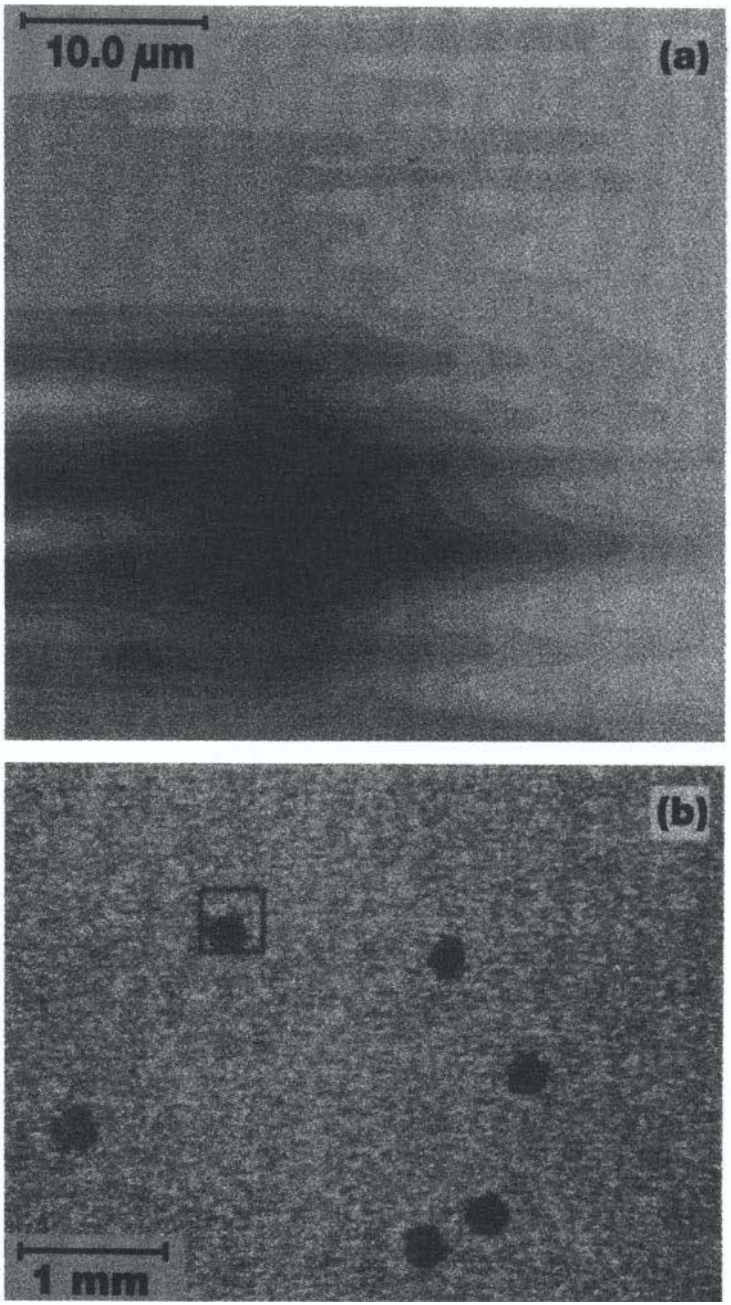
10.0 μm
(a)
(b)
1 mm

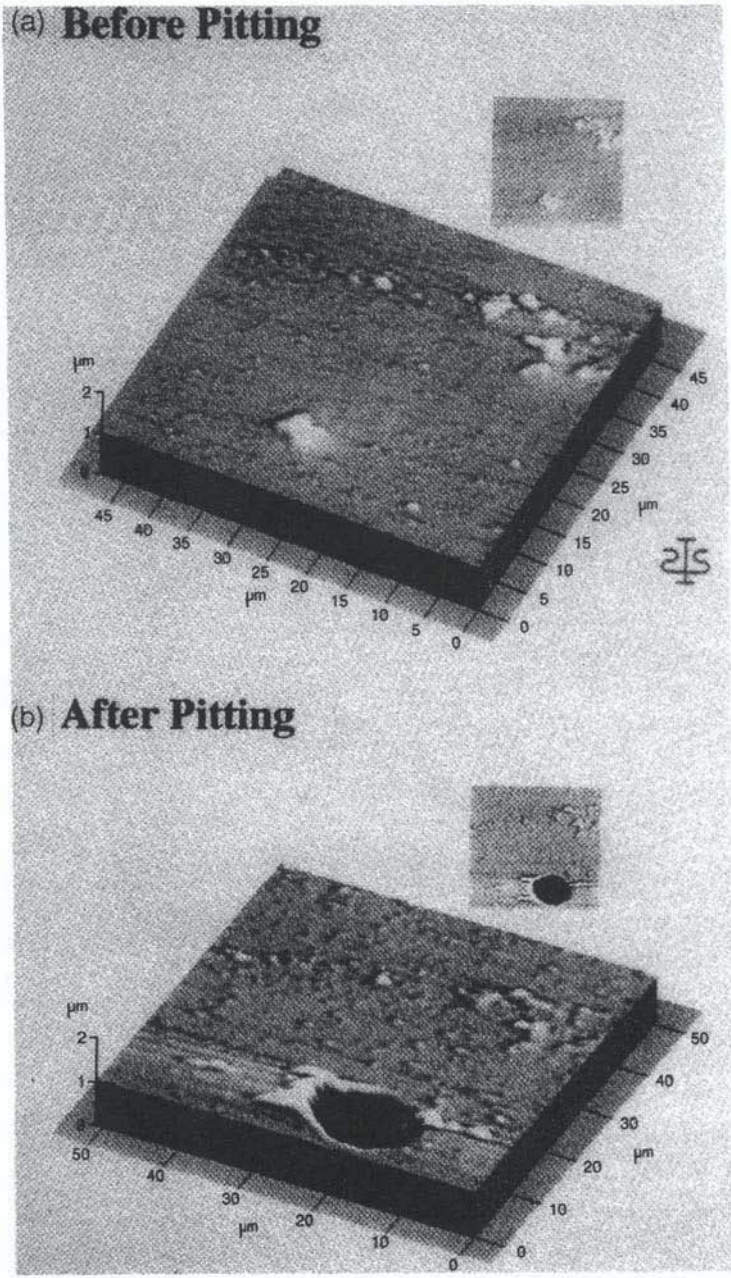
(a) Before Pitting
μm
2
1
0
45
40
35
30
25
20
15
10
5
0
μm
(b) After Pitting
μm
2
1
0
50
40
30
20
10
0
μm

shown by Casillas *et al.*[51] working with titanium surfaces in bromide–sulfuric acid media.

In an excellent combination of SECM imaging and optical microscopy, Casillas *et al.*[51] showed that the sites of pit nucleation on the surface can be predicted by SECM before any pitting appears. On the titanium surface, the pitting sites may represent oxygen vacancies, as discussed earlier, because they exhibit centers of high electronic conductivity. The high electronic conductivity correlated well with oxidation of bromide to bromine on the passivated titanium surface, the oxidation occurring rapidly on only a few microscopic surface sites.[51] Imaging of these sites of high faradaic activity thus provides a means for identifying precursor sites for pit formation. The number of active sites that were identified as sites of bromine generation was estimated to be approximately 50 sites/cm^2 for a 500 nm thick oxide film.[52–53] A detailed micrograph of a single precursor site of pitting corrosion imaged by SECM is shown in Figs. 9a and 9b.

Typically, oxidation of bromide generates only small measured currents. However, if it is assumed that all the current passes through the active sites within an area of approximately 500 nm diameter, the current density at the active regions would be very large indeed and on the order of 1 A/cm^2. Thus, the oxidation of bromide is associated with an intense but highly localized current.

These detailed microscopic studies show that it is possible to predict how and where pitting corrosion will occur on the surface. Like the titanium surface, an aluminum surface is passivated at normal temperatures by formation of an oxide layer in the ambient atmosphere. Despite formation of an oxide layer, aluminum surfaces can also be studied by STM.[54] Pitting corrosion can be observed after 10 h of immersion of an aluminum surface at –1.2 V/normal hydrogen electrode in a 10^{-2} *M* NaCl electrolyte.[30] The pitting on aluminum is observed as a general roughening

Figure 9. (a) SECM image of a precursor site for corrosion pitting of Ti obtained at 1.5 V in a 1*M* KBr/ 0.05*M* H_2SO_4 solution. (b) Optical photograph showing the position of oxide breakdown after the potential was increased to 3.0 V. The box outlined in part (b) corresponds to the area imaged by SECM in part (a). The location of three of the pits visible in the optical photograph were detected by SECM prior to oxide breakdown. (Reprinted from Ref. 51 by permission of The Electrochemical Society, Inc.)

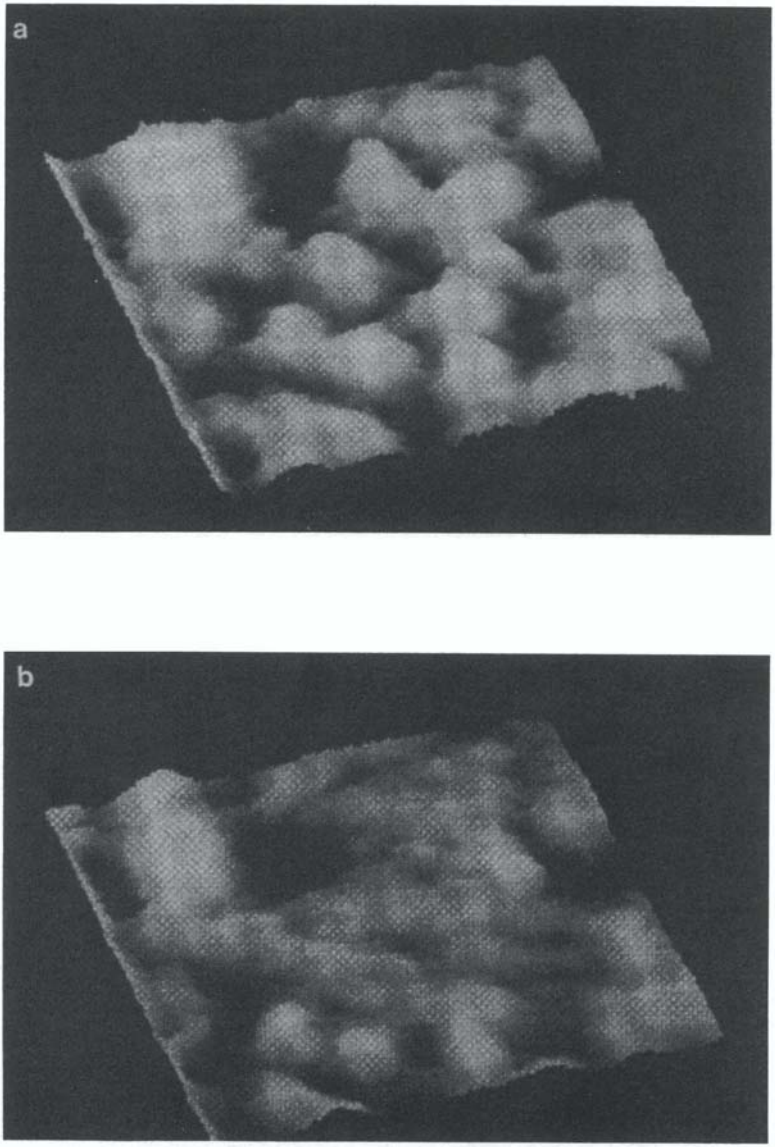

Figure 10. (A, B, C) AFM images of an aluminum surface corroding in seawater. The images were taken approximately 1 1/2 min apart. The scan area was 450 × 450 nm. Further microscope development is being focused on lowering the drift so that processes can be observed over smaller scan areas for times of up to an hour. (Reprinted from Ref. 30 by permission of Kluwer Academic Publishers.)

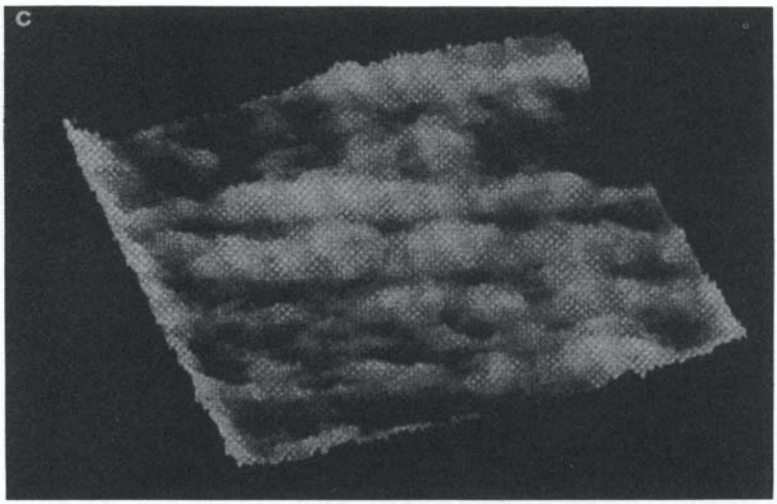

Figure 10. Continued

due to pits appearing randomly over the surface, as seen in Fig. 10 for an aluminum surface corroding in seawater. The mechanism of pitting on aluminum involves chemisorption of anions, resulting in formation of soluble hydroxide and chloride species, which thins the surface oxide locally. At the sites where the thinning is initiated, the electric field strength increases and attracts more anions, thus accelerating the process.[54,55] The soluble species involved are $Al(OH)_2Cl$, $Al(OH)Cl_2$, and $AlCl_3$. Aluminum surfaces do not seem to passivate in chloride-containing solutions.

3. Concluding Remarks

The most recent results of applying *in situ* STM/AFM to studies of corrosion convincingly demonstrate that novel and interesting images of solid–interface processes can be obtained. In fact, the images may be collected and presented consecutively, thereby enabling the viewer to follow the corrosion process as a moving picture in real time. In combination with simultaneous acquisition of electrochemical data, such as current–potential curves, these techniques provide excellent tools for

elucidation of corrosion mechanisms. The new techniques also present a challenge to authors and publishers in the sense that a single publication may not be able to accommodate all the images necessary to demonstrate fully the understanding of a corrosion process. Therefore we may anticipate references to the Internet services, for example, where film strips of certain corrosion processes can be transferred and viewed locally, thus giving a better understanding of the ideas expressed.

IV. CRITICAL PITTING TEMPERATURE

1. General

The critical pitting temperature (CPT) is widely used as a measure of the resistance of stainless steel against pitting attack.[56] Various methods for determination of the CPT are described here, special attention being given to the choice of test potential for the control of stainless steel quality.

The materials group "stainless steel"[56] contains alloys based on iron with a chromium content of a minimum of 12%. Chromium is far from the only alloying element in stainless steel, and from the corrosion resistance point of view, molybdenum and nickel are especially important elements. The corrosion resistance is due to a thin, invisible surface film, the passive layer, in which chromium oxide (Cr_2O_3) is the main component. It is formed by a reaction between the alloy and the oxygen in the environment. The passive layer is constantly breaking down and being rebuilt due to a reaction between the steel and the environment. In situations where the environment is too aggressive, so that rebuilding is impossible, a corrosion attack is started. If the entire passive layer is destroyed, the corrosion attack takes the form of uniform corrosion.

More often the passive layer is broken down locally and then the steel is said to be attacked by localized corrosion, the most important forms being pitting, crevice corrosion, and corrosion cracking. Most often the localized corrosion is caused by halogen ions such as chloride, bromide, and iodide. Pitting or pitting corrosion is seen as small pinholes on the surface of the steel. This section describes electrochemical instrumental methods to investigate and measure this form of corrosion attack.

The mechanism[57] of pitting is usually considered as involving two phases: (1) the nucleation phase (initiation phase) when the passive layer

is finally punctured at a susceptible site and (2) the propagation phase, involving growth of the pit.

It is not simple to give a measure of the resistance to pitting of a particular stainless steel, because it depends on many factors associated with the actual environment. The three main factors are potential, temperature, and concentration of initiating ions.

Experimental methods exist to determine a critical value for any one of these factors when the others are held constant. However, parameters such as pH, concentration of inhibiting ions (e.g., SO_4^{2-}), dissolved gas, test area, flow rate, and surface finish influence the resistance to pitting.[58–62]

In research laboratories, potential is often used as the critical value for comparison purposes. A "pitting potential" is determined at a given suitable constant temperature, recording the anodic polarization curve while keeping other factors constant (Fig. 11).

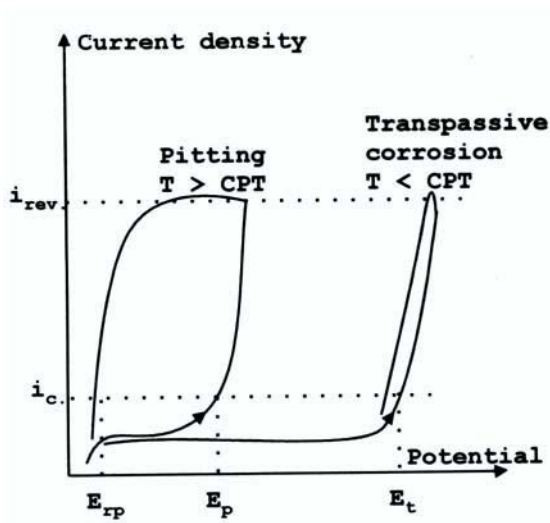

Figure 11. Schematic anodic polarization curves at a fixed temperature. Determination of either transpassive potential (E_t) or pitting potential (E_p) and repassivation potential (E_{rp}) at the critical current density (i_c). i_{rev} is the current density at which the scan is reversed.[72]

In the early 1970s, Brigham and Tozer were the first to make a systematic study, using temperature as the variable, of the connection between potential, temperature, and pitting corrosion (Fig. 12). They argued that in principle a critical pitting temperature should exist, but the data obtained showed a transition over a range of temperatures. The sharp transition was demonstrated experimentally by Quarfort[61] in 1989.

Experimental CPTs were determined by Brigham and Tozer[63–66] in three different ways based on chloride solutions: two electrochemical and one chemical. In electrochemical testing in sodium chloride (NaCl) solution, the methods involved recording the current while either increasing the potential at suitable selected temperatures (a potentiodynamic test) or increasing the temperature at suitable fixed potentials (a potentiostatic test). Alternatively, a potential was established by the redox couple (Fe(III)/Fe(II) in a simple immersion test in ferric chloride solution.

Over the years different researchers[58,60–61,67–69] have investigated the relationships between potential, temperature, and concentration of activat-

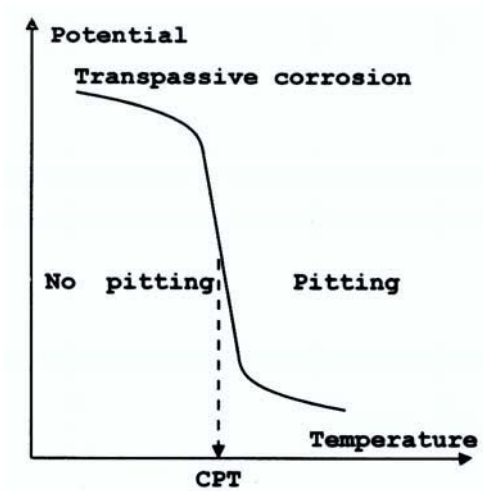

Figure 12. The limits of pitting as a function of potential and temperature according to the experimental results of Brigham and Tozer.[63–64] CPT, critical pitting temperature.

ing ions. The illustration in Fig. 13 was published in 1995 by Arnvig and Bisgaard.[69] It shows the existence of two different CPT values: a potential-dependent CPT and a potential independent CPT.

The potential-independent CPT can be determined by two different electrochemical methods: a potentiostatic test method using a sufficiently high potential, and a potentiodynamic test method. The potential-independent CPTs are well-defined, experimental results having a reproducibility of approximately ±1°C by potentiodynamic testing and approximately ±2°C by potentiostatic testing.

The potential-dependent CPT is determined by potentiostatic testing using a relatively low potential; the scatter of results is about ±5°C or higher.

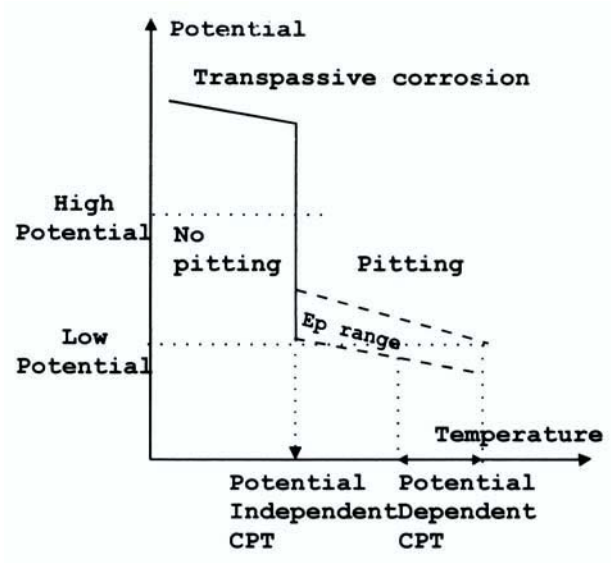

Figure 13. Extended version of Figure 12. Note the well-defined transition temperature, indicating a potential-independent CPT. (Reprinted from Ref. 69 by permission of NACE International, Houston, Texas.)

2. Experimental Equipment for CPT Testing

A common chemical laboratory test for corrosion resistance is a simple exposure test using metal coupons. The ASTM standard G48[70]—Pitting and Crevice Corrosion Resistance of Stainless Steels and Related Alloys by Use of Ferric Chloride Solution—describes a simple exposure test. The material coupons (e.g., 60 × 60 mm) are placed on a glass cradle and immersed in the solution in such a way that the coupons are evenly exposed.

In electrochemical measurements it is necessary to establish good insulated electrical contact with the sample and furthermore to have a well-defined exposed surface area. It is difficult to comply with these demands without creating, at the sample/mount interface, a crevice between the sample and the sample holder. If the bulk solution is not prevented from entering the crevice, crevice corrosion attack is often initiated.[62]

Crevice corrosion is another form of localized corrosion, which is easier to initiate than pitting. Since crevice corrosion will occur at lower potentials and temperatures than pitting, it is necessary to avoid crevice corrosion completely when trying to characterize resistance to pitting. Over the years, several suggestions have been presented for solving this problem.

If crevice corrosion occurs unintentionally, the pitting test results must be discarded. A visual inspection of the specimen using a light microscope readily shows whether crevice corrosion has occurred. Furthermore, unusually low CPT values or pitting potentials provide grounds for suspecting the development of crevice corrosion. Various setups for obviating some of these difficulties are described in the following section.

(i) Knife-Edge Teflon Washer

Stern *et al.*[62] describe a method using a knife-edge Teflon washer. A sample with a highly polished surface is tightened closely to the Teflon washer, avoiding any crevice between the sample and washer through which the solution might enter. A little scratch on either the sample or the Teflon washer is enough to produce a crevice, allowing capillary action to draw in electrolyte and leading to crevice corrosion.

(ii) Gas Purging of the Crevice

Bernhardsson *et al.*[60,67–68] used argon gas to avoid crevice corrosion. The cylindrical specimens (exposed area 3–10 cm^2) were placed vertically in the cell. The specimen holder was provided with a collar that was filled with argon during testing. The crevice between the specimen holder and specimen was filled with a stream of argon to hold back solution from the crevice. However, distribution of the gas is critical and difficult to control satisfactorily.

(iii) The Avesta Cell

Here distilled water[69,71–72] instead of argon is pumped into the test cell at the crevice between the sample and the sample mounting. With a few exceptions, the Avesta cell is like the usual electrochemical cell for corrosion measurements (Figs. 14 and 15). The Avesta cell is made up of two concentric cylindrical glass pieces with a top and bottom made of polyvinylidene fluoride pieces.

The electrolyte (the bulk solution) is in the inner of the two chambers, and thermostat fluid circulates in the outer chamber. In the top of the Avesta cell are mounted the salt bridge from the reference electrode, a thermometer, nitrogen gas inlet, counter electrode, and perhaps a mechanical stirrer.

Normally, square specimens are cut from 2–5-mm-thick sheet material. Two versions of the Avesta cell have been developed. One contains 120 ml of solution and uses specimens with an exposed area of 1 cm^2. The other contains 1200 ml of solution and uses specimens with an exposed area of 1–5–10 cm^2. The specimen is mounted as illustrated (Fig. 15). There is a small flow (0.1 ml/min) of distilled water through the pores of a ring of filter paper in the crevice between the specimen and the cell bottom. The filter paper ensures an even distribution of the flow of distilled water. In this way the liquid in the crevice is flushed constantly and the chloride ions do not enter the crevice and cannot initiate crevice corrosion.

The Avesta cell was originally used for testing sheet material as shown here. However, with a few changes, tubes and welds can be tested as well without preparatory machining.[72]

In 1991 Mathiesen and Maahn[73] published construction details of a modified form of the electrode holder used in ASTM G5[74] (Fig. 16). The

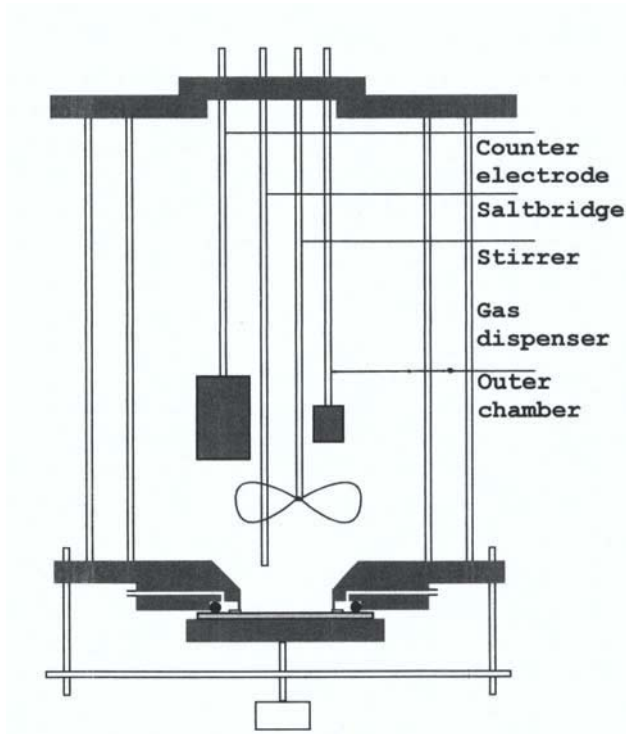

Figure 14. The Avesta cell.[72] See text for description.

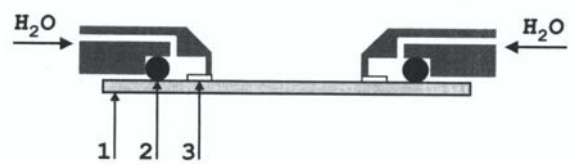

Figure 15. Detail of the bottom of the Avesta cell. Crevice corrosion is avoided by a small flow of distilled water through the pores of filter paper at the crevice at the specimen/mounting interface.[72] 1. specimen. 2. O-ring. 3. Filter paper ring.

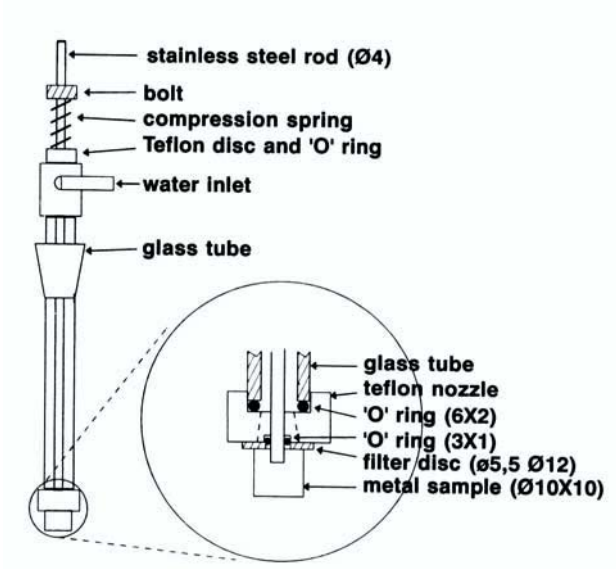

Figure 16. Electrode for pitting measurements with cylindrical specimens using the Avesta cell principle. The modification of the specimen holder is described in ASTM G5. Designed by Mathiesen and Maahn.[73] (Reprinted from Ref. 73 by permission of the authors.)

specimen is in cylindrical form and together with its mounting is suspended in the solution. This specimen holder can easily be introduced in the Avesta cell by covering the hole in the bottom and by making slight changes in the top of the cell.

In testing sheet, welded, and pipe material, the specimen is placed as a part of the bottom plate of the Avesta cell. Especially at higher temperatures there will be a difference between the temperature of the solution and the temperature of the specimen. This can be corrected for by calibration. When the modified ASTM G5 electrode holder is used, the specimen is totally immersed in the solution and no correction is needed.

Summarizing, the Avesta cell is a flexible and convenient device for measuring pitting corrosion without interference from crevice corrosion.

3. Methods for Pitting Characterization

(i) Pitting Potentials

For decades a common way to characterize the resistance of specimens to pitting corrosion has been determination of the pitting potential, E_p.[64,69,75–76] This is done by recording an anodic polarization curve at a suitable fixed temperature, as shown by the curve marked "pitting corrosion" (Fig. 11). If the temperature is too low, no pitting will occur, and eventually the material will be attacked by transpassive corrosion. Transpassive corrosion (uniform dissolution of the passive layer) occurs at higher extreme potentials (transpassive potentials, E_t), as shown by the curve marked "transpassive corrosion" (Fig. 11).

The pitting potential is a stochastic parameter.[76] The potential decreases as the area increases, because the chance of there being a weak spot for pit initiation is greater on a large surface than on a small surface.

The choices of electrolyte and concentration (e.g., chloride content), gas purging, and the presence of inhibitor ions must be controlled carefully if reproducibility is to be obtained.

(ii) CPT in $FeCl_3$

With small modifications, ASTM standard G48[70] can be used to determine a CPT. The test is used as a ranking parameter for the resistance to pitting of high-alloyed austenitic stainless steels. In this method, material coupons are typically exposed for 24 or 72 h to a 6% $FeCl_3$ (=1.11 mole/liter) solution at fixed temperatures (typically with 2.5°C intervals). The CPT is defined as the lowest temperature at which the specimen is attacked by pitting corrosion.

The redox couple (Fe(II)/Fe(III) causes a potential of approximately 450 mV/SCE (saturated calomel electrode).[62] Some of the Cl^- ions are bound in Fe(III) complexes. Melstrom and Bernhardsson[60] have measured the activity of Cl^- to be 0.53 mole/liter.

Using this method, it takes many days to determine a single reliable CPT value. Salinas-Bravo and Newman[77] published in 1994 what they called: "An alternative Method to Determine Critical Pitting Temperature of Stainless Steels in Ferric Chloride solution."

*(iii) Potential-*Dependent *CPT (Determined by a Potentiostatic Method)*

In 1980 Bernhardsson *et al.*[60,67,68] introduced an automated electrochemical method for CPT determination. The specimen is mounted as described in Section IV.2 (ii) using a stream of argon to avoid crevice corrosion and 0.02–5% sodium chloride as electrolyte. The CPT is determined by a potentiostatic test method using an instrument called the Santron CDT 400 for potential control, temperature control, and current measurements.

Testing starts at a temperature 30°C below the expected CPT using an applied anodic potential (200–600 mV/SCE). Current is measured for 15 min, and if pitting does not occur (current density is below $10\,\mu A/cm^2$), the temperature is raised 5°C and the potential is applied once again for a new test (Fig. 17). The CPT is defined as the lowest temperature at which pitting occurs.

Measurements of this kind have been made for many different steel grades and chloride concentrations (Figs. 18 and 19). The conclusion is that the CPT for a given material depends on the potential and the chloride concentration.

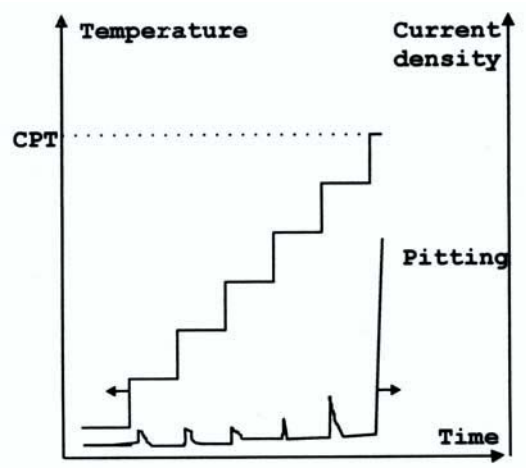

Figure 17. Measurement of the potential-dependent CPT using a potentiostatic test developed by Bernhardsson *et al.*[60,67–68]

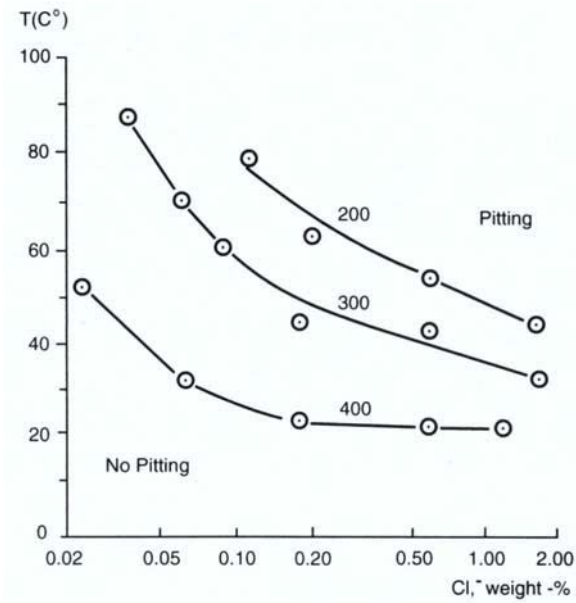

Figure 18. Correlations among chloride concentration, electrode potential (200–400 mV/SCE), and CPT, according to the data of Bernhardsson *et al.*[60,67–68] Material: AISI 316 stainless steel.

Normally seven different temperature steps are used to determine a CPT value. With a polarization measurement time of 15 min at each temperature step, it takes about 3 h to determine one CPT value. The reproducibility was claimed to be good[60] with temperature steps of 5°C.

(*iv*) *Potential*-Independent *CPT (Determined by a Potentiodynamic Method)*

In 1989 Quarfort[61] showed that the potential-independent CPT can be determined as a well-defined value (±1°C). The Avesta cell (1 cm^2 exposed area, 120 ml electrolyte volume) was used.

The potential-independent CPT determined by the potentiodynamic method[61,72] is defined as the lowest temperature at which pitting initiation occurs during a dynamic anodic polarization scan.[72]

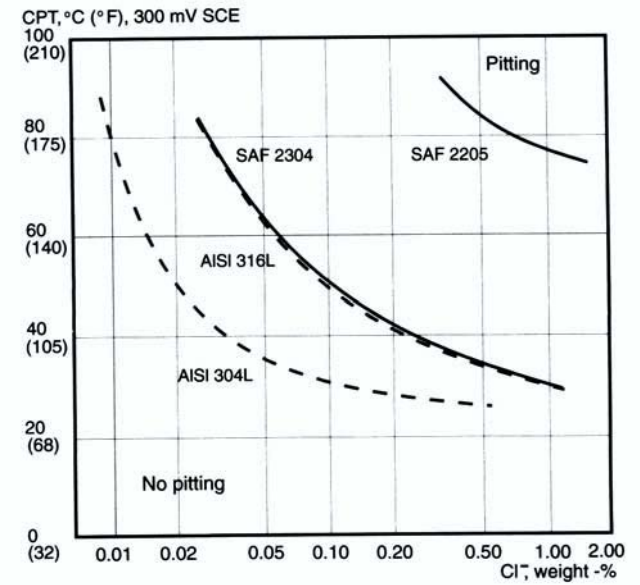

Figure 19. CPT as a function of chloride concentration for various stainless steels according to the data of Bernhardsson *et al.*[60,67-68] Potential: 300 mV/SCE.

Polarization curves are recorded at temperatures with intervals of 1°C around the expected CPT. A new specimen is used for each polarization. The specimen and the electrolyte (usually neutral 1 mole/liter NaCl) are thermostatted at the selected temperature. Referring to Fig. 11, when the temperature has stabilized, the anodic polarization is started at 300 mV SCE and reversed at a given current density (i_{rev} = 5 mA/cm^2); the polarization is stopped when the current density has decreased to a level of 10 μA/cm^2.

Figure 11 shows idealized polarization curves for the cases where the temperature is above the CPT (pitting) and below the CPT (transpassive corrosion). These polarization curves show the pitting potential (E_p), transpassive potential (E_t), and repassivation potential (E_{rp}). E_p and E_t are defined as the potentials at which the current density unambiguously

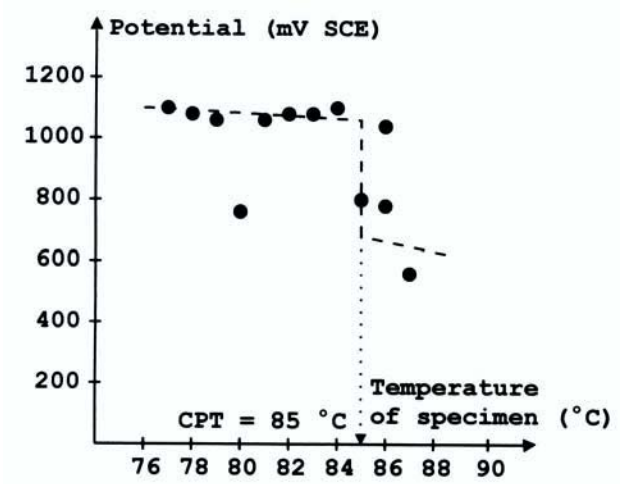

Figure 20. Evaluation of the potential-independent CPT by the potentiodynamic test according to Quarfort.[61] The plot of pitting and transpassive potentials vs. temperature yields a CPT of 85°C.[61,69,72] (Reprinted from Ref. 69 by permission of NACE International, Houston, Texas.)

exceeds 100 μA/cm^2, and E_{rp} is the potential at which the current density falls below 10 μA/cm^2.

Plotting the repassivation potentials (or the pitting potentials and the transpassive potentials) as a function of the specimen temperature evaluates the CPT. An example of an evaluation is shown in Fig. 20.

The potential-*independent* CPT determined by the potentiodynamic test method is found to be independent of both the chloride content of the solution in the range of 0.1–5 mole/liter of NaCl and the pH value (pH 1–7). Testing at different temperatures with different specimens, and evaluating the results from one test temperature before the next temperature is selected, is a time-consuming process. It takes several days to determine a single CPT value.

*(v) Potential-*Independent *CPT (Determined by a Potentiostatic Method)*

In response to the desire for a short testing time and high reproducibility, a potentiostatic CPT method was developed.[69] The larger version

of the Avesta cell (electrolyte volume 1200 ml) was used because it is easier to control a continuously increasing temperature in this cell, where mechanical stirring can be introduced.

The specimen is polarized to a constant anodic potential and the temperature is raised continuously by 1°C/min. The solution is 1 mole/liter NaCl.

The CPT is defined as the temperature of the specimen at which the current increases sharply. For practical reasons the CPT is taken as the temperature at which the current density unambiguously exceeds 100 $\mu A/cm^2$ for 60 s (Fig. 21). It is evaluated by plotting the current density as a function of the temperature of the specimen (Fig. 22).

To determine the potential-independent CPT by the potentiostatic method, it is necessary to select a potential placed between the pitting potential and the transpassive potential for the relevant stainless steel (Fig. 13). A suitable choice of potential is 700 mV SCE, and in order to obtain compatibility for a range of stainless steels, the polarization was always

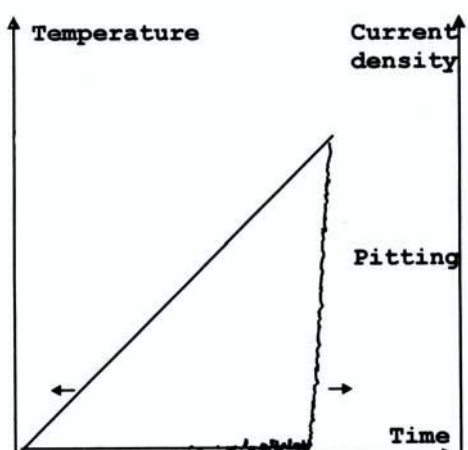

Figure 21. Determination of the potential-independent CPT by the potentiostatic test according to Arnvig and Bisgård.[69] Applied potential: 700 mV/SCE; rate of temperature rise: 1 °C/min. (Reprinted from Ref. 69 by permission of NACE International, Houston, Texas.)

started at approximately 0°C. The temperature was raised continuously until pitting occurred as indicated by a marked increase in the current.

As mentioned earlier, the pitting potential is sensitive to several experimental parameters. The influence of some of these parameters on the potentiostatically measured potential-independent CPT was examined by Arnvig and Bisgaard.[69]

Applied potential: Using a sample of type 316 stainless steel with a high content of molybdenum, the CPT was determined with an applied potential in the range of +400 to +800 mV/SCE (Fig. 23). It can be seen that the transition between the potential-dependent CPT and the potential-independent CPT is at about 550–600 mV/SCE, and that the standard deviation in CPT measurements decreases as the applied potential is increased (from about 5°C at low potentials and down to about 0.5°C at 800 mV/SCE).

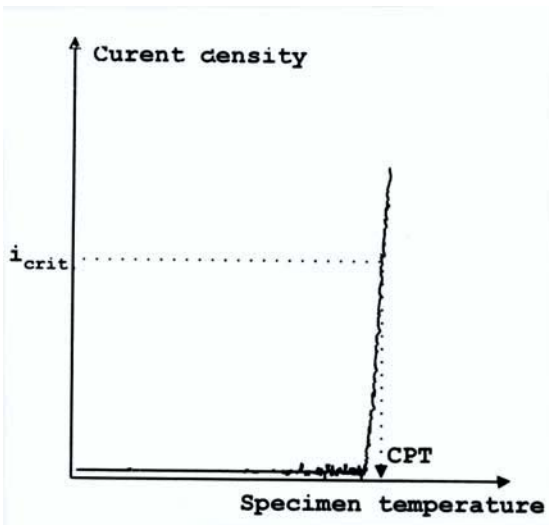

Figure 22. Evaluation of the potential-independent CPT. (Reprinted from Ref. 69 by permission of NACE International, Houston, Texas.)

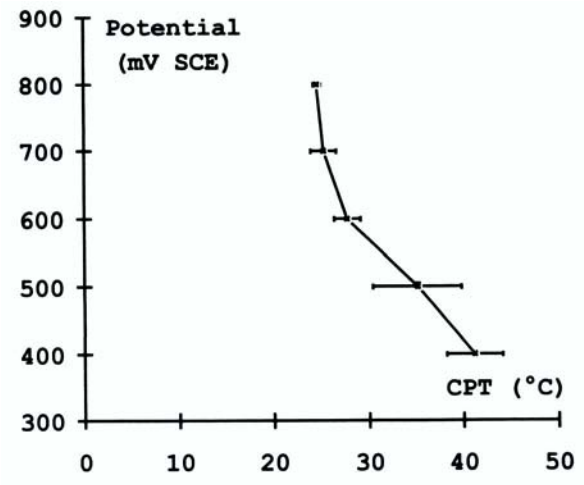

Figure 23. Average CPT values as a function of applied potential. Bars indicate standard deviations.[69] (Reprinted from Ref. 69 by permission of NACE International, Houston, Texas.)

Although there were small instrumental differences (e.g., temperature control and test cell), the potential-dependent CPTs[69] were similar to those found by Bernhardsson.[67]

Exposed test area: CPTs have been determined using exposed specimen areas of 1, 5, and 10 cm^2 (Fig. 24). In this range the CPT is seen to be independent of the exposed area, but the standard deviation is relatively higher at 1 cm^2 compared with 5 and 10 cm^2.

Solution: Neutral 1 mole/liter NaCl purged with nitrogen is the usually chosen standard electrolyte. CPTs have been determined in solutions purged with either nitrogen or oxygen. The conclusion is that purging with oxygen or nitrogen has no effect on the CPT. The effects of inhibitors such as SO_4^{2-} or NO_3^- in the solution have not been investigated so far.

4. Summary

Several methods to determine the resistance to pitting corrosion of stainless steel have been introduced. The methods are divided into two groups. The first group includes determination of pitting potential, CPT, in $FeCl_3$

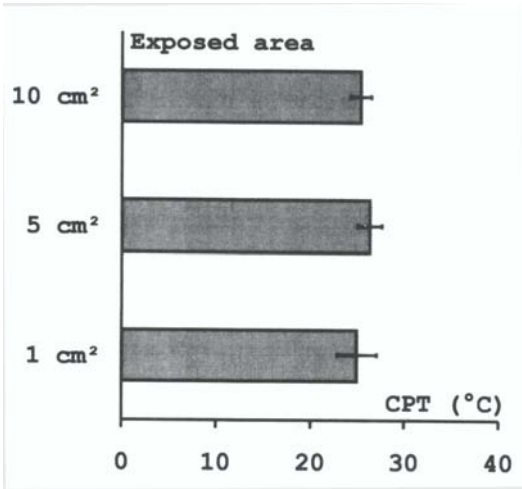

Figure 24. Relative distribution of CPT values with variation of exposed area (1, 5, and 10 cm^2).[69] Note that the standard deviations (indicated by bars) increase with decreasing exposed area. (Reprinted from Ref. 69 by permission of NACE International, Houston, Texas.)

and the potential-*dependent* CPT [sections IV.3(i)–3(iii)]. The second group includes the determination of the potential-*independent* CPT by potentiodynamic and potentiostatic testing [sections IV.3(iv)–3(v)].

The first group is characterized by low reproducibility and sensitivity to a range of experimental parameters. The second group is characterized by high reproducibility and less sensitivity to a range of experimental parameters, or none.

This difference between the two groups is probably due to different influences arising from pit initiation. The initiation is strongly dependent on the steel's surface condition, and therefore the methods in the first group are suitable for evaluating the effect of the surface condition.

The methods in the second group leading to the potential-independent CPT are practically independent of the surface condition and therefore more likely reflect the nature of the propagation part of the pitting process and characterize the steel's bulk material.

The choice of test method for examining pitting resistance depends on the objective. For evaluation of surface condition, the methods in the first group are preferable, while the methods in the second group give the best characterization of the alloy.

5. Concluding Remarks

The automation involved in CPT measurements is rather simple, but is necessary to more quickly provide reliable and reproducible data for the limits of application of stainless steel. The demonstration of correlations between CPT and chloride concentration at various potentials (Fig. 18) may help to further the understanding of the basic pitting phenomena.

V. APPLICATIONS OF THE ELECTROCHEMICAL HYDROGEN PERMEATION CELL

1. General

Application of the electrochemical hydrogen permeation cell provides a simple technique for measuring the amount of hydrogen being absorbed by a metal during a hydrogen evolution reaction. Ever since the important developments by Devanathan *et al.* in the early 1960s, the technique has been used increasingly for various purposes. These include basic studies of the hydrogen evolution reaction mechanisms, investigation of hydrogen trapping in metals, and examination of threshold hydrogen concentrations for hydrogen-related stress corrosion cracking. Commercial sensors for monitoring purposes have also been developed.

2. The Principle

The type of apparatus described here has been used by many workers since the early 1900s, but was not used much until the work of Devanathan and Stachurski[78] emphasized its potential in the early 1960s. The principle is quite simple and is illustrated in Fig. 25. Two electrochemical cells are separated by a metallic membrane, which acts as the working electrode in each of the cells.

In one of the cells (cathode chamber), conditions are such that the hydrogen evolution reaction occurs. This may be due to potentiostatic or galvanostatic polarization, or corrosion of the metal in an acidic solution.

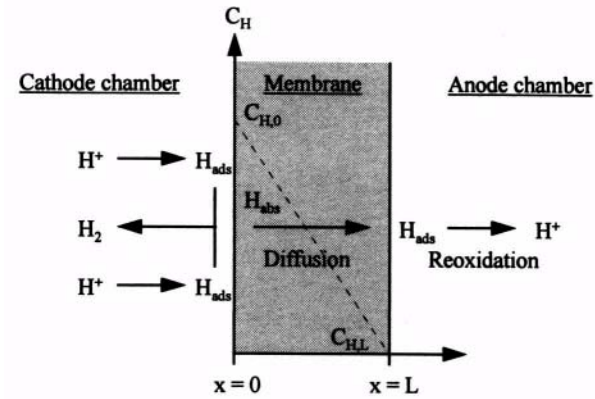

Figure 25. Schematic illustration of the principle of the electrochemical hydrogen permeation technique.

Atomic hydrogen formed as an intermediate in the hydrogen evolution reaction is adsorbed to the surface of the membrane. Molecular hydrogen is formed by one of at least two mechanisms, but parallel to this, a fraction of the atomic hydrogen is absorbed by the metal, eventually leading to an equilibrium between adsorbed and absorbed atomic hydrogen. In the absorbed state, the hydrogen atoms are able to diffuse as interstitials in the metal lattice.

In the other cell (the anode chamber) on the opposite side of the membrane, conditions are maintained, causing reoxidation of the hydrogen atoms exiting the membrane. By complete oxidation of the exiting hydrogen atoms, the current flowing in this cell becomes a measure of the amount of hydrogen diffusing across the membrane.

At least two factors should be considered in this context. First, the current should not include significant contributions from electrochemical reactions other than the oxidation of hydrogen. If the membrane is made of steel, this can be achieved by the choice of an alkaline electrolyte in the anode chamber and application of a potential that passivates the steel.

Second, care should be taken that the hydrogen atoms exiting the membrane do not escape by formation of molecular hydrogen. Otherwise, the current flowing in the cell will not account for the entire amount of

hydrogen diffusing across the membrane. This difficulty is usually overcome by plating the exit surface of the membrane with palladium, which catalyzes the hydrogen oxidation. A very clear demonstration of the effect of palladium plating has been given by Manolatos *et al.*,[79] who plated half the exit surface with palladium. Throughout a permeation experiment, this surface was examined with a camera, and the photographs showed that hydrogen bubbles were formed only on the part of the surface that was not covered with palladium.

3. Diffusion of Hydrogen into Metal

The transport of hydrogen from the entry side to the exit side of the membrane can be described by Fick's laws of diffusion. In the steady state, the hydrogen flux is given by Fick's first law of diffusion:

$$j_{H,ss} = -D(dC_H/dx) \tag{17}$$

where:

$j_{H,ss}$ = the steady state hydrogen flux,
D = the diffusion coefficient for hydrogen in the material,
dC_H/dx = the concentration gradient of absorbed hydrogen across the membrane.

Assuming that the exiting hydrogen atoms are oxidized sufficiently fast, the concentration of absorbed hydrogen directly beneath the exit surface may be taken as zero. Using Faraday's law, the steady-state hydrogen flux across the membrane is described by the steady-state hydrogen permeation current:

$$i_{H,ss} = FD(C_{H,0}/L) \tag{18}$$

where:

$i_{H,ss}$ = the steady-state hydrogen permeation current,
F = Faraday's number,
$C_{H,0}$ = the concentration of absorbed hydrogen just beneath the entry surface,
L = the thickness of the membrane.

For nonsteady-state conditions, Fick's second law of diffusion can be applied

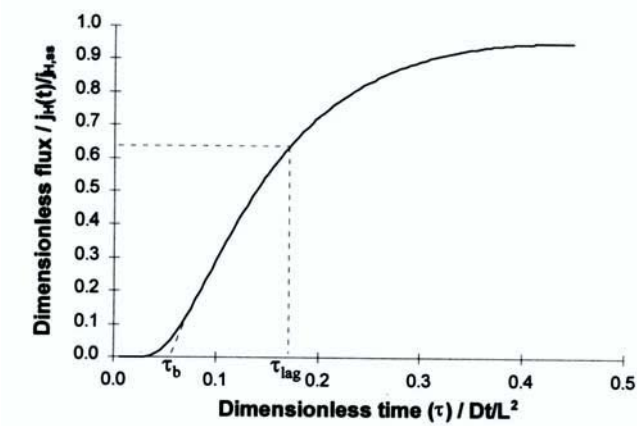

Figure 26. Rising permeation transient based on a solution to Fick's second law of diffusion.

$$dC_H(x,t)/dt = D(d^2C_H(x,t)/dx^2) \tag{19}$$

For a rising transient, this equation has been solved using Laplace transformation and appropriate initial and boundary conditions,[80] and Fig. 26 illustrates the expected rising transient so derived.

From the dimensionless time parameter (τ) used in the solution, the diffusion coefficient (D) can be obtained from

$$D = L^2/(6\tau_{lag}) = L^2/(15.3\tau_b) \tag{20}$$

where:

τ_{lag} = the time needed to achieve $(e-1)/e$ (63%) of the steady-state permeation level (time-lag method),

τ_b = the breakthrough time; referring to Fig. 26, this is defined as the intercept on the dimensionless time axis of the tangent to the curve at the point of inflexion.

4. Studies on the Hydrogen Evolution Reaction

The overall hydrogen evolution reaction can be expressed by

$$2H^+ + 2e^- \rightarrow H_2 \tag{21}$$

Two different reaction mechanisms are considered as being experimentally established[81]:

According to the Volmer–Tafel mechanism, the discharge of a proton forms an adsorbed hydrogen atom (Volmer reaction). Two such adsorbed hydrogen atoms then combine to form molecular hydrogen (Tafel reaction)

$$H^+ + e^- \rightarrow H_{ads} \tag{22}$$

$$2H_{ads} \rightarrow H_2 \tag{23}$$

Alternatively, according to the Volme–Heyrovsky mechanism, the Volmer discharge reaction is followed by the Heyrovsky electrochemical desorption reaction

$$H^+ + e^- + H_{ads} \rightarrow H_2 \tag{24}$$

In either case a fraction of the adsorbed atomic hydrogen may enter the metal

$$H_{ads} \rightarrow H_{abs} \tag{25}$$

The electrochemical hydrogen permeation technique has proved to be a valuable tool in the study of these reaction mechanisms. This is mainly due to the ability to estimate the amount of an intermediate (H_{ads}) in the reaction scheme. Such studies have been presented, for example, by Devanathan and Stachurski,[82] by Bockris *et al.*,[83] and by Iyer *et al.*[84,85] The applicability of the Volmer–Tafel reaction scheme can be evaluated by considering the kinetic expressions for reactions (22) and (23), together with equilibrium in the absorption process (25)

$$i_V = Fk_V\{H^+\}(1 - \theta)\exp[-(1 - \alpha)F\eta/(RT)] \tag{26}$$

$$i_T = Fk_T\theta^2 \tag{27}$$

$$\theta k_{abs} = C_{H,0}k_{des} \tag{28}$$

[Although no actual current is involved in the Tafel step, it is convenient to include F in (27) to express the rate in terms of a current. A similar argument applies to the inclusion of F in (30).]

The following symbols have been used:

i_i = current representing rate of reaction (Volmer, i_V; Tafel, i_T),
k_i = appropriate rate constant for reaction i (Volmer, Tafel, absorption, desorption),
$\{H^+\}$ = activity of H^+,
θ = activity of adsorbed H in terms of degree of surface coverage,
α = transfer coefficient for the Volmer discharge reaction,
η = hydrogen overvoltage,
$C_{H,0}$ = subsurface hydrogen concentration at the entry side of the membrane.

It can be assumed that the current representing the Volmer discharge reaction (26) equals the current representing the Tafel reaction (27), i.e., only a minor part of the discharge current (i_V) results in hydrogen atoms being absorbed into the membrane; the reverse Volmer reaction is taken to be negligible so that the observed current, $i_{obs} = i_V = i_T$. It follows from (27) that

$$\theta = (i_V/Fk_T)^{1/2} \tag{29}$$

Combining (18) and (28) gives

$$i_{H,ss} = FDk_{abs}\theta/(Lk_{des}) \tag{30}$$

[Regarding the inclusion of F in (30), see the comment for (27).]

Inserting (29) into (30) gives

$$i_{H,ss} = [(FDk_{abs}/(Lk_{des})]\,(i_V/Fk_T)^{1/2} \tag{31}$$

This equation predicts a linear relationship between $i_{H,ss}$ and $i_{obs}^{1/2}$; this behavior was established experimentally by Bockris *et al.*[83] The slope of the curve is inversely related to the thickness of the membrane, and in addition valuable information can be obtained regarding the rate constants involved.

In the analysis of Iyer *et al.*,[85] $i_{H,ss}$ is not assumed to be very much less than i_T, so that i_V at steady state equals the sum of the currents representing the Tafel recombination reaction and hydrogen permeation

$$i_v = i_T + i_{H,ss} \tag{32}$$

That is

$$\theta = (i_T/Fk_T)^{1/2}, \textit{ where } i_T = (i_{obs} - i_{H,ss})$$

and an analysis similar to that of Bockris *et al.* leads to the equation

$$i_{H,ss} = [FDk_{abs}/(Lk_{des})]\,(i_T/Fk_T)^{1/2} \tag{33}$$

In other words, the analysis of Iyer *et al.* differs from the analysis of Bockris *et al.* by predicting a linear relation between the steady-state hydrogen permeation current and $(i_{obs} - i_{H,ss})^{1/2}$ instead of $i_{obs}^{1/2}$. Figure 27 shows such plots according to the equations of Iyer *et al.* The experiments were carried out in an acetate–acetic acid buffer system at pH 6 under stagnant and stirred conditions, using carbon steel membranes of 1.0 and

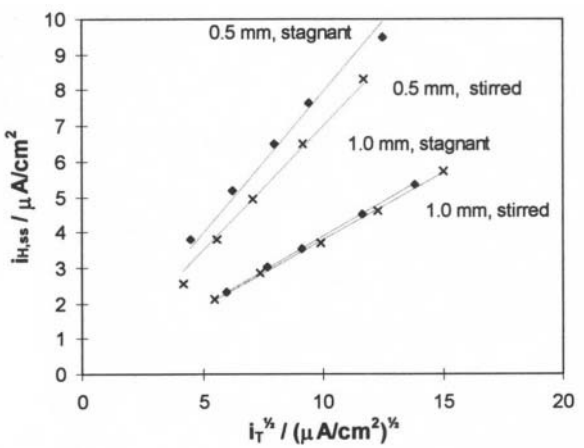

Figure 27. Plots of the permeation current density vs. the square root of the Tafel reaction current density [Eq. (33)], recorded in acetate/acetic acid buffers at pH = 6 and 30°C, using carbon steel membranes of 1.0 and 0.5 mm thickness.[86]

0.5 mm thickness.[86] The hydrodynamic conditions do not appear to affect the behavior, and the slopes correlate well with the membrane thicknesses.

The clear verifications of the equations of Bockris *et al.* and of Iyer *et al.* described above are interesting as fundamental studies, but they also provide confidence in the reliability of automated measurements made with probes designed on the basis of the verified theories.

5. Hydrogen-Related Stress Corrosion Cracking

Stress corrosion cracking (SCC) may develop due to either highly localized anodic dissolution processes or the specific effects of hydrogen. The latter case usually involves a localization of absorbed hydrogen atoms at specific trap sites, such as dislocations, grain boundaries, and microvoids within the metal. These trapping effects cause a deviation from the simple diffusion behavior, not only by immobilization, but also because interstitial sites and defect sites are differently affected when hosting hydrogen atoms.

(i) The Trapping of Hydrogen in Metals

A description of the trapping process may be based on the chemical potentials of the hydrogen absorbed in the metal.[88] In the general case, the chemical potential of interstitial or diffusible hydrogen may be described by the equation

$$\mu\,(\mathrm{H,diff}) = \mu^0\,(\mathrm{H,diff}) + RT\ln\{\mathrm{H,diff}\} \tag{34}$$

where

$\mu\,(\mathrm{H,diff})$ = chemical potential of diffusible absorbed hydrogen,
$\mu^0\,(\mathrm{H,diff})$ = standard chemical potential of diffusible absorbed hydrogen,
$\{\mathrm{H,diff}\}$ = activity of diffusible absorbed hydrogen.

The chemical potential of trapped hydrogen may similarly be expressed by

$$\mu\,(\mathrm{H,trap}) = \mu^0\,(\mathrm{H,trap}) + RT\ln\{\mathrm{H,trap}\} \tag{35}$$

Under equilibrium conditions, the chemical potential of diffusible hydrogen equals the chemical potential of trapped hydrogen, i.e.,

$$\mu^0(\text{H,diff}) - \mu^0(\text{H,trap}) = RT \ln(\{\text{H,trap}\}/\{\text{H,diff}\}) \quad (36)$$

Equation (36) states that the activity of hydrogen at trap sites increases with decreasing chemical potential of the trap; hence a trap involves a site where the chemical potential is lower than the chemical potential associated with an interstitial site. Consequently, the concentration of hydrogen in a trap site is higher than the concentration found in the surroundings of the trap. Further mathematical treatments and classifications of traps have been presented in several papers.[87–93] The effect of traps on the rising transient hydrogen permeation behavior (Fig. 26) is an increase in the observed breakthrough time (due to the time needed to saturate the traps) and a steepening of the rising curve (due to a larger hydrogen concentration gradient at the exit surface when the traps are saturated and until steady state is attained).[88]

(ii) The Threshold Hydrogen Concentration for Stress Corrosion Cracking

The electrochemical hydrogen permeation technique has been used in efforts to establish threshold hydrogen concentrations in steel below which no cracking occurs. The threshold concentration depends largely on the type of failure under investigation, the chemical and physical properties of the steel, and the magnitude of applied and residual stress.

Hydrogen-induced cracking (HIC) may develop in the absence of external stresses and is caused by the recombination of absorbed hydrogen atoms at, for example, microvoids present in the steel. Very high pressures may build up as a result of the formation of hydrogen gas; if the pressure sets up great enough stress, crack initiation will result. The threshold hydrogen concentration in this case may be assessed simply by establishing a suitably large concentration gradient ($C_{H,0}/L$ in Fig. 25) over the membrane. The subsurface hydrogen concentration just beneath the entry surface has to exceed the threshold concentration. This can be achieved by adding a recombination poison to the catholyte. Hydrogen sulfide is known to be such a poison, which inhibits the Tafel recombination reaction, thereby increasing θ and according to Eq. (28), also $C_{H,0}$.

Under steady-state conditions, the concentration of interstitially absorbed hydrogen can be established at any depth of the membrane (dotted line in Fig. 25). By subsequent metallographic examination of the mem-

brane, the maximum depth where cracks can be found is noted and compared with the hydrogen concentration profile found in the permeation experiment. A more elegant variant was demonstrated by Coudreuse and Charles.[94] By repeated permeation experiments, these authors managed to distinguish among diffusible, reversibly, and irreversibly trapped hydrogen and were thereby able to describe the threshold concentration as the sum of these three contributions.

In cases where the propagation of hydrogen-related cracks depends on externally applied stresses, the SCC test may be performed using fracture mechanical test specimens. In this case, the direct measurement of the hydrogen concentration in the specimen is difficult, since the electrochemical permeation technique involves the creation of a hydrogen concentration gradient in the membrane. For this reason, the test specimen itself cannot act as the membrane due to the need for a uniform concentration of diffusible hydrogen during the test.

Alternatively, as demonstrated by Robinson and Kilgallon,[95] the hydrogen concentration in the test specimen may be assessed by placing a hydrogen permeation cell in the same environment as that used for the fracture mechanical test. By charging the membrane of the hydrogen permeation cell in the same manner as the test specimen, a parallel permeation experiment can be performed, which can be used to assess the hydrogen concentration present in the actual test specimen. This procedure yields a description of the critical stress intensity factor for stress corrosion cracking (K_{1SCC}) as a function of the concentration of hydrogen absorbed by the test specimen. Robinson and Kilgallon offer the following empirical relation found by constant displacement tests in various environments using double-cantilever beam (DCB) specimens prepared from a quenched and tempered high-strength, low-alloy offshore steel[95]

$$K_{1SCC} = 43.1 \exp(-1.49 C_{0,H}) \tag{37}$$

For comparison, the following relationship has been found for an X70 pipeline steel (slow strain rate test using compact tension specimens with the precrack located in the heat-affected zone of a weld)[96]

$$K_{1SCC} = 89.0 \exp(-0.09 C_{0,H}) \tag{38}$$

The oil and gas sector in particular has an interest in such relationships, since offshore steel structures are cathodically protected and may be exposed in biologically active environments that involve activity of sulfate-reducing bacteria. These anaerobic bacteria produce sulfide, which in turn may enhance hydrogen uptake by the steel. There are similar concerns when pipelines are buried in anaerobic soil. The relations (37) and (38) can be compared with stress intensity factors actually present at flaws in the steel under operating conditions; the actual hydrogen concentration should be assessed as well, for example, by using hydrogen permeation units designed for this purpose.

6. Cell Types

Figure 28 illustrates a soil hydrogen permeation cell mounted in a general-purpose probe used for screening soil corrosivity.[97] Other examples of specific hydrogen probes are illustrated in Fig. 29.

The cells shown in Figs. 28 and 29 all operate according to the same principles, which have been developed by Arup.[98,99] The interior of the cell acts as the anode chamber, and a metal oxide cathode placed inside the cell in an alkaline electrolyte acts as the counter electrode. The hydrogen flux across the integrated membrane (coated with palladium on the internal surface) can be measured as the potential drop across a resistor placed between the membrane and the counter electrode.

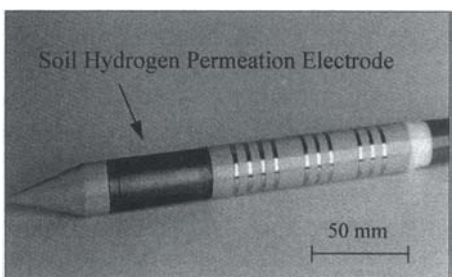

Figure 28. The soil hydrogen permeation electrode mounted in a general probe used for screening soil corrosivity.[97]

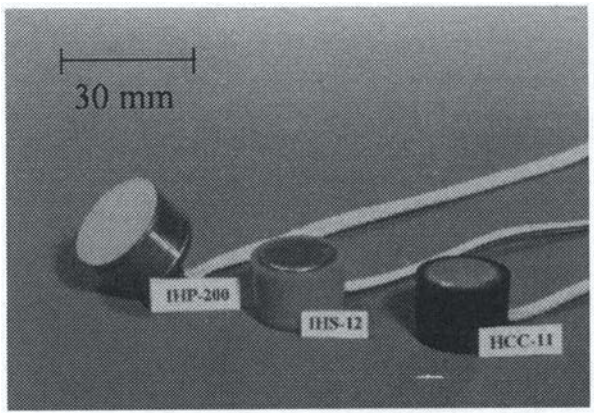

Figure 29. Commercial hydrogen sensors. (By permission of the Force Institute, Brøndby, Denmark.)

The intrusive hydrogen probe (IHP-200) shown in Fig. 29 can be placed in access fittings in industrial plants (pressure vessels, pipelines) and withstands pressures up to 200 bar. It is typically used to monitor the efficiency of measures taken to diminish the risks of hydrogen damage (use of inhibitors, H_2S scavengers, etc.).

The immersible hydrogen sensor (IHS-12 in Fig. 29) can be used to quantify hydrogen uptake by directly immersing it in the corrosive environment. Hydrogen uptake can also be measured under cathodic protection.

The hydrogen contact cell (HCC-11 in Fig. 29) does not have an integrated membrane, but merely a palladium "window," and is intended for "clamp-on" purposes. It can be used on any smooth or flat surface and measures the effluent hydrogen permeation through vessels, pipelines, etc., for example, during full-scale testing as demonstrated by Christensen *et al.*[100]

Owing to their simplicity, measurements with the hydrogen sensors are easily automated. Figure 30 shows a setup in which eight hydrogen contact cells are used in an investigation with a steel pipe filled with a corrosive test medium under pressure. Temperature, pressure, and hydro-

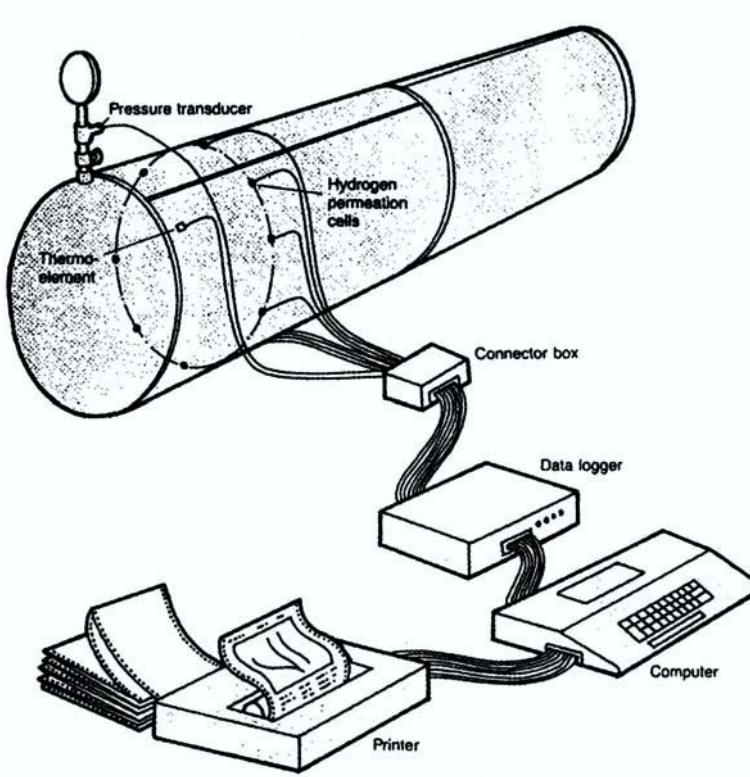

Figure 30. Automated hydrogen permeation measurements in a full-scale pipe test. (By permission of Teknisk Forlag A/S, Copenhagen, Denmark.)

gen permeation levels are recorded by a data logger and displayed on a computer screen.[101]

7. Summary

The electrochemical hydrogen permeation technique can be useful in a variety of investigations. Mechanistic information on the hydrogen evolution reaction can be obtained owing to the ability of the technique to quantify the amount of adsorbed atomic hydrogen intermediary formed in the process.

The method can be used for studies on hydrogen diffusion and trapping in metals, which, for example, are relevant within the field of hydrogen-related stress corrosion cracking. Critical hydrogen concentrations for various types of cracking can be assessed.

Commercial sensors suitable for automated measurements are available and can be used, for example, for field measurements of hydrogen uptake by cathodically protected steel buried in soil sediments. Other types can be mounted in process plants for monitoring purposes.

REFERENCES

[1]G. Bech-Nielsen, Abstracts, *SCAN-ELCHEM'90, Symposium*, Danish Electrochemical Society, Copenhagen, 1990.
[2]G. Bech-Nielsen and Anne D. Juhl, *Corros. Sci.* **34** (1993) 785.
[3]G. Bech-Nielsen, M. Kjaer Larsen, H. O. Ketting, and I. Chorkendorff, *Corros. Sci.* **36** (1994) 759.
[4]G. Bech-Nielsen, *Galvanotechnik* **85** (1994) 776.
[5]G. Bech-Nielsen, Abstracts, 47th ISE-meeting, (1996). Also *Electrochim. Acta* (in press).
[6]G. Bech-Nielsen, F. de Fontenay, and H. Poulsen, *Electrochim. Acta* **42** (1997) 1847.
[7]N. N. Greenwood and A. Earnshaw, *Chemistry of the Elements*, Pergamon Press, Oxford, 1984, p. 329.
[8]D. A. Vermilyea, *J. Electrochem. Soc.* **105** (1957) 11.
[9]M. E. Straumanis, *J. Electrochem. Soc.* **105** (1958) 284.
[10]Ya. M. Kolotyrkin and G. M. Florianovich, Z. *Phys. Chem.* **231** (1966) 145.
[11]G. Bech-Nielsen, P. T. Tang, and D. Ulrich, proceedings (in Danish), *SkanZink'91* (Scandinavian Conference on Cathodic Protection of Steel), Centre of Advanced Electroplating, The Technical University of Denmark, 1991, p. 11.
[12]P. T. Tang and G. Bech-Nielsen, in *Industrial Trends* No. 27, Jan. 1992, issued by Nihon Parkerizing Co., Ltd., Technical Division (Japan).
[13]G. Bech-Nielsen, M. Kjær Larsen, K. A. Jensen, and D. Ulrich, *Corros. Sci.* **36** (1994) 1907.
[14]G. Bech-Nielsen, proceedings, *INCOSURF '92,* East-West Convention on Surface Engineering, 1992.
[15]G. Bech-Nielsen, in *Modifications of Passive Films*, Ed. by P. Marcus, B. Baroux, and M. Keddam, EFC Publications No. 12, Institute of Materials, London, 1994, p. 195.
[16]G. Bech-Nielsen and T. Dörge, in proceedings, *SurFin'91 Technical Conference*, Toronto, Canada, 1991, p. 995.
[17]D. W. Siitari, M. Sagiyama, and T. Hara, *Transactions ISIJ*, **23** (1983) 959.
[18]G. W. Loar, K. R. Romer, and T. Aoe, *Plating and Surface Finishing* (March 1991) 74.
[19]G. Bech-Nielsen, *Corros. Sci.* **38** (1996) 1385.
[20]G.Bech-Nielsen, in *Electrochemical Methods in Corrosion Research*, *IV*, Ed. by O. Forsén, Materials Science Forum, Vols. 111–112. Trans. Tech. Publications, Aedermannsdorf, Switzerland, 1992, p. 525.
[21]N. N. Greenwood and A. Earnshaw, *Chemistry of the Elements*, Pergamon Press, Oxford, 1984, p. 718.

[22]G. G. Penov, Z. Ya. Kosakovskaya, A. P. Botneva, L. A. Andreeva, and N. P. Zhuk, *Zashchita Metallov (Protection of Metals)* **6** (1970) 544.
[23]Ya. M. Kolotyrkin, *Trans. SAEST* **12** (1977) 311.
[24]R. C. Bhardwaj, A. Gonzalez-Martin, and J. O'M. Bockris, *J. Electrochem. Soc.* **139** (1992) 1050.
[25]C. M. Vitus and A. J. Davenport, *J. Electrochem. Soc.* **141** (1994) 1291.
[26]U. H. Bapst, *Surface Sci.* **181** (1987) 157.
[27]D. O. Wipf and A. J. Bard, *J. Electrochem. Soc.* **138** (1991) L4.
[28]D. O. Wipf and A. J. Bard, *J. Electrochem. Soc.* **138** (1991) 469.
[29]T. P. Moffat, F.-R. F. Fan, and A. J. Bard, *J. Electrochem. Soc.* **138** (1991) 3224.
[30]P. K. Hansma, R. Sonnenfeld, J. Schneir, O. Marti, S. A. C. Gould, C. B. Prater, A. L. Weisenhorn, B. Drake, H. Hansma, G. Slough, W. W. McNairy, and R. V. Coleman, in *Scanning Tunneling Microscopy and Related Methods*, Ed. by R. J. Behm, N. Garcia, and H. Rohrer, Kluwer, Deventer, The Netherlands, 1990, 299.
[31]A. J. Melmed, *J. Vac. Sci. Technol.* **B 9** (1991).
[32]C. E. Bach, R. J. Nichols, W. Beckmann, H. Meyer, A. Schulte, J. O. Besenhard, and P. D. Jannakoudakis, *J. Electrochem. Soc.* **140** (1993) 1281.
[33]R. Sonnenfeld and P. K. Hansma, *Science* **232** (1986) 211.
[34]A. I. Danilov, *Russ. Chem. Rev.* **64** (1995) 767.
[35]D. M. Kolb, in *Structure of Electrified Interfaces*, Ch. 3, Ed. by J. Lipkowski and P. N. Ross, VCH Publishers, New York, 1993.
[36]P. Marcus and V. Maurice, *Materials Science Forum* **185–188** (1995) 221.
[37]V. E. Henrich, G. Dresselhaus, and H. J. Zeiger, *Phys. Rev. Lett.* **36** (1976) 1335.
[38]H. Onishi and Y. Iwasawa, *Surface Sci.* **357/358** (1996) 773.
[39]R. A. Goschke, K. Vey, M. Mayer, U. Walter, E. Goering, M. Klemm, and S. Horn, *Surface Sci.* **348** (1996) 305.
[40]M. P. Ryan, R. C. Newman, S. Fujimoto, G. E. Thompson, S. G. Corcoran, and K. Sieradzki in *Modifications of Passive Films,* Ed. by P. Marcus, B. Baroux, and M. Keddam, EFC Publication No. 12, Institute of Materials, London, 1994, p. 66.
[41]V. Maurice, H. Talah, and P. Marcus, in *Modifications of Passive Films,* Ed. by P. Marcus, B. Baroux, and M. Keddam, EFC Publication No. 12, Institute of Materials, London, 1994, p. 62.
[42]V. Maurice, H. Talah, and P. Marcus, *Surface Sci.* **304** (1994) 98.
[43]V. Maurice, W. P. Yang, and P. Marcus, *J. Electrochem. Soc.* **143** (1996) 1182.
[44]V. Maurice, W.P. Yang, and P. Marcus, *J. Electrochem. Soc.* **141** (1994) 3016.
[45]B. J. Cruickshank, A. A. Gewirth, R. M. Rynders, and R. C. Alkire, *J. Electrochem. Soc.* **139** (1992) 2829.
[46]O. Lev, Fu-Ren Fan, and A. Bard, *J. Electrochem. Soc.* **135** (1988) 783–784.
[47]R. C. Bhardwaj, A. González-Martin, and J. O'M. Bockris, *J. Electrochem. Soc.* **138** (1991) 1901.
[48]M. P. Green, *International Laboratory* **July/August** (1993) 25.
[49]F.-R. F. Fan and A. J. Bard, *J. Electrochem. Soc.* **136** (1989) 166.
[50]G. Gugler, J. D. Neuvecelle, P. Mettraux, E. Rosset, and D. Landolt in *Modifications of Passive Films*, Ed. by P. Marcus, B. Baroux, and M. Keddam, EFC Publication No. 12, Institute of Materials, London, 1994, p. 277.
[51]N. Casillas, S. J. Charlebois, W. H. Smyrl, and H. S. White, *J. Electrochem. Soc.* **140** (1993) L142.
[52]N. Casillas, S. J. Charlebois, W. H. Smyrl, and H. S. White, *J. Electrochem. Soc.* **141** (1994) 636.

[53]S. B. Basame and H. S. White, *J. Phys. Chem.* **99** (1995) 16430.
[54]R. C. Bhardwaj, A. González-Martin, and J. O'M. Bockris, *J. Electrochem. Soc.* **139** (1992) 1050.
[55]Ya. M. Kolotyrkin, *Corrosion* **19** (1963) 261.
[56]Avesta Sheffield, *Corrosion Handbook for Stainless Steels*, Avesta, Sheffield, 1994.
[57]M. G. Fontana and N. D. Greene, *Corrosion Engineering*, 2nd ed., McGraw-Hill, New York, 1978.
[58]P. C. Pistorius and G. T. Burstein, *Corros. Sci.* **36** (1994) 525.
[59]Z. Szklarska-Smialowska, *Corrosion* 27 (1971) 223.
[60]R Melström and S. Bernhardsson, in *Proc. 9th Scandinavian Corrosion Congress*, Vol. 1, Korrosionscentralen ATV, Brøndby, Denmark, 1983, p. 43.
[61]R. Quarfort, *Corros. Sci.* **29** (1989) 987.
[62]R. G. Kelly, in *Corrosion Tests and Standards: Application and Interpretation*, Ed. by R. Baboian, ASTM Manual Series, MNL 20 (1995) 166.
[63]R. J. Brigham, *Corrosion* **28** (1972) 177.
[64]R. J. Brigham and E. W. Tozer, *Corrosion* **29** (1973) 33.
[65]R. J. Brigham and E. W. Tozer, *Corrosion* **30** (1974) 161.
[66]R. J. Brigham and E. W. Tozer, *Corros. Sci.* **15** (1975) 579.
[67]S. Bernhardsson, R. Melström and B. Brox, in *Corrosion/80-NACE*, NACE International, Houston, Texas. (1980) p. 85.
[68]P. Lau and S. Bernhardsson, in *Proc. Winter Meeting ofthe Danish Metallurgical Society*, (in English), Danish Metallurgical Society, 1986, p. 225.
[69]E. Arnvig and A. D. Bisgård, in *Corrosion/96-NACE*, NACE International, Houston, Texas, 1996, p. 437.
[70]ASTM G48 - 92. *Annual Book ofASTM Standards*, Vol. 03.02, 1996.
[71]R. Quarfort, *Corros. Sci.* **28** (1988) 135.
[72]P. E. Arnvig and R. M. Davison, in *Corrosion/93-NACE*, NACE International, Houston, Texas, 1993.
[73]T. Mathiesen and E. Maahn, "Guide to the Pitting Electrode," pamphlet (in Danish), Institute of Metallurgy, The Technical University of Denmark, 1991.
[74]ASTM G5 - 94 *Annual Book ofASTM Standards*, Vol. 03.02, 1996.
[75]Z. Szklarska-Smialowska, *Pitting Corrosion of Metals*, National Association of Corrosion Engineers, Houston, Texas, 1986.
[76]T. Shibata and T. Takeyama, *Corrosion* **33** (1977) 243.
[77]V. M. Salinas-Bravo and R. C. Newman, *Corros. Sci.* **36** (1994) 67.
[78](a) M. A. V. Devanathan and Z. Stachurski, *Proc. Roy. Soc. (Lond.)* **270A** (1962) 90; (b) K. J. Vetter, *Electrochemical Kinetics*, Academic Press, New York, 1967, pp. 609–614; (c) J. O. M. Bockris and S. U. M. Khan, "Surface Electrochemistry," Plenum Press, New York, 1993, 808.
[79]P. Manolatos, M. Jerome, and J. Galland, in *Hydrogen Transport & Cracking in Metals*, Ed. by A. Turnbull, Institute of Materials, London, 1995, p. 155.
[80]P. K. Subramanyan, in *Comprehensive Treatise of Electrochemistry*, Ed. by J. O.'M. Bockris, B. E. Conway, E. Yeager, and R. E. White, Vol. 4, Plenum Press, New York, 1981, p. 411.
[81]K. J. Vetter, *Electrochemical Kinetics*, Academic Press, New York, 1967, p. 516.
[82]M. A. V. Devanathan and Z. Stachurski, *J. Electrochem. Soc.* **111** (1964) 619.
[83]J. O.'M. Bockris, J. McBreen, and L. Nanis, *J. Electrochem. Soc.* **112** (1965) 1025.
[84]R. N. Iyer, H. W. Pickering, and M. Zamanzadeh, *Scripta Metallurgica* **22** (1988) 911.
[85]R. N. Iyer, H. W. Pickering, and M. Zamanzadeh, *J. Electrochem. Soc.* **136** (1989) 2463.

[86]L. V. Nielsen, "The Effect of Cathodic Protection and Microbiological Activity on Hydrogen-Related Cracking in Steel," PhD thesis, The Technical University of Denmark, 1995.
[87]G. M. Pressouyre, *Metallurg. Trans.* **10A** (1979) 1571.
[88]A. Turnbull, *Corros. Sci.* **34** (1993) 921.
[89]A. J. Kumnick and H. H. Johnson, *Acta Metallurgica* **28** (1980) 33.
[90]M. Iino, *Acta Metallurgica* **30** (1982) 377.
[91]M. Iino, *Acta Metallurgica* **30** (1982) 367.
[92]J. B. Leblond and D. Dubois, *Acta Metallurgica* **31** (1983) 1459.
[93]R. A. Oriani, *Acta Metallurgica* **18** (1970) 147.
[94]L. Coudreuse and J. Charles, *Corros. Sci.* **27** (1987) 1169.
[95]M. J. Robinson and P. J. Kilgallon, *Corrosion* **50** (1994) 626.
[96]L V. Nielsen, *Evaluation of Soil Corrosivity: Design of an Electrochemical Soil Probe*, technical report, Department of Manufacturing Engineering, Corrosion and Surface Technology, The Technical University of Denmark, 1996.
[97]L V. Nielsen, *Evaluation of Hydrogen-Related Stress Corrosion Cracking in High-Pressure Pipelines*, Technical report, Department of Manufacturing Engineering, Corrosion and Surface Technology, The Technical University of Denmark, 1996.
[98]H Arup, in *9th Scandinavian Corrosion Congress*, Korrosionscentralen ATV, Glostrup, Denmark, 1983, p. 825.
[99]H Arup, in *10th Scandinavian Corrosion Congress*, Swedish Corrosion Institute, Stockholm, 1986, p. 1.
[100]C. Christensen, H. Arup, P. Press, and P. B. Mortensen, in *Hydrogen Transport & Cracking in Metals*, Ed. by A. Turnbull, Institute of Materials, London, 1995, p. 161.
[101] NDE STÅBI (NDE Handbook), Ed. by K. G. Bøving, Teknisk Forlag A/S, Copenhagen, 1987, Fig. 4, p. 38 (English version published by Woodhead Publishing, England).

This Page Intentionally Left Blank

Cumulative Author Index for Numbers 1–31

This Page Intentionally Left Blank

Cumulative Title Index for Numbers 1–31

Index